Near-Surface-Mounted Fiber-Reinforced Polymer Strips for Strengthening of Reinforced Concrete Girders

by

Eric Arthur Bertolotti

A thesis submitted to the Graduate Faculty of
Auburn University
in partial fulfillment of the
requirements for the Degree of
Master of Science

Auburn, Alabama
7 May 2012

Keywords: bridges, repair, retrofit,
debonding, testing

Approved by

Robert W. Barnes, Chair, Associate Professor of Civil Engineering
Justin D. Marshall, Assistant Professor of Civil Engineering
Anton K. Schindler, Associate Professor of Civil Engineering

ABSTRACT

The AL 97 bridge over I-65 near Letohatchee, Alabama, has been found to have deficient negative-moment capacity under current loading standards. A near-surface-mounted fiber-reinforced polymer (NSM FRP) strengthening system has been proposed (Alexy 2009) to repair the deficiency. A survey of relevant literature regarding the intermediate-crack (IC) debonding of NSM FRP revealed tests generally with reinforcement ratios and concrete compressive strengths higher than those present in the Letohatchee bridge; similarly, few previous tests involved specimens cracked prior to strengthening. To generate experimental data for direct correlation with the bridge, a laboratory test series was developed to study the performance of the NSM system.

Eight specimens were fabricated with Grade 40 steel reinforcement and 3000 psi concrete, cracked, repaired with NSM FRP strips, subjected to service-load cycles, and tested by monotonic loading until failure. Simultaneously, a nonlinear, layer-by-layer flexural analytical model—to account for strain hardening in the steel, tension stiffening of the concrete, and the cracked nature of the specimens at repair—was used to produce theoretical performance data for comparison to the experimental results alongside the capacity predictions resulting from the limiting design values recommended by ACI 440 (2008), Standards Australia (2008), and Seracino et al. (2007).

Analysis of the data obtained from both the service-load cycles and the monotonic loading showed no evidence of bond degradation; on the contrary, examination of the state of the

specimens after failure and all experimental results indicates a strong bond through ultimate capacity. The capacities predicted by the three evaluated design methods were nearly equivalent at all levels of reinforcement for the parameters of the test and proved conservative. The viability of the design recommended by Alexy (2009) was confirmed.

ACKNOWLEDGEMENTS

I would like to start by thanking Dr. Robert Barnes for his invaluable wisdom and expertise and continual guidance throughout my collegiate career. I would like to thank Dr. Justin Marshall and Dr. Anton Schindler for their time and input as my committee members and their knowledge as professors and engineers, as well as the numerous other professors at Auburn University who have helped to shape my thought process as an engineer. The help provided by the countless graduate and undergraduate research assistants who contributed aid during fabrication and strengthening is greatly appreciated; special thanks belong to Kaylor McCain for his help in carrying out the innumerable details during all phases of testing. The support provided by the Alabama Department of Transportation (ALDOT) for this research is greatly appreciated.

Finally, I am eternally grateful to my parents Marion and Melisa Bertolotti, my sister Claire, and the rest of my family for their steadfast love, encouragement, and wisdom—without which I would not be the man I am today.

TABLE OF CONTENTS

LIST OF TABLES

LIST OF FIGURES

CHAPTER 1: INTRODUCTION

1.1 General Background

The Alabama Department of Transportation (ALDOT) has received Federal Highway Administration (FHWA) funding to strengthen The AL 97 bridge over I-65 in Lowndes County, near Letohatchee, Alabama—Bridge Inventory Number (BIN) 8847, seen in Figure 1.1—through the TEA-21 Innovative Bridge Research and Construction (IBRC) program. For this particular bridge design, concerns exist regarding the negative-moment capacity of the girders in portions of each span.

Figure 1.1 Letohatchee Bridge (Alexy 2009)

Fiber-reinforced polymer (FRP) laminates have been shown to provide adequate flexural strengthening for reinforced concrete bridge girders. For the negative-moment strengthening of girders, the FRP can be applied in a near-surface-mounted (NSM) configuration—as opposed to an externally-bonded (EB) configuration—that provides the necessary reinforcement with limited exposure to traffic and environmental distress and requires little surface preparation of the concrete beyond the grooves needed for installation. Figure 1.2 shows a simplified example of the two main FRP configurations, with Figure 1.3 depicting the application of an NSM system into epoxied grooves.

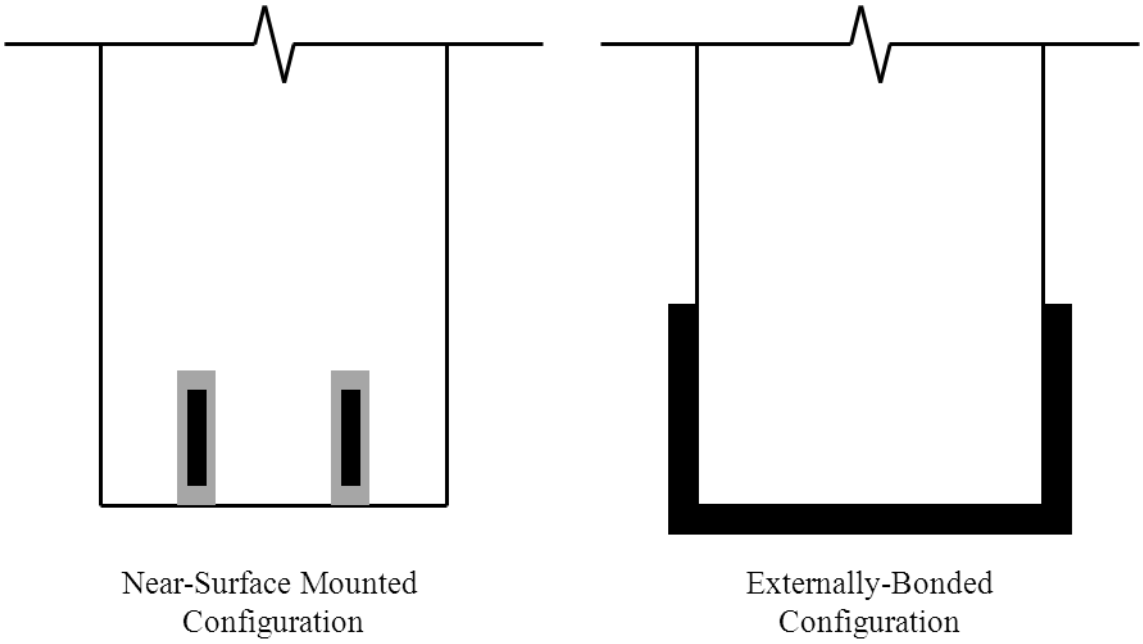

Figure 1.2 Basic Configuration of NSM and EB FRP Reinforcements

Figure 1.3 Field Installation of NSM FRP (Hughes Brothers 2011)

However, among the previous research conducted using NSM FRP strips as flexural strengthening, no test data readily correlate to the low reinforcement ratios, likely concrete compressive strength, and cracked nature of the girders in the Letohatchee bridge. Thus, in order to properly assess the effectiveness and performance of any proposed strengthening scheme, specimens representative of the state of the Letohatchee bridge girders needed to be fabricated, strengthened, and tested.

Alexy (2009), after performing strength calculations for the bridge, proposed an NSM FRP strengthening scheme generated from an appraisal of multiple arrangements of carbon FRP strips paired with the limiting values produced by three design methods—ACI 440 (2008), Standards Australia (2008) and Seracino et al. (2007)—over a range of concrete compressive strengths. If the strengthening scheme proves effective for this bridge, similar systems could be

applied to strengthen other bridges that were constructed using the same ALDOT standard design.

1.2 Research Objectives

The primary objective of this research was to evaluate the behavior of cracked reinforced concrete (RC) beams retrofitted with NSM FRP. To accomplish this main objective, several secondary objectives were targeted:

1. Study the effect of varying steel and FRP reinforcement ratios on the strengthened moment capacity of retrofitted specimens with concrete compressive strengths that are conservatively representative of in-service 50-yr-old RC bridges.
2. Evaluate existing intermediate-crack debonding models and limits against experimentally obtained flexural results.
3. Correlate flexural test results to existing Letohatchee bridge girders in order to verify or improve upon the previously proposed FRP strengthening scheme.

1.3 Organization of Thesis

Background on FRP research relevant to the Letohatchee project is presented in Chapter 2. The material properties, applications, and failure modes associated with FRP are discussed. Design models pertaining to the prediction and limiting of intermediate-crack (IC) debonding in near-surface-mounted reinforcement are detailed, as well as existing experimental tests regarding the IC debonding resistance of near-surface-mounted FRP applications. The strength assessment of the Letohatchee bridge by Alexy (2009), with a proposed strengthening scheme and testing program, is reviewed.

An overview of the design and fabrication of the test specimens is presented in Chapter 3. The controlling parameters for design are discussed. The fabrication process and accompanying

laboratory material tests are detailed. The cracking of the completed specimens in preparation for repair is described. Chapter 4 details the FRP installation process. Suggestions are made for field application based on experienced gained. A description of the testing program is given in Chapter 5. The instrumentation and loading configuration of the test specimens are detailed. The applications of service-load cycles and monotonic loading for each specimen are described.

The analytical procedures applied to the specimens for comparison with the experimental results are discussed in Chapter 6. The details regarding the establishment of the parameters for analysis are given. An evaluation of the resulting predicted moment-curvature behavior is provided. The determination of the predicted nominal moment capacities relative to established failure limits is described.

The results for the eight specimens tested in flexure and accompanying relevant discussions are presented in Chapter 7. Specifically, the service-load performance, strength testing performance, level of strain in the FRP reinforcement, experimental and predicted moment capacities, longitudinal strain distribution of the FRP, and internal force contribution of the FRP are described in detail. Chapter 8 summarizes the thesis and lists conclusions and recommendations based on the evaluation of the results from the testing program. Recommendations for future testing and application are also given.

CHAPTER 2: PROJECT BACKGROUND AND LITERATURE REVIEW

2.1 FRP Strengthening of Reinforced Concrete Beams

Much recent research has been performed to qualitatively understand the behavior of fiber-reinforced polymer (FRP) used to strengthen existing structures and to quantity the increase in capacity provided by the material, as FRP has been found to be both stronger and lighter than steel. Premature debonding has been often observed in externally-bonded applications as well as some near-surface-mounted systems; understanding the conditions that result in this behavior is important for the effective implementation of FRP as a strengthening material (Vasquez 2008). The survey of previous research and discussion of FRP applications and behavior in this chapter is focused on near-surface-mounted systems—the application method used for the research described in this thesis—and intermediate-crack debonding—the predicted failure mode of the FRP-repaired specimens in this project.

2.1.1 Applications of FRP

FRP applications to existing structures can be divided into two main categories: externally-bonded (EB) systems and near-surface-mounted (NSM) systems. Regardless of application type, the composition of FRP typically involves one of three fiber types—carbon, glass, or aramid fibers (ACI 440 2008)—with compositions involving carbon fiber being the most prolifically applied in available literature on bridge strengthening and repair, while aramid fibers are the least applied (Alexy 2009).

Generally, FRP materials have a higher ultimate tensile strength than steel. Table 2.1 lists typical values for tensile strength and Young's modulus encountered for FRP.

Table 2.1 FRP Material Properties (Adapted from ACI 440.2R-08)

FRP Fiber Type	Ultimate Tensile Strength	Young's Modulus
Carbon	150–350 ksi (1,020–2,080 MPa)	15,000–21,000 ksi (100–140 GPa)
Glass	75–200 ksi (520–1,400 MPa)	3,000–6,000 ksi (20–40 GPa)
Aramid	100–250 ksi (700–1,720 MPa)	7,000–10,000 ksi (48–68 GPa)

As shown, all of these FRP materials have a greater ultimate tensile strength relative to the yield strength of 60 ksi (420 MPa) and ultimate strength of 75 ksi (520 MPa) typically associated with reinforcing steel and have a smaller modulus of elasticity than the typical steel value of 29,000 ksi (200 GPa). Behaviorally, unlike steel reinforcement, FRP reinforcement does not yield, remaining linear-elastic until failure. As a result, FRP ruptures with a brittle failure in tension. FRP ruptures at an approximate strain of 1–3%; by comparison, steel typically ruptures at approximately 30% (Vasquez 2008).

Another important property of FRP relative to steel is its density. As seen in Table 2.2, the typical density of FRP falls at a magnitude approximately 4–6 times less than that of steel.

Table 2.2 Material Density Values (ACI 440.2R-08)

Steel	CFRP	GFRP	AFRP
490 pcf (7.9 g/cm^3)	90–100 pcf (1.5–1.6 g/cm^3)	75–130 pcf (1.2–2.1 g/cm^3)	75–90 pcf (1.2–1.5 g/cm^3)

The lower density of the FRP coupled with the higher ultimate tensile strength relative to steel allows for the strengthening of deficient members with little change to the overall weight.

2.1.1.1 Externally-Bonded (EB) FRP

The most common implementation of FRP for the strengthening of existing reinforced concrete structures has been externally-bonded (EB) systems, where sheets of unidirectional or multidirectional FRP are bonded to the external surface of the concrete. Typical EB applications are either (a) wet-layup systems—where FRP sheets are saturated on site with resin, bonded to the concrete with the appropriate adhesive, and cured in place—or (b) precured systems—consisting of FRP sheets that are saturated and cured prior to site delivery and applied to the concrete surface with adhesive. Figure 2.1 shows the installation of precured FRP in externally bonded configuration. Both EB systems can provide strengthening for beams in flexure and shear and strengthening for columns, especially for seismic confinement (ACI 440 2008). However, EB FRP systems have been found—as discussed in previous research (Seracino et al. 2007; Liu, Oehlers, and Seracino 2006)—to debond from the concrete surface at relatively low values of FRP axial strain.

Figure 2.1 Installation of a Precured System (Carmichael and Barnes 2005)

2.1.1.2 Near-Surface-Mounted (NSM) FRP

In response to the sensitivity of EB systems to debonding behavior, the implementation of near-surface-mounted (NSM) FRP reinforcement has become more prevalent (Seracino et al. 2007). Rather than bonding the laminate to the exterior of the concrete member, NSM systems bond the FRP via an epoxy or similar adhesive in grooves cut into the concrete surface. A detailed description of the NSM FRP installation procedure is presented in Chapter 4. Figure 2.2 shows the field application of an NSM system for positive-moment strengthening, while Figure 2.3 shows the laboratory installation of NSM strips to represent negative-moment strengthening.

Figure 2.2 Field Installation of NSM FRP (Hughes Brothers 2011)

Figure 2.3 Laboratory Installation of NSM FRP

If strengthening requires more than one NSM strip or bar, one or more parallel grooves are cut a specified distance away from the initial groove. NSM FRP reinforcement is commonly produced in two types: rods and strips. The rods are typically manufactured as FRP versions of deformed steel reinforcement, with a circular cross section, deformations along the length, and a cross-sectional area equivalent to that of a U.S. Customary size #3 or #4 (SI #10 or #13) steel reinforcing bar. NSM strips have a rectangular cross section, with typical dimensions of 2–4.5 mm (0.079–0.177 in.) thick by 16 mm (0.63 in.) wide. The rods are typically delivered to the site cut to the required length, while the NSM strips are delivered in rolls no greater than 250 feet in length (Hughes Brothers 2011).

One of the inherent advantages of NSM systems over EB systems is that bond can be established between the FRP and the concrete on three faces of the strip rather than just one face. As EB systems are known to fail due to FRP debonding, the increased bond capacity of NSM strips should theoretically increase the debonding resistance of the FRP.

2.1.2 Failure Modes of FRP-Strengthened Members

The controlling failure mode for FRP strengthening systems depends on multiple parameters, such as the location of FRP termination, the compressive strength of the concrete, the bonded width of the FRP, and the rupture stress of the FRP. Strengthened members can fail as a result of (a) debonding of the FRP, caused either by plate-end (PE) debonding or intermediate-crack (IC) debonding, (b) rupture of the FRP reinforcement, (c) failure in the concrete, or any combination of these modes.

2.1.2.1 Plate-End (PE) Debonding

Plate-end (PE) debonding occurs when shear stresses in the FRP reinforcement at the terminus become too high and cause the plate to detach from the concrete, with the failure occurring either

in the concrete or the adhesive layer. Figure 2.4 illustrates the debonding mechanism for this failure mode.

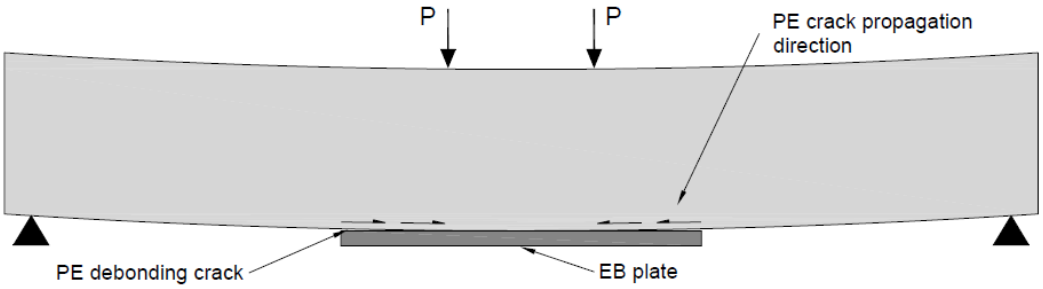

Figure 2.4 Illustration of PE Debonding (Vasquez 2008)

2.1.2.2 Intermediate-Crack (IC) Debonding

Intermediate-crack (IC) debonding occurs when a flexural crack in the concrete—typically within or near the maximum moment region of the member (Vasquez 2008)—creates a stress concentration in the FRP reinforcement. Figure 2.5 depicts an illustration of the IC-debonding mechanism.

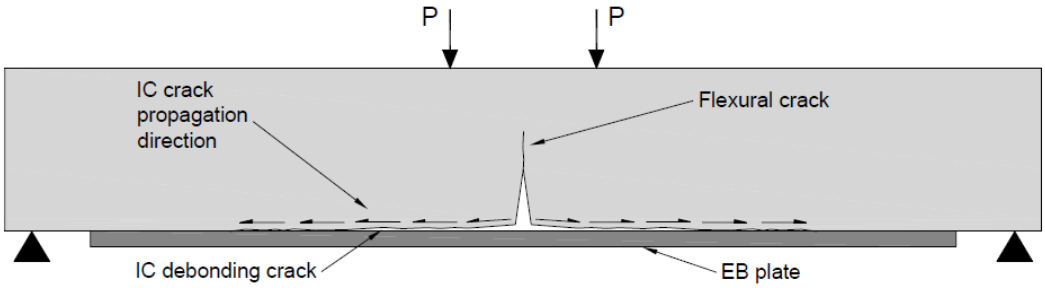

Figure 2.5 Illustration of IC Debonding (Vasquez 2008)

Once the stress exceeds a limiting value at the FRP-to-concrete interface, the FRP reinforcement begins to delaminate from the concrete. Subsequently, the debonding propagates from the flexural crack to flexural crack to the end of the reinforcement, rendering the FRP ineffective (Vasquez 2008).

2.1.2.3 FRP Rupture

Failure due to FRP rupture maximizes the efficiency of the FRP reinforcement, allowing the strengthening material to attain full capacity. As previously discussed, the FRP reinforcement remains in the linear-elastic range of behavior until rupture. Once the rupture stress is achieved, the FRP material does not yield, but rather fails in a brittle manner; thus, the reinforcement provides no further strengthening to the member and cannot sustain additional loading.

2.1.2.4 Concrete Failure

If the strength of the concrete is low enough or if a large amount of FRP is used to reinforce the member, the concrete can fail before any failure occurs in the FRP reinforcement. Concrete failure can occur due to concrete crushing in the compressive region of the member or due to shear failure.

2.1.2.5 Combined Failure Modes

Frequently, FRP-strengthened members can fail by a combination of failure modes, wherein the differing failure modes occur almost simultaneously, resulting in difficulty in distinguishing the mode responsible for collapse.

Some researchers have given designations to the more prevalent of these combined failure modes. One such mode—termed critical diagonal crack (CDC) debonding—results from a combination of PE and IC debonding caused by a diagonal shear crack (Vasquez 2008). If the shear crack that occurs within the shear span of the member reaches the FRP reinforcement near the end of the plate, peel-off failure could occur due to stress concentrations at the crack and limited bond length beyond the crack. Figure 2.6 illustrates the CDC-debonding mechanism.

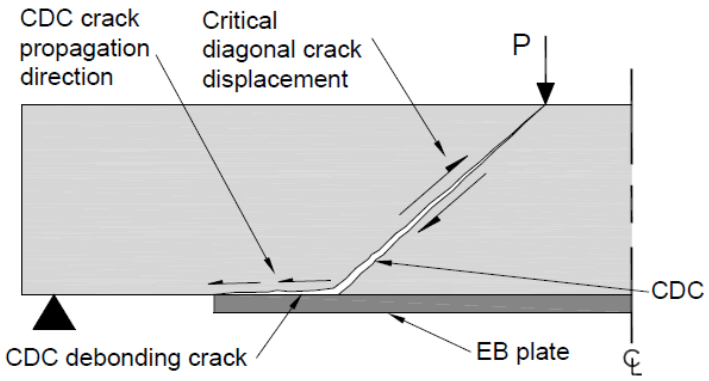

Figure 2.6 Illustration of CDC Debonding (Vasquez 2008)

Another commonly observed combined failure mode is cover delamination—a combination of debonding and concrete failure. Similar to PE debonding, when the shear stresses at the terminus of the FRP reinforcement get too large, separation of the plate begins. However, in cover delamination, the failure plane continues into the concrete section up to the longitudinal tensile reinforcing steel. Rather than merely the FRP plate debonding, the entire concrete cover, beginning at the terminus of the plate, separates from the beam (ACI 440 2008).

2.1.3 Design Approaches for IC-Debonding Resistance of NSM FRP

Currently, neither the American Concrete Institute (ACI), the International Federation for Structural Concrete (*fib*), nor Standards Australia have set forth any building code requirements that specifically address FRP systems for strengthening concrete structures; however, these organizations have published guides and recommendations for design and implementation of EB FRP systems, with some additional guidelines for NSM FRP applications.

Similarly, multiple researchers have developed design limits calibrated from their experimental data for IC-debonding resistance as a function of either the tensile strain or force experienced by the FRP reinforcement. More recently, Oehlers et al. (2011) proposed a unified approach for reinforced concrete beams retrofitted with FRP reinforcement hinging on the

separation of the behavior within reinforced concrete specimens between undisturbed regions controlled by conventional moment-curvature analyses and disturbed regions defined by discrete rotations. The discrete-rotation model depends on three fundamental principles: linear rigid-body displacements, shear friction or aggregate interlock, and IC theory—the partial-interaction behavior (interface slip) from the commencement of crack widening to debonding. The researchers theorized that this approach can be used to produce specific models to deal with the behavior of FRP-strengthened concrete structures regarding flexure, shear, moment redistribution, ductility, and confinement; however, as of the completion of this thesis, no definite models for limiting IC debonding have been generated from this theory.

2.1.3.1 ACI 440.2R-08

ACI Committee 440—"Fiber Reinforced Polymer Reinforcement"—has published ACI 440.2R-08, entitled "Guide for the Design and Construction of Externally Bonded FRP Systems for Strengthening Concrete Structures", to offer guidelines in the application of FRP. The main focus of the document is EB FRP reinforcement, but NSM FRP reinforcement—the focus of this thesis—is briefly addressed.

The design recommendations portion of ACI 440.2R-08 is divided into six main categories: general design considerations; flexural strengthening; shear strengthening; strengthening of members subjected to axial force or combined axial and bending forces; FRP reinforcement details; and drawings, specifications, and submittals. Under general design considerations, the ultimate FRP rupture stress and strain—as reported by the manufacturer—are reduced by an environmental reduction factor, C_E, to account for possible degradation resulting from "exposure to certain environments, such as alkalinity, salt water, chemicals, ultraviolet

light, high temperatures, high humidity, and freezing-and-thawing cycles." Table 2.3 lists the recommended values for C_E based on fiber type and exposure conditions.

Table 2.3 Environmental Reduction Factor Values Given in ACI 440.2R-08

Exposure Conditions	Fiber Type	C_E
Interior exposure	Carbon	0.95
	Glass	0.75
	Aramid	0.85
Exterior exposure (bridges, piers, and unenclosed parking garages)	Carbon	0.85
	Glass	0.65
	Aramid	0.75
Aggressive environment (chemical plants and wastewater treatment plants)	Carbon	0.85
	Glass	0.50
	Aramid	0.70

The reduction in rupture stress and strain can be computed with Equation 2.1 and Equation 2.2:

$$f_{fu} = C_E f_{fu}^* \quad \textbf{Equation 2.1}$$

$$\varepsilon_{fu} = C_E \varepsilon_{fu}^* \quad \textbf{Equation 2.2}$$

where

f_{fu} = design ultimate strength of FRP
f_{fu}^* = ultimate tensile strength of FRP as reported by manufacturer
ε_{fu} = design rupture strain of FRP
ε_{fu}^* = ultimate rupture strain of FRP

Chapter 10 of ACI 440.2R-08 details the determination of the flexural capacity of FRP-strengthened reinforced concrete members. To prevent failure modes governed by IC debonding,

Section 10.1.1 limits the effective strain in the FRP reinforcement for NSM systems by Equation 2.3:

$$\varepsilon_{fd} = 0.7\varepsilon_{fu} \qquad \textbf{Equation 2.3}$$

where

ε_{fd} = debonding strain of FRP

The debonding strain for the FRP might fall between $0.6\varepsilon_{fu}$–$0.9\varepsilon_{fu}$, depending on member dimensions, reinforcement ratios, and the surface roughness of the FRP, though ACI 440 (2008) does not recommend the use of these values without supporting data. For EB applications, the effective strain limit is governed by a more complex equation calibrated from a database of flexural tests experiencing IC-debonding failures.

To accurately calculate the strain experienced in the FRP, the strain in the concrete prior to strengthening must be estimated to account for existing strain at the level of the FRP at the time of installation. The initial strain level can be calculated using an elastic cracked-section analysis of the unstrengthened section, applying only the loads that will be present on the member during strengthening. Using the existing substrate strain and assuming strain compatibility, the effective strain level in the FRP at the ultimate limit state can be found using Equation 2.4:

$$\varepsilon_{fe} = \varepsilon_{cu}\left(\frac{d_f - c}{c}\right) - \varepsilon_{bi} \leq \varepsilon_{fd} \qquad \textbf{Equation 2.4}$$

where

ε_{fe} = effective strain level in FRP at failure
ε_{cu} = maximum usable strain of unconfined concrete, generally taken as 0.003 in/in
d_f = effective depth of FRP reinforcement
c = neutral axis depth
ε_{bi} = strain in concrete substrate at time of FRP installation

Assuming perfectly elastic behavior, the effective stress in the FRP at ultimate can be calculated as follows:

$$f_{fe} = E_f \varepsilon_{fe} \qquad \textbf{Equation 2.5}$$

where

f_{fe} = effective stress in FRP at failure
E_f = modulus of elasticity for FRP reinforcement

Based on the strain level in the FRP reinforcement, the strain in the steel reinforcement for nonprestressed application can be determined from the equation

$$\varepsilon_s = \left(\varepsilon_{fe} + \varepsilon_{bi}\right)\left(\frac{d - c}{d_f - c}\right) \qquad \textbf{Equation 2.6}$$

where

ε_s = strain in nonprestressed steel reinforcement
d = effective depth of steel reinforcement

Using the calculated strain in the steel, the stress in the steel reinforcement can be found using Equation 2.7, assuming linear-elastic, perfectly-plastic behavior:

$$f_s = E_s \varepsilon_s \leq f_y \qquad \textbf{Equation 2.7}$$

where

f_s = stress in tensile steel reinforcement
E_s = modulus of elasticity for steel reinforcement
f_y = yield stress of steel

Having determined the stress and strain levels for both the steel and FRP reinforcement, the neutral axis depth, c, at failure can be calculated using Equation 2.8:

$$c = \frac{A_s f_s + A_f f_{fe}}{\alpha_1 f_c' \beta_1 b} \qquad \textbf{Equation 2.8}$$

where

A_s = area of tensile steel reinforcement
A_f = area of FRP
α_1 = multiplier on f_c' to determine intensity of equivalent rectangular stress distribution
β_1 = ratio of depth of equivalent stress block to depth of neutral axis
b = width of member compression block

The calculated value for c relies on the establishment of internal force equilibrium and strain compatibility by simultaneously satisfying Equation 2.4–Equation 2.8, using iteration until convergence is achieved. If concrete crushing is the controlling failure mode, α_1 and β_1 can be taken as the values associated with the Whitney stress block as defined in ACI 318-08. If the controlling failure mode is governed by FRP rupture or debonding prior to the concrete reaching the limiting compression strain, ε_{cu}, α_1 and β_1 can be calculated using the following equations derived from the stress-strain relationship for concrete, as found in the design examples in Chapter 15 of ACI 440 (2008, 51):

$$\beta_1 = \frac{4\varepsilon_c' - \varepsilon_c}{6\varepsilon_c' - 2\varepsilon_c} \qquad \textbf{Equation 2.9}$$

$$\alpha_1 = \frac{3\varepsilon_c'\varepsilon_c - \varepsilon_c^2}{3\beta_1 \varepsilon_c'^2} \qquad \textbf{Equation 2.10}$$

where

ε_c' = maximum strain of unconfined concrete corresponding to $f_c^{'}$ = 1.7 $f_c^{'}/E_c$
ε_c = concrete strain in extreme compression fiber

Figure 2.7 depicts the internal strain and stress distribution for a strengthened rectangular section under flexure at the ultimate limit state.

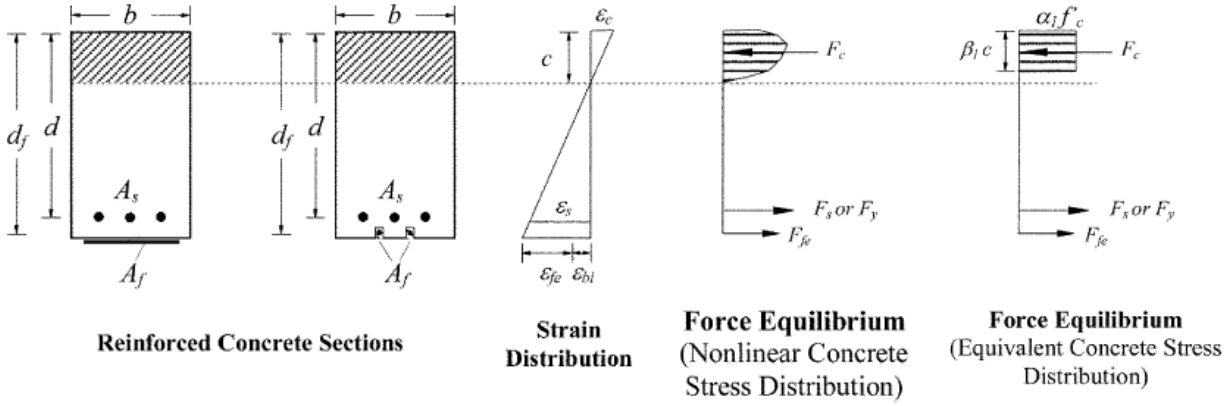

Figure 2.7 Internal Strain and Stress Profiles for Section under Flexure (ACI 440.2R-08)

After the neutral axis depth has been determined, the nominal moment capacity of the member can be found using Equation 2.11:

$$M_n = A_s f_s \left(d - \frac{\beta_1 c}{2}\right) + \psi_f A_f f_{fe} \left(h - \frac{\beta_1 c}{2}\right) \qquad \textbf{Equation 2.11}$$

where

M_n = nominal moment capacity
ψ_f = additional strength reduction factor for FRP = 0.85 for flexure
h = overall height of member

The two minus signs present in Equation 2.11 were erroneously omitted from the equation printed in ACI 440.2R-08.

Section 13.3 establishes the development length for NSM FRP systems by Equation 2.12:

$$l_{df} = \frac{d_b}{4\tau_b} f_{fd} \qquad \text{for circular bars}$$

Equation 2.12

$$l_{df} = \frac{a_b b_b}{2(a_b + b_b)\tau_b} f_{fd} \qquad \text{for rectangular bars}$$

where

l_{df} = development length of FRP
d_b = FRP bar diameter
τ_b = average bar stress for NSM FRP = 1000 psi (6.9 MPa)
f_{fd} = design stress of FRP
a_b = smaller cross-sectional dimension for rectangular FRP bars
b_b = larger cross-sectional dimension for rectangular FRP bars

Regarding serviceability, Section 10.2.8 of ACI 440.2R-08 limits the internal steel reinforcement to $0.80f_y$ and the concrete to $0.45f_c^{'}$ under service load to avoid inelastic deformations of reinforced concrete members.

2.1.3.2 Standards Australia

In 2008, Standards Australia published a design guide entitled "Design Handbook for RC Structures Retrofitted with FRP and Metal Plates: Beams and Slabs". The handbook outlines the generic and fundamental behaviors of plated beams and slabs. Some design rules and recommendations are given in the commentary, but none within the actual guidelines.

The Australian guide for FRP directly references ACI 440.2R-08 regarding the implementation of an environmental reduction factor, using the values listed in Table 2.3. One of the main focuses for the handbook concerns plate debonding, specifically PE debonding and IC debonding. For these debonding types, the guidelines state that debonding failure will occur within the concrete substrate, as the tensile strength of the adhesive is typically an order of magnitude stronger than that of the concrete.

Regarding IC debonding, the design guide describes two types of models: a basic IC-debonding model based on push-pull tests for use as a lower bound for beam capacity predictions and a more representative IC-debonding model for describing the actual behavior of plated beams. The only model applicable to the basic IC-debonding resistance of NSM applications is a generic model taken from Seracino, Raizal Saifulnaz, and Oehlers (2007).

Seracino, Raizal Saifulnaz, and Oehlers (2007) conducted fourteen push-pull tests using specimens with NSM FRP and derived an analytical model to predict the IC-debonding resistance of FRP-strengthened reinforced concrete members. The resulting model was used to analyze the fourteen tests as well as existing push-pull test data from the reference literature for NSM and EB applications.

Based on the local interface shear stress-slip relationship (τ-δ) relationship of the debonding interface, the derived model specifically uses a simplified linear-softening interface bond-slip relationship and a unique confinement ratio to yield a generic model applicable for both EB and NSM FRP and for any adhesively bonded plate cross section and material. The employed confinement ratio is given as the aspect ratio of the IC-debonding failure plane. Figure 2.8 depicts the IC-debonding failure planes for both EB and NSM applications.

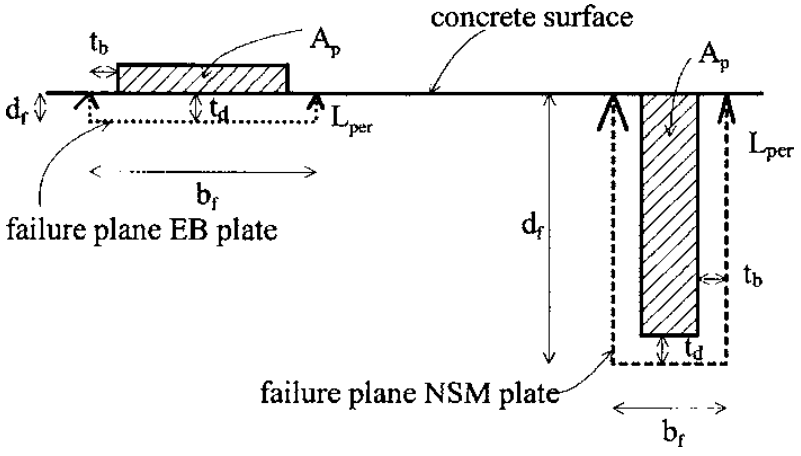

Figure 2.8 IC-Debonding Failure Planes (Seracino, Raizal Saifulnaz, and Oehlers 2007)

Using these debonding planes, the confinement ratio can be found using Equation 2.13:

$$\varphi_f = \frac{d_f}{b_f} \qquad \textbf{Equation 2.13}$$

where

φ_f = confinement ratio
d_f = length of failure plane perpendicular to concrete surface = $d_p + t_d$
d_p = FRP plate dimension perpendicular to concrete surface
b_f = length of failure place parallel to concrete surface = $b_p + t_b$
b_p = FRP plate dimension parallel to concrete surface
$t_d = t_b$ = distance to failure plane from face of FRP

Using a parametric analysis of the available data concerning the debonding, the authors recommend the value for both t_b and t_d as 0.04 in. (1 mm). The total length of the debonding failure plane, L_{per}, can be calculated using

$$L_{per} = 2d_f + b_f \qquad \textbf{Equation 2.14}$$

Once the above cross-sectional values are computed, the IC-debonding resistance can be determined using Equation 2.15:

$$P_{IC} = \alpha_p 0.85 \varphi_f^{0.25} f_c^{0.33} \sqrt{L_{per}(EA)_p} < f_{rupt} A_p \quad \text{for N-mm units}$$

$$P_{IC} = \alpha_p 0.393 \varphi_f^{0.25} f_c^{0.33} \sqrt{L_{per}(EA)_p} < f_{rupt} A_p \quad \text{for lb-in. units} \qquad \textbf{Equation 2.15}$$

where

P_{IC} = tensile resistance force to IC debonding
α_p = confidence factor = 1.0 for mean; 0.85 for lower 95% confidence limit
f_c = concrete compressive strength
$(EA)_p$ = axial rigidity of FRP
f_{rupt} = rupture stress of FRP
A_p = cross-sectional area of FRP plate = $d_p b_p$

This model is only a function of geometric and material properties and, as such, can be applied to any plate material. Once the debonding resistance is computed, the debonding stress and strain and corresponding moment capacity can be determined.

2.1.3.3 Seracino et al. (2007)

Thirty-six push-pull tests were conducted by Seracino et al. (2007) using NSM FRP strips, with a nonlinear statistical analysis of the resulting data used to develop a model to predict the maximum axial plate force for IC debonding at the NSM strip-to-concrete interface. The schematic for the NSM push-pull tests performed is shown in Figure 2.9.

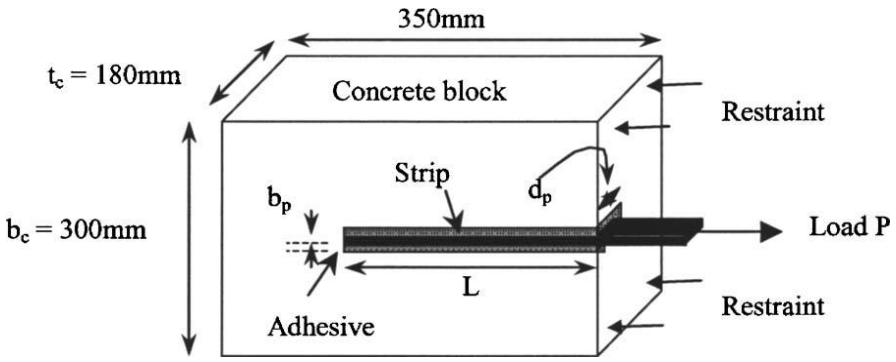

Figure 2.9 Schematic of NSM Push-Pull Test (Seracino et al. 2007)

From the analysis, the researchers found that the necessary parameters for determining the IC-debonding force are the concrete compressive strength and the dimensions of the NSM FRP strip. Using these variables and conducting a nonlinear regression analysis for optimization, the following formula was derived:

$$P_{IC} = \alpha\beta\sqrt{f_c}\, d_p^{1.36} b_p^{0.21} \leq f_{rupt} A_p \quad \text{for SI units}$$

$$P_{IC} = 3\alpha\beta\sqrt{f_c}\, d_p^{1.36} b_p^{0.21} \leq f_{rupt} A_p \quad \text{for U.S. Customary units}$$

Equation 2.16

where

α = confidence factor = 0.19 for mean values; 0.16 for characteristic values
β = bond-length factor
L = bonded length of FRP

Regarding the application of this model, f_c is limited to a range of 30–65 MPa (4400–9400 psi); d_p, to 10–20 mm (0.39–0.79 in.); and b_p, to 1.2–2.4 mm (0.047–0.094 in.). β, for any bonded length of FRP L, can be determined using

$$\beta = \begin{cases} 1.0 \\ L/200 \end{cases} \text{ for } \begin{matrix} L \geq 200 \text{ mm} \\ L < 200 \text{ mm} \end{matrix} \quad \text{for units of mm}$$

$$\beta = \begin{cases} 1.0 \\ L/7.9 \end{cases} \text{ for } \begin{matrix} L \geq 7.9 \text{ in.} \\ L < 7.9 \text{ in.} \end{matrix} \quad \text{for units of in.}$$

Equation 2.17

The researchers assert that the range of values considered for the tests—and subsequently applicable to the proposed model—covers reasonable expectations for material and geometric properties to be encountered in many practical applications. To maximize the achieved debonding resistance, the researchers recommend a minimum critical bonded length for the FRP of 200 mm (7.9 in.). The efficiency of the bond increases as the depth of the FRP into the concrete increases—an increase attributed to the improved confinement effect away from the concrete surface.

2.1.3.4 Said and Wu (2008)

Said and Wu (2008) surveyed two hundred previous EB test results of IC-debonding failures in beams and slabs to propose an IC-debonding model that would accurately predict the debonding strain of FRP strips. Although calibrated using EB tests, the proposed model was not specifically

restricted to EB applications and therefore might be applied to NSM systems. The authors assumed that debonding strain, ε_{db}, is a function of the compressive strength of the concrete, the modulus of elasticity of the FRP, and the thickness of the applied FRP plate, t_f. Using these parameters, the following equation was formulated:

$$\varepsilon_{db} = C1(f_c')^{C2}/\left(E_f t_f\right)^{C3} \quad \textbf{Equation 2.18}$$

The values $C1$, $C2$, and $C3$ are constants, with the dimensions of the parameters in N and mm. Using the two hundred tests from previous literature, Said and Wu calibrated the model to most accurately predict the debonding strain, ultimately arriving at values of 0.23, 0.2, and 0.35 for $C1$, $C2$, and $C3$, respectively. The authors used these values to generate a closed-form empirical solution for the debonding strain, as shown in Equation 2.19:

$$\varepsilon_{db} = 0.23(f_c')^{0.2}/\left(E_f t_f\right)^{0.35} \quad \textbf{Equation 2.19}$$

Said and Wu applied this model to the previous tests in order to predict the debonding strain, noting that the derived model more accurately predicted the IC-debonding capacity than any of the other models mentioned in the paper.

2.1.3.5 Additional Considerations for NSM Systems

Two factors involved in NSM placement are thought to affect strengthened capacity and debonding resistance: the spacing of the individual NSM strips and the depth of embedment within the concrete.

Appropriate spacing of NSM strips will result in individual failure planes. Conversely, too little spacing between strips can result in a singular common failure plane that will diminish the accuracy of the predicted ultimate load-carrying capacity. Similarly, inadequate distance

from the edge of the concrete to the FRP reinforcement can result in the spalling of the corner of the concrete (Blaschko 2003) or the premature debonding of the FRP strip (ACI 440 2008). Alexy (2009) summarized the recommendations from relevant literature, as seen in Table 2.4.

Table 2.4 Summary of NSM Groove Spacing and Side Cover Recommendations (Alexy 2009)

Source	Clear Spacing of Strips	Side Cover Distance
ACI Committee 440 (2008)	2 × (groove depth)	4 × (groove depth)
Hassan and Rizkalla (2004)	2 × (FRP bar diameter)	4 × (FRP bar diameter)
Kang et al. (2005)	40 mm (1.6 in.)	40 mm (1.6 in.)
Rashid, Oehlers, and Seracino (2008)	53 mm (2.1 in.)	3.5 × (FRP depth)
Vasquez (2008)	2.5 × (groove width)	—

Regarding embedment, Section 13.3 of ACI 440.2R-08 defines the minimum groove dimensions recommended for NSM systems, as seen in Figure 2.10, to provide adequate embedment depth.

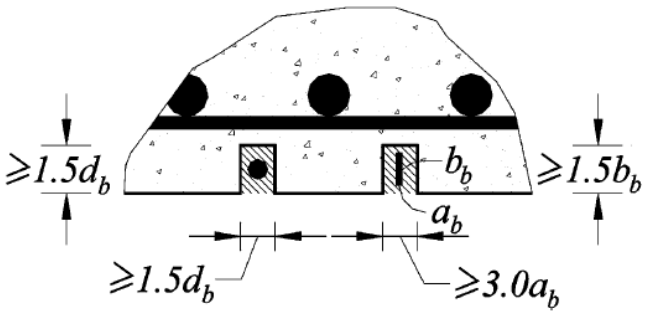

Figure 2.10 Minimum Recommended Groove Dimensions (ACI 440.2R-08)

With the embedment of NSM strips resulting in increased confinement and increased IC-debonding strains over EB systems, deeper embedment of the FRP into the concrete substrate provides a larger, and better confined, bonded surface between the two materials. Theoretically,

this extra embedment yields higher IC-debonding strains and, as a result, greater ductility (Oehlers et al. 2008).

Oehlers et al. (2008) conducted twenty pull tests to investigate the effects of embedding NSM strips at various groove depths. From the research, mathematical expressions were developed to describe the effects of embedment on IC-debonding resistance and the local bond-slip relationship. The authors stated that embedding NSM strips at deeper groove depths can increase debonding resistance up to three times over strips embedded at shallower depths. The improved FRP bond was also stated to allow the use of larger FRP cross sections. The authors also suggest that embedment may improve the fire resistance of FRP material.

2.1.4 Flexural Tests for NSM-FRP-Strengthened Beams

2.1.4.1 El-Hacha and Rizkalla (2004)

Eight reinforced concrete specimens were tested in the research performed by El-Hacha and Rizkalla (2004), with the goal of comparing multiple FRP strengthening methods. Seven of the beams were reinforced using FRP, four using NSM systems; the eighth beam was left unstrengthened for use as a control. The setup used for testing and the typical specimen cross section are displayed in Figure 2.11.

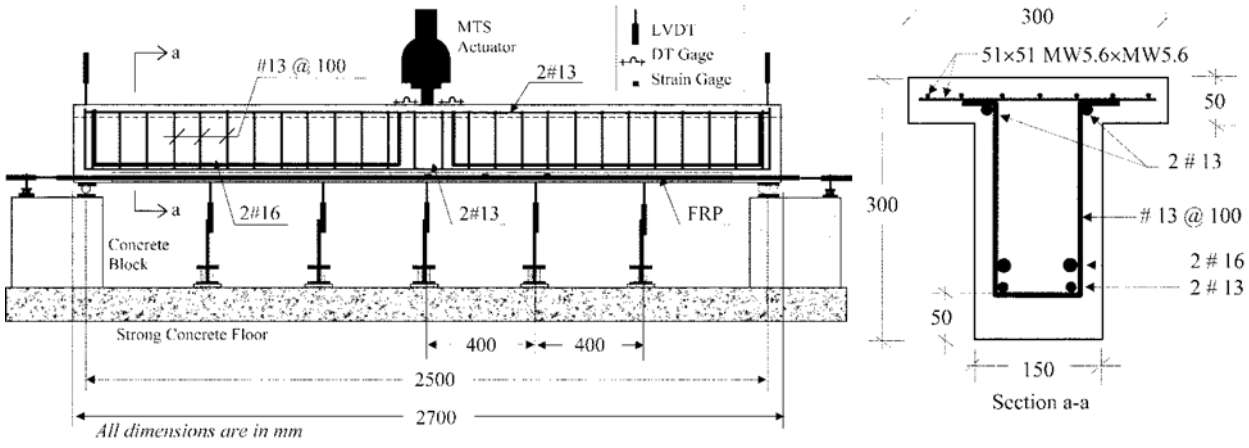

Figure 2.11 Testing Setup and Cross Section (El-Hacha and Rizkalla 2004)

The beams were reinforced using NSM bars, NSM strips, or EB strips composed of either carbon fiber-reinforced polymer (CFRP) or glass fiber-reinforced polymer (GFRP). The arrangement of the tensile steel reinforcement within the cross section was selected to ensure that flexural failure would occur within the midspan and to simulate corroded or damaged conditions encountered in the field. Three of the four NSM specimens had an f_c of 48 MPa (6900 psi) at the time of testing, with the four exhibiting a compressive strength of 57 MPa (8300 psi).

The application of FRP was found to have little impact on load-deflection behavior prior to cracking but significantly improved behavior after cracking, with the NSM systems also limiting deflections and crack widths. The comparison of NSM applications revealed that the NSM CFRP strips provided higher capacity than NSM CFRP bars with the same axial stiffness. The authors attributed this behavior to premature debonding of the NSM bars and to the smaller debonding surface of the bars relative to the strips.

2.1.4.2 Jung et al. (2005)

Jung et al. (2005) examined the change in flexural behavior of reinforced concrete beams strengthened by the addition of EB and NSM FRP reinforcement. Eight 3.00-meter-long specimens—with measured f_c of 31 MPa (4500 psi)—were tested in four-point bending to failure. Five of the eight beams were reinforced using NSM FRP, with two of the five also employing mechanical interlocking grooves to improve performance. Figure 2.12 shows the test setup and specimen dimensions, while Figure 2.13 depicts the NSM strengthening schemes employed during testing.

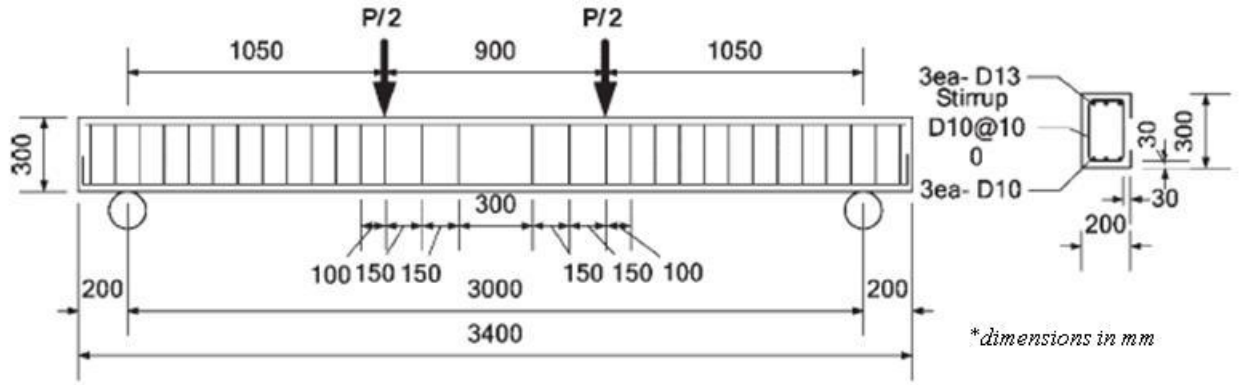

Figure 2.12 Test Setup and Specimen Dimensions (Jung et al. 2005)

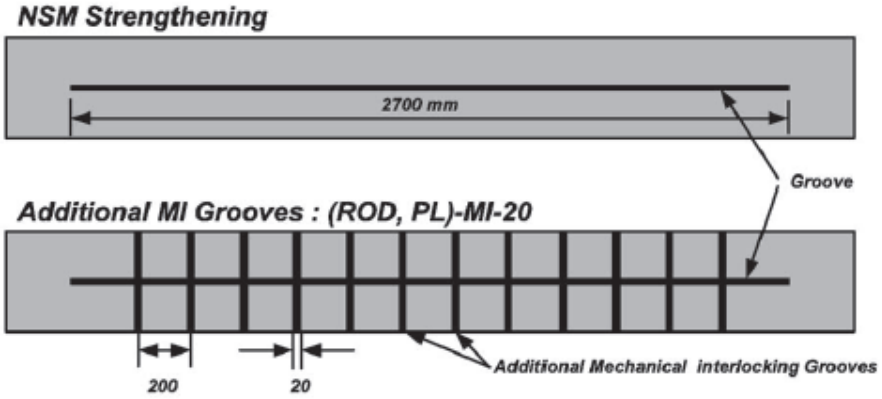

Figure 2.13 Bottom View of NSM Strengthening Schemes (Jung et al. 2005)

The researchers found that, prior to cracking, the FRP reinforcement made no significant contribution to capacity or stiffness within the elastic domain. However, after cracking and the yielding of the steel reinforcement, the NSM-strengthened specimens attained an increase in capacity of 39 to 65% over the unstrengthened specimen; by comparison, the EB applications only increased capacity by 30 to 47%.

Failure in two of the NSM-strengthened beams was governed by IC debonding of the CFRP and epoxy from the concrete, with the remaining three specimens—including both beams employing mechanical interlocking grooves—experiencing rupture of the FRP at failure. Ultimately, Jung et al. concluded that NSM strips provide a greater increase in moment capacity

than EB applications, with mechanical interlocking grooves further improving the efficiency and capacity of NSM applications by preventing premature debonding.

2.1.4.3 Harrison et al. (2006)

Harrison et al. (2006) tested four strengthening techniques for concrete beams—EB FRP, NSM FRP, EB steel reinforced polymer, and NSM stainless steel bars—aiming to achieve an approximate 33% increase in flexural capacity with a designed failure mode of concrete crushing.

The six specimens—two controls and one for each strengthening method—were cast from two batches with an average f_c of 5000 psi. Design was based on 60 ksi yield stress for the tensile steel; however, manufacturer testing showed that the specimen with NSM FRP had steel with a yield limit of 90 ksi. The primary flexural reinforcement for the 18 in. by 10 in. cross section was four #9 bars placed 16.25 in. from the extreme compression fiber, with the compression steel comprised of two #3 bars at a depth of 1.6 in. Transverse reinforcement was provided by #3 stirrups placed 6 in. on center along the length of the beam. Loading was applied over a span of 15.5 ft using a three-point loading scheme. Figure 2.14 shows the arrangement of the reinforcement in the specimen strengthened with NSM FRP, with the transverse strips placed at 8 in. on center.

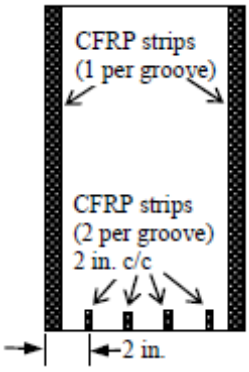

Figure 2.14 NSM FRP Cross Section Layout (Harrison et al. 2006)

Failure of the NSM-FRP-strengthened specimen occurred by concrete crushing of the core with significant capacity increase following the initial spalling of the top cover. Although longitudinal cracks were observed in the epoxy surrounding the FRP strips, no splitting or debonding was noted. Ultimate capacity was increased approximately 46% over the control specimen. The authors concluded that despite the greater number of man hours required for installation, NSM applications provide more protection against loss of strengthening through integration with the existing member, which also aids in preventing splitting or separation of the NSM reinforcement.

2.1.4.4 Liu, Oehlers, and Seracino (2006)

A study conducted by Liu, Oehlers, and Seracino (2006) used two-span continuous reinforced concrete members strengthened using NSM strips to investigate the ductility and capacity of strengthened specimens by examining the extent of moment redistribution within the members. Nine specimens—six with slab-shaped cross sections and three with beam-shaped cross sections—were loaded as shown in Figure 2.15.

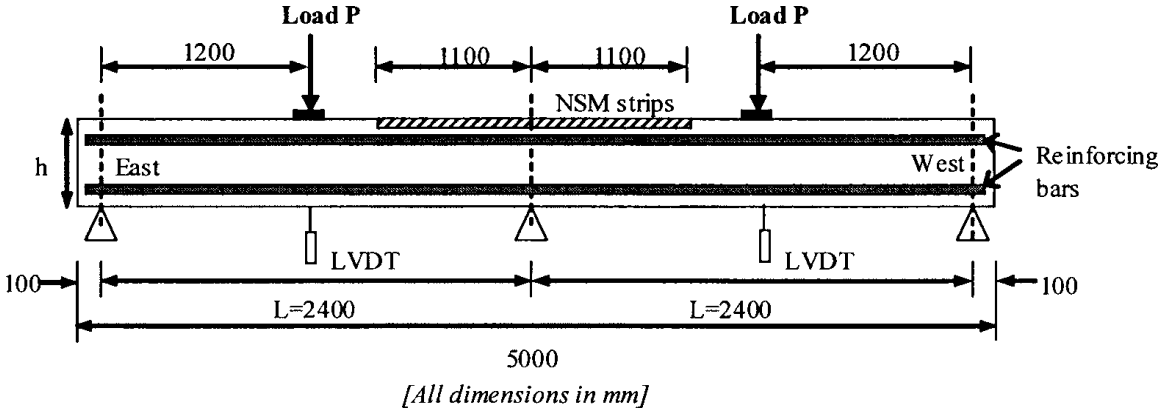

Figure 2.15 Specimen Testing Layout (Liu, Oehlers, and Seracino 2006)

NSM strips were installed at the top of the concrete section over the middle support for strengthening in all specimens and terminated beyond the point of contraflexure to avoid PE

debonding. The beam-equivalent specimens were found to have an average f_c of 35 MPa (5100 psi).

Two of the three beams failed as a result of IC debonding, with the failure of the third resulting from crushing of the concrete. The authors found that significant moment redistribution occurred in all specimens, with the beams achieving moment redistribution ranging from 34 to 40% at ultimate. The authors note that observed moment redistribution exceeds the levels noted by previous researchers for EB applications, concluding that NSM systems are more applicable than EB plates in retrofits where ductility is of primary importance.

2.1.4.5 Teng et al. (2006)

Teng et al. (2006) investigated the effect of FRP bond length on the capacity of NSM-strengthened reinforced concrete specimens using five beams. Four of the beams were strengthened using NSM strips, each with a different embedment length—500, 1200, 1800, and 2900 mm; the fifth specimen was left unstrengthened to serve as a control. Cube testing yielded an average f_c of 44 MPa (6400 psi). Each specimen was loaded monotonically in four-point bending until failure. The specimen dimensions and testing setup are shown in Figure 2.16.

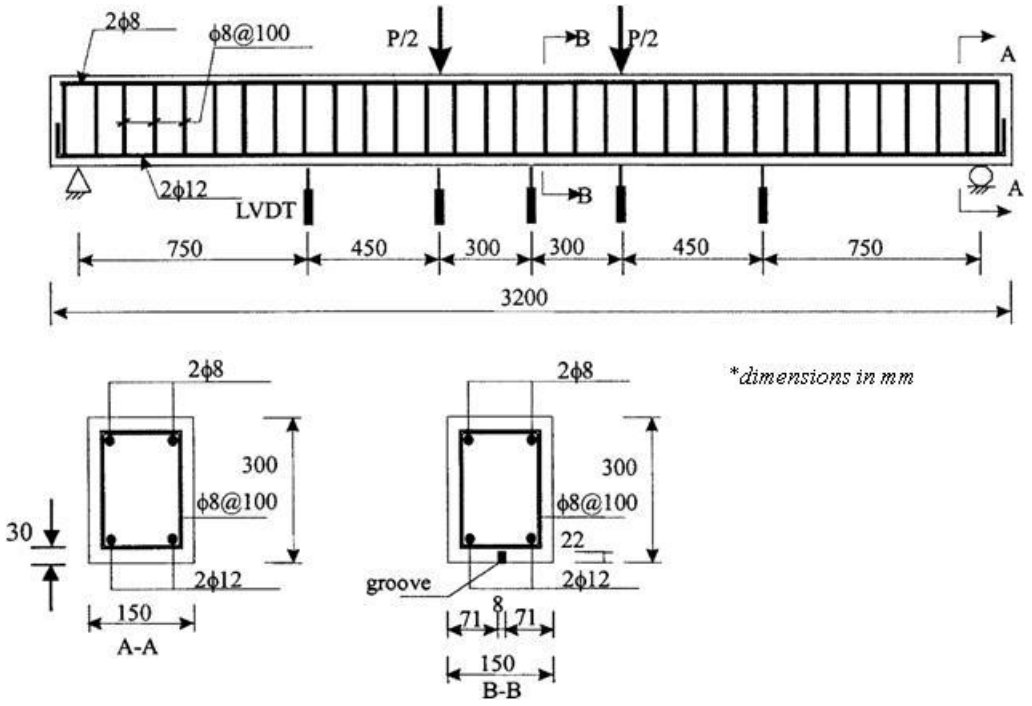

Figure 2.16 Test Specimen and Setup (Teng et al. 2006)

The beam with the shortest embedment length showed no improvement in stiffness or capacity over the unstrengthened specimen, as the bond length was shorter than the length of the maximum moment region. The beams with embedment lengths of 1200, 1800, and 2900 mm produced increases in capacity of 30, 90, and 106%, respectively, prior to failure, with increasing post-cracking stiffness. The three specimens with the shorter embedment lengths failed in PE debonding evidenced by concrete cover separation beginning at the cutoff section. The beam with an FRP bond length of 2900 mm failed due to concrete crushing followed closely by IC debonding in the maximum moment region accompanied by debonding at the epoxy-concrete interface and localized epoxy splitting.

2.1.4.6 Taljsten and Nordin (2007)

The tests conducted by Taljsten and Nordin (2007) were aimed at comparing the effect of externally applied prestressing on the capacity of strengthened members. Eight six-meter-long

specimens were tested in four-point bending until failure. Two of the eight beams—with f_c values of 50 and 53 MPa (7300 and 7700 psi)—were strengthened using nonprestressed rectangular FRP bars. The authors found that these specimens cracked at the same level as the control beam, with no significant contribution to the stiffness or strength of the specimen within the elastic range. However, after the cracking of the concrete, the NSM reinforcement contributed to both stiffer behavior and higher capacity relative to the control specimen until failure occurred as a result of the rods debonding from the surrounding concrete.

2.1.4.7 Yost et al. (2007)

Fifteen specimens were evaluated in four-point loading until failure by Yost et al. (2007) to observe the effect of NSM FRP strengthening on flexural capacity. Three tensile steel reinforcement ratios, ρ_s, were used among the specimens alongside two different FRP reinforcement ratios, ρ_f, with a measured f_c of 37 MPa (5400 psi) for all specimens. NSM FRP reinforcement was applied to twelve of the beams, with the remaining three used as control specimens. The test setup and cross section configurations are displayed in Figure 2.17.

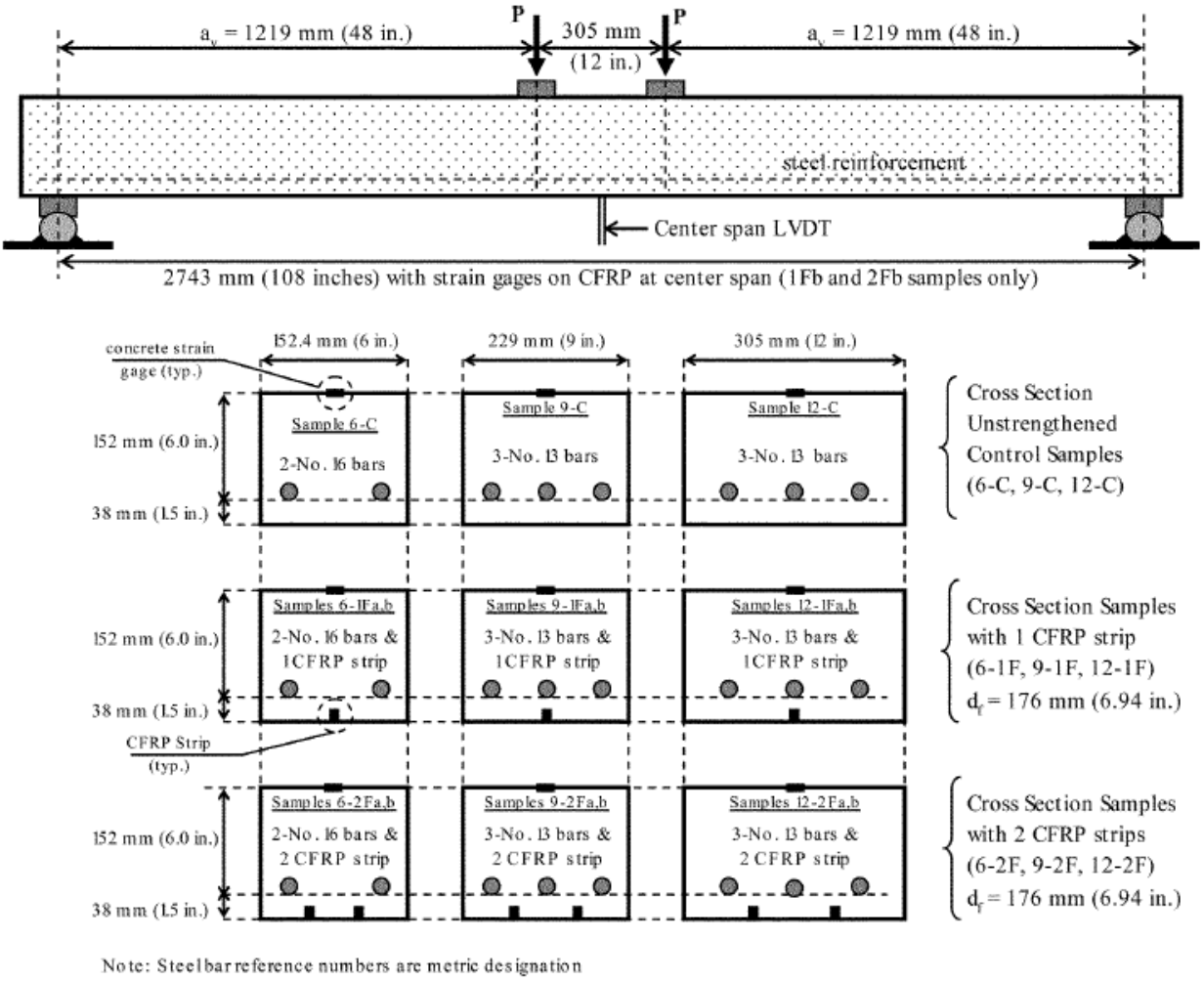

Figure 2.17 Test Setup and Cross Sections (Yost et al. 2007)

Two of the specimens failed as a result of FRP rupture, with the remainder failing due to steel yielding followed by concrete crushing. No debonding or slipping of the NSM reinforcement was detected.

2.1.4.8 Bonaldo, Barros, and Lourenco (2008)

Bonaldo, Barros, and Lourenco (2008) proposed a strengthening technique for slabs that combines NSM FRP in the extreme tension fibers with a steel fiber RC (SFRC) layer bonded to the compression zone of the existing slab to increase the capacity of RC slabs. Figure 2.18 displays the specimen design attached to the series consisting only of NSM FRP strengthening.

A target capacity increase of 50% in the slab was used to determine the number of strips applied. The NSM strengthening procedure was carried out at an approximate concrete age of 28 days with an accompanying approximate f_c of 26 MPa (3800 psi).

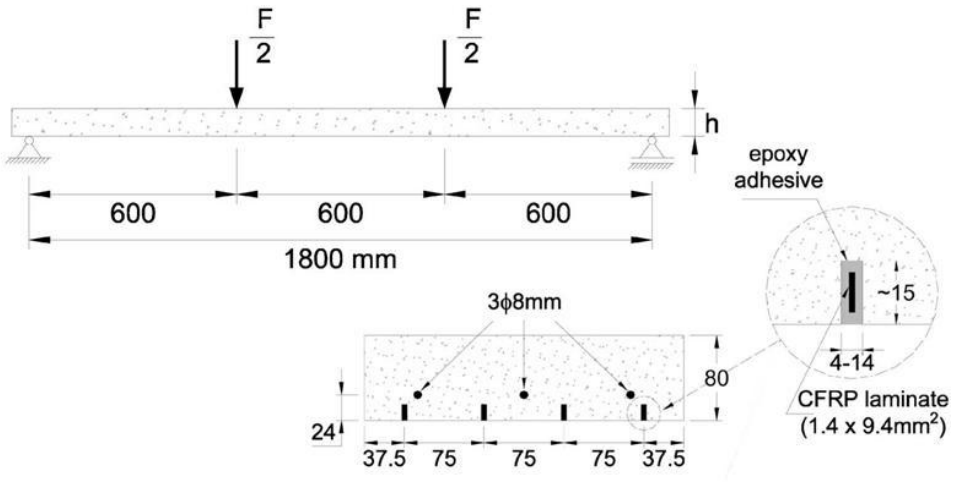

Figure 2.18 Specimen and Retrofit Details (Bonaldo, Barros, and Lourenco 2008)

The researchers reported a 55% increase in service load capacity as a result of the strengthening procedure. The NSM FRP was also observed to provide significant improvement in crack behavior by reducing the crack spacing within RC slabs and to significantly increase the stiffness and deformability of the slab—behavior consistent with high stress redistribution as a result of effective composite action between the FRP and concrete.

2.1.4.9 Wahab, Soudki, and Topper (2011)

Wahab, Soudki, and Topper (2011) constructed six specimens in order to investigate the bond behavior of NSM-FRP-strengthened beam under static loading. Two of the six specimens, with an average f_c of 60 MPa (8700 psi), contained both internal tensile steel reinforcement and nonprestressed CFRP rods. The specimen dimensions and reinforcement layout are detailed in Figure 2.19.

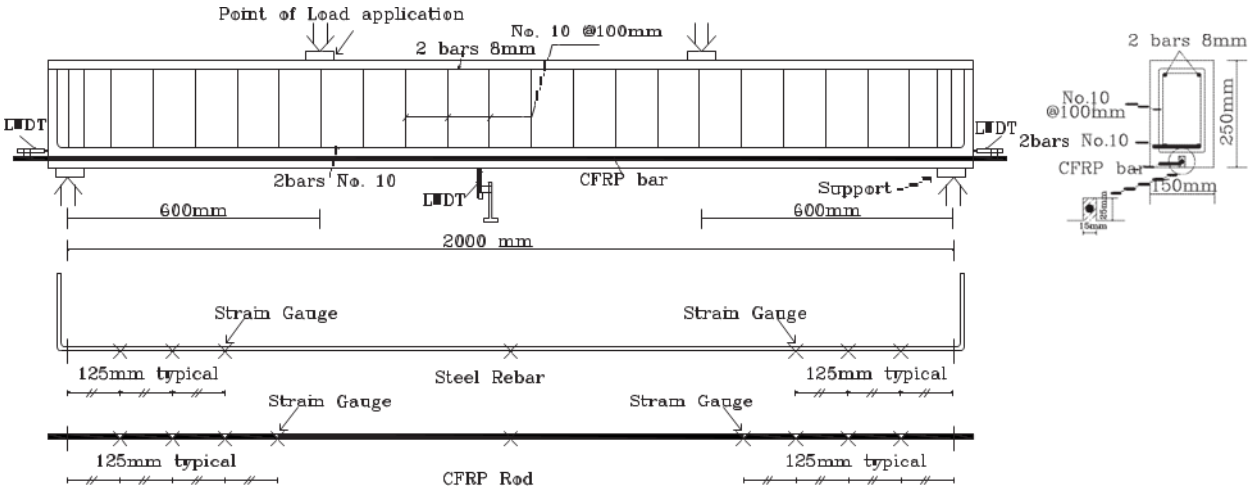

Figure 2.19 Specimen and Instrumentation Schematic (Wahab, Soudki, and Topper 2011)

During the loading process, cracks were more uniformly and closely spaced within the shear span than those in the specimens without tensile steel. The observed failure mode for both strengthened, nonprestressed specimens was CFRP rod pull-out from the epoxy initiating as debonding at midspan which progressed toward the supports. For the first nonprestressed specimens, failure was accompanied by the propagation of horizontal cracks along the steel-to-concrete interface, with some regions showing longitudinal cracks surrounding the epoxy while others displayed cracks through the epoxy and rod followed by inclined cracks from the rod to the beam edge. In both instances, chunks of epoxy and concrete began to separate from the beam. The second strengthened, nonprestressed specimen experienced the horizontal propagation of a near-support crack toward midspan at failure, resulting in the debonding of the CFRP rod from the epoxy and concrete.

Wahab, Soudki, and Topper postulate that debonding can result from closely spaced cracks, where the distribution of shear stresses due to cracking overlap and cause a continuous state of higher shear stress between the two cracks. The authors also reason that nearly equivalent strains between midspan gages and gages closer to the supports indicate fully

debonded behavior, while measured strains higher than those predicted by strain compatibility analysis indicate partially debonded behavior.

2.1.5 Flexural Tests for NSM FRP-Strengthened Slabs

2.1.5.1 Hamilton, Michael, and O'Neill (2007)

In conjunction with the Florida Department of Transportation Structures Research Center, Hamilton, Michael, and O'Neill (2007) evaluated the efficacy of cement-based grout as an alternative adhesive to epoxy in NSM installation procedures. Seven specimens were constructed as specified in Figure 2.20, cast from a single concrete batch with f_c experimentally determined as 5700 psi, and tested under four-point loading configuration.

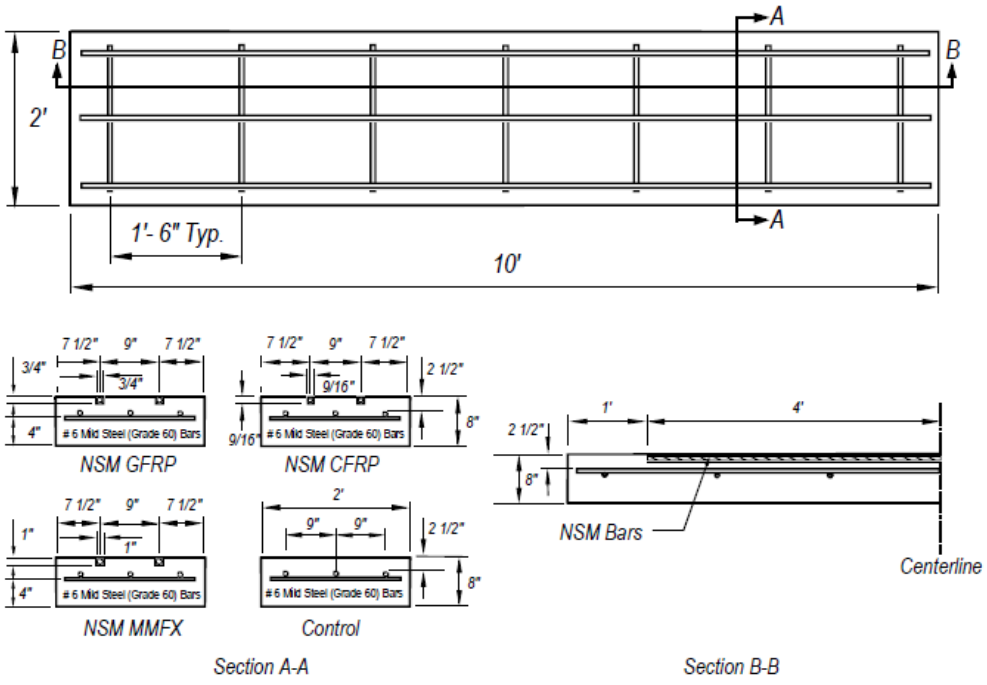

Figure 2.20 Specimen Drawings (Hamilton, Michael, and O'Neill 2007)

The specimens employing epoxy adhesive had higher strength increases than the grouted specimens. Epoxy specimens had flexural failure modes characterized by concrete crushing with no rupture of the NSM bars, while the grouted specimens experienced bond failures due either to

slippage of the bars or splitting of the cement grout. Crack sizes were significantly reduced by the presence of NSM reinforcement. Overall, reinforcement attached with epoxy adhesive performed better than that attached with cement-based grout; however, since the issue of long-term durability under exposure to ultraviolet radiation remains, the researchers pose the possibility of cutting deeper grooves to allow for proper bond between the FRP and the epoxy with enough remaining depth to introduce a top layer of cement-based grout to function as a protective coating against environmental exposure.

2.1.5.2 Lee and Cheng (2011)

Lee and Cheng (2011) studied the effect of multiple variables regarding NSM FRP—material type, cross-sectional shape, surface treatment, and prestressing—on the performance of RC bridge slab overhangs. Two batches of specimens were cast, with the second batch—f_c = 36.7 MPa (5300 psi)—containing the specimen reinforced with CFRP strips. The specimen details for the test are depicted in Figure 2.21.

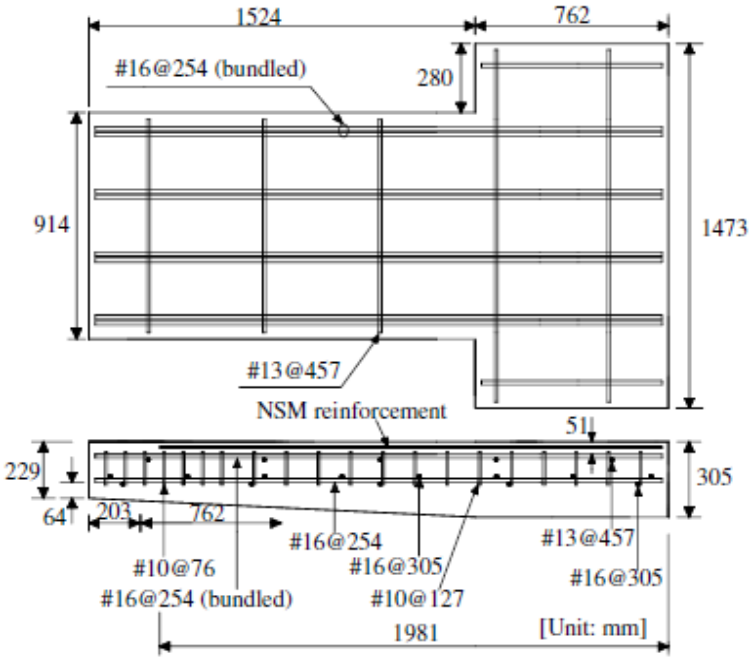

Figure 2.21 Specimen and Reinforcement Details (Lee and Cheng 2011)

Specimens to be repaired were monotonically loaded to 35.6 kN (8 kips) to induce a precracked state with visible damage in the form of cracks. Grooves were then cut into the surface of the concrete, cleaned, and subsequently filled with epoxy and the requisite FRP; the epoxy was allowed to cure at room temperature for seven days.

The authors concluded that material type has little effect on the performance of the FRP and that any textured surface treatment of the strips increases the capacity of the reinforced slab. Regarding cross-sectional shape, the test specimen with textured strips failed due to both compressive failure of the concrete and splitting of the epoxy in the grooves, with a measured tensile strain 95% of the strain limit and no rupture of the FRP observed. The authors determined that the strip shape could be more efficient than other shapes due to the larger perimeter-to-sectional area ratio, which could result in lower bond stresses. Concurrently, the textured strips experience the lowest bond stress at 1.03 MPa (150 psi) relative to the highest measured bond stress of 16.5 MPa (2400 psi). Prestressing provides no significant effect on the capacity, although it does delay the onset of crack formation.

2.1.6 Flexural Fatigue Tests for NSM FRP-Strengthened Beams

2.1.6.1 Quattlebaum, Harries, and Petrou (2005)

Quattlebaum, Harries, and Petrou (2005) constructed specimen sets using three flexural retrofit options—the conventional adhesive application (CAA) of FRP, NSM FRP, and powder-actuated fastener-applied (PAF) FRP—to analyze the behavior of each system under fatigue and monotonic loading with the goal of improving bond performance. NSM FRP was chosen to confirm the improvement in bond characteristics due to the embedment of the FRP and adhesive in the concrete substrate. A total of twelve reinforced concrete beams were cast from a single batch of Type I PCC with f_c determined as 29.5 MPa (4300 psi). Three of the twelve

specimens—two for fatigue testing and the third for monotonic loading—were fitted with the NSM system in the manner shown in Figure 2.22 approximately 1–2 months after casting.

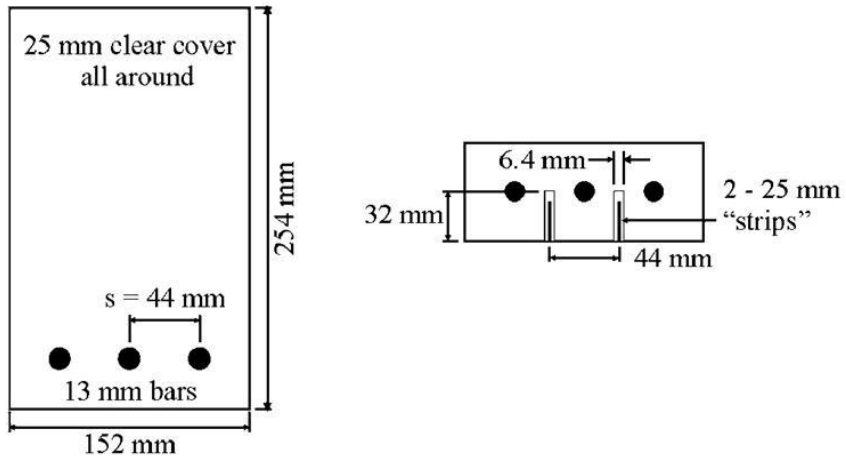

Figure 2.22 Specimen Cross Section and Retrofit Details (Adapted from Quattlebaum, Harries, and Petrou 2005)

All specimens were simply supported with a clear span of 4572 mm (180 in.) and tested under midpoint bending. Fatigue specimens were divided into two groups, low-stress and high-stress, based on an approximate steel stress range on the order of 180 MPa ($0.40f_y$) and 250 MPa ($0.56f_y$), respectively. Failure was defined as the cycle in which the first reinforcing bar ruptured. If failure did not occur within the first two million cycles in low-stress range, the load range was increased to induce the high-stress range until failure.

Monotonic testing yielded an ultimate load increase of 33% over the control specimen using NSM FRP, with concrete crushing as the dominant failure mode. Regarding fatigue, the NSM system performed the best of the low-stress group, with consistent damage accumulation rates before and after the increase in load range, and had the second-best fatigue life of the high-stress specimens. No bond degradation or debonding was detected in any of the three NSM FRP

specimens, with post-test destructive evaluation of the monotonically loaded beam indicating sound FRP, adhesive, and concrete local to the groove.

2.1.6.2 Badawi and Soudki (2009)

Badawi and Soudki (2009) investigated fatigue behavior for RC specimens strengthened with NSM FRP rods. The specimens were constructed as shown in Figure 2.23 with a concrete mixture design experimentally determined to produce an f_c of 40 MPa (5800 psi).

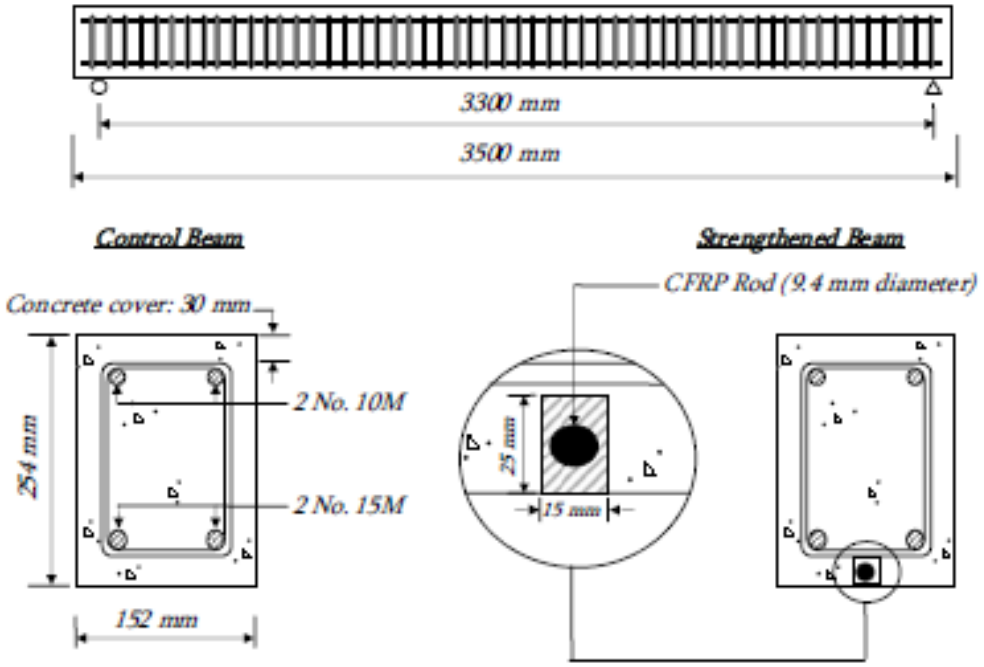

Figure 2.23 Specimen Dimensions and Details (Badawi and Soudki 2009)

The reference beam—loaded monotonically—for the NSM FRP strengthened series failed as a result of concrete crushing with no indication of debonding, slip, or rupture in the FRP rod. All fatigue failures resulted from the rupture of the tensile reinforcing steel. During fatigue testing, the strengthened specimens showed a slight increase in deflection during early load cycles then a stabilized deflection reading until the onset of fatigue failure, resulting in significantly different behavior from the control beams due to the presence of the NSM FRP. As the fatigue crack initiated in the tension steel of the strengthen beam, higher stress was

transferred to the FRP rod allowing for a consistent deflection until complete rupture of the steel. The authors concluded that the addition of NSM FRP increased the fatigue life limit by 24% and produced superior monotonic flexural behavior in comparison to the control specimens.

2.1.7 Tests of Actual Structures Strengthened with NSM FRP

2.1.7.1 Aidoo, Harries, and Petrou (2006)

The tests conducted at the University of South Carolina by Aidoo, Harries, and Petrou (2006) aimed to investigate the midspan debonding behavior of three CFRP strengthening systems—CAA, NSM, and PAF—applied to full-scale highway bridge girders that had been in service for 42 years with the average f_c of 45 MPa (6500 psi) determined from core samples. Figure 2.24 shows the arrangement in which the FRP was applied to the cross section of the two girders to be tested using NSM application.

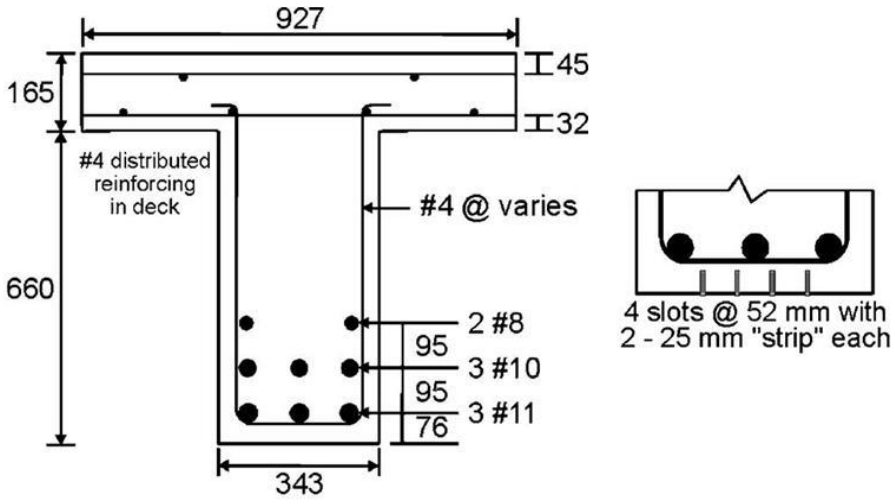

Figure 2.24 Specimen Cross Section and Retrofit Details (Adapted from Aidoo, Harries, and Petrou 2006)

All girders were subjected to midpoint loading over a shortened span of 8025 mm (26 ft 4 in.) as a result of damage to bearing zones during removal from the bridge. The girders exhibited behavior dominated by flexure without exceeding the shear capacity. During monotonic testing, the repaired girder reached an ultimate load 5.6% greater than the control specimen before

failing due to the propagation of a shear crack to the lowest tensile reinforcement level and the resulting splitting failure that detached some of the concrete cover. This failure was not directly linked to debonding of the FRP but rather explained by the creation of a weak horizontal plane near the bottommost layer of reinforcement as a result of cutting the slots for NSM application.

Fatigue testing showed that the NSM retrofit method provided better crack control and stress transfer, indicating superior bond performance over other retrofit methods, with no evidence of debonding, i.e. no decrease in FRP strains as steel strains increase during loading. Regarding the limits proposed in ACI 440.2R, the authors recommends the reduction factor for the design rupture strain that has since been implemented for NSM applications as well as the establishment of a limit state that considers the weakened horizontal plane between the installation grooves and the longitudinal steel reinforcement.

2.1.7.2 Tumialan, Vatovec, and Kelley (2007)

The project described in Tumialan, Vatovec, and Kelley (2007) involved the establishment of a design approach for repairing cracks and strengthening the negative-moment regions of the deficient areas of decks within a parking garage in Massachusetts and the implementation of a load testing program to evaluate performance.

To ascertain the existing conditions of the decks, ground-penetrating radar was employed to survey the location of the negative-moment reinforcing steel, resulting in the discovery of excess concrete cover around the misplaced top mat of reinforcement. Sounding with chains and hammers was used to identify areas of concrete delamination. Slab performance was also assessed using measured vertical deflection at midspan of each column bay—with recorded values as high as 4.5 in.—and observed cracking. The as-built condition of the concrete decks was modeled using finite-element software to account for geometry changes across the entire

floor plan as well as boundary conditions associated from columns and drop panels, edge beams, etc. The resulting structural analysis indicated that multiple negative-moment slab regions were deficient to support the required design loads, with the overstress in some areas as high as 50%. An NSM FRP system was selected to supply the required increase in capacity over simple CFRP sheets to minimize premature deterioration risks resulting from the wear and tear associated with a parking garage. The typical configuration for the retrofit is shown in Figure 2.25.

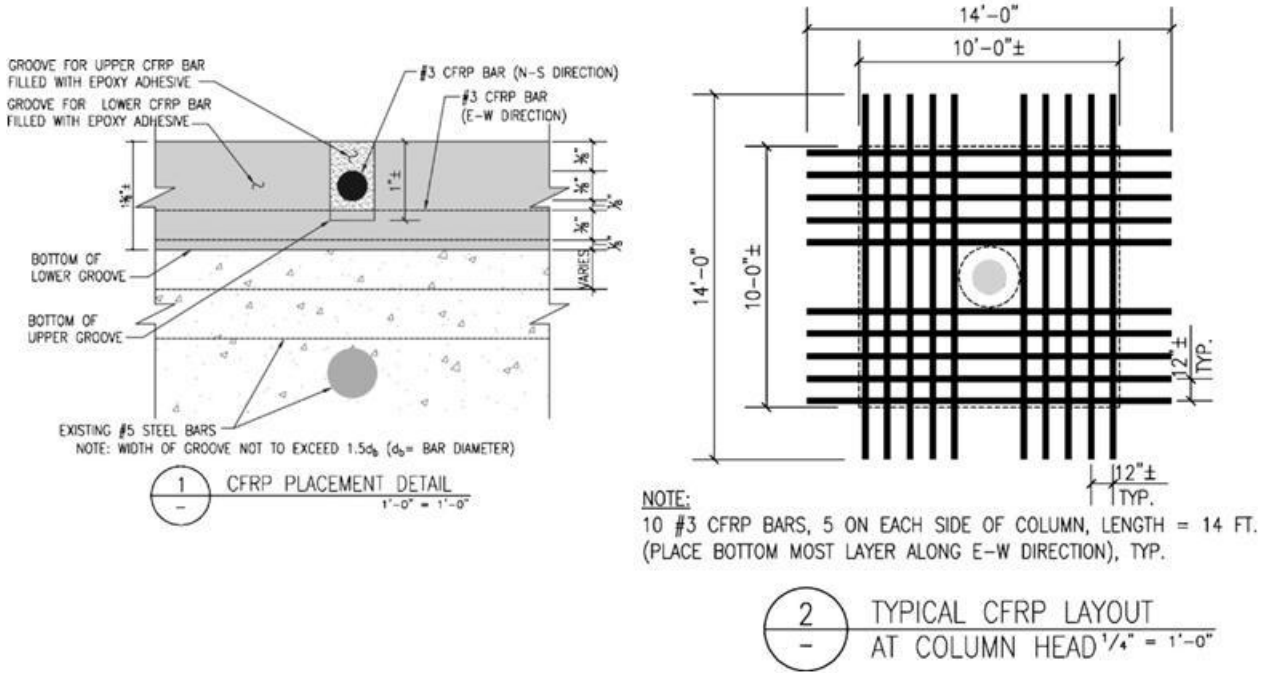

Figure 2.25 CFRP Strengthening Configuration (Tumialan, Vatovec, and Kelley 2007)

Two types of load tests were performed: threshold load tests to demonstrate that the structure possessed the requisite reserve capacity to resist short-term service loads without failure and design load tests to ensure that the repaired structure could carry the code-prescribed loads. Having confirmed that threshold conditions were met, the strengthened sections were loaded to 85% of the factored design capacity of the deck and displayed linear load-deflection behavior in all cases with acceptable residual deflections and a slight increase in stiffness after strengthening.

Based on these test results, all typical bays were expected to be able to support the required loads once strengthened. The designed retrofit was ultimately applied to the negative-moment slab regions of the entire structure both to reestablish structural adequacy where necessary and to increase durability.

2.1.7.3 Bergstrom, Taljsten, and Carolin (2009)

Bergstrom, Taljsten, and Carolin (2009) used NSM FRP rods to increase the flexural capacity of a decommissioned railway bridge in Ornskoldsvik, Sweden, in order to force a shear failure so as to determine the actual shear capacity of the structure after a service period of 50 years. The eighteen CFRP rods—nine in each beam—required to provide the additional bending capacity were installed over a two-day period with at least four days allotted after installation for the proper curing of the adhesive.

No debonding was noticed prior to the final shear failure, and then only as a secondary failure. No slip between the rod and concrete was detected in the midsection; however, some slip was indicated at the end of the FRP rod. The presence of NSM FRP reduced the strain in the tensile steel reinforcement by approximately 20% and increased the extent of the compression zone in the concrete. Ultimately, the addition of the FRP rods provided enough flexural capacity to force the occurrence of shear failure; however, flexural failure was imminent, as indicated by the 100% utilization of the yielded tensile reinforcement and the 87.5% utilization of the FRP rods.

2.1.8 Summary of NSM FRP Research

The failure modes reported for the presented research are split between debonding of the NSM FRP and failure in the concrete, with only two sets of researchers reporting FRP rupture as the main cause of failure. For two sets of specimens (Aidoo, Harries, and Petrou 2006; Bergstrom,

Taljsten, and Carolin 2009) that had been in service prior to failure testing—and therefore cracked prior to repair—debonding was only observed as a secondary failure mode caused by an initial failure in the concrete. None of the other specimens were cracked prior to strengthening.

Table 2.5 provides a survey the specimens within experimental test series from the literature using the following properties:

- the concrete compressive strength, f_c
- the steel reinforcement ratio, ρ_s
- the FRP reinforcement ratio, ρ_f
- the normalized FRP reinforcement ratio, ρ_f^*
- the relative strengthening ratio, ρ_f^*/ρ_s

The listed specimen IDs correspond to the labels given by the original researchers. The reinforcement ratios mentioned can be calculated using the following equations:

$$\rho_s = \frac{A_s}{bd} \qquad \textbf{Equation 2.20}$$

$$\rho_f = \frac{A_f}{bd_f} \qquad \textbf{Equation 2.21}$$

$$\rho_f^* = \rho_f \left(\frac{E_f}{E_s}\right) \qquad \textbf{Equation 2.22}$$

where

A_s = area of tensile steel reinforcement
b = width of member compression block
d = effective depth of steel reinforcement
A_f = area of FRP reinforcement
d_f = effective depth of FRP reinforcement
E_f = modulus of elasticity for FRP reinforcement
E_s = modulus of elasticity for steel reinforcement

The normalized FRP reinforcement ratio (ρ_f^*) allows for the comparison of the relative amount of FRP force in beams strengthened with FRP of different stiffnesses, while the relative strengthening ratio (ρ_f^*/ρ_s) allows for the comparison of the amount of strengthening with the

original strength of the beam. The values in the table represent the parameters within which the results from the research are applicable. Section 2.3 includes a discussion of the relevance of these results to the Letohatchee bridge project.

Table 2.5 Specimen Properties for Experimental Tests from Literature

Test Series	Specimen ID	f_c (psi)	ρ_s (%)	ρ_f (%)	ρ_f^* (%)	ρ_f^*/ρ_s
El-Hacha and Rizkalla (2004)	B1	6900	0.34	0.10	0.058	0.17
	B2	8300	0.34	0.085	0.060	0.17
	B3	6900	0.34	0.080	0.060	0.17
	B4	6900	0.34	0.27	0.060	0.17
Jung et al. (2005)	NSM-PL-15	4500	0.39	0.039	0.032	0.082
	NSM-PL-25	4500	0.39	0.065	0.054	0.14
	CRD-NSM	4500	0.39	0.12	0.072	0.18
Harrison et al. (2006)	Specimen 2	5000	1.08	0.23	0.15	0.14
Liu., Oehlers, and Seracino (2006)	NS_F1	5700	0.72	0.40	0.35	0.48
	NS_F2	5700	0.72	0.12	0.11	0.15
	NS_F3	5700	0.72	0.061	0.053	0.074
	NS_F4	5700	0.72	0.14	0.10	0.14
	NB_F2	5700	1.09	0.18	0.16	0.15
	NB_F3	5700	1.09	0.40	0.28	0.26
Teng et al. (2006)	B2900	6400	0.56	0.079	0.057	0.10
Taljsten and Nordin (2007)	NSMR 1	7700	0.33	0.17	0.12	0.36
	NSMR 2	7300	0.33	0.17	0.12	0.36
Yost et al. (2007)	6-1Fa	5400	1.72	0.16	0.11	0.064
	6-1Fb	5400	1.72	0.16	0.11	0.064
	6-2Fa	5400	1.72	0.32	0.22	0.13
	6-2Fb	5400	1.72	0.32	0.22	0.13
	9-1Fa	5400	1.11	0.11	0.073	0.066
	9-1Fb	5400	1.11	0.11	0.073	0.066
	9-2Fa	5400	1.11	0.22	0.15	0.13
	9-2Fb	5400	1.11	0.22	0.15	0.13
	12-1Fa	5400	0.83	0.081	0.055	0.066
	12-1Fb	5400	0.83	0.081	0.055	0.066
	12-2Fa	5400	0.83	0.16	0.11	0.13
	12-2Fb	5400	0.83	0.16	0.11	0.13
Bonaldo, Barros, and Lourenco (2008)	SL4S	3800	0.90	0.24	0.19	0.21
	SL3S	3800	0.90	0.24	0.19	0.21
Wahab, Soudki, and Topper (2011)	B3	8700	0.69	0.18	0.12	0.18
	B4	8700	0.69	0.20	0.13	0.19
Hamilton, Michael, and O'Neill (2007)	GLEP	4000	1.00	0.25	0.050	0.050
	GLCE	4000	1.00	0.25	0.050	0.050
	CAEP	4000	1.00	0.11	0.068	0.068
	CACE	4000	1.00	0.11	0.068	0.068
Lee and Cheng (2011)	C-st-T	5300	0.98	0.11	0.067	0.068
Quattlebaum, Harries, and Petrou (2005)	N-L	4300	1.15	0.38	0.15	0.12
	N-H	4300	1.15	0.38	0.15	0.12
	N-S	4300	1.15	0.38	0.15	0.12
Badawi and Soudki (2009)	SS	5800	1.27	0.19	0.13	0.10
	SF 7-45	5800	1.27	0.19	0.13	0.10
	SF 7-50	5800	1.27	0.19	0.13	0.10
	SF 7-60	5800	1.27	0.19	0.13	0.10
	SF 7-65	5800	1.27	0.19	0.13	0.10
Aidoo, Harries, and Petrou (2006)	NS	6500	1.03	0.038	0.014	0.014
	NF	6500	1.03	0.038	0.014	0.014
Bergstrom, Taljsten, and Carolin (2009)	EAST	9900	0.78	0.053	0.067	0.085
	WEST	9900	0.78	0.053	0.067	0.085

2.2 Evaluation of Bridge Condition

The Alabama Department of Transportation (ALDOT) has identified the AL 97 bridge spanning over I-65 near Letohatchee, Lowndes County, Alabama, as having inadequate strength for certain truck load configurations. ALDOT's Bridge Inventory Number (BIN) for the bridge is 8847. Hereafter, the bridge will be referred to as the "Letohatchee bridge". Figure 2.26 shows the location of the Letohatchee bridge along I-65, with Figure 2.27 depicting the actual bridge span.

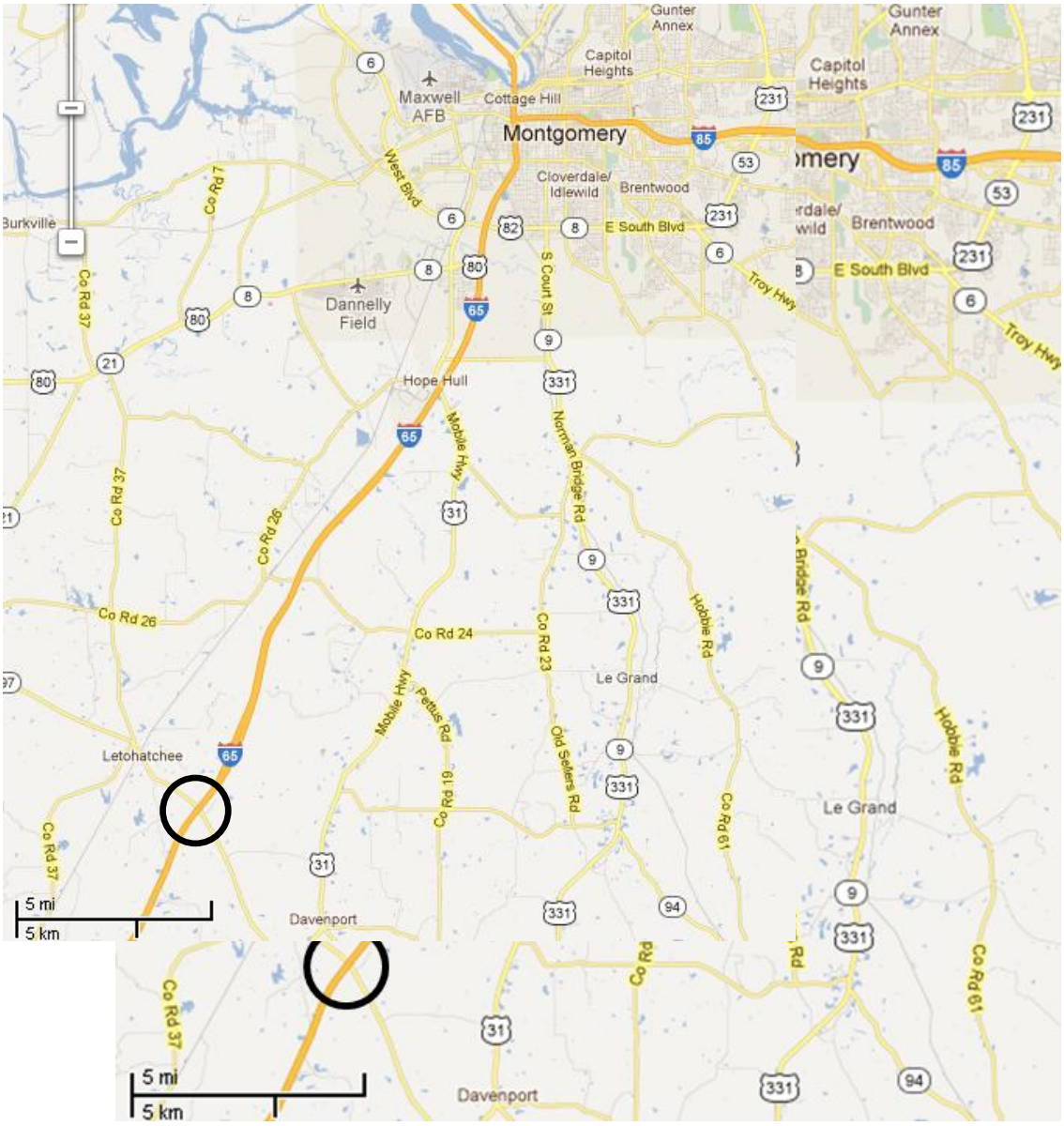

Figure 2.26 Location of the Letohatchee Bridge (Google Maps 2011)

Figure 2.27 Image of the Letohatchee Bridge (Alexy 2009)

The Letohatchee bridge was analyzed by ALDOT Bridge Rating and Load Testing engineers using the Bridge Rating and Analysis of Structural Systems (BRASS^{TM}) program (Wyoming DOT 2009). For this analysis and for all necessary capacity calculations, *AASHTO Standard Specifications for Highway Bridges* (1996) was used. Alexy (2009) performed capacity calculations to determine the amount of strengthening required for the bridge, the results of which are summarized in this discussion. The demand on the existing bridge was determined from the results of the analysis performed by ALDOT engineers. The BRASS^{TM} output revealed that shear is not critical for the Letohatchee bridge; thus, flexure was the main focus of the analysis. Simultaneously, the exterior girder was found to be more critical than the interior girder, resulting in a focus on the exterior girder for determining necessary and provided capacities.

To discover any deficiencies, a comparison was made between the calculated flexural demand and capacity for the existing Letohatchee bridge, with the demand values slightly modified to account for the shift in the flexural demand on the tension steel along the girder caused by diagonal shear cracks. Figure 2.28 shows the comparison of the resulting factored demand and the factored capacity of the Letohatchee bridge under the loading of ALDOT-standard load posting trucks—trucks and the corresponding weights that appear on load-posting signs—and the *operating* load condition, with distances measured from the centerline (CL) of the girder end bearing.

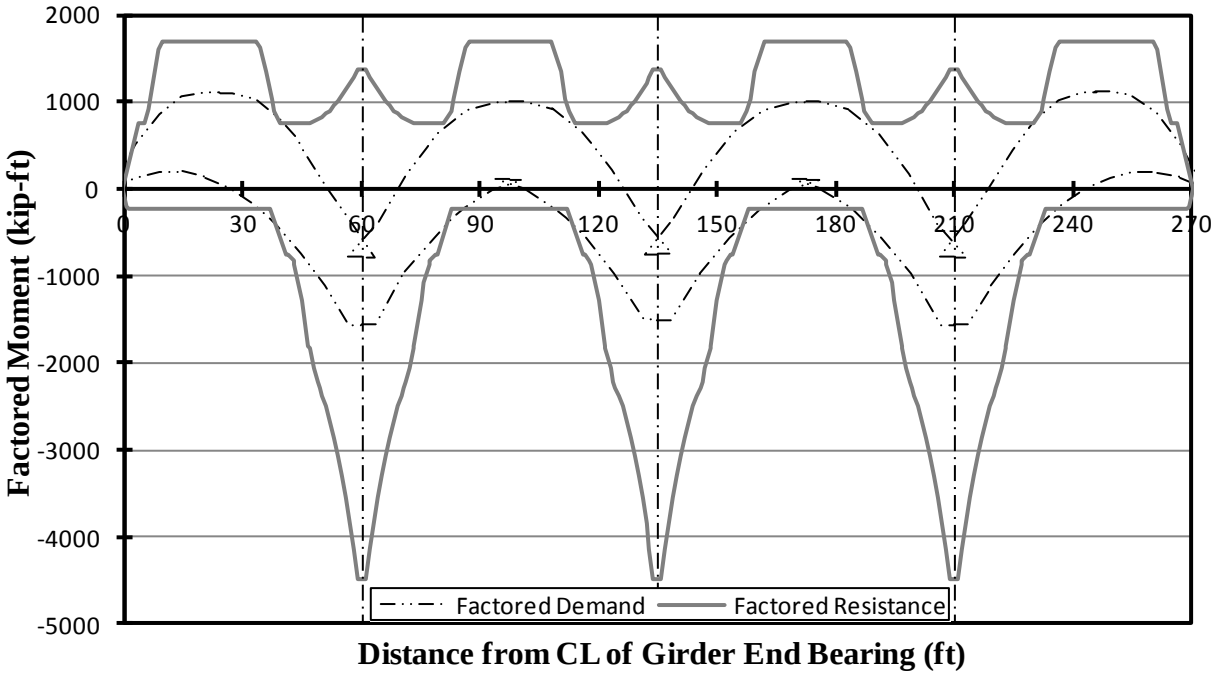

Figure 2.28 Factored Demand Versus Factored Resistance for Posting Trucks (Alexy 2009)

For positive moment, a deficiency of less than 6% occurs approximately 40 ft from the centerline of the girder end bearing over a length of approximately two feet; with such a small region affected by an almost negligible deficiency, positive moment strengthening was deemed unnecessary.

For negative moment, the capacity of Letohatchee bridge was found deficient in six separate seven-foot regions, with the regions of greatest deficiency requiring an approximate increase in strength of 55%. The approximate locations of each deficient region are shown in Figure 2.29, with the hatched areas denoting the deficient regions of the bridge.

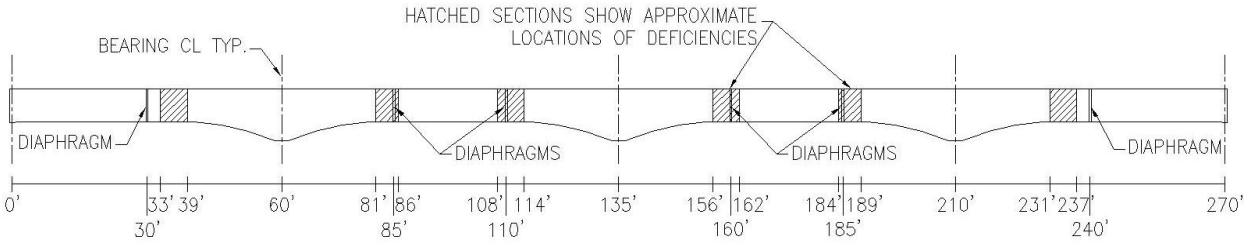

Figure 2.29 Elevation View of Locations of Deficiencies of Letohatchee Bridge (Alexy 2009)

The negative-moment deficiencies for the Letohatchee bridge are not attributable to a shortage of internal steel reinforcement at the support—the deficient region occurs approximately 21 ft from the interior support centerline—but by premature termination of negative-moment steel reinforcement. As detailed in Figure 2.30, most of the top bars were terminated well before the deficient region.

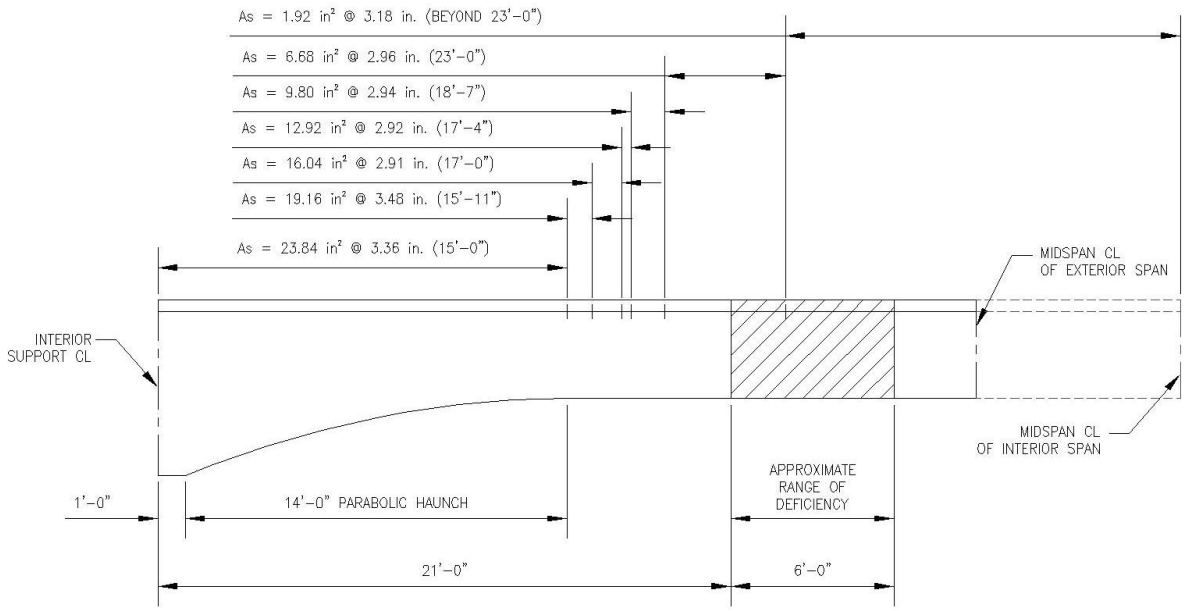

Figure 2.30 Locations of Bar Termination Relative to Deficient Region (Alexy 2009)

The application of an NSM system employing FRP strips is one of the possible strengthening techniques. However, prior to proposal or implementation, the increase in capacity that NSM FRP strips can provide needed to be investigated and quantified using models that can appropriately be applied to evaluate the Letohatchee bridge.

2.3 Shortcomings for the Letohatchee Bridge

Table 2.6 lists the reinforcement ratios for the Letohatchee bridge, with the ratios listed for the FRP reinforcement derived from the proposed design discussed in Section 2.4.1. By comparison to the values presented in Table 2.5, the steel reinforcement ratio, the FRP reinforcement ratio, the normalized FRP reinforcement ratio, and the relative strengthening ratio for the Letohatchee bridge fall at or below the boundary values from previously tested FRP-strengthened flexural specimens.

Table 2.6 Reinforcement Ratios for Letohatchee Bridge (Alexy 2009)

ρ_s	ρ_f	ρ_f^*	ρ_f^*/ρ_s
0.29%	0.030%	0.018%	0.064

Similarly, the concrete compressive strength assumed for the Letohatchee bridge—3000 psi, as discussed in Section 3.1—falls below the compressive strengths found in all previously tested flexural specimens.

2.4 Project Proposal

The proposal for the strengthening of the Letohatchee bridge includes two complementary components: an NSM FRP system based on existing IC-debonding models and a testing program to evaluate the performance of NSM FRP with a direct correlation to the existing bridge. NSM FRP strips were chosen as the strengthening scheme based on the advantages over EB for this application: specifically, to mitigate wear and tear from vehicular exposure if attached on the deck and to avoid altering the diaphragms to attach the FRP below the deck. Of the three common fiber types, carbon-fiber products were chosen over glass- or aramid-fiber products due to higher average strengths, as seen in Table 2.1, and broader availability by comparison. Three of the design approaches for NSM FRP—ACI 440 (2008), Standards Australia (2008), and Seracino et al. (2007)—were employed to design the strengthening scheme for the bridge (Alexy 2009). The accuracy of the same three methods will be evaluated using the results from the laboratory testing program.

2.4.1 Proposed Design

Strips manufactured with two different thicknesses—designated #2 or thin strips (2 mm thick) and #3 or thick strips (4.5 mm thick)—were chosen to create a potential strengthening scheme. Considering varying numbers of the strips, capacity calculations using each design method were

performed by Alexy (2009) for a range of possible concrete compressive strength values of 3000–8000 psi. Figure 2.31 and Figure 2.32 summarize the results determined from the analyses for thin and thick strips, respectively.

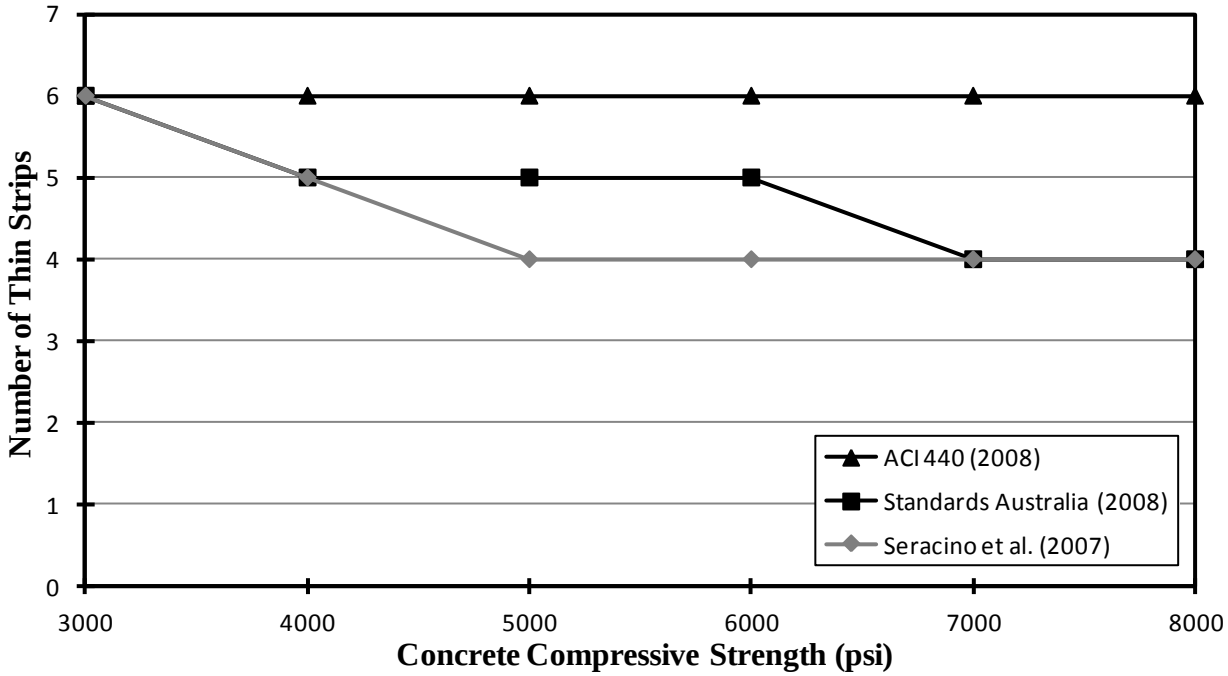

Figure 2.31 Required Thin NSM Strips based on Models (Alexy 2009)

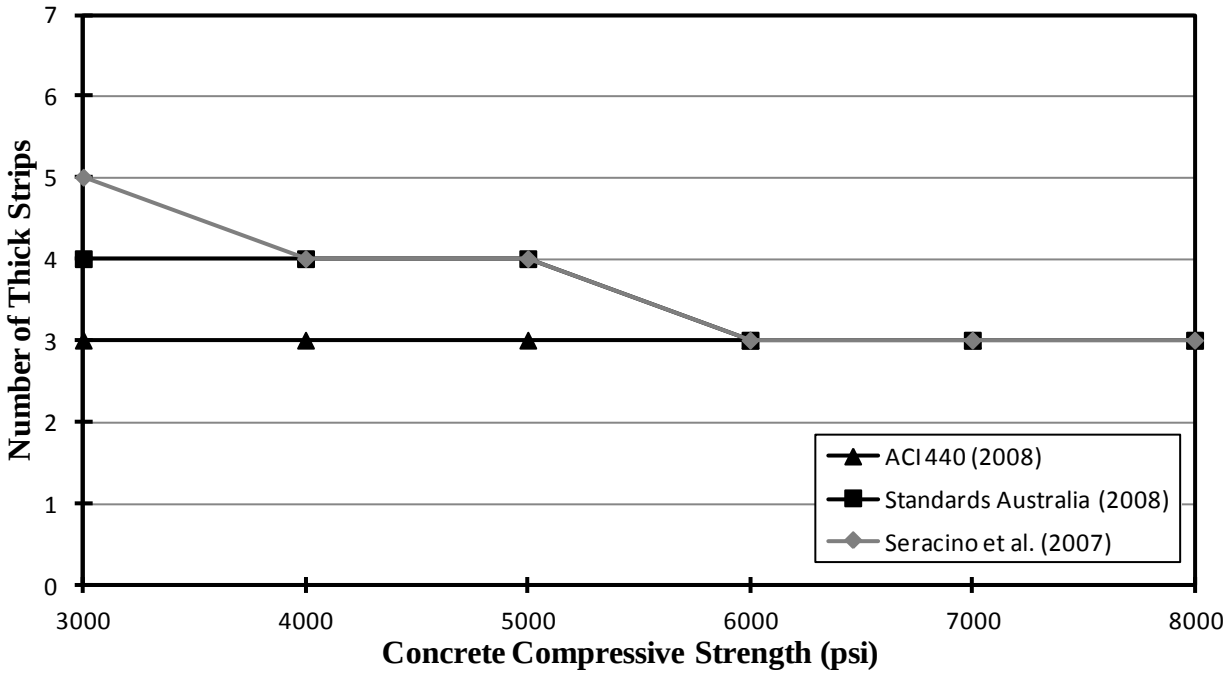

Figure 2.32 Required Thick NSM Strips based on Models (Alexy 2009)

Regardless of the compressive strength of the concrete in the bridge, the design proposed by applying the most conservative results from the analyses calls for either twenty-four thin strips or twenty thick strips—six thin or five thick strips per girder. Fewer strips could be applied based on the results from testing cores taken from the bridge and the evaluation of the applied models from testing program.

The two main approaches for preventing PE debonding for the NSM FRP recommend terminating the strips either at a point of contraflexure (ACI 440 2008, Standards Australia 2008)—which does not exist as a fixed point in a continuous bridge girder subjected to moving loads—or on the compression face of a continuous beam (Standards Australia 2008). For the Letohatchee bridge, examination of the negative-moment envelope, as seen in Figure 2.28, reveals four locations along the length of the bridge where the top of the girder is always in

compression. These four locations will act as the termination points for the strips and, as a result, determine the necessary lengths for the applied strips, as shown in Figure 2.33. All proposed strip arrangements allow ample space across the width of the bridge to satisfy the minimum FRP spacing requirements presented in Table 2.4 while simultaneously limiting flexural cracking, which tends to result in increased crack widths directly over the girder (ACI 318 2008).

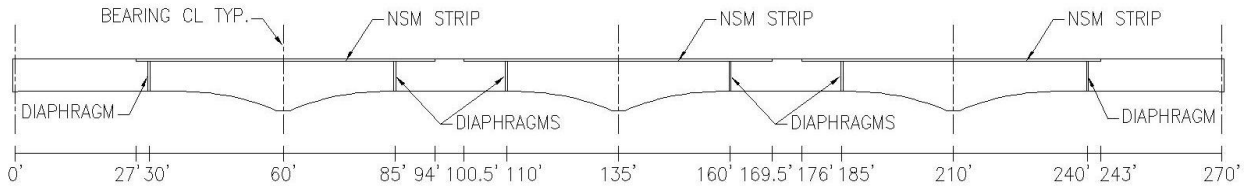

Figure 2.33 Elevation View of Recommended NSM FRP Lengths for Letohatchee Bridge (Alexy 2009) (not to scale)

2.4.2 Proposed Testing Program

The main objectives for the proposed laboratory testing program and their corresponding means of accomplishment are fourfold:

1. Correlate the test specimens to the Letohatchee bridge girders to more efficiently and more effectively propose an NSM FRP-strengthening scheme as discussed in Section 3.1.
2. Study IC-debonding behavior to better quantify when and if it will occur and to evaluate existing IC-debonding models as discussed in Section 6.2.1.
3. Study effect on the strengthened moment capacity of concrete compressive strength, steel reinforcement ratio, FRP reinforcement ratio, and cross-sectional shape.
4. Evaluate the effectiveness of an NSM system in a strengthening role by cracking the unstrengthened specimens prior to the application of the FRP as discussed in Section 3.4.

Four separate test series were proposed to accomplish these objectives. The balance of this thesis describes the fabrication, testing, and analysis of the first test series.

CHAPTER 3: SPECIMEN DESIGN AND FABRICATION

3.1 Design of Testing Series

The main objective of this testing series was to fabricate NSM FRP-strengthened specimens and observe flexural behavior for correlation and comparison to both the existing bridge and the strengthening recommended by Alexy (2009). In doing so, the contribution of the three material constituents was considered: concrete, steel reinforcement, and FRP reinforcement.

For the concrete, the mixture design had a target compressive strength, f_c, at 28 days of 3000 psi to correspond to a conservative lower-bound for the historically representative strength in the bridge and to establish a lower bound for the range of strengths relative to other proposed testing series outside the scope of this thesis. Additionally, the specimens were sized in such a way as to allow all eight to be cast from a single batch, thereby ensuring consistent concrete properties across all test specimens.

The existing state of reinforcement at the critical bridge cross sections served as the target for the design of the steel reinforcement. To create an equivalent level of reinforcement, the mechanical reinforcement ratio, ω_s, was used, as defined in Equation 3.1:

$$\omega_s = \frac{f_y}{f_c}\rho_s = \frac{f_y}{f_c}\left(\frac{A_s}{bd}\right) \qquad \textbf{Equation 3.1}$$

where

f_y = yield stress of steel reinforcement, psi
f_c = concrete compressive strength, psi
ρ_s = steel reinforcement ratio = $A_s/(bd)$
A_s = area of the tensile steel reinforcement, sq. in.
b = width of the member compression block, in.
d = effective depth of steel reinforcement, in.

This relationship was applied because specimens with an equivalent ω_s should have approximately the same level of post-yield steel strain, ε_s, demand. For the Letohatchee bridge, ω_s is nominally 0.0380 (ρ_s = 0.3% with f_y = 40,000 psi), which serves as the target for the design of the series (Alexy 2009). The closest approximation possible using standard bar sizes and actual tensile yield stress (f_y) results in ω_s = 0.0353 (ρ_s = 0.2% with f_y = 50,000 psi). A secondary layout including three times the tensile reinforcement present in its counterpart (ρ_s = 0.6%) acts to establish a reasonable range over which to determine the effect of a variable reinforcement ratio on FRP performance. The two reinforcement arrangements are shown in Figure 3.1.

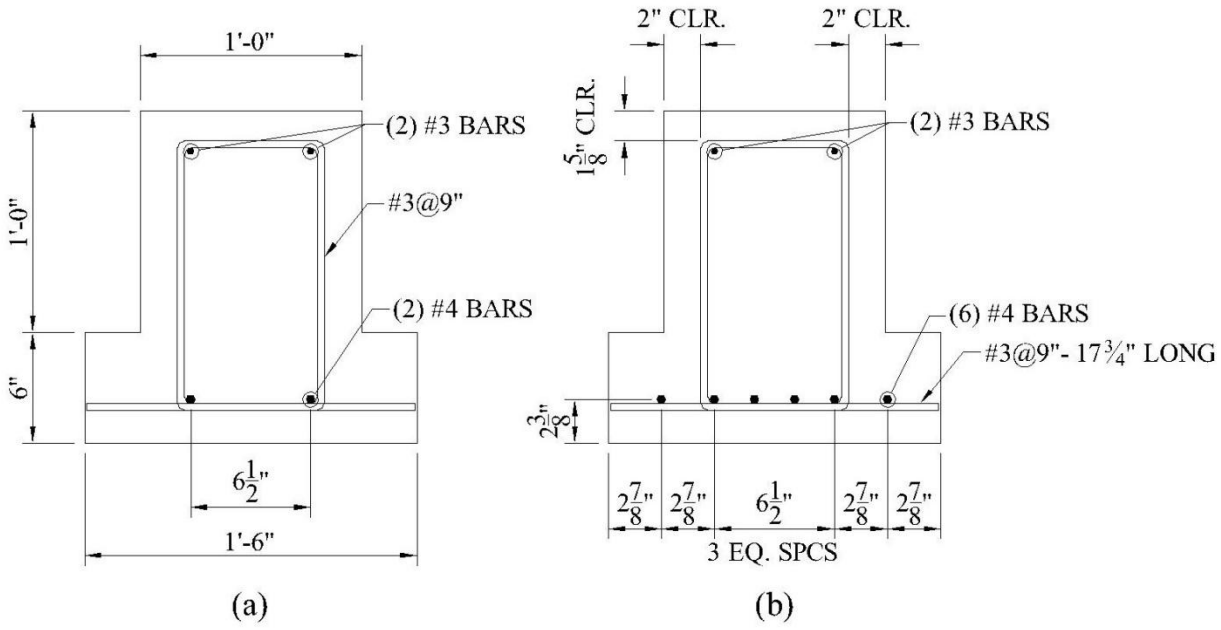

Figure 3.1 Specifications for Specimens with (a) ρ_s = 0.2% and (b) ρ_s = 0.6% (Alexy 2009)

Having established the necessary tensile reinforcement for the two layouts, standard reinforced-concrete design guidelines were used to determine the required transverse reinforcement and spacing along the length of the beam as well as the necessary concrete cover corresponding to the exposure conditions of the bridge. The only exception to standard design limits lay with the cover for the ends of the transverse bars, as the specimens are not designed to represent T-beams, but rather composite sections with a continuous deck across adjacent beams as present in the Letohatchee bridge.

Regarding the FRP reinforcement, the initial reinforcement benchmark was designed to match the FRP reinforcement ratio (ρ_f = 0.03%) derived via the six-thin-strip strengthening scheme proposed by Alexy (2009) using Equation 3.2:

$$\rho_f = \frac{A_f}{bd_f}$$ **Equation 3.2**

where

A_f = area of the FRP reinforcement, sq. in.
b = width of the member compression block, in.
d_f = effective depth of FRP reinforcement, in.

The upper bound for the range of test behavior was determined by the minimum recommended spacing for the FRP strips across the designed width of the flange, which corresponds to ρ_f = 0.16%. To provide another point for the collection of behavioral data, an arrangement of strips was established to yield an approximate midpoint between the upper and lower bounds of reinforcement, which fell to ρ_f = 0.08%. Including a control beam with no FRP, four reinforcement variations were included in the series, as shown in Figure 3.2.

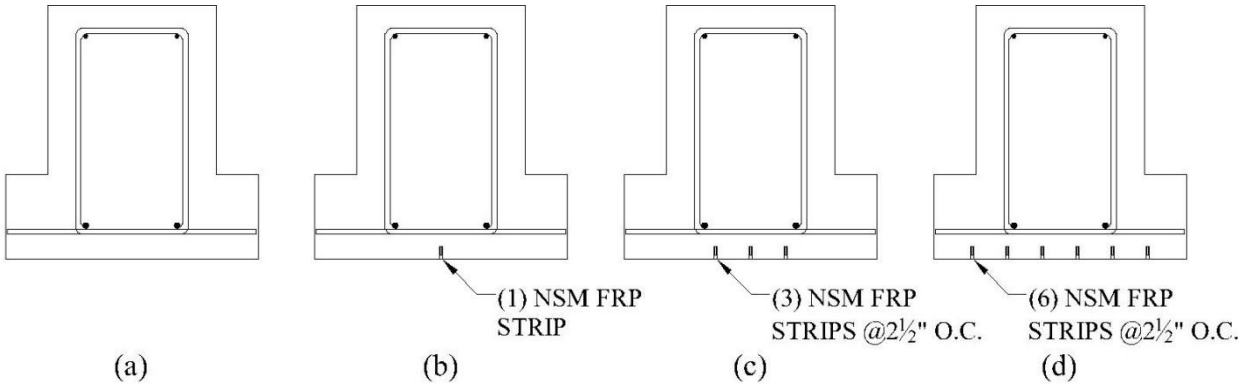

Figure 3.2 FRP Layout for Specimens with ρ_f of (a) 0.00%, (b) 0.03%, (c) 0.08%, and (d) 0.16% (Alexy 2009)

To achieve the desired reinforcement ratio with the size of each specimen, thin FRP strips were chosen over thick FRP strips to provide strengthening.

Ultimately, these three variables—concrete compressive strength, ρ_s,and ρ_f—were used as the basis to establish a nomenclature to differentiate specimens, shown and detailed in Figure 3.3. These designations are also applied within the body this thesis.

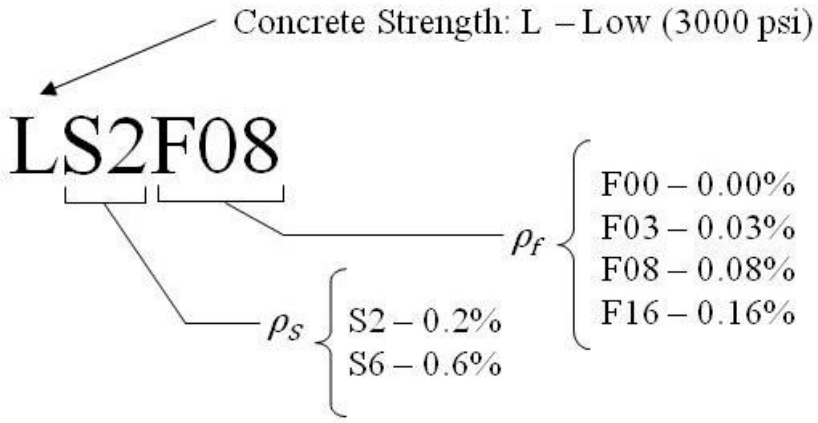

Figure 3.3 Specimen Designation

3.2 Specimen Fabrication

Eight specimens were fabricated in the Auburn University Structural Research Laboratory. All phases of construction—the assembly of formwork, the bending of stirrups and assembly of reinforcement cages, the casting and curing of the concrete for the specimens, and the cutting of grooves for future NSM FRP placement—were completed by personnel on-site.

3.2.1 Formwork

Formwork for the casting of all eight specimens was constructed by laboratory staff. The forms were constructed of polyurethane-sealed plywood facing attached to timber frames, as shown in Figure 3.4, to provide a smooth face for marking the beams during testing. Plywood ribs were also included to resist the outward forces from the weight of the concrete during casting. Block-outs were installed in the corners of the forms to create a rectangular cross section at the end of each specimen to facilitate the rotation of members between the stages of casting, cracking, repair, and testing. The forms were designed with the flange of the members up to provide a surface for the installation of the NSM FRP that was representative of the state of the actual bridge. This orientation mimics the casting orientation for the original structure and the resulting weaker state of the concrete encountered in the surface to be repaired (bridge deck).

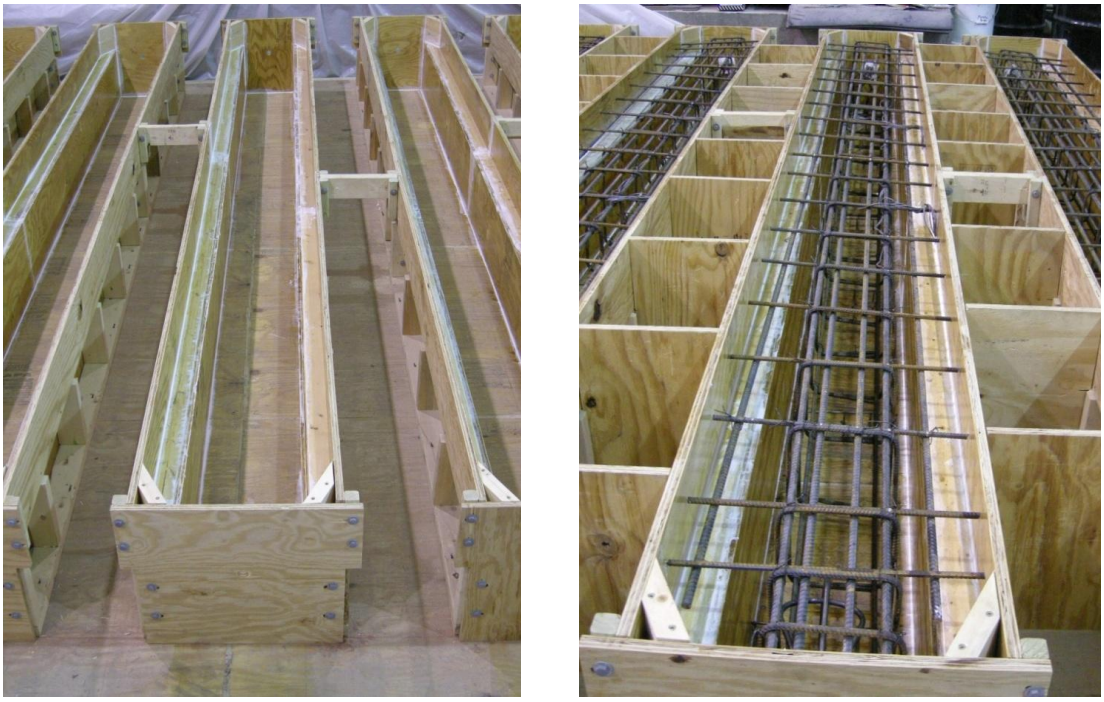

Figure 3.4 Formwork for Specimen Fabrication

3.2.2 Steel Reinforcement

The reinforcing steel for the entire project was obtained in a single batch from a local supplier of construction materials and was cut and bent as required in the laboratory. All longitudinal reinforcing bars were continuous along the length of the member with no splices.

The stirrups were cut to length and bent to specification using an industry-standard rebar cutter and bender, thus achieving the required minimum bend radius (ACI 318 2008). The reinforcing cages were assembled outside of the formwork, as seen in Figure 3.5, and subsequently placed into the forms, as seen in Figure 3.6.

Figure 3.5 Assembled Reinforcement Cage

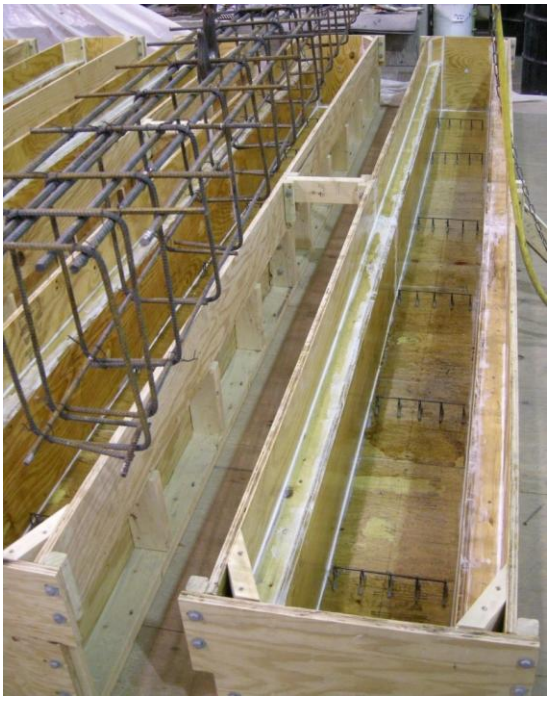

Figure 3.6 Installation of Reinforcement Cage

During construction, strain gages were attached to the longitudinal tension reinforcement. The type and location of these gages is detailed in Section 5.2.1.

Attaching the strain gages required the creation of a smooth surface by removing the ridges from small sections of the deformed bars using a mechanical grinder. Once the surface had been ground smooth, the gages were attached using the specifications prescribed by the manufacturer. The gages were finally coated in nitrile rubber and sealed with heat-shrink tubing to provide protection from moisture during the casting and curing of the concrete.

3.2.3 Lifting Hardware

In order to facilitate the necessary movement and orientation of the specimens, two sets of lifting hardware—pictured in Figure 3.7—were installed alongside the reinforcement cages. The more robust set of hardware was fitted into the ends of the specimens to allow for the rotation of the members between the required orientations of flange-down for cracking and final testing and flange-up for the application of the NSM FRP for repair. The more traditional hardware was attached to the cage and installed in the bottoms of the forms so that, upon reorientation, the lift points would be available for moving the specimens and placing them in the testing apparatus.

Figure 3.7 Configuration of Lifting Hardware

3.2.4 Casting and Curing of Specimens

Casting of the specimens was accomplished in the laboratory at Auburn University. All eight specimens and all requisite material property specimens were cast within a two-hour period from a single batch of concrete delivered from a local supplier. Table 3.1 details the properties of the concrete mixture—both the mixture components and the fresh-tested properties—used in an attempt to yield specimens with a target concrete compressive strength of 3000 psi. The water-to-cementitious materials ratio, w/cm, was computed in laboratory based upon the actual moisture content of the components in the mixture after approximately 65 pounds per cubic yard (pcy) of water were added to the batch in order to improve the workability of the concrete prior to placement. River gravel coarse aggregate was used.

Table 3.1 Concrete Properties

	Item	Value	
Mixture Proportions	SSD Coarse Agg. #67	1851	pcy
	SSD Fine Agg.	1478	pcy
	Type I Cement	344	pcy
	Class C Fly Ash	87	pcy
	Water	238	pcy
	w/cm	0.55	
Fresh Tests	Slump	5	in.
	Unit Weight	145.8	lb
	Air Content	3.6	%

The concrete was placed using a 1.5 yd^3 concrete bucket lifted by means of an overhead crane, as shown in Figure 3.8, and consolidated by means of a mechanical vibrator, as shown in Figure 3.9. The excess concrete for each specimen was struck off using 2 x 4 dimensioned lumber, as shown in Figure 3.10, and finished using wood floats, as shown in Figure 3.11.

Figure 3.8 Introduction of Concrete to Crane Bucket

Figure 3.9 Mechanical Consolidation of Concrete

Figure 3.10 Striking of Excess Concrete

Figure 3.11 Finishing of Specimen Surface

The beams were covered in wet burlap and plastic, as shown in Figure 3.12, to provide a moist curing environment and were kept in this condition by periodically wetting the burlap for the first seven days following casting. After seven days, the specimens were removed from the forms and they remained in this condition until 28-day strength was achieved. The beams sat an extra 14 days before grooving for the NSM strips began.

Figure 3.12 Curing of Specimens

3.2.5 Groove Cutting

The grooves were cut in the laboratory over a two-day period by a local concrete cutting company using a track saw, shown in Figure 3.13. The track saw was chosen over the standard walk-behind concrete saw for the ease of operation and stability provided on the narrow, elevated surface of the specimen flanges and the consistency in controlling the depth of the cuts. All grooves were cut using a 1/4-in.-thick diamond blade running on a wet saw to a target depth of 7/8 in., as shown in Figure 3.14.

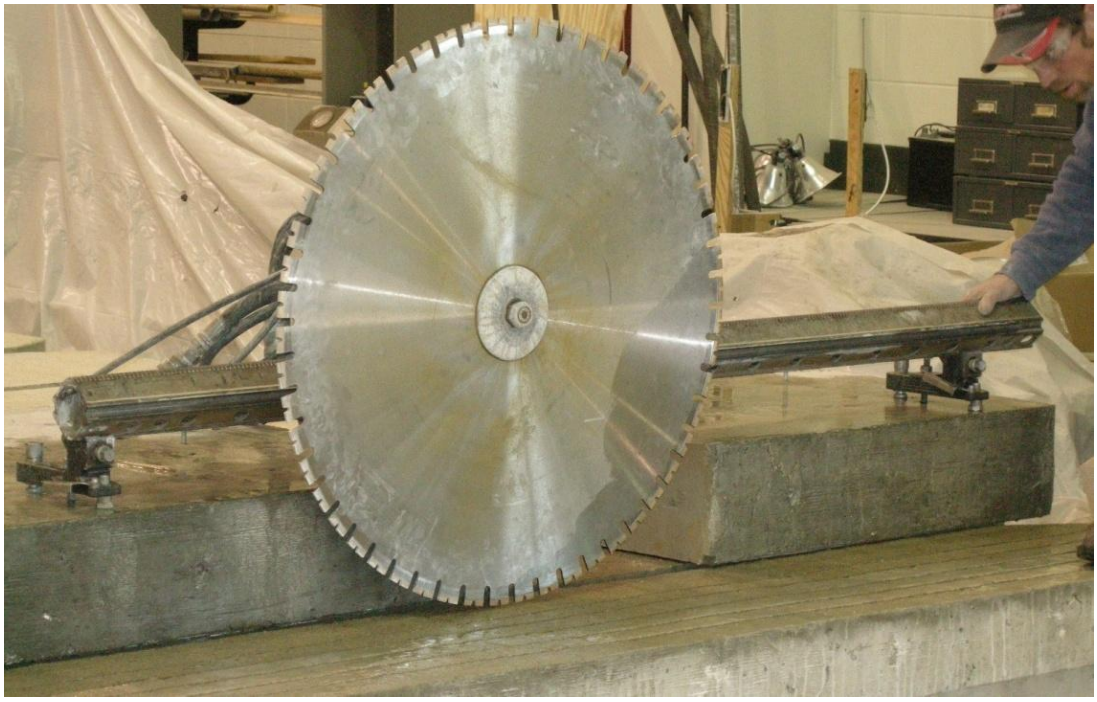

Figure 3.13 Saw Assembly for Groove Cutting

Figure 3.14 Cutting of Grooves

3.3 Material Properties

Material properties for the concrete, steel reinforcement, and FRP reinforcement used in the specimens were tested at Auburn University by researchers to confirm previous assumptions and determine appropriate values for use in theoretical analyses.

3.3.1 Concrete

Concrete cylinders and flexural specimens were cast at the same time as the laboratory specimens in accordance with standard ASTM procedures as specified in ASTM C 192. Twenty-four cylinders and six flexural specimens were cured under moist conditions for a minimum of seven days. After seven days, all forms were broken to coincide with breaking the formwork from the laboratory specimens; the majority of the property specimens were moved back into the laboratory environment at this point so that their curing process would mimic that of the test beams—designated "Air Cure" in Table 3.2. Three cylinders were left in the environmental chamber to provide ASTM-standard 28-day moist cure data for the compressive strength, f_c.

Table 3.2 displays the concrete compressive strength, f_c, at key times during the testing process: Day 7 coinciding with the removal of forms from the laboratory specimens, Day 28 corresponding to the usual strength acceptance testing age, Day 147 marking the beginning of the beam cracking process, and Days 190 and 253 denoting the beginning and end, respectively, of testing. The compressive strength gain for the length of the project can be viewed in Figure 3.15.

Table 3.2 Concrete Strength Milestones

Age (days)	Curing	f_c (psi)
7	Air Cure	2070
28	Moist Cure	3000
28	Air Cure	3300
147	Air Cure	3310
190	Air Cure	3310
253	Air Cure	3440

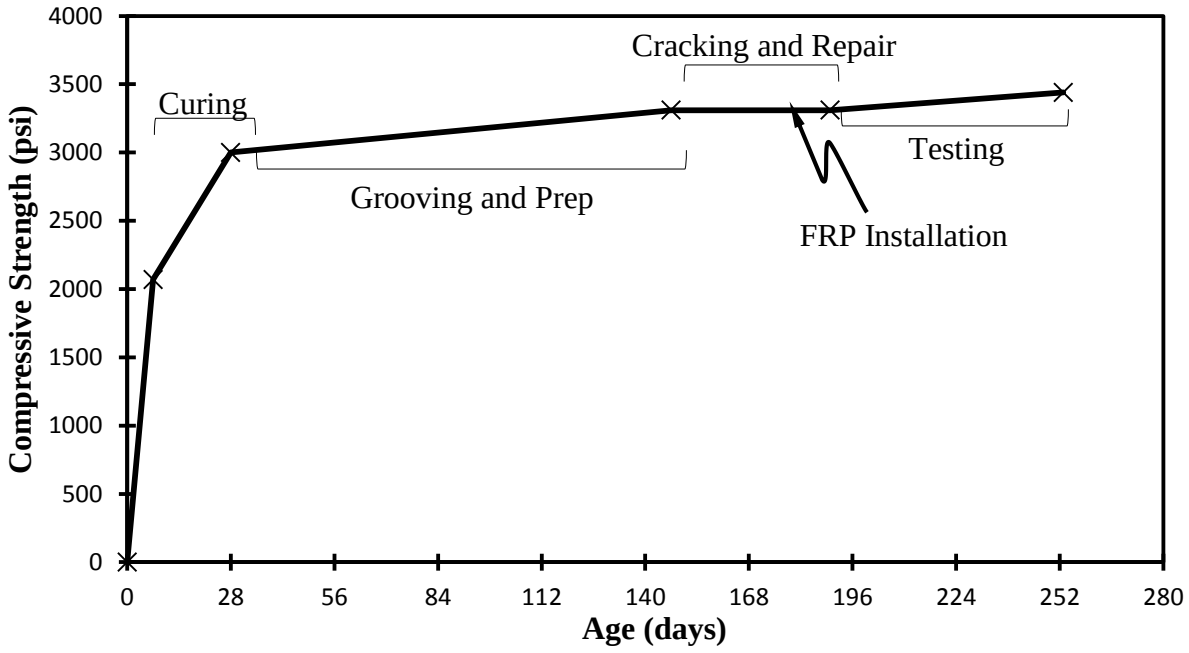

Figure 3.15 Compressive Strength Gain of Concrete over Time

3.3.2 Steel Reinforcement

Using a representative sample from the batch of reinforcing steel, tension tests were performed in a Tinius-Olsen universal testing machine—as seen in Figure 3.16—to determine the modulus of elasticity, yield stress, and strain hardening behavior of the tensile reinforcement for the specimens. Gages were attached to the test specimens alongside an extensometer in order to verify the consistency and accuracy of the gages and the method in which they were applied.

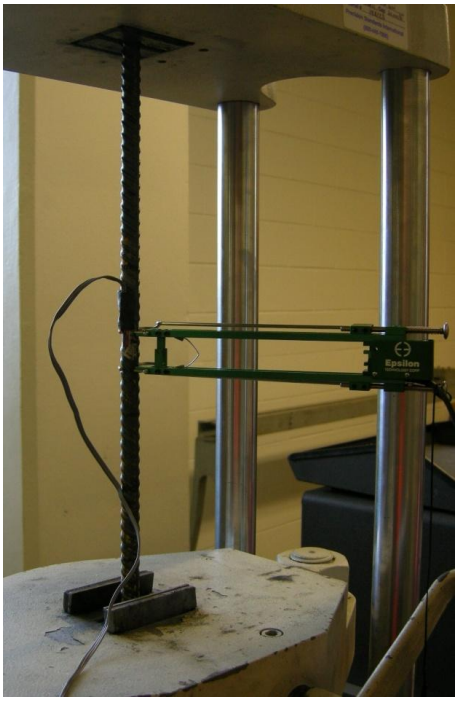

Figure 3.16 Axial Testing of Steel Tensile Strength

Previous testing at Auburn University (Reed 2003) has shown that locally available ASTM A 615 Grade 40 reinforcing steel has an actual approximate yield stress of 50 ksi, therefore 50 ksi was assumed in the design of the test series. The current testing confirmed this assumption, with the data showing an average yield stress of 53 ksi, as well as a modulus of elasticity for the steel, E_s, of 29,300 ksi. Curves were fit to the average data, as shown in Figure 3.17, from all three of the gaged test specimens in order to generate a theoretical equation of the stress in the steel, f_s, as a function of the strain, ε_s, for the entire range of behavior of the reinforcing steel, displayed in Equation 3.3.

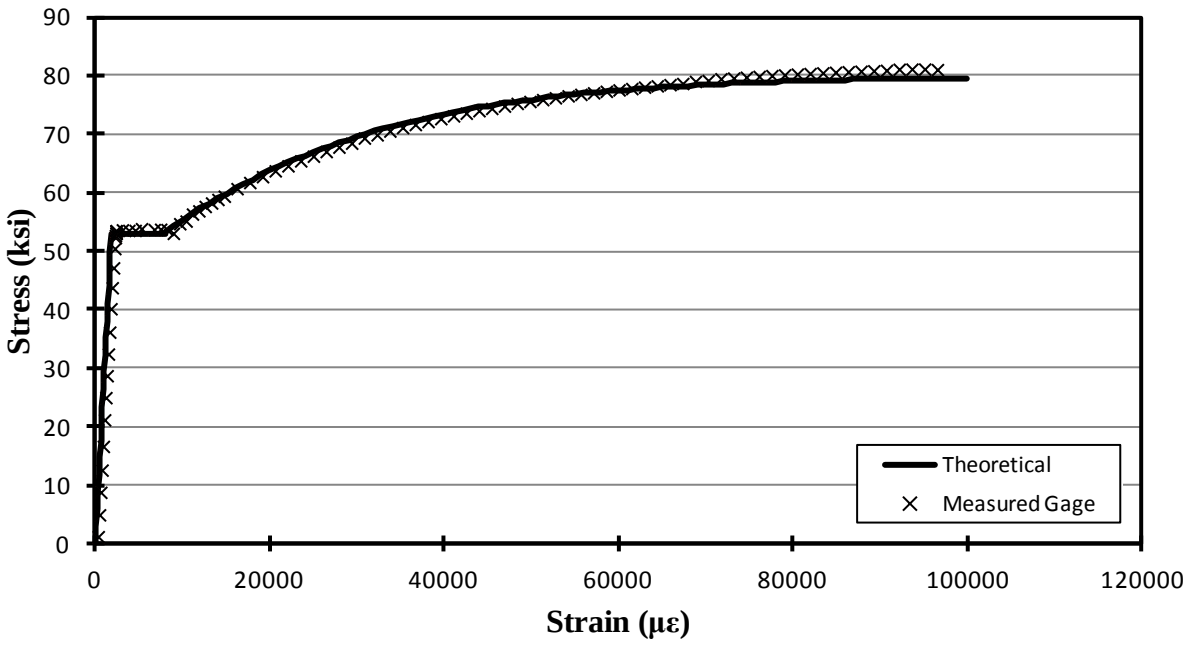

Figure 3.17 Stress-Strain Relationship for Steel Reinforcement

$$f_s = \begin{cases} 29300\varepsilon_s & 0 \le \varepsilon_s < 0.0018 \\ 53 & 0.0018 \le \varepsilon_s < 0.0079 \\ -498000\varepsilon_s^4 + 166000\varepsilon_s^3 - 22000\varepsilon_s^2 + 1400\varepsilon_s + 43.3 & 0.0079 \le \varepsilon_s \le 0.1 \end{cases} \quad \textbf{Equation 3.3}$$

f_s in ksi, ε_s in in./in.

3.3.3 FRP Reinforcement

Samples were also taken from the two rolls of NSM FRP received from Hughes Bros. and tested in the universal testing machine for comparison to published values provided by the manufacturer. The behavior of gages attached to FRP was also observed to confirm the accuracy of the readings and the consistency of the application method. Figure 3.18 shows the elastic behavior of the FRP and Figure 3.19 displays the tested behavior to failure. The testing method employed yields a lower average ultimate stress than published due to consistent failure of the FRP in the grips of the testing apparatus, as shown in Figure 3.20.

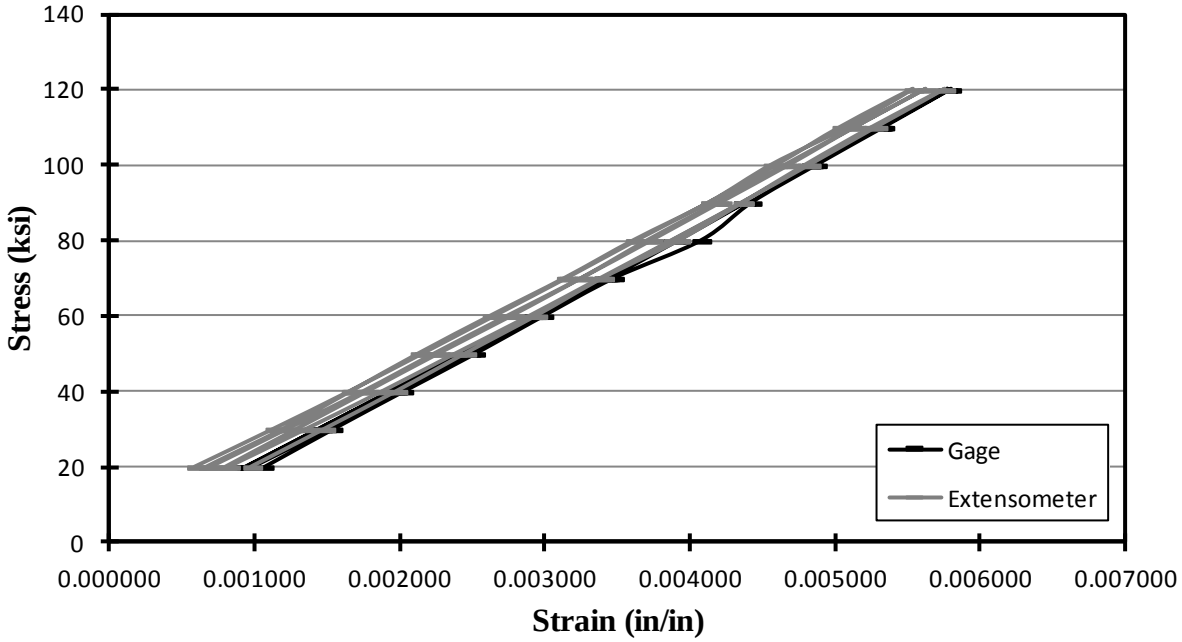

Figure 3.18 Elasticity Testing Results for FRP Reinforcement

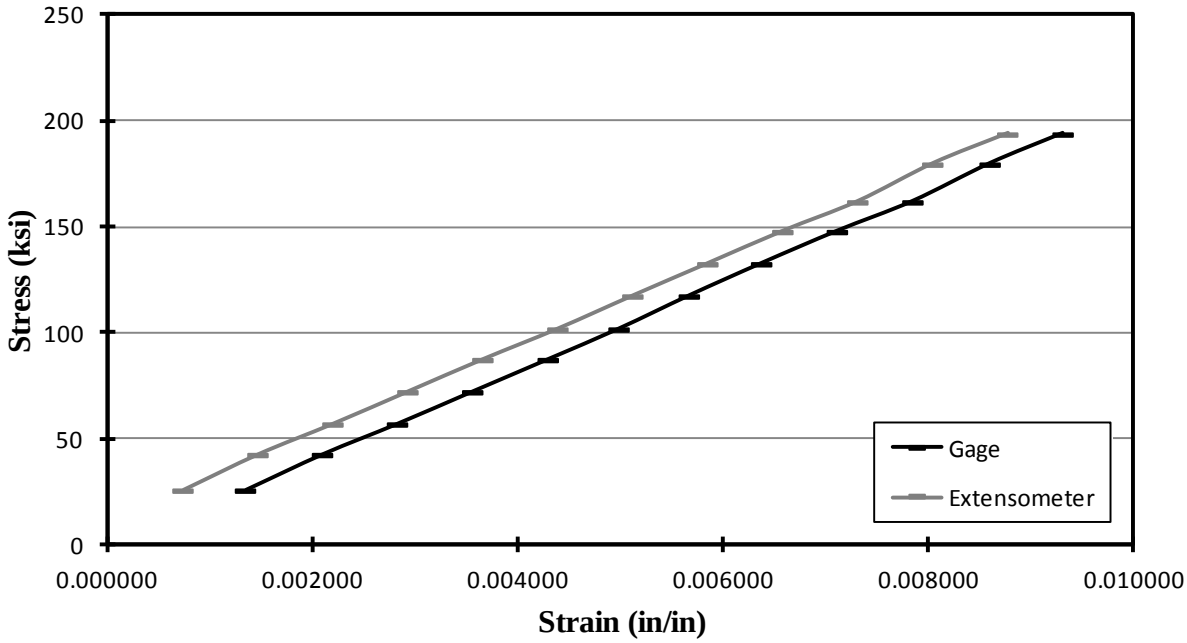

Figure 3.19 Stress-Strain Results for FRP Reinforcement

Figure 3.20 Results of Axial Testing for FRP Strips

The difference in the strain readings taken from the gage and the extensometer can be attributed to the slip of the extensometer during elastic testing; however, the measurements from the gages—not the extensometer—were used to determine the material properties of the FRP reinforcement. The data also tend toward a slightly higher average modulus of elasticity for the FRP, E_f—21000 ksi—than the published value of 18000 ksi. The experimentally determined E_f was used to derive a theoretical equation for FRP stress, f_f, as a function of FRP strain, ε_f, shown in Equation 3.4, that closely follows the obtained data from testing, as shown in Figure 3.21. The theoretical curve continues to a rupture stress of 345 ksi—the average value reported under manufacturer test methods—which results in an approximate rupture strain of 0.016 in/in. These values were used instead of the data provided by the manufacturer (300 ksi and 0.017 in/in) to more closely approximate the full behavior of the FRP in the analytical model, as discussed in Section 6.1.3.

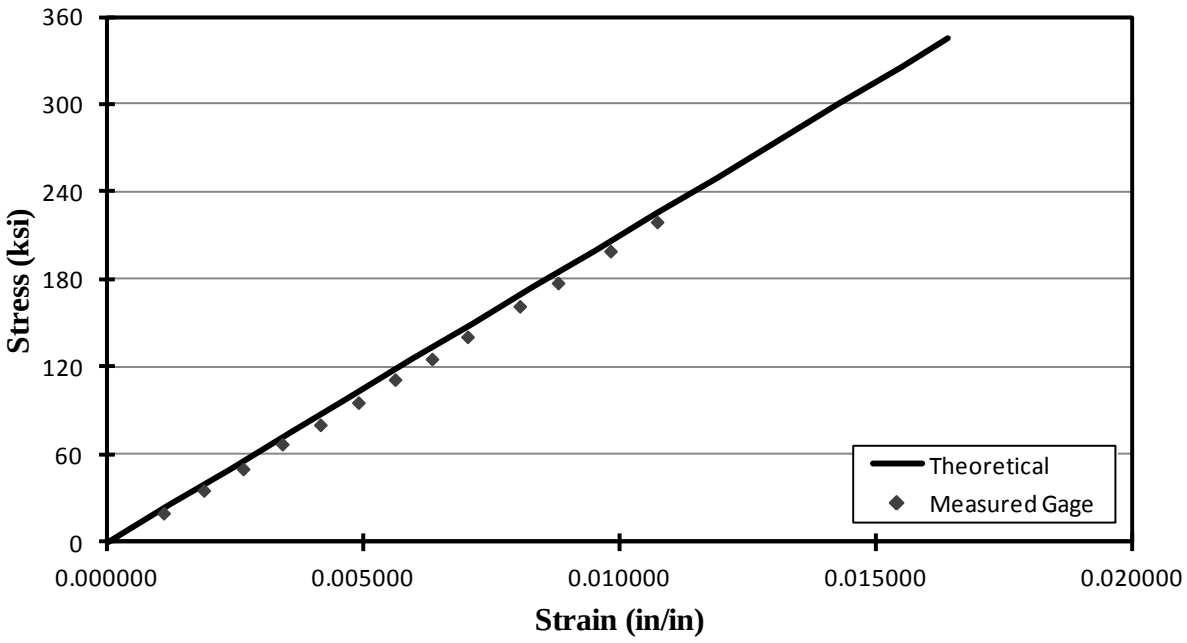

Figure 3.21 Theoretical Stress-Strain Relationship for FRP Reinforcement

$$f_f = (21000\ \text{ksi})\varepsilon_f \leq 345\ ksi \qquad \textbf{Equation 3.4}$$

3.4 Cracking of Specimens

In order to more accurately represent actual in-service bridge conditions, the specimens were cracked prior to the application of the FRP reinforcement—a step rarely taken before the strengthening of most laboratory test specimens described in the available literature. To accomplish this requirement, the beams were inverted to put the flange (bridge deck) in tension as it would be in the negative-moment region of an actual bridge. A four-point loading scheme—shown in Figure 3.22—was used to apply the loads necessary to crack the specimens. The complete details for specimen loading are discussed in Section 5.1.

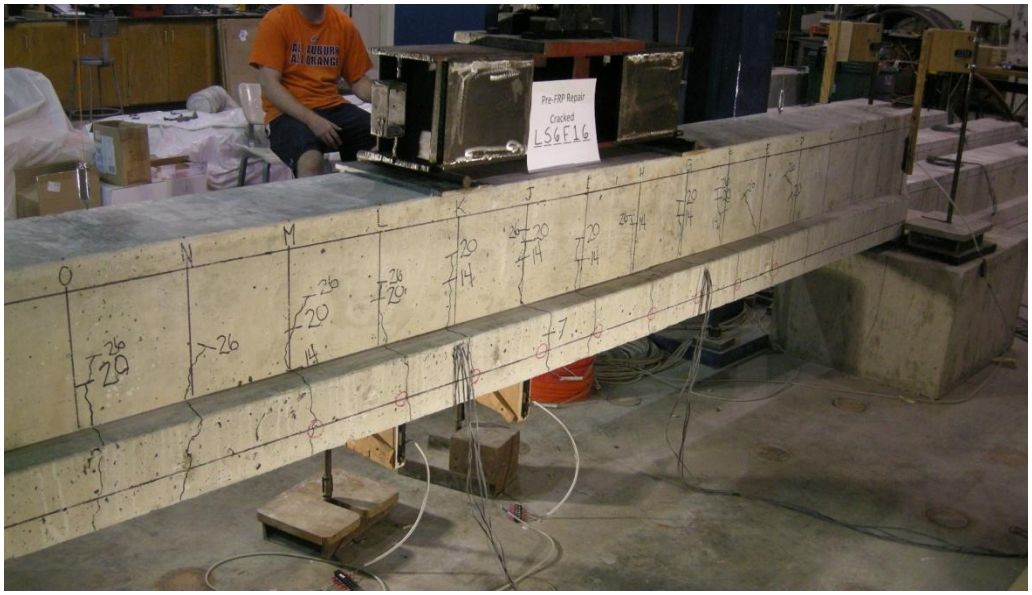

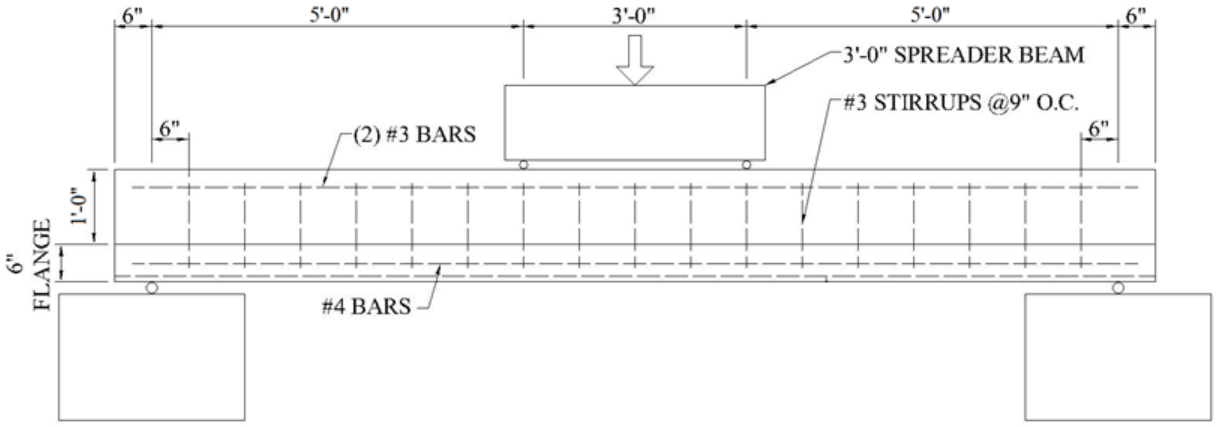

Figure 3.22 Specimen Loading Arrangement

Each specimen was loaded to ninety percent of M_y—the bending moment at yielding of the tension steel assuming linear-elastic, cracked-section behavior—to stress the longitudinal steel reinforcement past typical levels seen under service-load conditions but still within the linear-elastic behavior range. A similar cracking procedure was applied to all eight beams, exhibited in Figure 3.23 and Figure 3.24, consisting of

1. Three cycles between zero and five kips;

2. Monotonic loading until the prescribed peak load—9 kips for the specimens with ρ_s = 0.2% and 26 kips for those with ρ_s = 0.6%
3. Three cycles between the applicable prescribed peak and zero.

During monotonic loading, all cracks and crack extensions were marked as they formed with a black permanent marker.

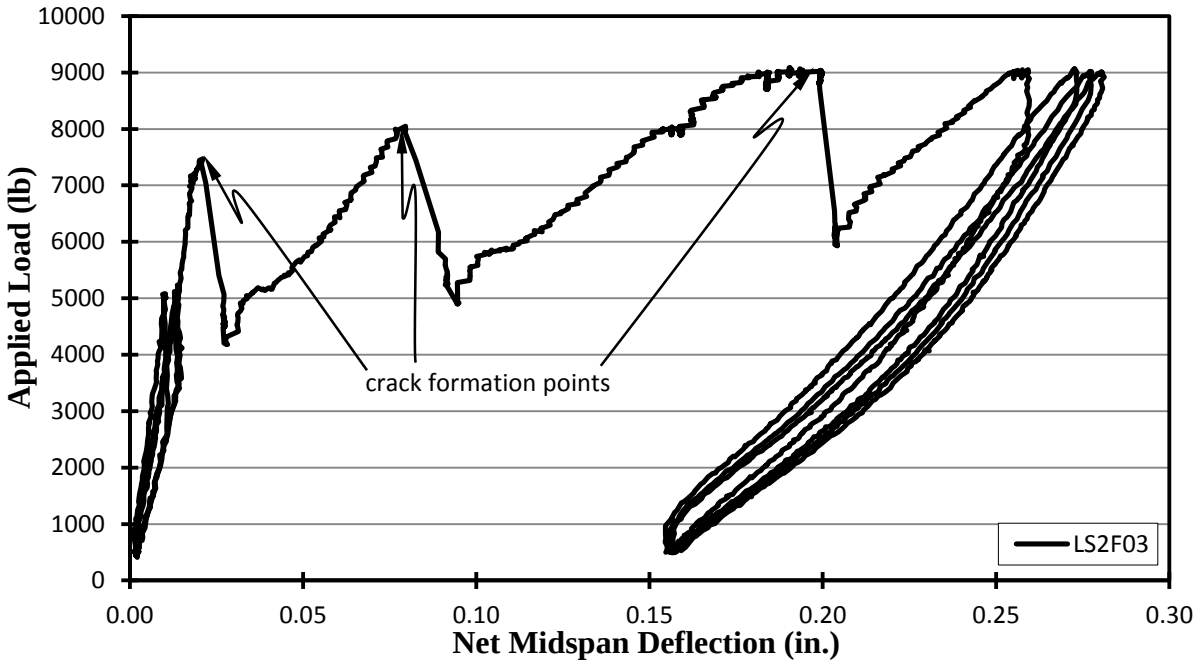

Figure 3.23 Typical Cracking Behavior for Specimens with ρ_s = 0.2%

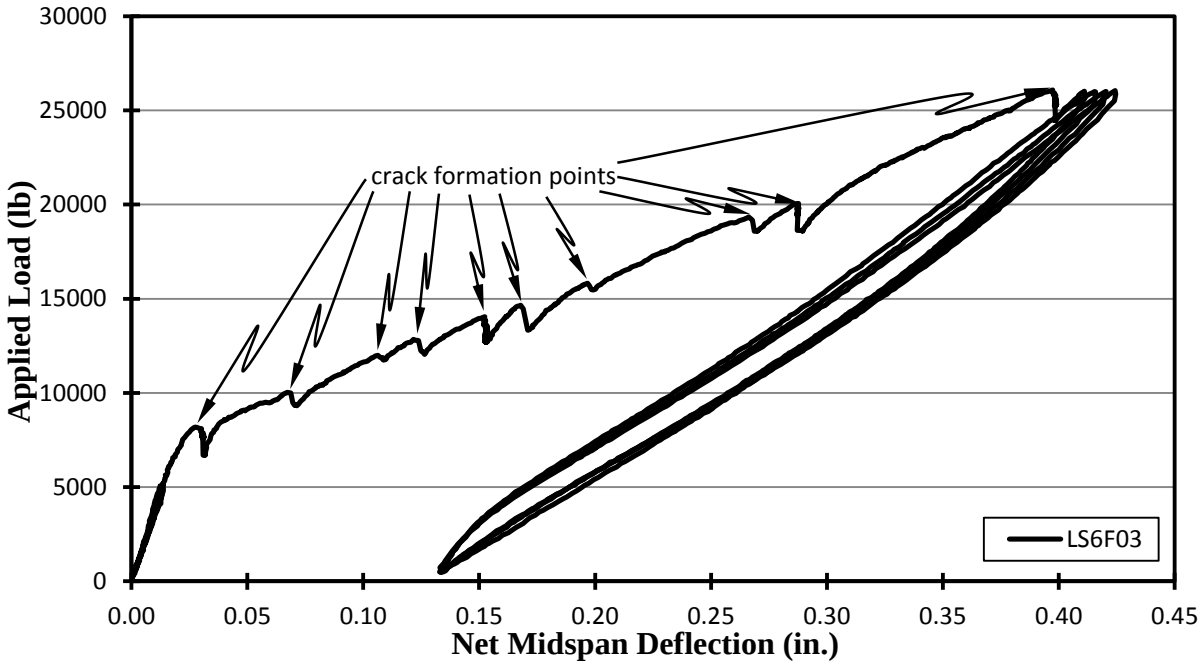

Figure 3.24 Typical Cracking Behavior for Specimens with ρ_s = 0.6%

During the application of load to the specimens, cracks began to form at lower magnitude moments than expected. This behavior is summarized in Table 3.3.

Table 3.3 Specimen Cracking Data

Beam ID	P_{cr} (kips)	M_w (kip-ft)	M_{app} (kip-ft)	M_{cr} (kip-ft)	f_r (psi)	$7.5\sqrt{f_c}$ (psi)	$f_r/\sqrt{f_c}$	$f_{r,ASTM}$ (psi)
LS2F00	7.96	5.55	19.9	25.5	340	430	5.9	740 ($12.9\sqrt{f_c}$)
LS2F03	7.48		18.7	24.3	325		5.7	
LS2F08	6.86		17.2	22.7	305		5.3	
LS2F16	6.90		17.3	22.8	305		5.3	
LS6F00	-		-	-	-		-	
LS6F03	8.20		20.5	26.1	335		5.8	
LS6F08	7.52		18.8	24.4	315		5.4	
LS6F16	6.96		17.4	23.0	295		5.1	

The apparent rupture stress, f_r, for each specimen is computed using transformed-section properties and the applied cracking moment, M_{cr}—gleaned from the combination of the maximum moment due to self-weight, M_w, and the maximum applied moment, M_{app}, as derived from the applied load at cracking, P_{cr}, for each specimen—and compared with the standard theoretical rupture-stress assumption for concrete of $7.5\sqrt{f_c}$. As shown, the actual stresses reached before cracking fall at magnitudes between approximately 70 and 80 percent of the predicted rupture stress—behavior that can be attributed to the weakened nature of the tension face of the concrete due to the presence of bleed water during curing as a result of the flange-up casting orientation of the specimens. Similarly, the results of the rupture test specimens as specified by ASTM C 78, $f_{r,ASTM}$, are more than twice the stresses observed during the beam cracking process—an anomaly that might be connected to early fracture initiation in the extreme tensile layer of the concrete in the test beams due to size effect (Bazant 1995) related to

specimens of differing scale as well as to the previously mentioned effect of the casting orientation.

For the specimens with ρ_s = 0.6%, cracks formed along the stirrups within the middle 50 percent of the span, as shown in Figure 3.25. At the peak load, the specimens exhibited reinforcement strains near the yield limit due to the larger-than-normal contribution of the self-weight to the moment for a smaller cross section.

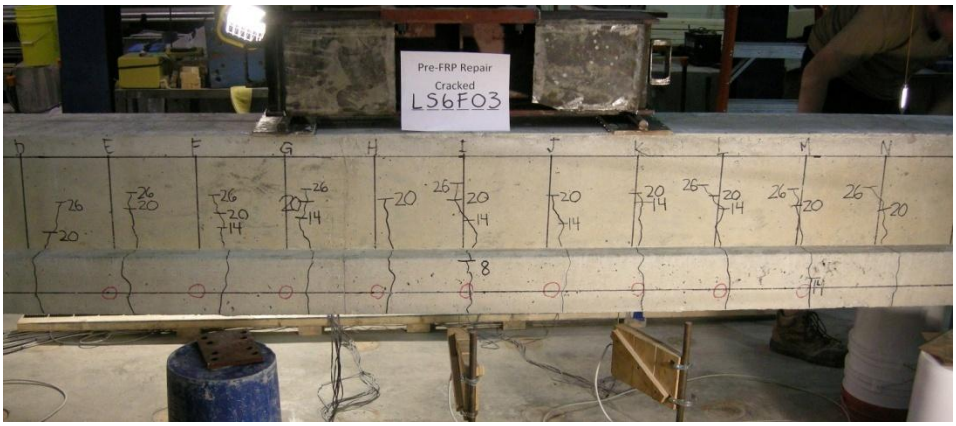

Figure 3.25 Typical Cracking Pattern for Specimens with ρ_s = 0.6%

More care was required when loading the specimens with ρ_s = 0.2% to avoid overstressing the steel before repair. As previously seen in Figure 3.23, the large stiffness drop as each crack formed indicates the under-reinforced nature of these specimens (as well as the corresponding cross sections of the Letohatchee bridge). Combined with the overall weaker nature of a lesser-reinforced cross-section, fewer cracks formed per beam, as seen in Figure 3.26, and tended to only occur within the maximum moment region of the specimen. Additionally, due to the same self-weight oversight as occurred with the more moderately reinforced specimens, the reinforcing steel registered strain values above the yield limit of the steel, though not significantly enough to alter the ultimate behavior of the beams.

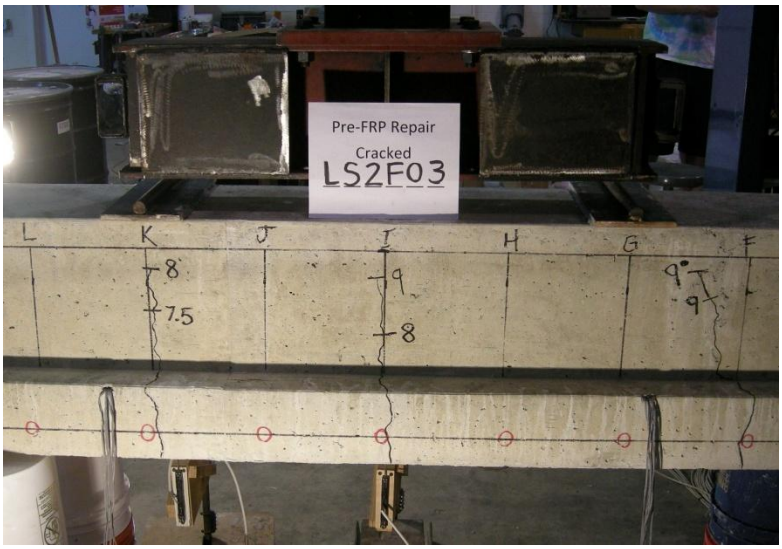

Figure 3.26 Typical Cracking Pattern for Specimens with ρ_s = 0.2%

Upon completion of the cracking procedure, all eight specimens were again inverted to provide access to the flange for the installation of the FRP reinforcement. The beams were placed directly onto the laboratory strong floor so that the specimens would be fully supported along their length during the repair process, allowing for a uniform level of strain along the length of the member as well as minimizing the difference in strain between the concrete near the tensile face and the installed FRP, thereby creating a state similar to the low-dead-load-moment condition of the bridge cross sections to be repaired.

CHAPTER 4: FRP INSTALLATION

.

This chapter details the NSM FRP installation procedure applied in the laboratory—including the preparation and cleaning of the grooves, the application of the epoxy and FRP, and the curing of the epoxy prior to final loading— as well as a recommended procedure for field installation based upon experience gained.

The installation process began with the cutting of the grooves necessary for the NSM FRP strips, as discussed in Section 3.2.5, prior to cracking the specimens in preparation for repair and with placing the specimens into proper support conditions, as described at the end of Section 3.4.

4.1 Groove Preparation

Prior to final preparation, a marked screwdriver was used as a depth gauge to confirm a minimum depth of 7/8 in. along the length of each groove. Slight high-points and offsets were present at the end of each cut due to the nature of track saw assembly used in the laboratory. To rectify this condition, a standard circular saw with an abrasive disc was employed to knock down any ridges and to smooth all transitions between cuts along the length of the grooves.

Each of the grooves was then thoroughly cleaned using compressed air and a wire brush in order to provide a proper bonding surface for the epoxy. Both edges of each groove were taped, as shown in Figure 4.1, in order to maintain an epoxy-free surface on the rest of the specimen and to limit the addition of loose particulates from the flange after cleaning. After taping was complete, each groove was checked for any remaining dried slurry—using a screwdriver to scrape the bottom and corners along the length of the groove, as seen in Figure

4.2—and compressed air was again applied to remove any fine particulates introduced from within the laboratory. All grooved specimens were finally covered with plastic to prevent the addition of particulates within the laboratory until the application of the epoxy.

Figure 4.1 Taping of Grooves

Figure 4.2 Scraping of Grooves

4.2 Application of FRP

Small-scale mockups were used to observe the behavior of FRP and epoxy during application and to develop a method to ensure the proper implementation of the system within the specimens prior to the final application process. As seen in Figure 4.3, the FRP displayed a tendency to push toward the sides of the groove; simultaneously, the observation of the epoxy at multiple cross sections along the length of the mockups showed that, if the epoxy was not properly consolidated, voids would form beneath and beside the FRP strips. Proper installation also required the establishment of an appropriate method to insert the FRP to proper depth without leaving the top exposed or pushing the strip to the bottom of the groove, thereby providing space for the epoxy to properly bond to the NSM FRP and to provide environmental protection.

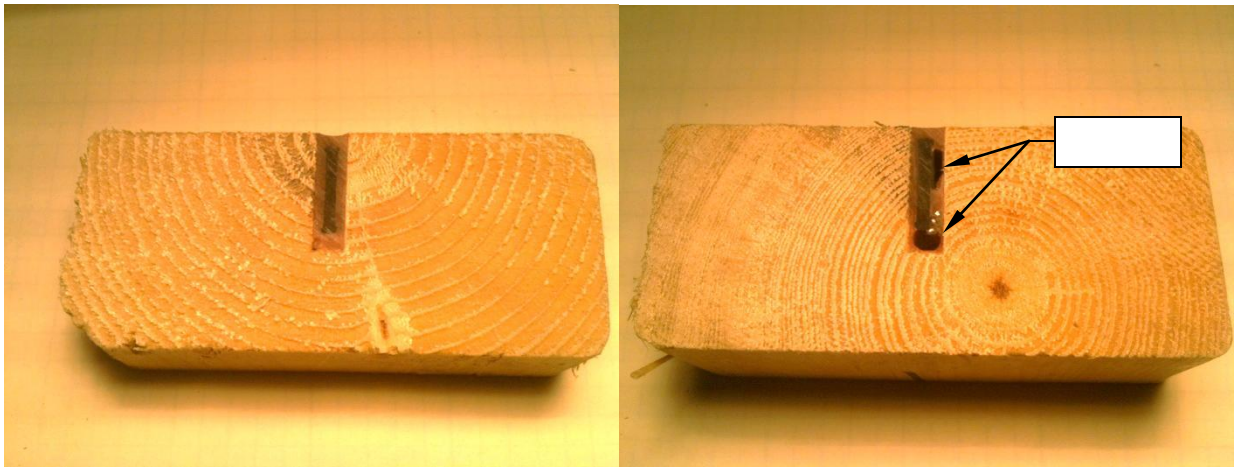

Figure 4.3 Cross Sections of Application Method Test Specimens

In order to combat these issues, a four-stage process was developed and implemented. First, the epoxy—in this instance, Hilti RE 500-SD 2-part epoxy—was injected into the groove through a static mixer via a gun, as seen in Figure 4.4. Second, the epoxy was manually consolidated using a putty knife, shown in Figure 4.5, in order to remove any voids left from the initial injection process.

Figure 4.4 Initial Injection of Epoxy

Figure 4.5 Manual Consolidation of Epoxy

After the consolidation process reduced the epoxy to approximately two-thirds of the depth of the groove, the FRP strip was inserted into the groove, as shown in Figure 4.6, and made flush with the face of the specimen. Figure 4.7 displays the centering process during this stage, wherein the putty knife was employed both to create and to measure a 1/16 in. gap between the FRP strip and the sides of the groove. Having centered the FRP within the groove, the strip was pushed to appropriate depth using a modified concrete grooving trowel, as seen in Figure 4.8. The trowel, when modified, provided the 1/4 in. wide and 1/8 in. deep surface necessary to press the FRP down to the proper depth without causing lateral displacement of the strip within the groove.

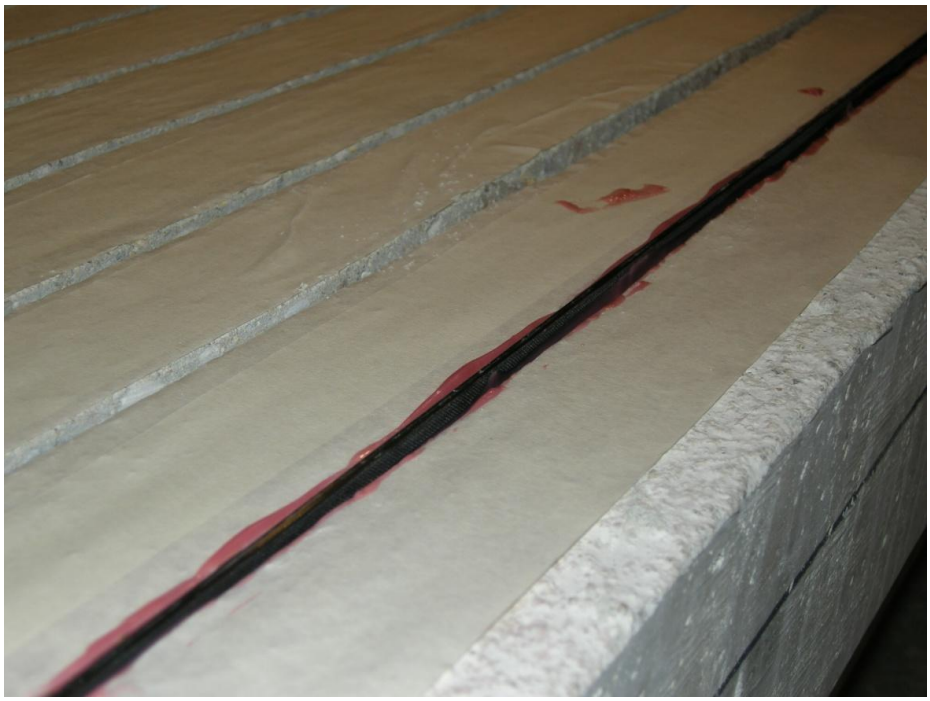

Figure 4.6 Insertion of FRP Strip into Epoxied Groove

Figure 4.7 Centering of FRP Strip within Groove

Figure 4.8 Setting of FRP to Depth Using the Modified Grooving Trowel

The final stage, as shown in Figure 4.9, involved the application of a single bead of epoxy to the top of the groove in order to provide the necessary cover for the FRP strip and to make the epoxy flush with the face of the specimen. Simultaneously, a putty knife was used to strike off any excess epoxy, as seen in Figure 4.10, from the groove and to create the flush surface desired for the groove. Figure 4.11 displays the results of the process that, for the six specimens and accompanying twenty grooves from this series, took approximately two hours to complete.

Figure 4.9 Final Application of Epoxy to Groove

Figure 4.10 Striking Off Excess Epoxy

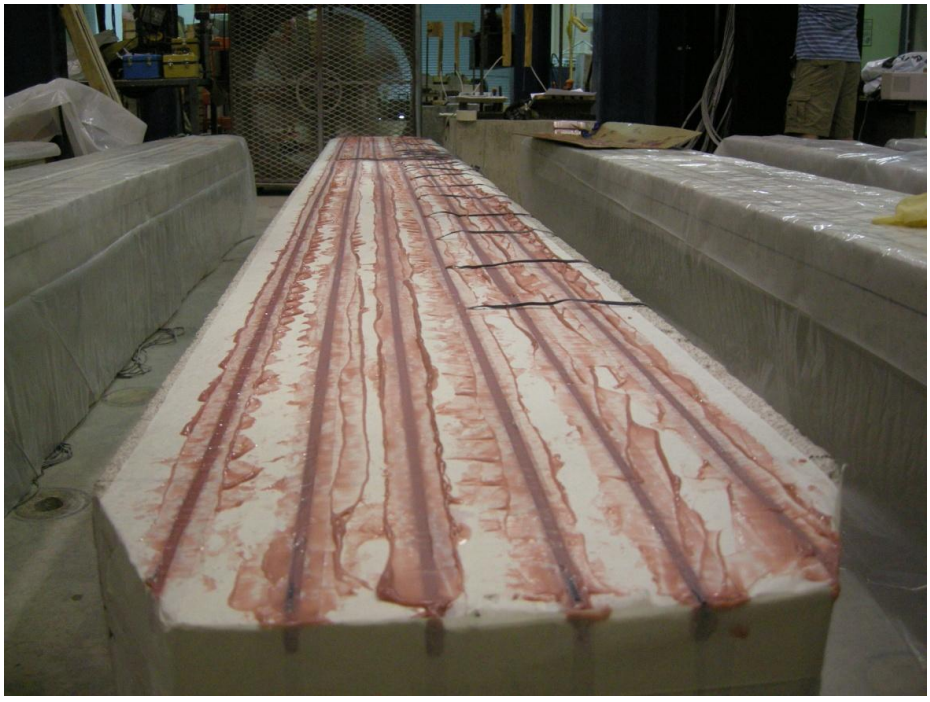

Figure 4.11 Completed Specimen Before Removal of Tape

4.3 Curing of Epoxy

The technical documentation for the chosen epoxy (Hilti 2008) recommends a 6 hr initial cure time, $t_{cure,ini}$, and 12 hr full cure time, $t_{cure,full}$—alongside a workable time limit, t_{work}, of 30 min— based on the approximate ambient temperature of 68 °F within the laboratory, as detailed in Table 4.1.

Table 4.1 Epoxy Cure Times (Adapted from Hilti 2008)

°F	°C	t_{work}	$t_{cure,ini}$	$t_{cure,full}$
41	5	2.5 hr	18 hr	72 hr
50	10	2 hr	12 hr	48 hr
59	15	1.5 hr	8 hr	24 hr
68	20	30 min	6 hr	12 hr
86	30	20 min	4 hr	8 hr
104	40	12 min	2 hr	4 hr

However, the epoxy in these specimens was allowed to cure undisturbed for 7 days, seen in Figure 4.12, after initial application in order to disqualify any inconsistencies in the curing of the epoxy among the various grooves as a variable to be considered during final testing. At this point, all tape was removed from the specimens, as shown in Figure 4.13, and all gage wires were checked to ensure proper operation for the remainder of the testing program.

Figure 4.12 Cured Specimens

Figure 4.13 Cured Specimens with Taped Removed

4.4 Field Application

Based upon experience gained during the laboratory installation process, a recommended field application procedure for NSM FRP has been developed as follows:

1. Cut grooves using diamond-bladed concrete wet saw to required thickness. The thickness of the groove shall be no less than 3 times the thickness of the FRP strip and no more than 4 times the strip thickness. The groove shall not deviate more than 1/4 in. from the prescribed straight line. Any kinks created by discontinuous cuts must be ground to create a smooth transition in the identified region. The minimum depth for a groove shall be no less than 1.5 times the width of the FRP strip. The maximum depth of the groove shall be no more than 2.0 times the FRP strip width.
2. Clearance to existing deck reinforcement should be verified using non-destructive means such as ground-penetrating radar.
3. Use compressed air to clear grooves of slurry at the time of groove cutting. If traffic flow has been allowed over the unfinished grooves between the initial cleaning of the groove and the installation of the FRP, compressed air shall again be used to remove any particulates.
4. Inject epoxy along the length of the groove. Consolidate epoxy to eliminate air voids in groove. Epoxy shall not be applied during rain. Grooves shall be surface dry before epoxy is applied. Grooves may be dried using compressed air following wet conditions.
5. Center and insert the NSM FRP strip in the groove. The strip shall be inserted until approximately flush with the surface of the concrete and shall be approximately centered in the groove before final seating.

6. Set strip to proper depth using appropriate tool. Seated FRP strip shall be at least 1/8 in. below the concrete surface to provide necessary space for epoxy coverage without the strip bottoming in the groove.
7. Apply finishing bead of epoxy and strike off excess to make flush with surface of concrete.
8. Hardened epoxy shall extend no more than 1/4 in. from the edge of the groove.
9. Cure epoxy until full recommended time limit before resuming traffic flow. The recommended time limit shall be based on conditions during application. The epoxied grooves can be protected with plastic if wet conditions are expected before the initial cure time is reached.

Several recommendations can be offered to expedite and ease the application process. Maintaining proper depth and thickness are priorities when cutting the grooves. Any configuration of blades is allowable, as long as the minimum required thickness and depth can be achieved. When choosing a saw for cutting the grooves, three viable options exist: a track-mounted saw, a hand saw, and a standard joint-cutting saw. The advantage of the track-mounted saw lies in the ability to easily and consistently control the depth of the cut, with the disadvantage arising with the need to anchor the saw to the cutting surface and to move the saw when it reaches the end of its track, requiring an overlap of cutting to ensure a consistent depth over the length of the groove. The advantage of a hand saw or joint-cutting saw lies in the speed of operation, allowing for the cutting of each groove in a single pass. The only foreseeable disadvantage exists in the realm of depth control, which is key for both the proper provision of surface area for the FRP and for the efficient application of material—a disadvantage that can be overcome through the assembly of a depth guide for use with the saw, similar to that attached to

a standard circular saw. Ultimately, equipment availability and cost efficiency will determine the best method for cutting, as the disadvantage of each method can be overcome with proper preparation.

For consolidating the epoxy, any tool with a small profile—roughly one-quarter the width of the groove —will provide the necessary disruption of any voids created during the injection process. Likewise, any implement with an approximate thickness of 1/16 in. can be employed to center the FRP strip in the groove during insertion and, as a result, ensure a proper epoxy bond on both faces of the NSM FRP strip. To seat the strip to the appropriate depth—thus providing room for epoxy both above and below the strip for proper bonding and environmental protection—experimentation showed the most efficient tool to be a concrete grooving trowel modified to provide the necessary depth in profile. To aid in creating a finished surface without excess epoxy, applying tape to the edges of the groove is recommended. If this method is applied, the tape should be removed toward the end of the workable period as defined by the ambient temperature or when the epoxy seems to have sufficiently set to prevent hardening of the excess epoxy to the point of making tape removal impractical.

CHAPTER 5: TESTING PROGRAM

5.1 Test Assembly

5.1.1 Loading Configuration

To obtain the desired four-point loading scheme as seen in Figure 5.1, a steel W-section with a 36 in. span was used as a spreader beam for the application of load, while a pair of rollers were employed as supports.

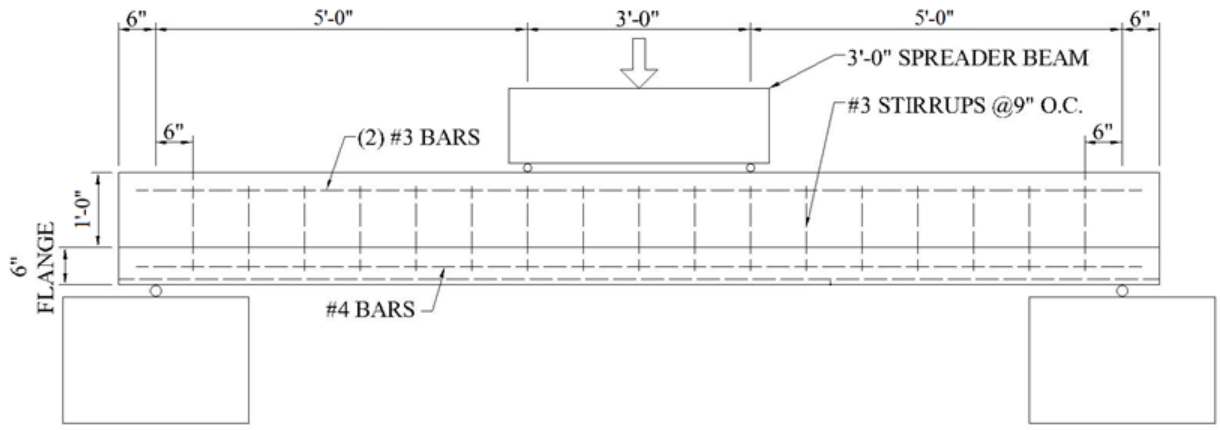

Figure 5.1 Specimen Loading Scheme

5.1.2 Load Application

An 82 kip hydraulic actuator attached to a steel loading frame was used to apply all loads for this program via an attached spreader beam. The spreader beam rested on a pair of 1 in. diameter steel cylinders welded to 4 x 12 in. steel plates in order to lessen the load concentration effects on the specimen. Simultaneously, the load plates were seated in gypsum cement, allowing for the even transmission of the concentrated loads through the plates to the concrete surface.

5.1.3 Supports

To create proper support conditions, a true roller—composed of a 1 in. diameter steel cylinder placed between two 6 x 18 in. plates and depicted in Figure 5.2—was used in place of a fixed support system due to the symmetric nature of the loading scheme.

Figure 5.2 Initial Roller Assembly

The rollers were later modified to include high-radius indentations in order to prevent sudden lateral displacement at higher load levels.

5.2 Instrumentation and Data Acquisition

The instrumentation used for all tests consisted of

- Electrical resistance strain gages (ERSGs) for measuring steel reinforcement, FRP reinforcement, and concrete surface strains at various locations within and on the specimen
- Linear potentiometers for measuring overall vertical deflection of the member, and

- Load and displacement transducers built into the hydraulic actuator for measuring load application to the beam.

Figure 5.3 shows the basic locations of each instrument type for a typical repaired specimen.

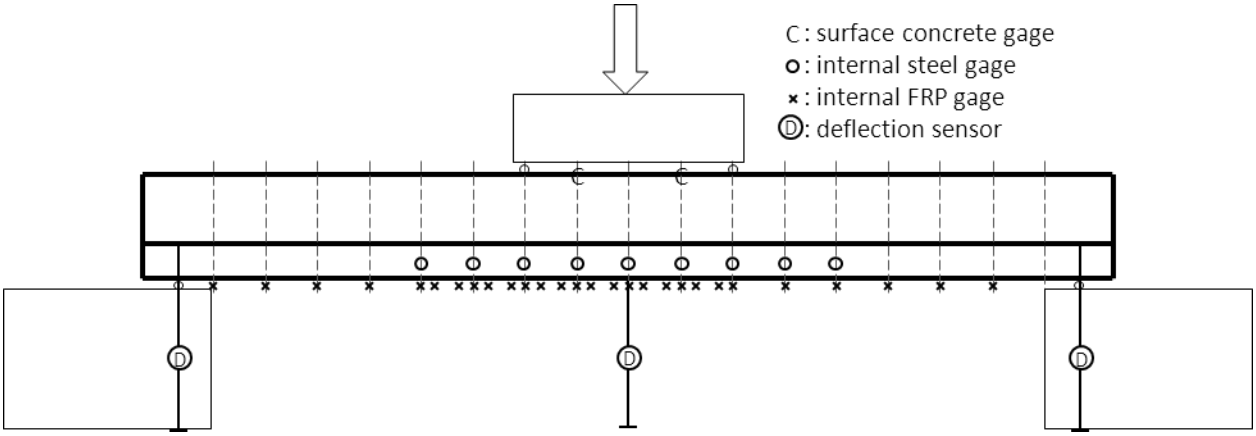

Figure 5.3 Instrumentation Arrangement

In order to measure the relative displacement of the specimen, a system of five linear displacement potentiometers was used: two placed on the flange over the support on each end and one placed at midspan beneath the specimen. The displacements measured by the potentiometers at the supports were averaged and subtracted from the midspan displacement measurement in order to compensate for the relative movement of the supports or any torsion due to a load not aligned with the longitudinal centerline of the specimen.

All strain gages used were self-temperature compensating with pre-attached lead wires. For the steel and FRP reinforcement, the applied gages were foil-based; for concrete, wire-based. Table 5.1 includes the details of the strain gage types employed.

Table 5.1 Strain Gage Information

Gage Use	Gage Name	Resistance (Ω)	Gage Length (mm)	Gage Factor
Steel Reinforcement	FLA-6-350-11	350	6	2.12
FRP Reinforcement	FLA-6-350-11	350	6	2.12
Concrete	PL-60-11	120	60	2.12

5.2.1 Steel Instrumentation

The longitudinal tensile steel strains were measured by directly instrumenting the bars at various locations within the specimen in the manner displayed in Figure 5.4.

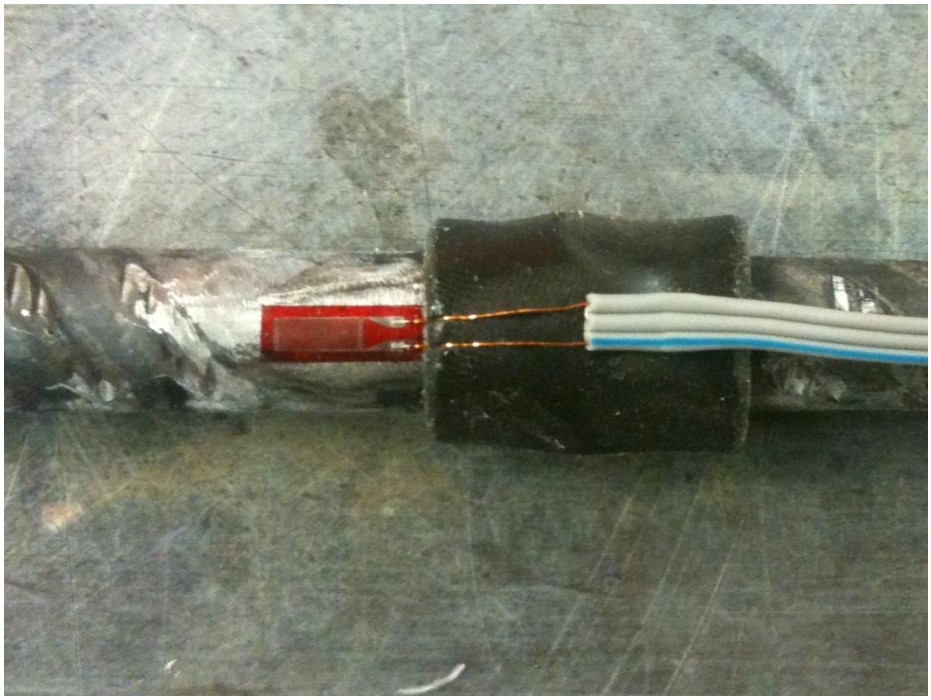

Figure 5.4 Typical Steel Gage

As one set of specimens contained two #4 deformed bars acting as tensile reinforcement while the other contained six, the two bars common to both sets of beams—those located at the bends in the stirrups—were instrumented. To gain more accurate strain data, the gages were placed at locations along the length of the specimen coinciding with stirrup locations, where flexural

cracks were expected to occur. Each beam contained a minimum of eleven steel reinforcing strain gages, with nine instrumented cross sections—as shown in Figure 5.5—and an extra gage placed at each of the load point locations for redundancy and confirmation of strain distribution. The more moderately reinforced control specimen, LS6F00, contained an additional four gages— denoted by squares in Figure 5.5—under one of the load points in order to monitor strain distribution among the six bars within the cross section.

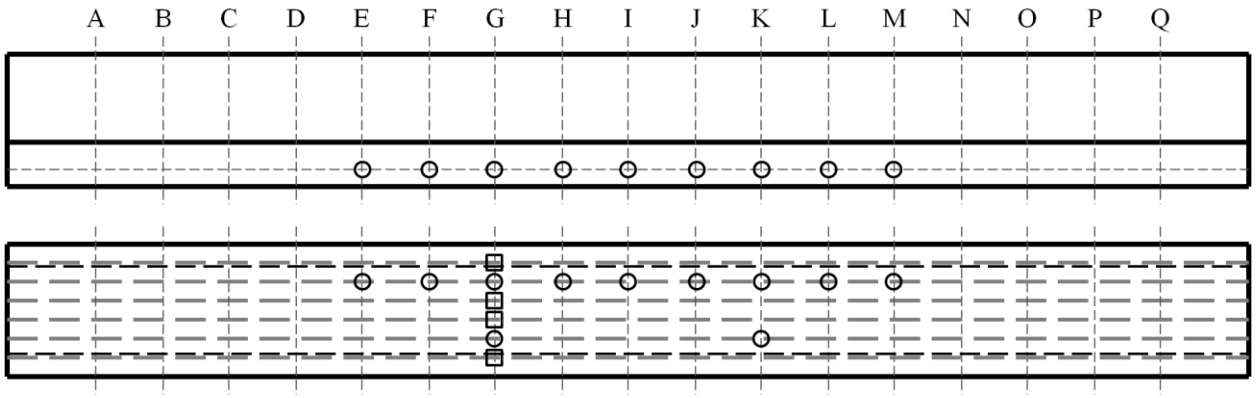

Figure 5.5 Steel Gage Locations (Side and Bottom Views)

To properly attach the gages to the reinforcing steel, the deformations were removed via mechanical grinder at each gage location. Each location was prepared and gaged in accordance with the standard procedure for gaging steel. The lead wires were separated from the steel by mastic tape to allow the proper transfer of the signal from the gage, after which the gages were coated in nitrile rubber and covered with heat shrink tubing to prevent exposure to moisture during concrete placement.

5.2.2 FRP Instrumentation

Prior to installation, at least one FRP strip was instrumented per beam to be repaired. Gages were installed at actual crack locations—given that each crack that coincided with the placement of a reinforcing steel gage was within 1 in. of the predicted location—and 2.5 in. on either side of

each crack in order to monitor the relative behavior of the FRP for debonding. Figure 5.6 to Figure 5.11 indicate the crack locations and the locations of the gages along the FRP relative to the cracks.

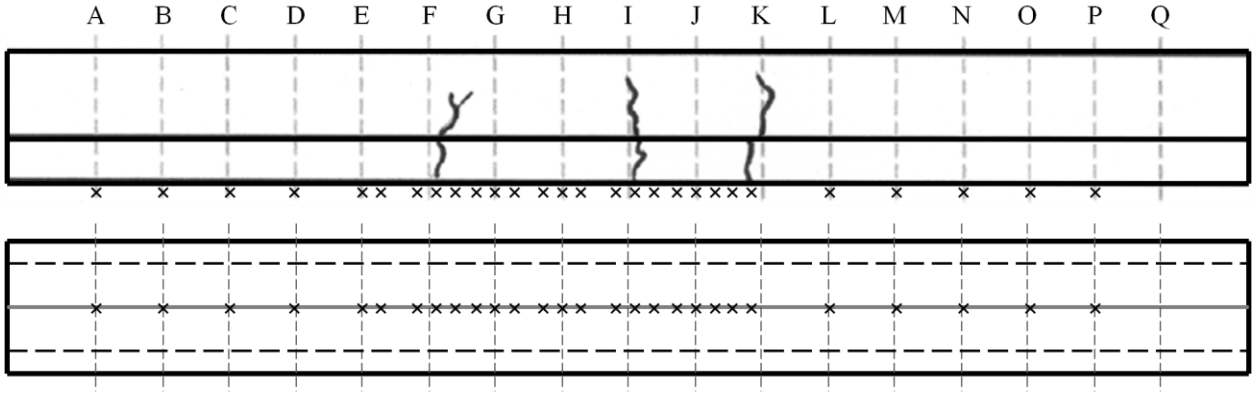

Figure 5.6 FRP Gage Locations—LS2F03 (Side and Bottom Views)

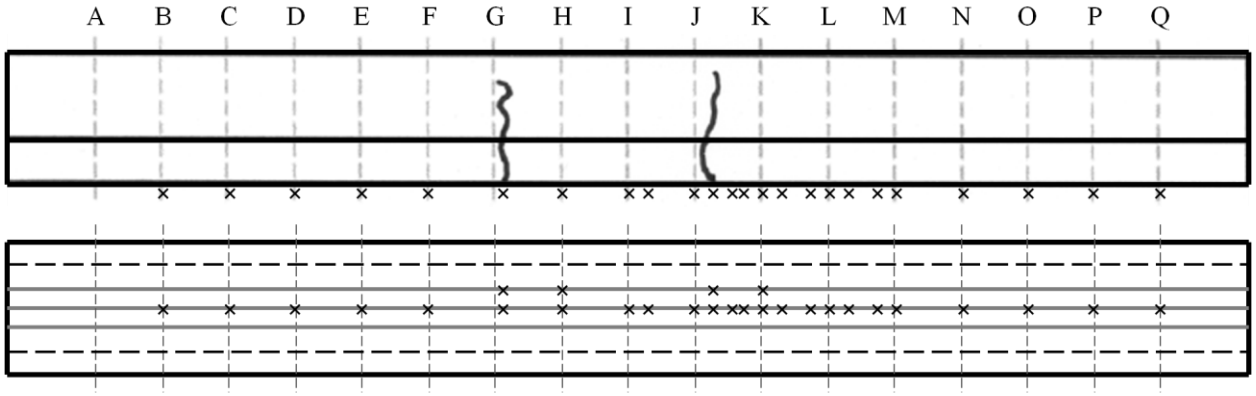

Figure 5.7 FRP Gage Locations—LS2F08 (Side and Bottom Views)

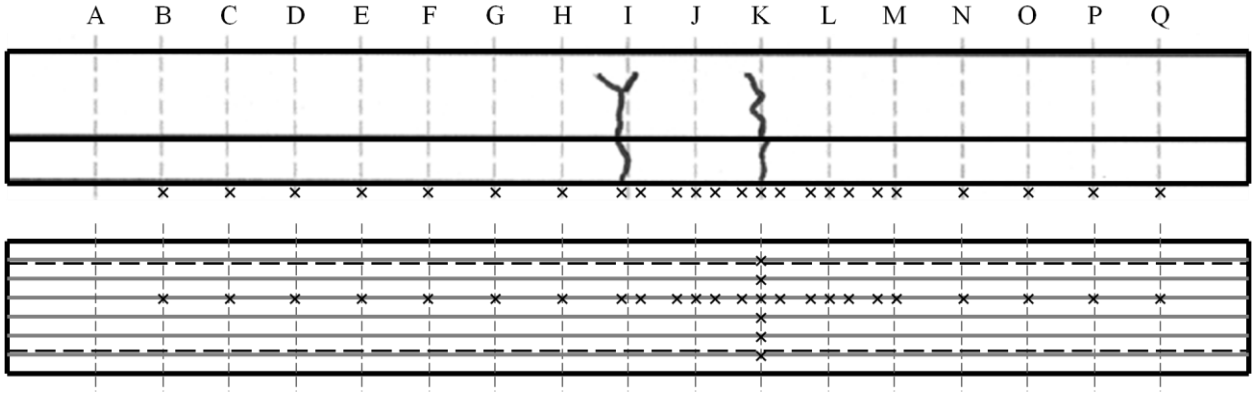

Figure 5.8 FRP Gage Locations—LS2F16 (Side and Bottom Views)

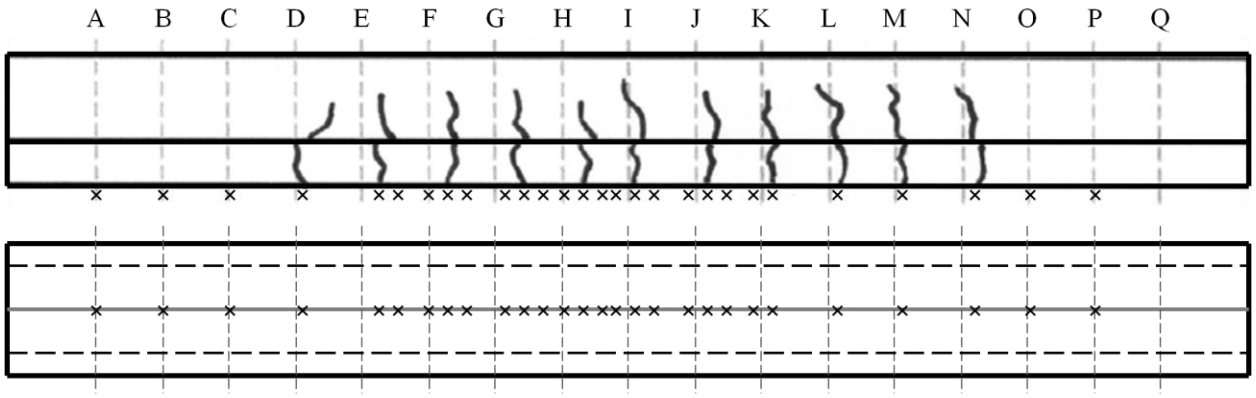

Figure 5.9 FRP Gage Locations—LS6F03 (Side and Bottom Views)

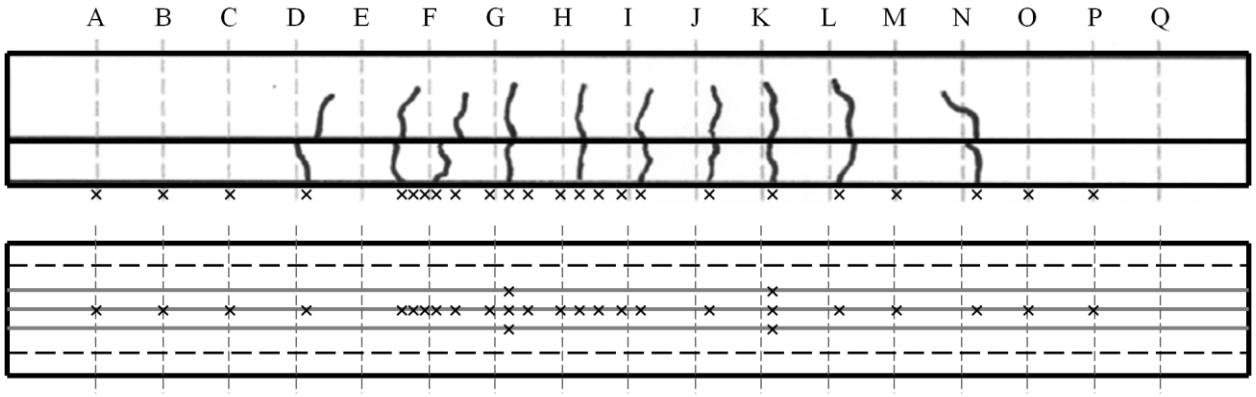

Figure 5.10 FRP Gage Locations—LS6F08 (Side and Bottom Views)

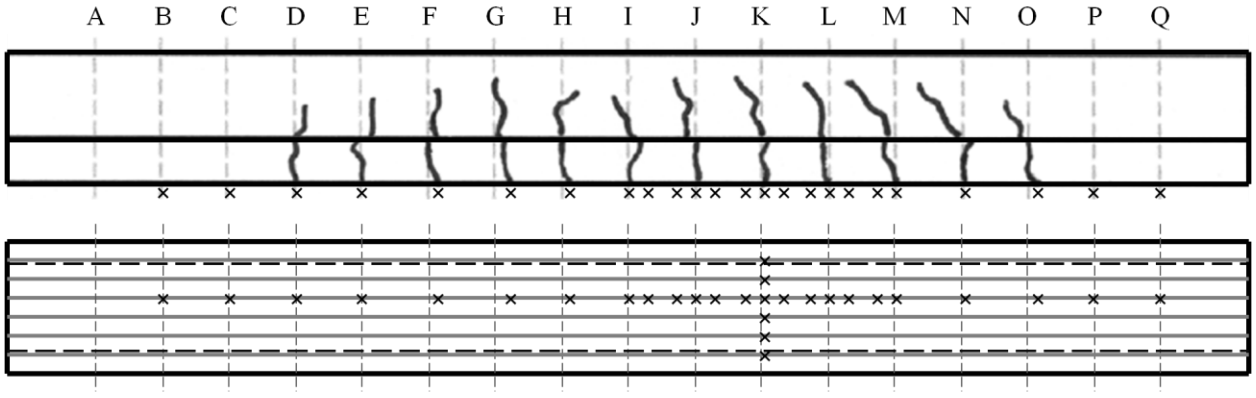

Figure 5.11 FRP Gage Locations—LS6F16 (Side and Bottom Views)

In order to properly secure the gages to the strips, 100% solids epoxy was applied and sanded, as seen in Figure 5.12, to provide a smooth surface for installation. Each location was thoroughly cleaned before the gage was applied using the bonding agent, as shown in Figure 5.13.

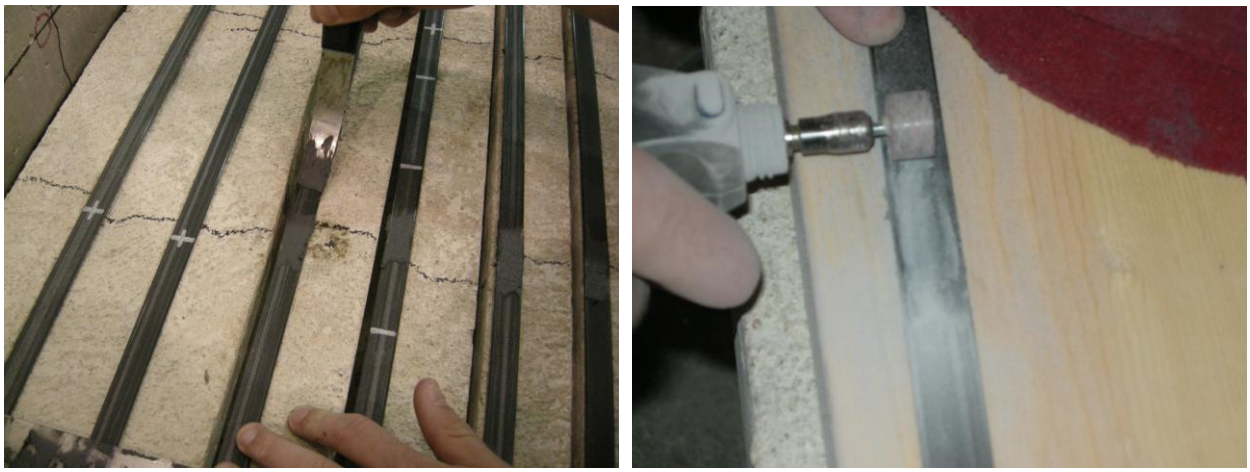

Figure 5.12 Preparation of Gage Location

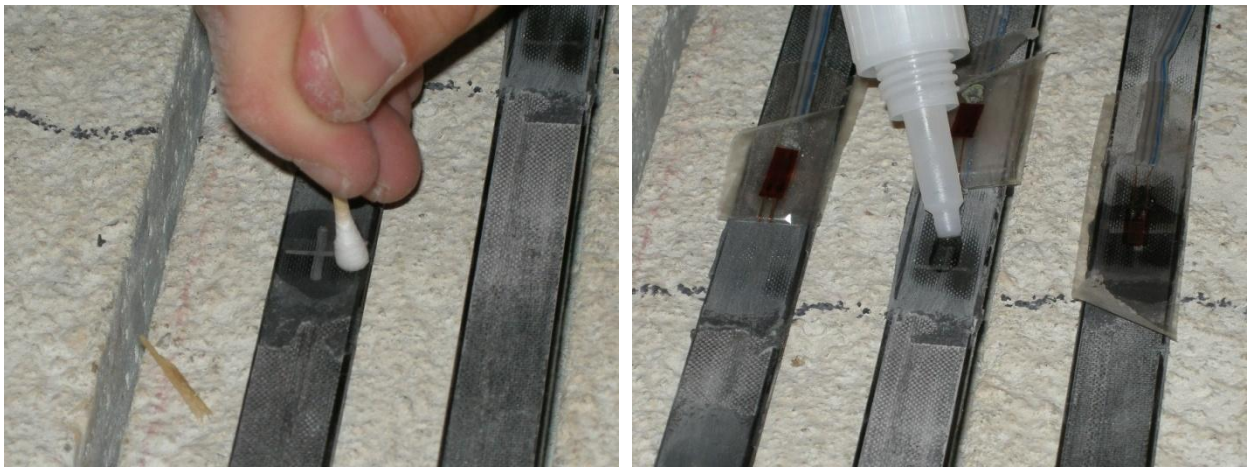

Figure 5.13 Installation of FRP Gage

The gages were finally covered in nitrile rubber as protection against any moisture in the epoxy, and the area around each gage was scrubbed clean in order to ensure a proper bond between the FRP and the epoxy, as displayed in Figure 5.14.

Figure 5.14 Final FRP Gage Preparation

5.2.3 Concrete Instrumentation

Surface-mounted strain gages were used to measure concrete strains, with each location prepared and each gage attached using epoxy. Two gages were used for each specimen, placed along the longitudinal axis within the maximum moment region of the beam. The location of the gages varied between specimens, as the goal of the gage placement was to match an existing crack in order to create a complete strain profile for a cracked cross section within the highest moment region of the specimen.

5.2.4 Data Acquisition

In order to process the data from the strain gages and potentiometers, a Pacific Instruments 6000 Data Acquisition System was employed alongside the accompanying software necessary for the visualization of the data as it was collected. The data were archived after each testing period and subsequently compiled by specimen and processed as needed.

5.3 Application of Post-Repair Cycles

In field application, the repaired bridge will experience stress cycles due to traffic loading. To represent years of repaired service cycles—so that the long-term viability and behavior of the FRP can be observed—post-repair load cycles were imposed on the laboratory specimens.

Each specimen, including the control beams, was subjected to 50,000 cycles with the loading system operating in load-control mode. Each cycle spanned between a maximum and minimum load based on the service-load condition of the beam. The maximum load applied during cycling corresponded to a calculated FRP stress (f_f) of 25 ksi, which resulted in an approximate stress in tension steel (f_s) of 30 ksi. This level of stress in the reinforcement coincides with a load equivalent to approximately 60% of the yield condition for each specimen. The minimum load condition was established as 11% of the yield load, based on the load necessary to maintain contact between the spreader and the load points during the cycling process. Data were recorded at the 1st, 10th, 100th, 1,000th, 10,000th, and 50,000th cycle.

5.4 Test to Failure

Having been cracked as detailed in Section 3.4, subsequently repaired, and cyclically loaded within the service-load range, the beams were loaded monotonically in displacement-control mode to avoid the application of load past the failure of the beam. Loading was stopped at the apparent yield and subsequently at intervals corresponding to the observed propagation of cracks until failure to collect physical measurements. Crack widths were measured within the maximum moment region and new cracks and crack extensions were marked on the beam with a blue permanent marker to distinguish new cracking from cracks resulting from the initial cracking process. Data were recorded throughout each test and later processed to yield two data sets per second. The failure mode for all repaired specimens was characterized by a significant drop in the load applied to the beam under the continued application of displacement, while the ultimate strength of the control specimens was established by a lack of load increase under continuous displacement.

CHAPTER 6: ANALYTICAL PROCEDURES

6.1 Modeling of Nonlinear Constituent Material Behavior

A nonlinear, layer-by-layer flexural analysis was performed as described by Collins and Mitchell (1991) for each specimen in order to evaluate the moment-curvature performance of the beams as well as to provide theoretical data for comparison with experimentally generated results. The specimen cross section was discretized into thin layers, as shown in Figure 6.1.

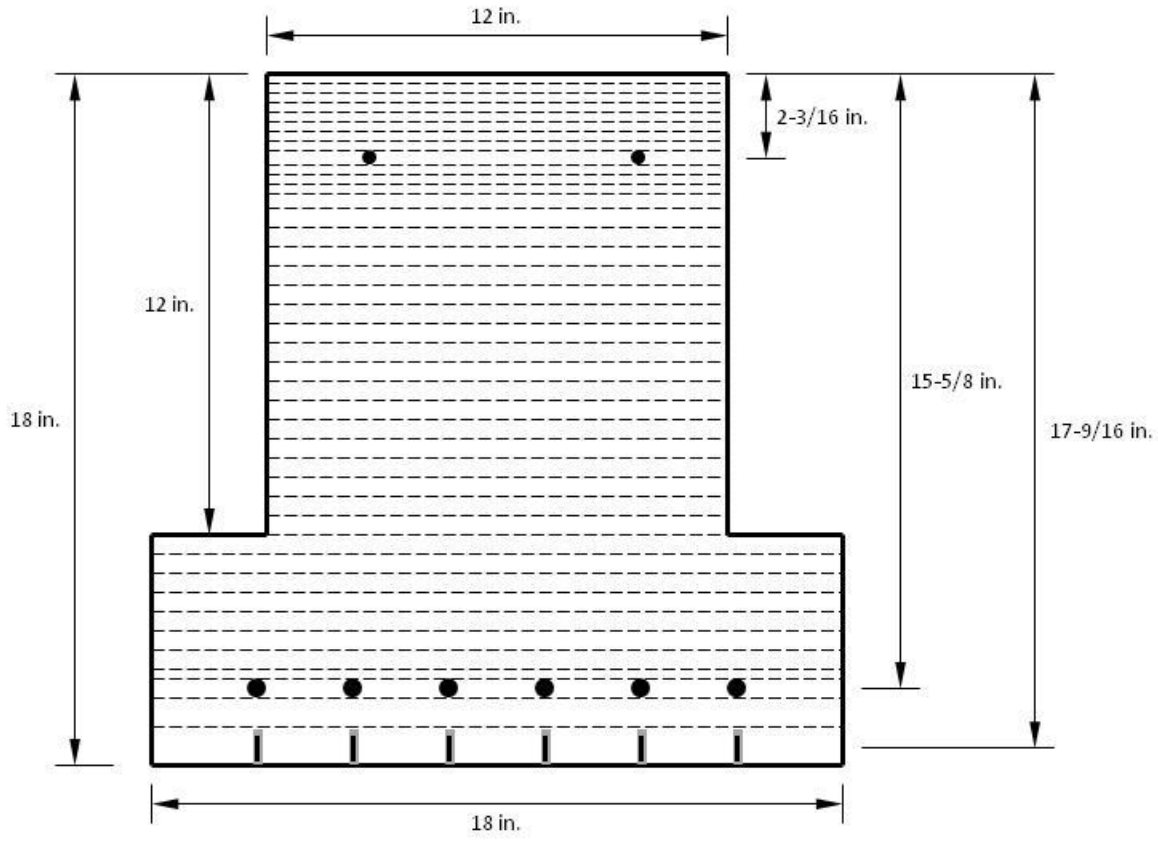

Figure 6.1 Discretized Layers for Sectional Analysis

Each of the layers was individually evaluated as an axial member, with the relative deformation of the layers constrained to be proportional to the depth from the neutral axis. The concrete of the cross section was divided into forty-two layers, with 1/4-in. layers used in the compression region of the web to account for the expected nonlinear behavior of the concrete, while the remainder of the web and the entire flange were mainly composed of 1/2-in. layers. The rows of longitudinal compression and tension steel reinforcement and FRP reinforcement represented an additional three layers. All layers were assumed to begin in a state of neutral strain based on the conditions under which repairs to the specimen were made.

For an assumed value of strain in the extreme compression fiber of the concrete, the corresponding neutral axis position and curvature were determined by an iterative approach that relied upon the establishment of equilibrium as a zero sum of the axial forces present in the individual layers. The moment within the cross section was calculated by summing the individual moments created from the axial forces of the layer about the established neutral axis. Repetition of this process for multiple extreme compression fiber strains resulted in the development of a moment-curvature response for each specimen.

6.1.1 Concrete Modeling

The general behavior of the concrete at a singular cross section was modeled using the nonlinear relationship given in Equation 6.1 (Collins and Mitchell 1991), with the concrete compressive strength, here defined as $f_c^{'}$, and modulus of elasticity, E_c, based upon cylinder tests performed at the time of flexural testing and an assumed tensile stress termination at the concrete cracking stress, f_{cr}.

$$f_c = f_c' \left[\frac{n\left(\frac{\varepsilon_c}{\varepsilon_c'}\right)}{n - 1 + \left(\frac{\varepsilon_c}{\varepsilon_c'}\right)^{nk}} \right] \qquad \textbf{Equation 6.1}$$

where

f_c = concrete stress
n = curve-fitting factor = $0.8 + \frac{f_c'}{2500}$
ε_c = concrete strain
ε_c' = concrete strain at $f_c' = \frac{f_c'}{E_c}\frac{n}{n-1}$
k = decay factor = $0.67 + \frac{f_c'}{9000}$ if $\varepsilon_c \geq \varepsilon_c'$, otherwise 1.0

6.1.1.1 Tension Stiffening

To reflect the stiffness of a reinforced concrete member resulting from cracked and uncracked sections acting in concert, tension stiffening was applied in accordance with the general procedure outlined in Collins and Mitchell (1991) to examine the overall response of the repaired specimen. Within this thesis, tension stiffening was only applied to predict beam load-deflection response for comparison with the experimental results. All other theoretical data regarding strains, moment capacities, and internal forces were generated from a precracked, unstiffened model of a cracked cross section.

If the concrete at a layer located within $7.5d_b$ (steel bar diameters) of the steel reinforcement reached a tensile stress corresponding to the cracking stress, an average tensile stress—to account for the integrated tensile contribution of adjacent cracked and uncracked sections—was calculated according to the following relationship:

$$f_c = \frac{\alpha_1 \alpha_2 f_{cr}}{1 + \sqrt{500\varepsilon_c}}$$ **Equation 6.2**

where

α_1 = reinforcement bond factor = 1.0 for deformed bars
α_2 = sustained/repeated loading factor = 1.0 for monotonic loading
f_{cr} = cracking stress of concrete in specimen = $7.5\sqrt{f_c'}$

The resulting stress was applied to the regions within the cross section affected by tension stiffening, as depicted in Figure 6.2.

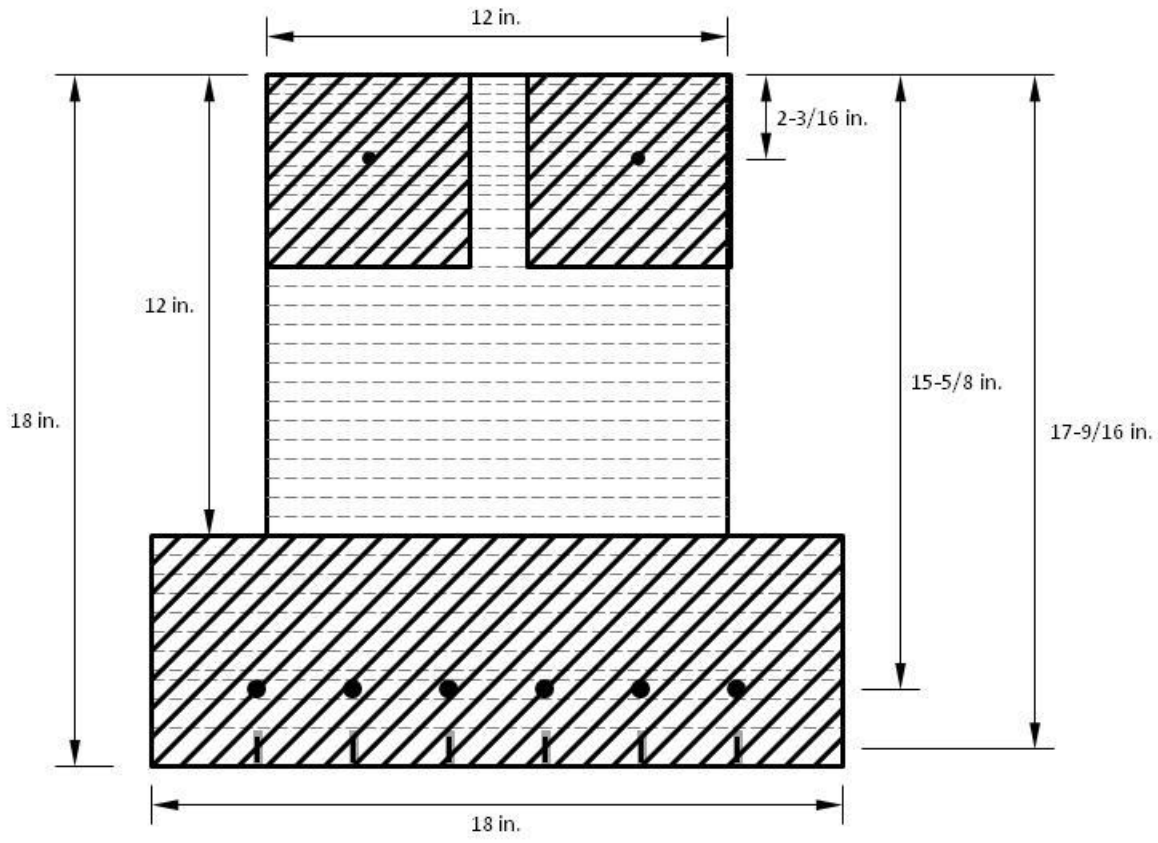

Figure 6.2 Tension-Stiffened Zones

The model employed tension stiffening to calculate the stress in any layer within the designated regions of the zone that transitions from a state of compression to a state of tension, even if the longitudinal reinforcement in that zone is not in tension. Fortunately, the tensile

contribution of the layers near the neutral axis under these conditions is slight and should not have significantly affected the load-deflection response predictions. To rectify this oversight, the model should be amended for future application to only apply tension stiffening if the reinforcement that contributes to the integrated behavior of the specimen at a specific layer is in tension.

The tension stiffening relationship from Collins and Mitchell (2001)—designed to approximate the integrated behavior of an uncracked beam under an initial loading—does not reflect the precracked condition of the repaired specimens, where the concrete surrounding the tensile reinforcement at cracked sections cannot contribute any tensile resistance. To account for the precracked nature of the specimens, a linear approximation was created by the researchers of this thesis, defined as follows:

$$f_c = \left(\frac{0.387 f_{cr}}{0.005}\right)\varepsilon_c \qquad \textbf{Equation 6.3}$$

The relationship above was designed to link the state of zero stress (and strain) resulting from the cracked cross section to the tension stiffening relationship in Equation 6.2 at an assumed tensile strain of 0.005 in/in, thereby reflecting the decrease in the resistance to deformation expected in a precracked specimen. The full modeled behavior for all possible assumed specimen conditions can be seen in Figure 6.3.

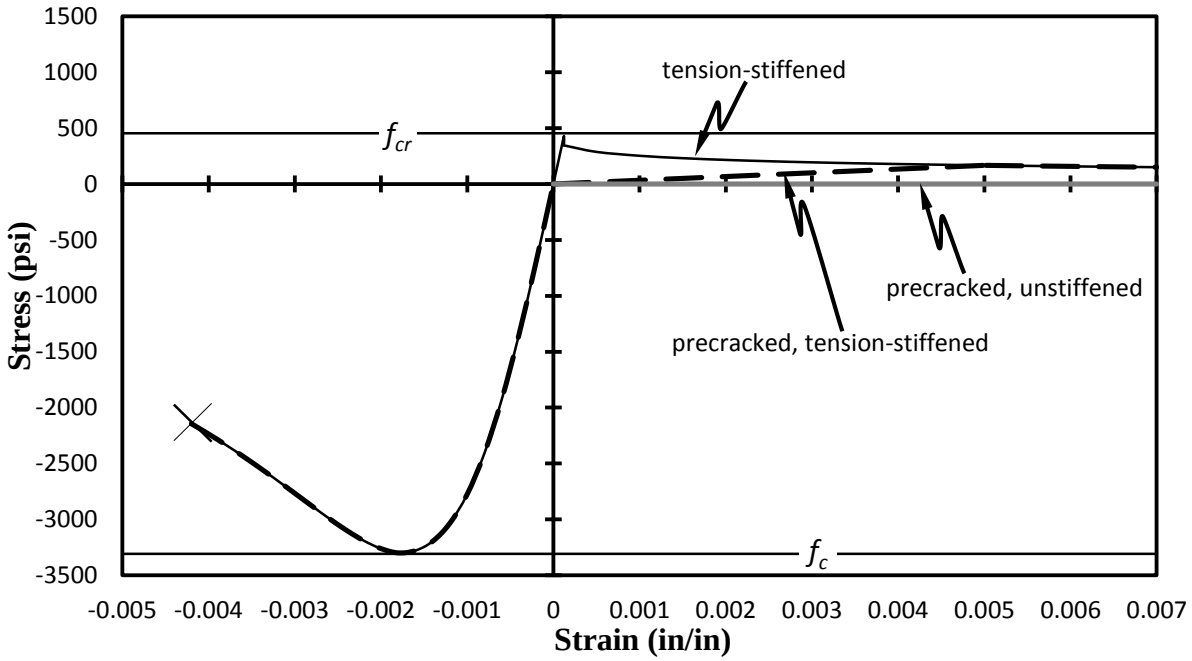

Figure 6.3 Theoretical Stress-Strain Relationship for Concrete

6.1.2 Steel Modeling

The behavior of the steel reinforcement was modeled using the following nonlinear relationship:

$$f_s = \begin{cases} 498000\varepsilon_s^4 + 166000\varepsilon_s^3 + 22000\varepsilon_s^2 + 1400\varepsilon_s - 43.3 & -0.1 \le \varepsilon_s \le -0.0079 \\ -f_y & -0.0079 \le \varepsilon_s < -0.0018 \\ E_s\varepsilon_s & -0.0018 \le \varepsilon_s < 0.0018 \\ f_y & 0.0018 \le \varepsilon_s < 0.0079 \\ -498000\varepsilon_s^4 + 166000\varepsilon_s^3 - 22000\varepsilon_s^2 + 1400\varepsilon_s + 43.3 & 0.0079 \le \varepsilon_s \le 0.1 \end{cases}$$ **Equation 6.4**

where

f_s = stress in tensile steel reinforcement, in ksi
ε_s = steel in tensile steel reinforcement, in in/in
f_y = yield stress of steel reinforcement
E_s = modulus of elasticity for steel reinforcement

The values of f_y and E_s, as well as the polynomial describing strain-hardened behavior up to ultimate strain, were determined from material testing performed in the laboratory, as described in Section 3.3.2. Figure 6.4 depicts the theoretical curve representing the full range of both the compressive and tensile behavior of the steel reinforcement.

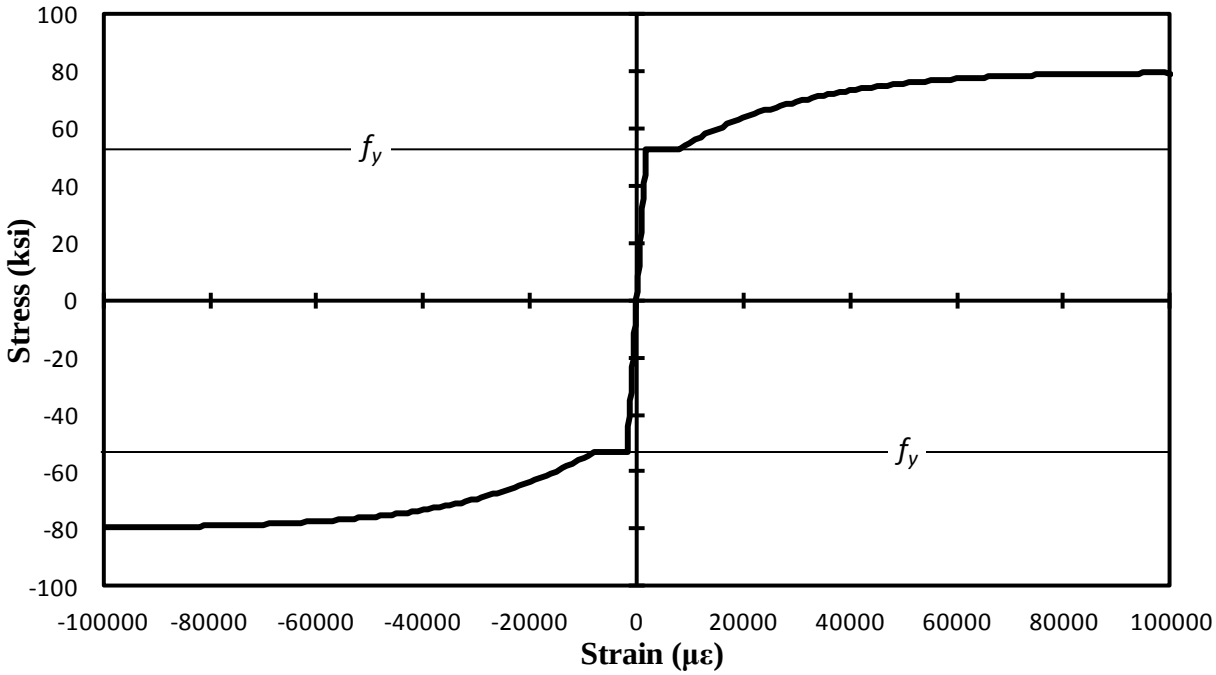

Figure 6.4 Theoretical Stress-Strain Relationship for Steel Reinforcement

6.1.3 FRP Modeling

The behavior of the FRP reinforcement was modeled using the following relationship:

$$f_f = E_f \varepsilon_f \leq f_{fu} \qquad \textbf{Equation 6.5}$$

where

f_f = stress in FRP reinforcement
ε_f = strain in FRP reinforcement
E_f = modulus of elasticity for FRP reinforcement
f_{fu} = design ultimate strength of FRP

The value of E_f was determined from on-site material testing of the FRP, as discussed in Section 3.3.3. The FRP model assumes purely tensile, linear-elastic behavior until rupture is achieved. Figure 6.5 displays the theoretical curve of FRP behavior up to a rupture stress of 345 ksi. Traditional design and analysis use a design ultimate strength, f_{fu}—which is 300 ksi for this specific FRP reinforcement—that lies three standard deviations below the actual average rupture

stress. The actual stress of 345 ksi was used for the layer-by-layer analysis in order to closely approximate the actual behavior of the FRP during the experiment.

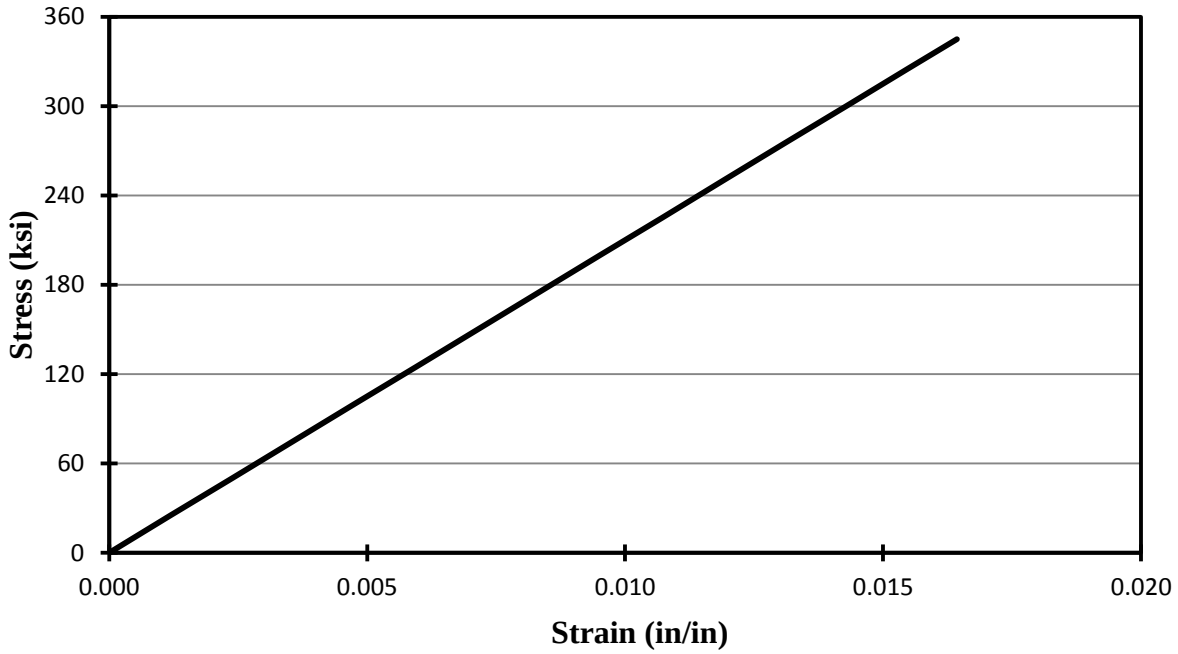

Figure 6.5 Theoretical Stress-Strain Relationship for FRP Reinforcement

6.1.4 Moment-Curvature Evaluation

Figure 6.6 to Figure 6.13 show the moment-curvature results for all eight specimens for the four analysis conditions: unstiffened and tension-stiffened initially-uncracked flexural response and unstiffened and tension-stiffened precracked flexural response. The displayed relationships terminate at values consistent with a non-anchorage failure (for a unstiffened analysis) indicated either by an extreme compressive fiber strain of 0.003 in/in—crushing of the concrete—or by a stress of 345 ksi in the FRP layer—FRP rupture—with the assumption that the FRP reinforcement does not experience debonding before either of these conditions occurs.

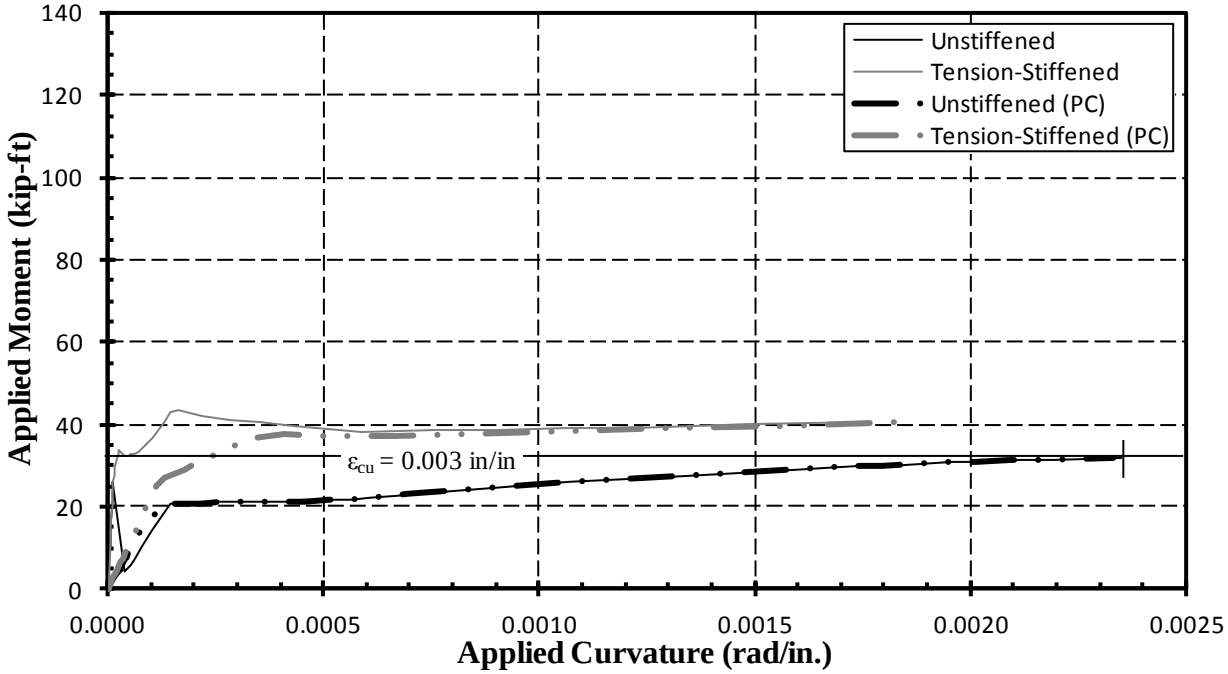

Figure 6.6 Moment-Curvature Relationships—LS2F00

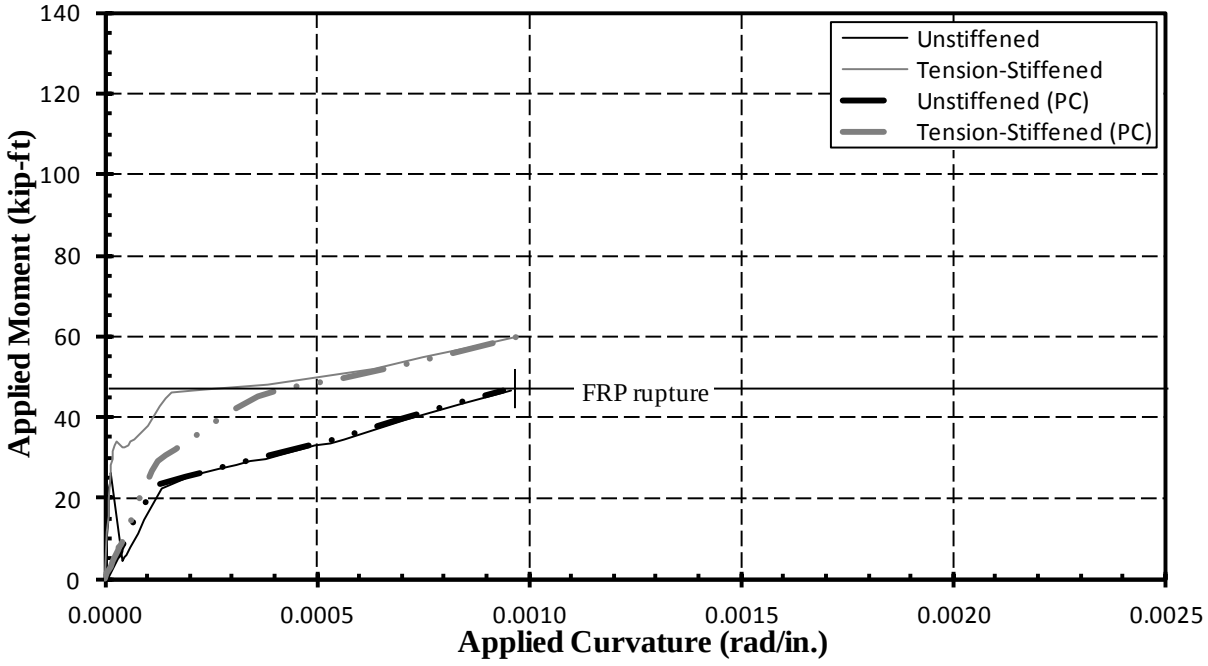

Figure 6.7 Moment-Curvature Relationships—LS2F03

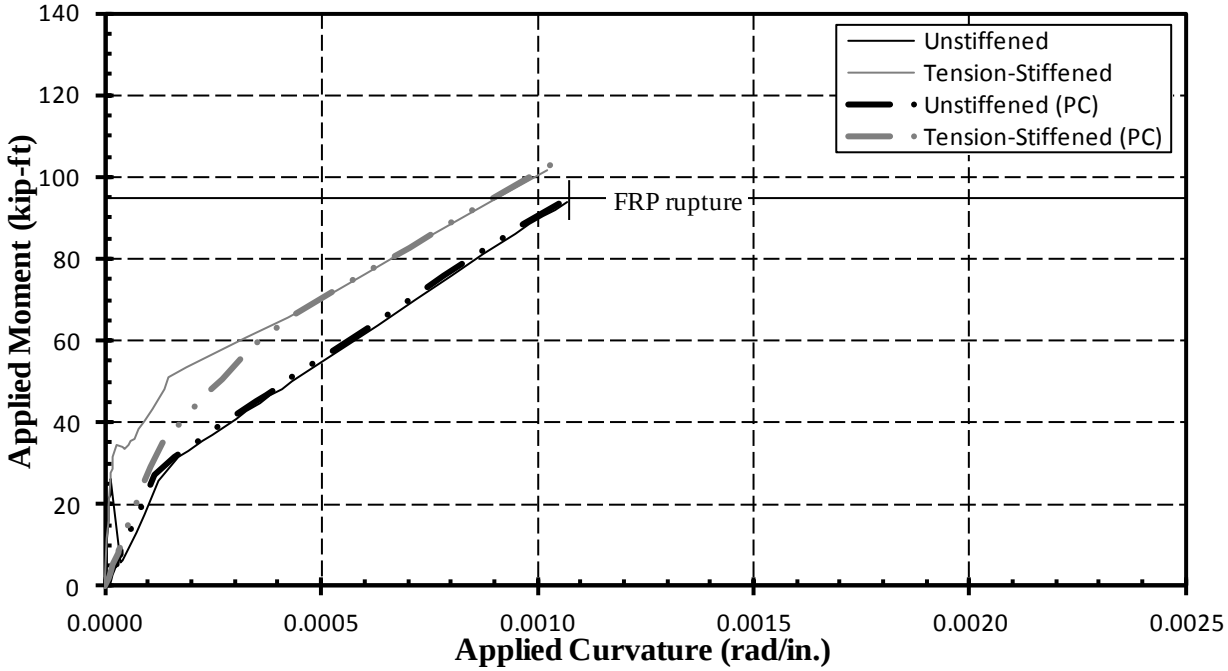

Figure 6.8 Moment-Curvature Relationships—LS2F08

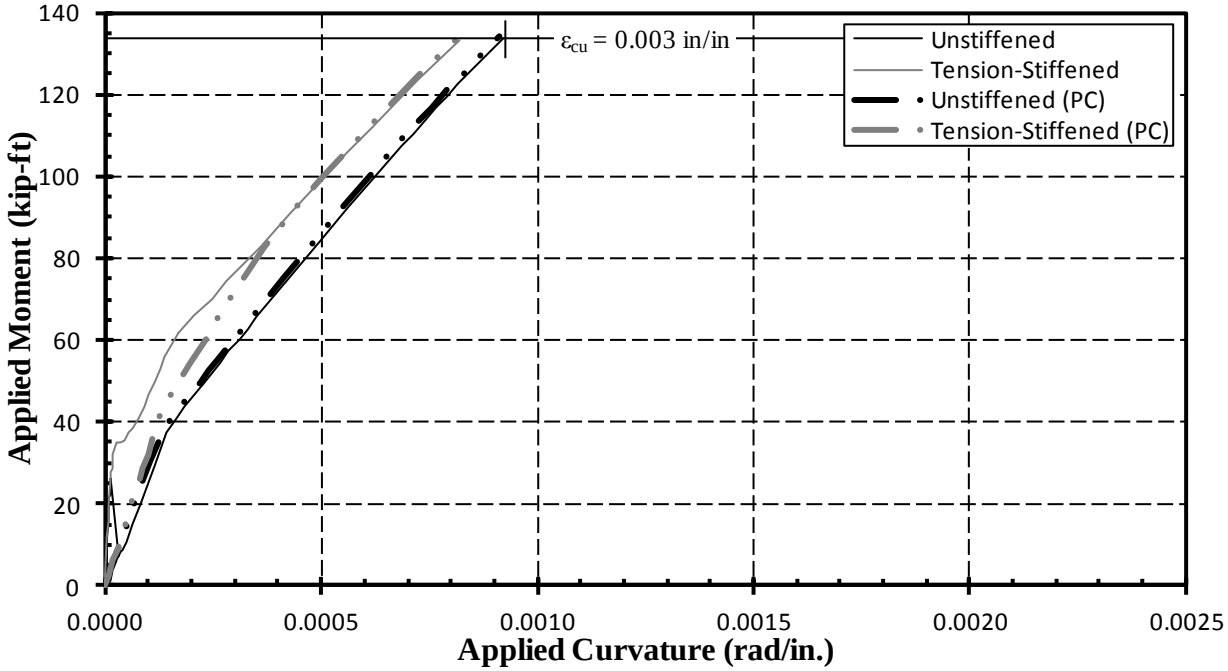

Figure 6.9 Moment-Curvature Relationships—LS2F16

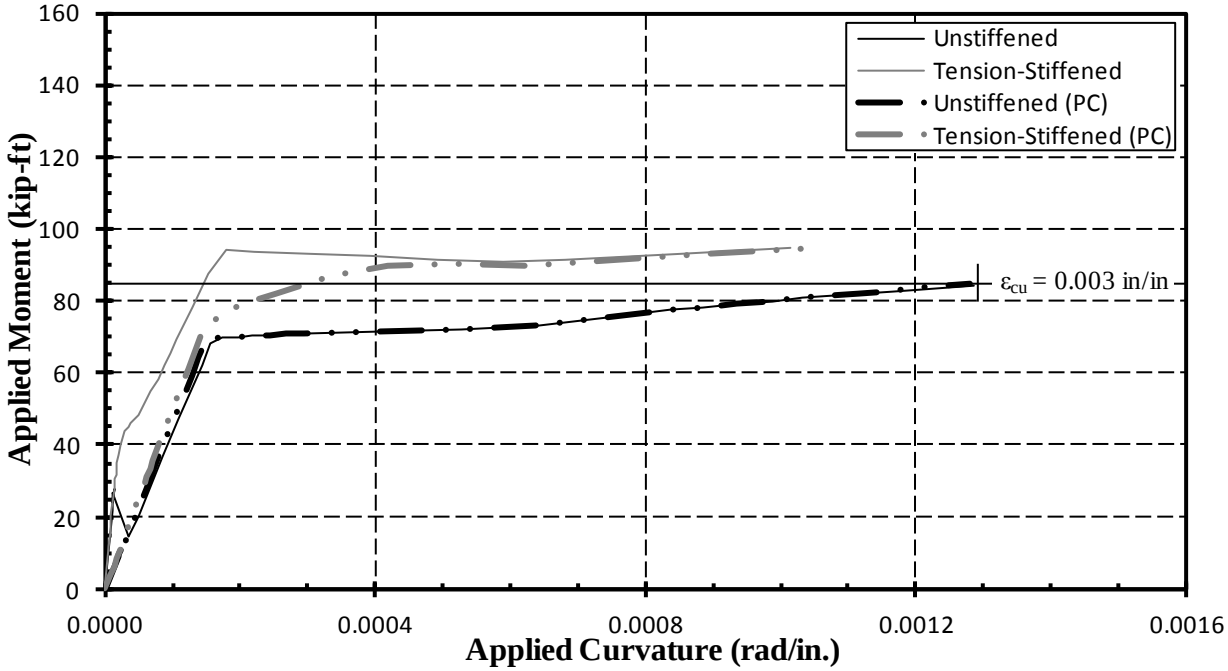

Figure 6.10 Moment-Curvature Relationships—LS6F00

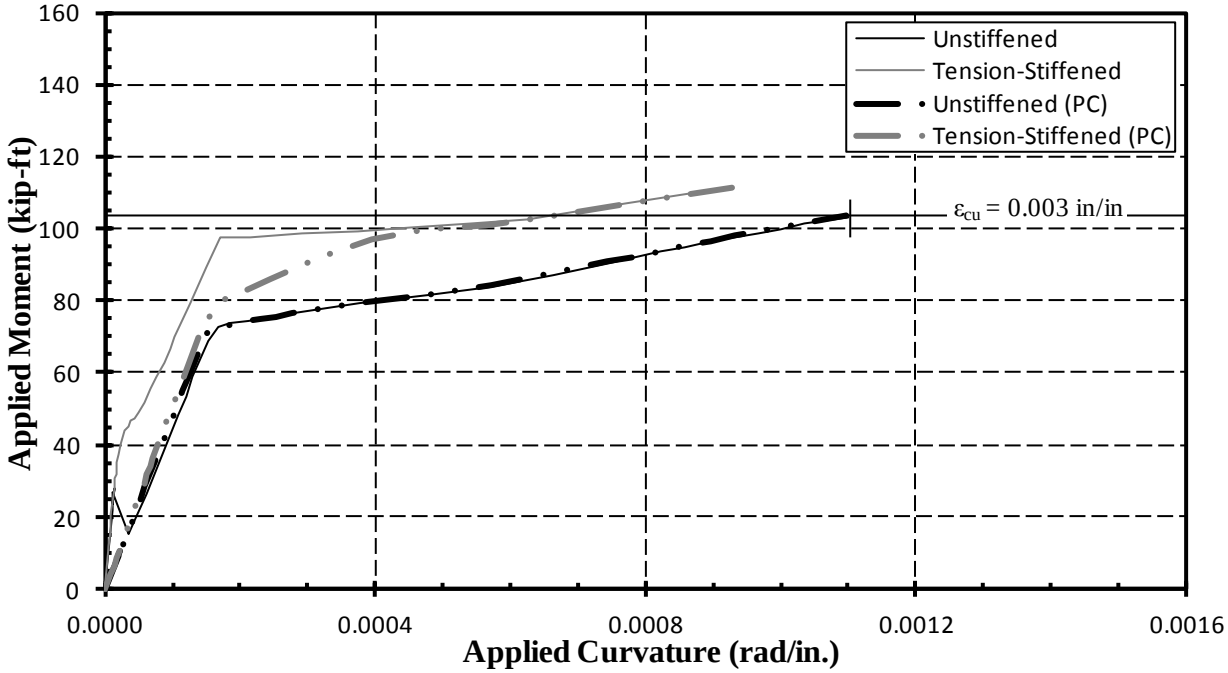

Figure 6.11 Moment-Curvature Relationships—LS6F03

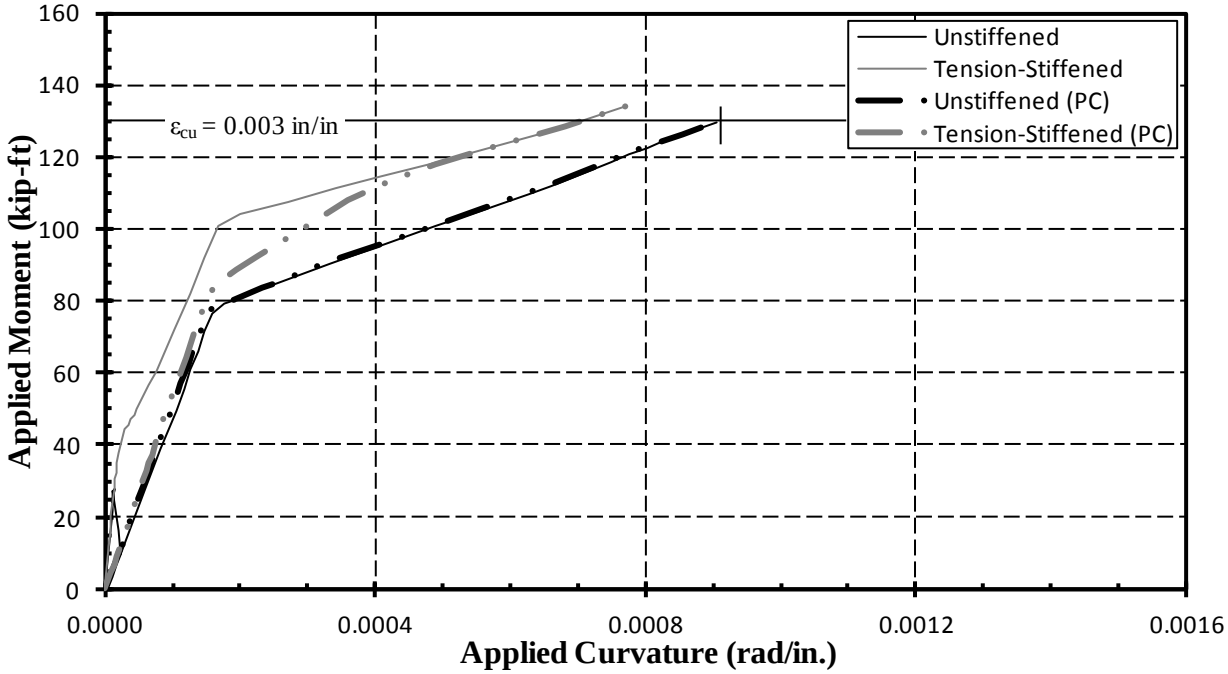

Figure 6.12 Moment-Curvature Relationships—LS6F08

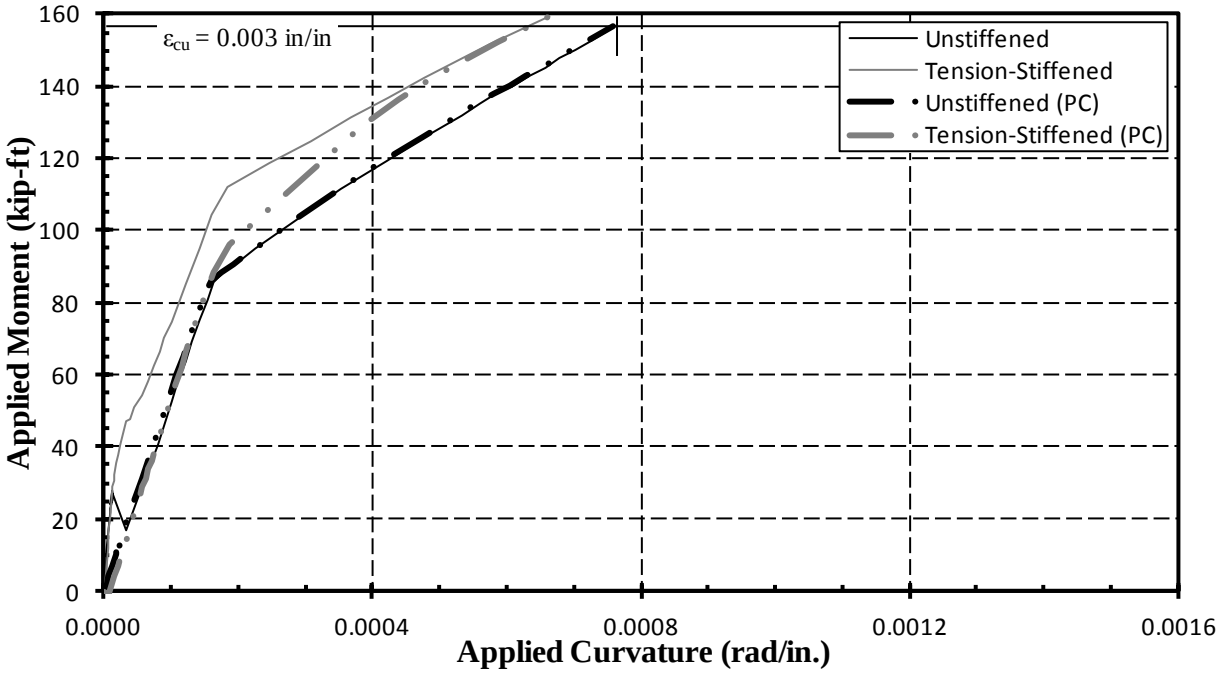

Figure 6.13 Moment-Curvature Relationships—LS6F16

Figure 6.14 and Figure 6.15 consolidate the results for the unstiffened, precracked analyses in order to compare moment capacity and predicted curvature among specimens with equal amounts of tensile steel reinforcement. The model predicts linear-elastic behavior in the service-load range for both sets of specimens. Within each set, the yielding of the steel reinforcement occurs at approximately the same curvature with a consistent predicted increase in the required moment for yielding over the unstrengthened specimen. Likewise, the ultimate predicted moment increases consistently as the amount of FRP increases. The ultimate curvature trend seen in the moderately reinforced specimens does not hold for the under-reinforced series, as the predicted failure mode (FRP rupture) for both LS2F03 and LS2F08 differs from the failure mode (concrete crushing) of the other six specimens.

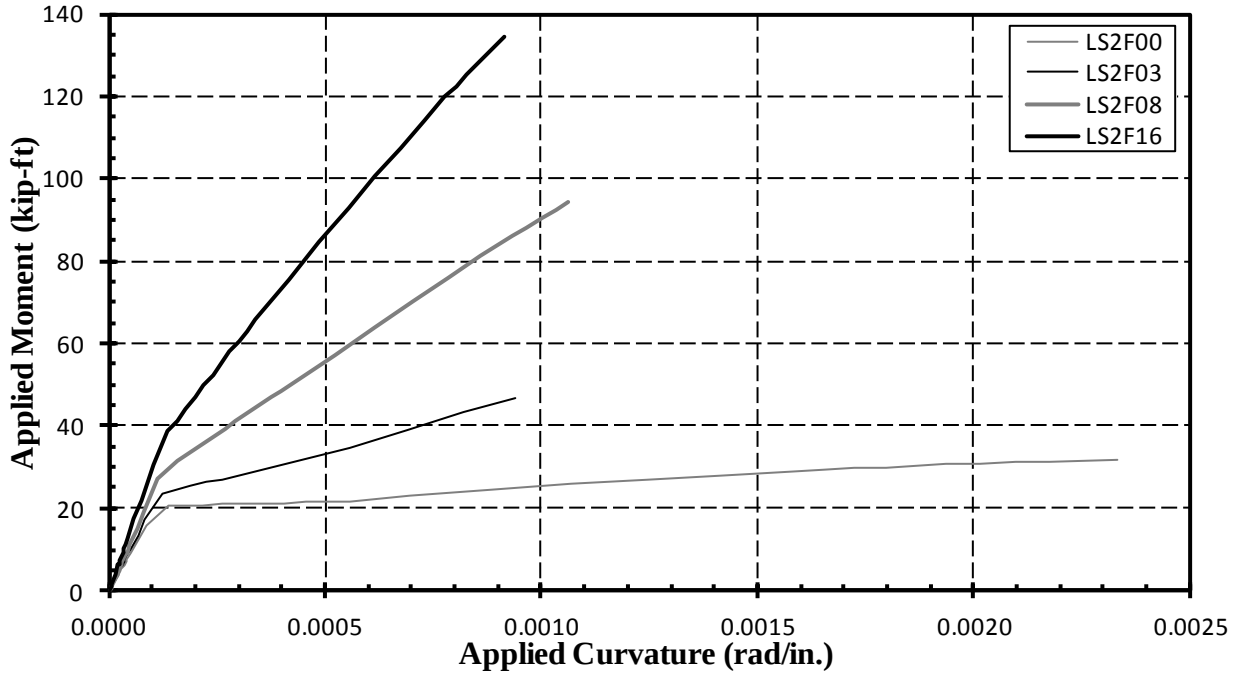

Figure 6.14 Unstiffened, Precracked Moment-Curvature Relationships—ρ_s = 0.2%

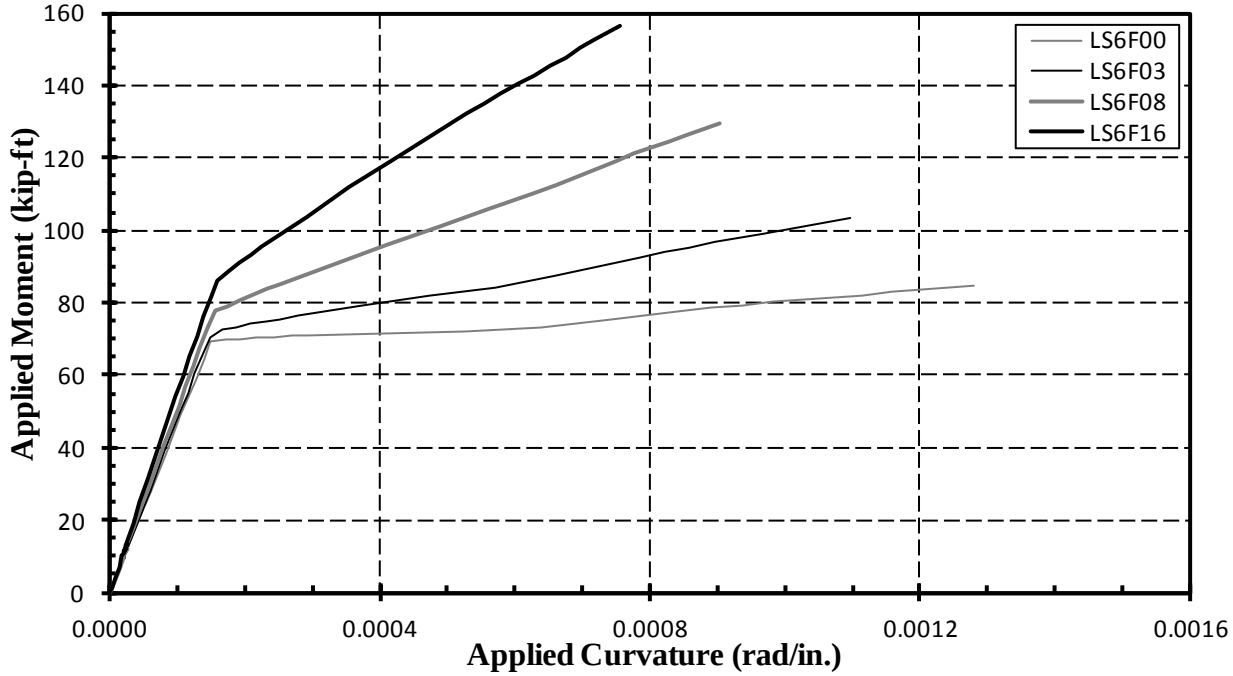

Figure 6.15 Unstiffened, Precracked Moment-Curvature Relationships—ρ_s = 0.6%

6.2 Determination of Nominal Moment Capacity

6.2.1 Accepted Design Limits

In determining nominal moment capacity, the design limits from ACI 440 (2008), Standards Australia (2008), and Seracino et al. (2007)—described by the relationships in Equation 6.6, Equation 6.7, and Equation 6.8, respectively—were applied to the data generated from the discretized sectional analyses previously described, and the resulting predictions were compared to the experimental data to evaluate the accuracy of each model.

$$\varepsilon_{fd} = 0.7\varepsilon_{fu} \qquad \textbf{Equation 6.6}$$

where

ε_{fd} = debonding strain of FRP
ε_{fu} = design rupture strain of FRP

$$P_{IC} = \alpha_p 0.393 \varphi_f^{0.25} f_c^{0.33} \sqrt{L_{per} E_{FRP} A_p} \quad \textbf{Equation 6.7}$$

where

P_{IC} = tensile resistance force to IC debonding
α_p = confidence factor = 1.0 for mean value comparison
φ_f = confinement ratio = $\frac{d_f}{b_f}$
d_f = length of failure plane perpendicular to concrete surface = $d_p + t_d$
d_p = FRP plate dimension perpendicular to concrete surface
b_f = length of failure place parallel to concrete surface = $b_p + t_b$
b_p = FRP plate dimension parallel to concrete surface
$t_d = t_b$ = distance to failure plane from face of FRP = 0.04 in.
f_c = concrete compressive strength
L_{per} = length of debonding failure plane = $2d_f + b_f$
A_p = cross-sectional area of FRP plate = $d_p b_p$

$$P_{IC} = 3\alpha\beta\sqrt{f_c}\, d_p^{1.36} b_p^{0.21} \quad \textbf{Equation 6.8}$$

where

α = confidence factor = 0.19 for mean value comparison
β = bond-length factor = 1.0 for $L \geq 7.9$ in.
L = bonded length of FRP

In each case, the resulting ε_{fd} or P_{IC} was compared with the strain or axial force values, respectively, generated in the FRP layer during the full-spectrum analysis of each specimen and the bending moment in the cross section at the prescribed magnitude was taken as the nominal moment capacity based on the corresponding design limit. Linear interpolation was used to determine the appropriate moment capacity in the event that a limiting value fell between two analyzed cross sections. The application of the design limits to the results of the nonlinear analyses in this manner accounts for the strain hardening that occurs within the steel reinforcement and the higher performance threshold of an assumed FRP failure at the average rupture stress rather than the design rupture stress.

6.2.2 Non-Anchorage Failure

The predicted moment capacities were also established based on the earliest predicted occurrence of two non-anchorage failure conditions: either the extreme compressive fiber reaching a strain of 0.003 in/in or the FRP reinforcement reaching a stress of 345 ksi, thus theoretically rupturing. The theoretical nominal moment capacity for each specimen was established using the same data assessment described for the determination of the design limit capacities.

CHAPTER 7: RESULTS AND DISCUSSION

7.1 Service Load Behavior

Upon repair but prior to final testing, each specimen was subjected to 50,000 cycles under expected service load levels. Figure 7.1 depicts the typical load-deflection behavior for each set of recorded cycles for LS6F08. Appendix B contains cyclic load-deflection curves for all specimens.

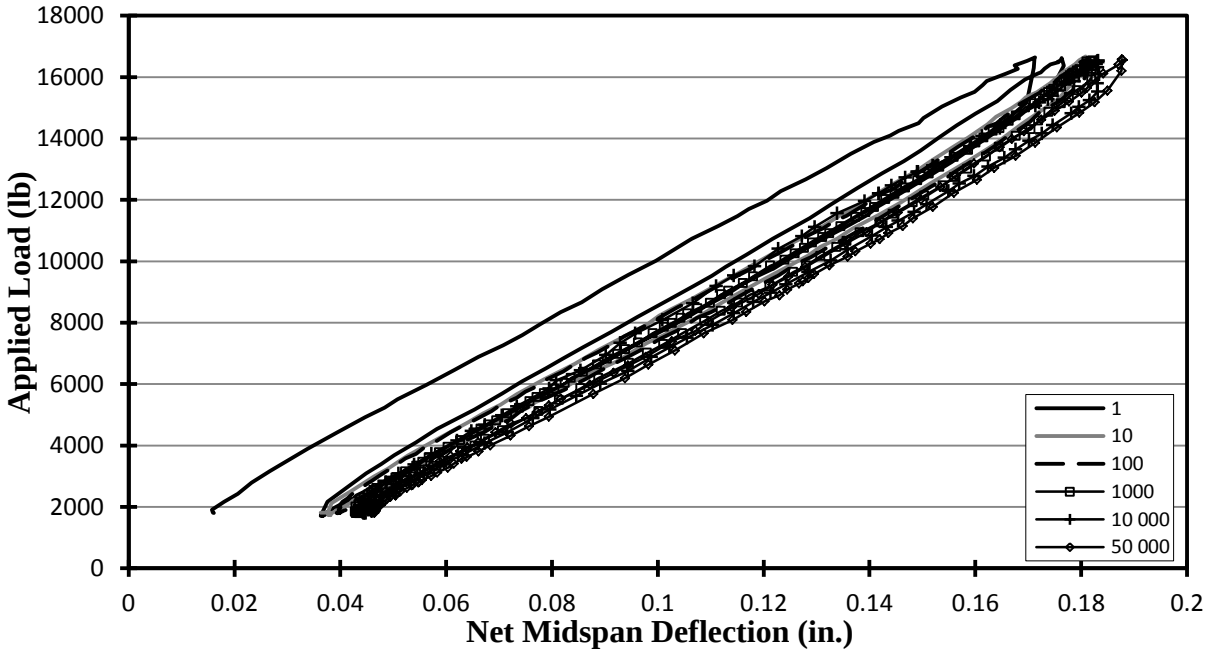

Figure 7.1 Cyclic Load versus Deflection—LS6F08

As observed, the recorded deflection of the specimens covers a similar range during each cycle following the application of the initial loading cycle after repair. Likewise, little variation exists between the magnitude of deflection reached during each cycle—behavior consistent with

almost no degradation in the bond or performance of the FRP under the consistent application of service loads. The following equations were employed to ascertain a theoretical range of strain for both the steel and FRP that could be compared with data gleaned from the cycling process:

$$\Delta\varepsilon_s = \frac{\Delta M(d - c_{cr})}{E_c I_{cr,FRP}} \quad \textbf{Equation 7.1}$$

$$\Delta\varepsilon_f = \frac{\Delta M(d_f - c_{cr})}{E_c I_{cr,FRP}} \quad \textbf{Equation 7.2}$$

where

$\Delta\varepsilon_s$ = expected change in strain in tensile steel during service load cycle
$\Delta\varepsilon_f$ = expected change in strain in FRP during service load cycle
ΔM = change in bending moment experienced during service load cycle
d = effective depth of steel reinforcement = 15-5/8 in.
d_f = effective depth of FRP reinforcement = 17-9/16 in.
c_{cr} = neutral axis depth computed using linear-elastic, cracked-section analysis
E_c = modulus of elasticity of concrete = 3500 ksi
$I_{cr,f}$ = cracked-section moment of inertia

Table 7.1 summarizes the results of applying Equation 7.1 and Equation 7.2 to the service-load ranges from the repaired specimens. For comparison, the experimental strains taken from gages at cracked cross sections located within the maximum-moment region of each specimen are listed in Table 7.2.

Table 7.1 Calculation of Theoretical Strain Change over a Cycle

	c_{cr} (in.)	$I_{cr,FRP}$ (in.^{4})	P_{app} (kips) min	P_{app} (kips) max	M_{app} (kip-ft) min	M_{app} (kip-ft) max	ΔM (kip-in.)	$\Delta\varepsilon_s$ (με)	$\Delta\varepsilon_f$ (με)
LS2F00	2.67	638	0.42	3.78	1.05	9.45	100.8	580	-
LS2F03	2.78	704	0.48	4.39	1.20	10.98	117.4	610	700
LS2F08	3.00	834	0.63	5.72	1.58	14.30	152.6	660	760
LS2F16	3.30	1020	0.85	7.69	2.13	19.23	205.2	710	820
LS6F00	4.29	1613	1.62	14.73	4.05	36.83	393.4	790	-
LS6F03	4.35	1666	1.68	15.27	4.20	38.18	407.8	790	920
LS6F08	4.47	1770	1.82	16.53	4.55	41.33	441.4	790	930
LS6F16	4.65	1922	2.00	18.40	5.00	46.00	492.0	800	940

Table 7.2 Measured Change in Strain over a Cycle

Measured Change in Reinforcement Strain (in/in x 10^{-6})							
	Cycle	**1**	**10**	**100**	**1000**	**10000**	**50000**
LS2F00	**Steel**	700	640	650	630	650	650
LS2F03	**Steel**	470	480	470	460	510	460
	FRP	1720	1710	1670	1650	1630	1620
LS2F08	**Steel**	380	360	390	380	400	420
	FRP	1660	1590	1540	1490	1460	1450
LS2F16	**Steel**	370	320	330	390	390	420
	FRP	1160	1130	1120	1120	1110	1120
LS6F00	**Steel**	870	840	840	820	820	840
LS6F03	**Steel**	960	950	920	930	940	910
	FRP	2150	2060	1960	1960	1890	1870
LS6F08	**Steel**	840	780	810	830	800	800
	FRP	1510	1440	1390	1340	1310	1330
LS6F16	**Steel**	550	530	540	550	550	550
	FRP	1240	1160	1090	1090	1090	1080

The FRP reinforcement experienced consistently higher strains than predicted due to the smaller cracked neutral axis resulting from the overestimated load necessary to produce the targeted maximum moment during the cracking process, as mentioned in Section 3.4.

Regarding the steel reinforcement, the smaller-than-predicted strains can be attributed to the cracks not directly crossing the gages. As previously discussed in Section 5.2, gages were installed on the steel reinforcement prior to casting and cracking; by contrast, gages were attached to the FRP reinforcement at locations usually coinciding with an existing crack. The higher-than-predicted steel strains can be explained as a result of the combination of a smaller neutral axis and the proximity of the gages to the cracks, resulting in a smaller difference than seen in the FRP strain values. The decrease over time in the FRP strains might be a result of slight softening of the epoxy or the bond between the concrete and FRP-epoxy composite; the strain plateau that occurs in the later cycles seems to support this assumption. The relative consistency of both the strain readings across the cycles and the crack widths measured at the peak service load—as seen in Table 7.3—confirm that very little bond degradation occurred.

Table 7.3 Measured Crack Width at Peak Service Load

	Maximum Crack Width for Each Cycle (mm)						
Cycle	**1**	**10**	**100**	**1000**	**10000**	**50000**	**Monotonic**
LS2F00	0.90	0.90	0.90	0.90	0.90	0.95	1.00
LS2F03	0.65	0.65	0.65	0.65	0.65	0.65	0.50
LS2F08	0.70	0.70	0.70	0.70	0.80	0.80	0.70
LS2F16	0.50	0.60	0.60	0.65	0.70	0.70	0.70
LS6F00	0.25	0.25	0.25	0.30	0.30	0.30	0.35
LS6F03	0.25	0.25	0.25	0.25	0.25	0.30	0.30
LS6F08	0.40	0.40	0.40	0.40	0.40	0.40	0.40
LS6F16	0.35	0.30	0.30	0.30	0.30	0.30	0.30

7.2 Strength Testing

7.2.1 Specimen Behavior

7.2.1.1 Load-Deflection Response

LS2F00—the control specimen for the under-reinforced series—performed as expected of a typical reinforced concrete beam. Figure 7.2 shows both the predicted and observed load-deflection behavior of the specimen. The linear-elastic range of the experimental behavior falls near the midpoint of the both predicted curves (one assuming that the section was uncracked prior to loading and the other one utilizing the precracked tension behavior estimated as described in Section 6.1.1.1). These theoretical results include the stiffness contribution of the steel and (for the strengthened specimens) FRP in order to display the integrated behavior of the cracked and uncracked sections in the tension region along the specimen; however the predicted ultimate loads are controlled by the failure point of the unstiffened models, as the capacity of a specimen cannot exceed the largest moment attainable by a single cracked cross section. The post-yield response indicates a much higher deformation capacity prior to concrete crushing than

is incorporated in the theoretical concrete compressive stress-strain relationship. This beam—like the deficient regions of the Letohatchee bridge—is grossly under-reinforced. This may explain why the precracked tension stiffening relationship does not closely match the cracked-section behavior of this beam.

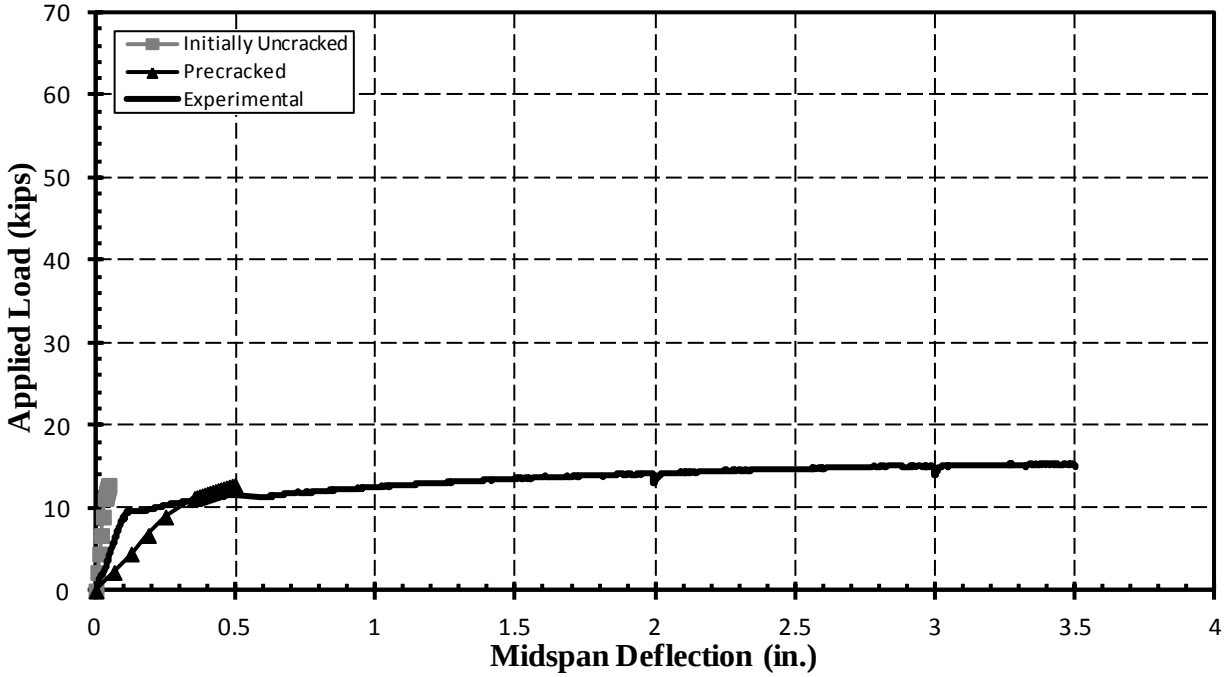

Figure 7.2 Load versus Deflection—LS2F00

LS6F00—the control specimen for the more moderately reinforced series—also performed as expected of a typical reinforced concrete beam. Unlike its under-reinforced counterpart, the measured load-displacement response, as observed in Figure 7.3, nearly matches the result predicted using a precracked model of the specimen cross section. This beam also showed significantly more post-yield deformation capacity than is predicted using the theoretical concrete compressive stress-strain response.

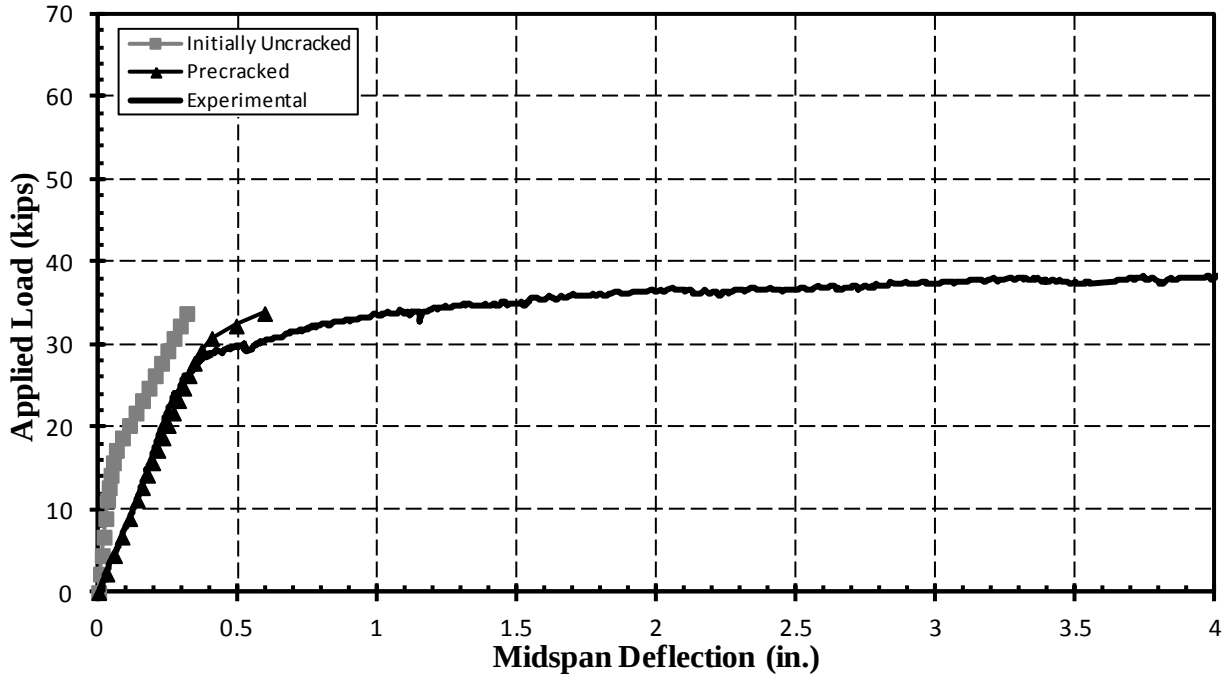

Figure 7.3 Load versus Deflection—LS6F00

The three repaired specimens with ρ_s = 0.2%—LS2F03, LS2F08, and LS2F16—presented similar load-deflection behavior, as seen in Figure 7.4 to Figure 7.6. For each specimen, the linear-elastic portion of the experimental curve falls between the two predicted curves, as seen in LS2F00. After yield, the theoretical models predict stiffer specimen behavior and ultimate capacities at or above the experimental result. The higher stiffness could result from a lower stiffness in the FRP-epoxy composite in the actual beam compared to the stiffness value generated from the laboratory testing of the NSM strips.

For correlation to the Letohatchee bridge girders, LS2F03 represents the cross section that most closely matches the bridge girder with the current repair recommendations. This specimen experienced a 50% increase in the experimental load capacity relative to the unstrengthened section as well as a 20% increase in the yield moment.

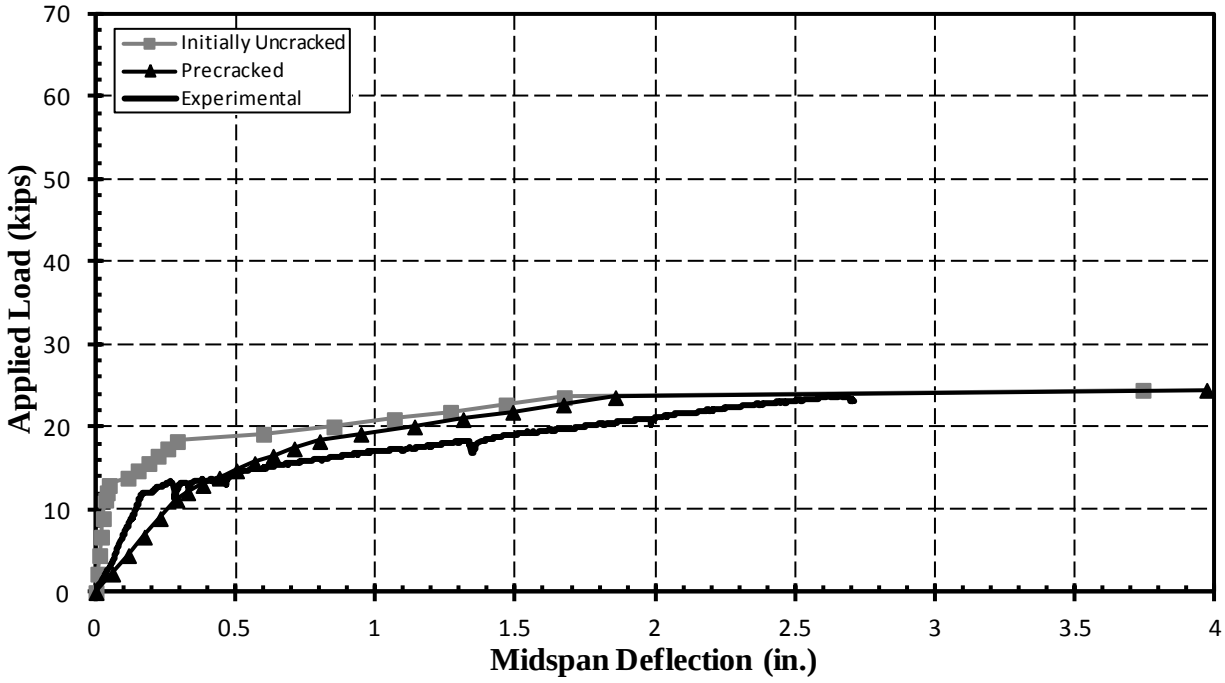

Figure 7.4 Load versus Deflection—LS2F03

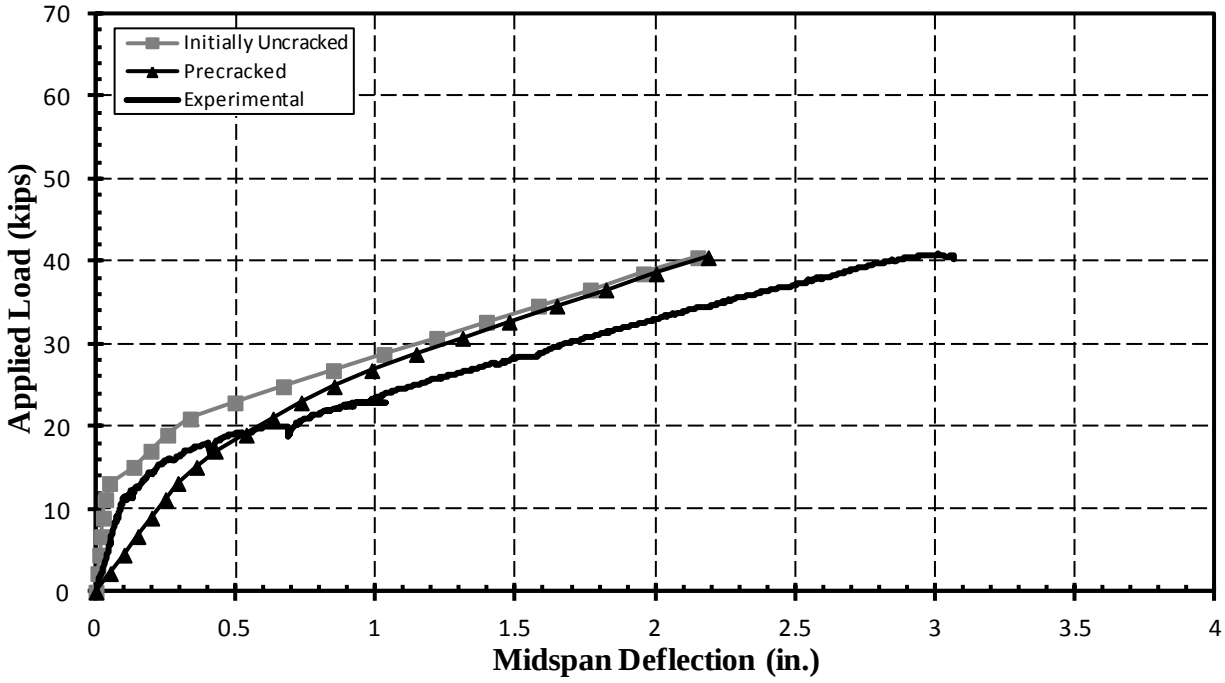

Figure 7.5 Load versus Deflection—LS2F08

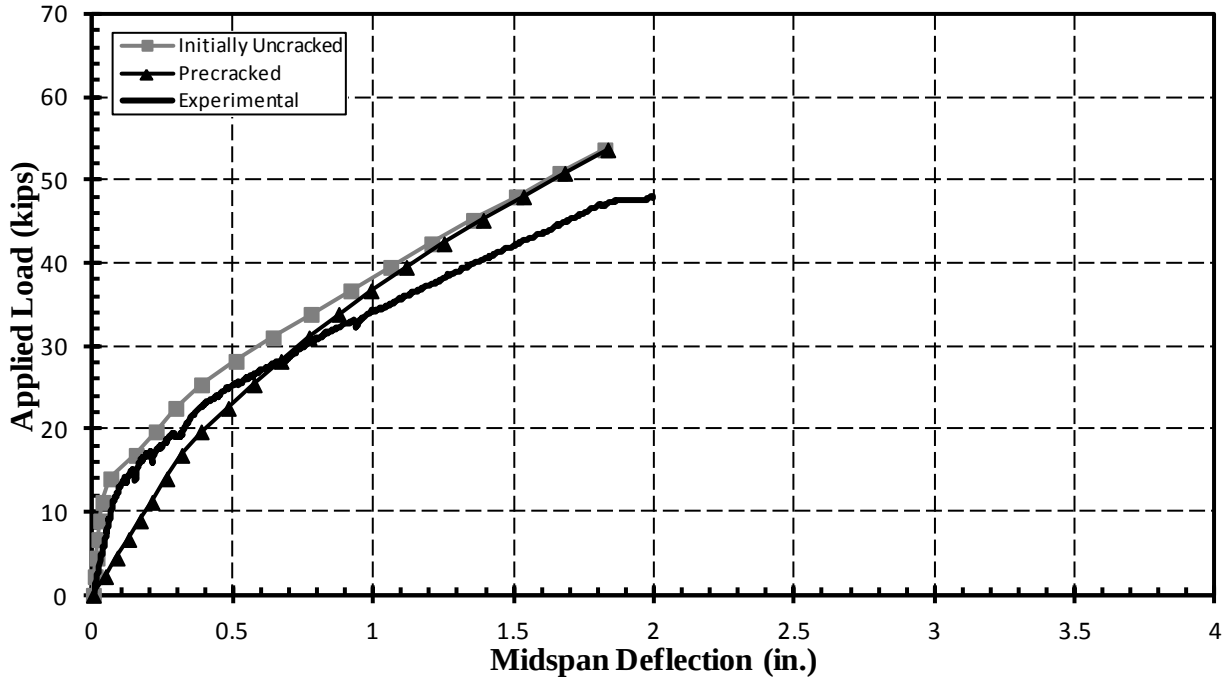

Figure 7.6 Load versus Deflection—LS2F16

The three specimens with the higher level of reinforcing steel (ρ_s = 0.6%)—LS6F03, LS6F08, and LS6F16—behaved in the same manner during loading, as shown in Figure 7.7 to Figure 7.9. The experimental load-deflection behavior for each specimen closely matches the precracked model prediction through yield, at which point the theoretical model predicts stiffer behavior terminating at a lesser ultimate capacity than observed.

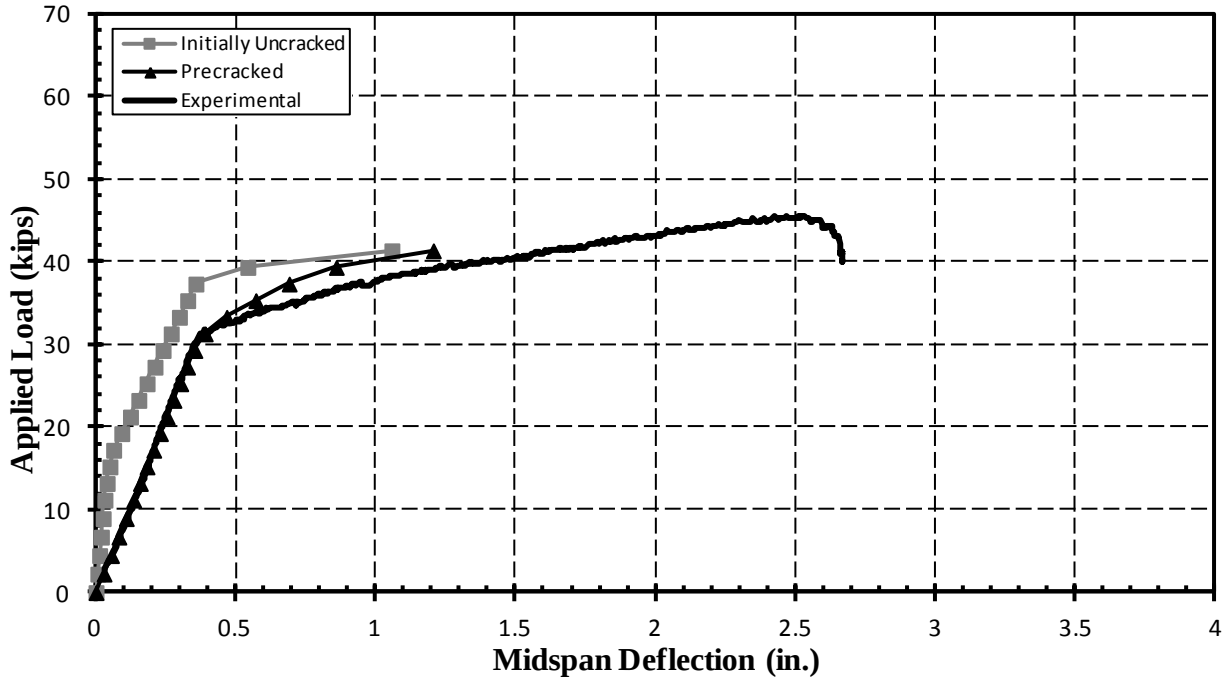

Figure 7.7 Load versus Deflection—LS6F03

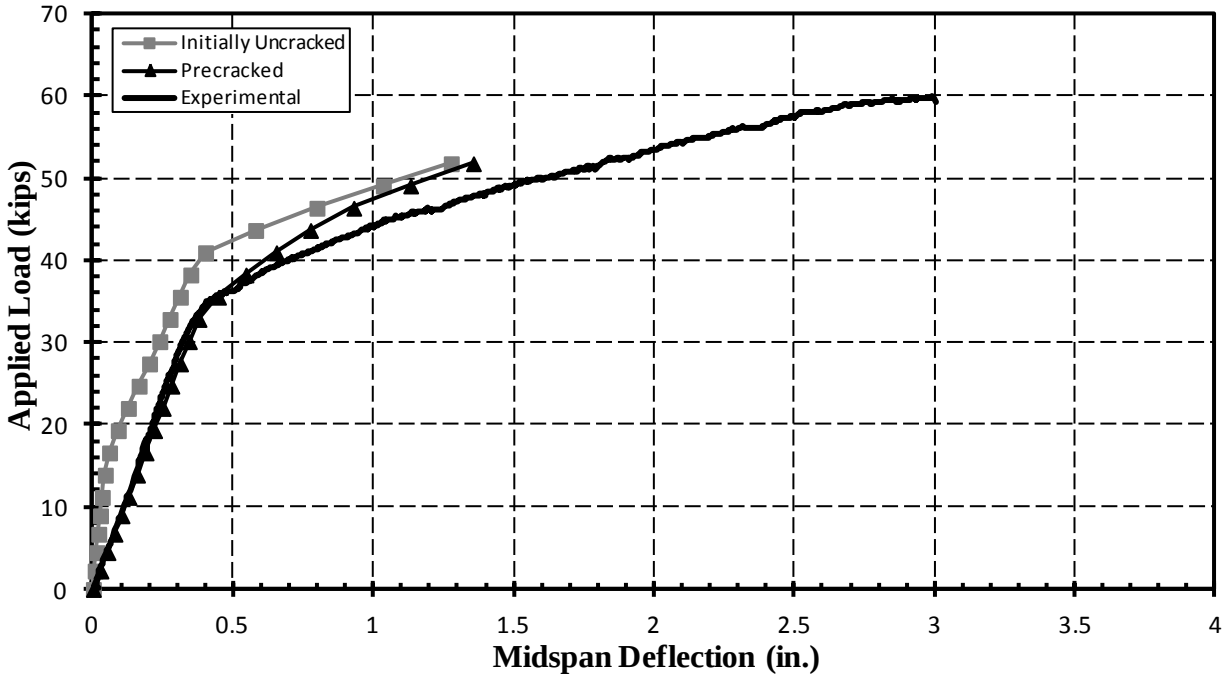

Figure 7.8 Load versus Deflection—LS6F08

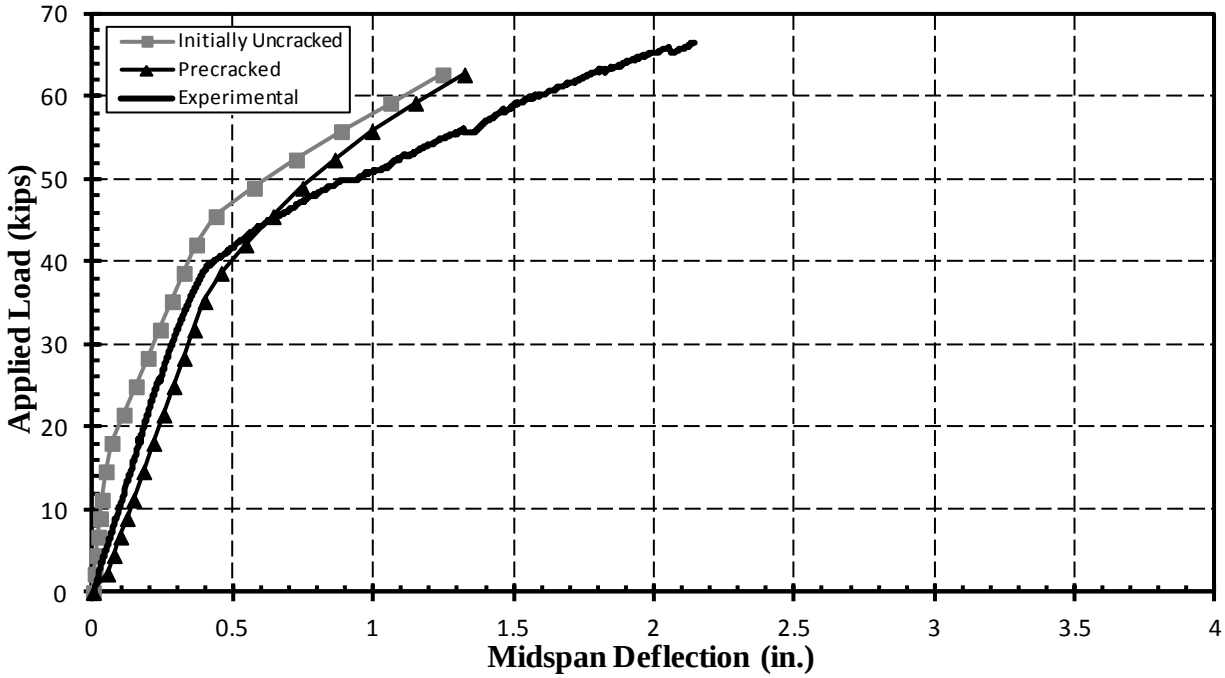

Figure 7.9 Load versus Deflection—LS6F16

For all specimens, the precracked model produced a conservative estimate for behavior prior to yield, after which the results from the layer-by-layer analysis predicted a higher stiffness than was achieved during testing.

7.2.1.2 Failure

Figure 7.10 depicts the condition of the LS2F00 after failure. Within the cracking diagram, the lighter line weight represents the extent of cracking prior to the application of the NSM FRP, while the heavier line weight indicates the formation and propagation of cracks during monotonic loading up to failure. As expected of an excessively under-reinforced section, cracking was limited to four locations with a maximum measured crack width of approximately 14 mm. Failure occurred due to crushing of the concrete at the extreme compression fiber of the specimen within the maximum moment region of the beam—the central 36 in. surrounding midspan—with the detailed region marked by a rectangle within the cracking diagram.

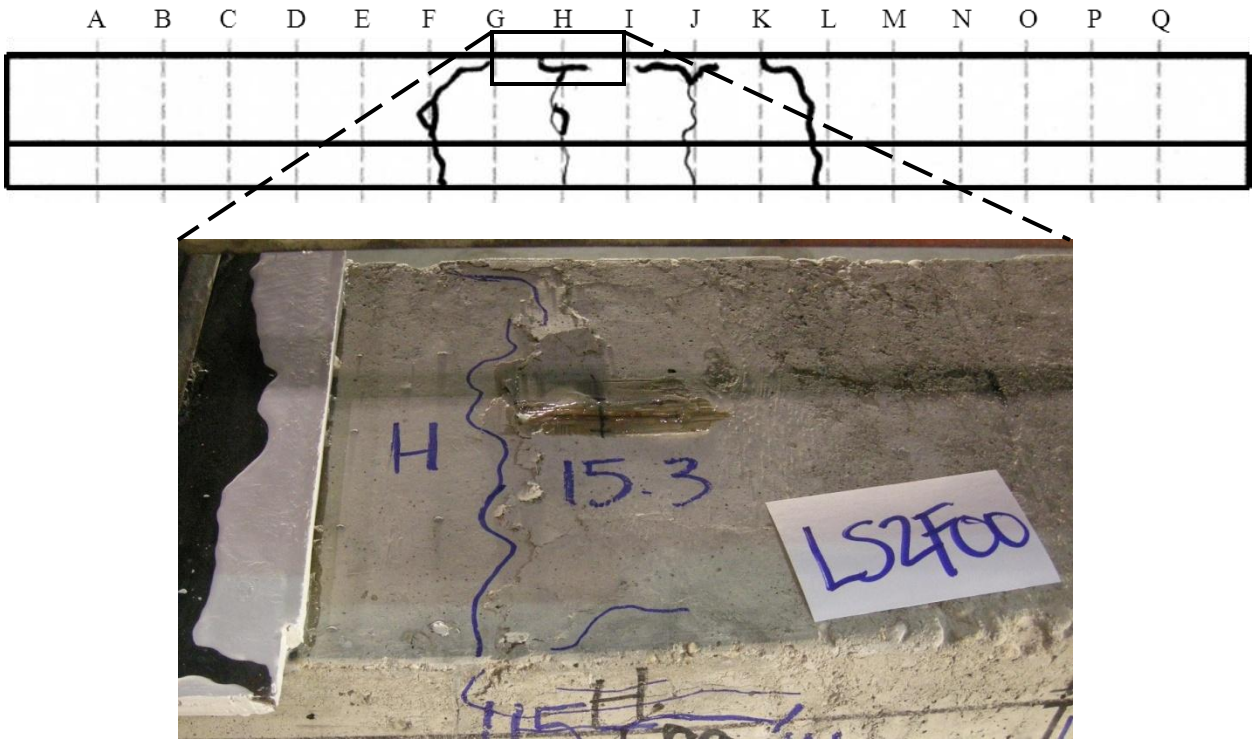

Figure 7.10 Crack Pattern and Detail at Failure—LS2F00

LS6F00—a more moderately reinforced specimen—failed as a result of the simultaneous crushing of the concrete at two cross sections within the maximum moment region of the beam, as seen in Figure 7.11. The numerous cracks that occurred during the cracking process propagated further toward the extreme compression fiber, with the larger crack widths occurring near midspan limited to approximately 10 mm due to the presence of more steel reinforcement than the other control specimen.

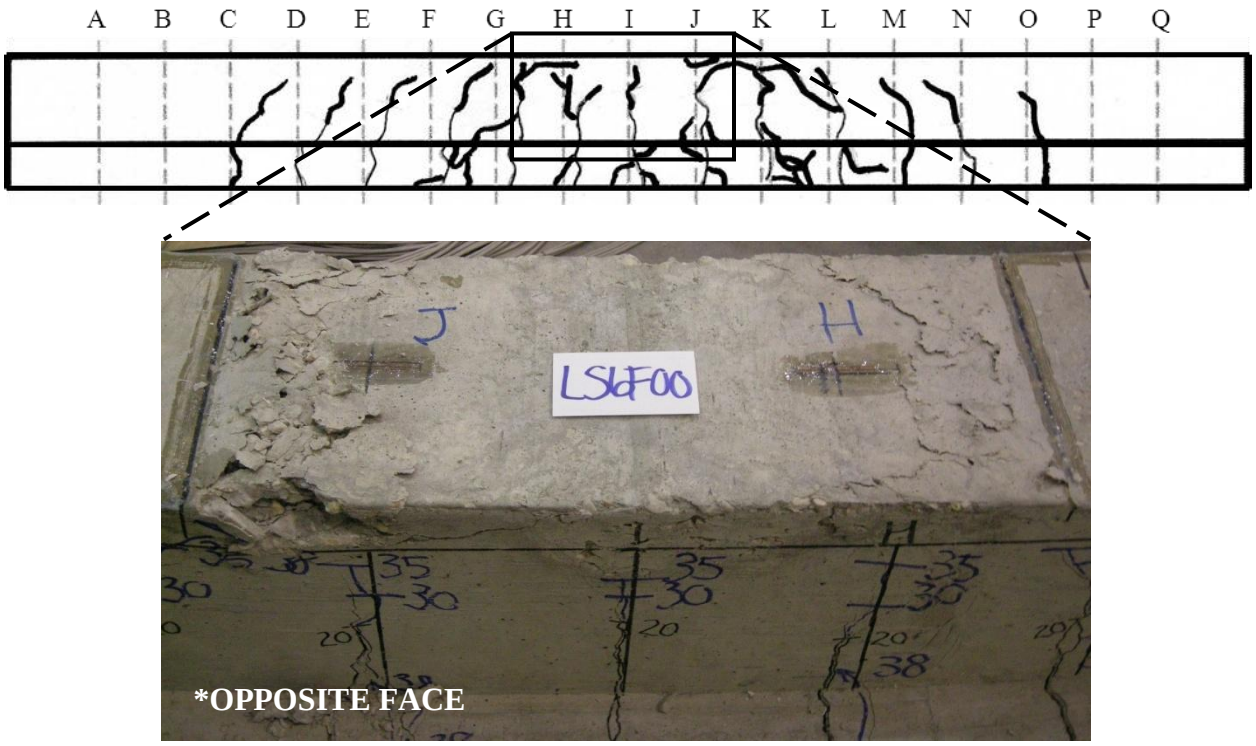

Figure 7.11 Crack Pattern and Detail at Failure—LS6F00

Figure 7.12 depicts the state of LS2F03 at failure—resulting from crushing of the concrete in flexure—with the formation of multiple new post-repair cracks outside the maximum moment region of the beam. As in LS2F00, the existing cracks tend to grow wider to account for the increasing curvature experienced by the specimen. Figure 7.13 shows the spalling of the combined concrete-epoxy cover around the FRP strip at the failure plane under the large strains experienced prior to failure.

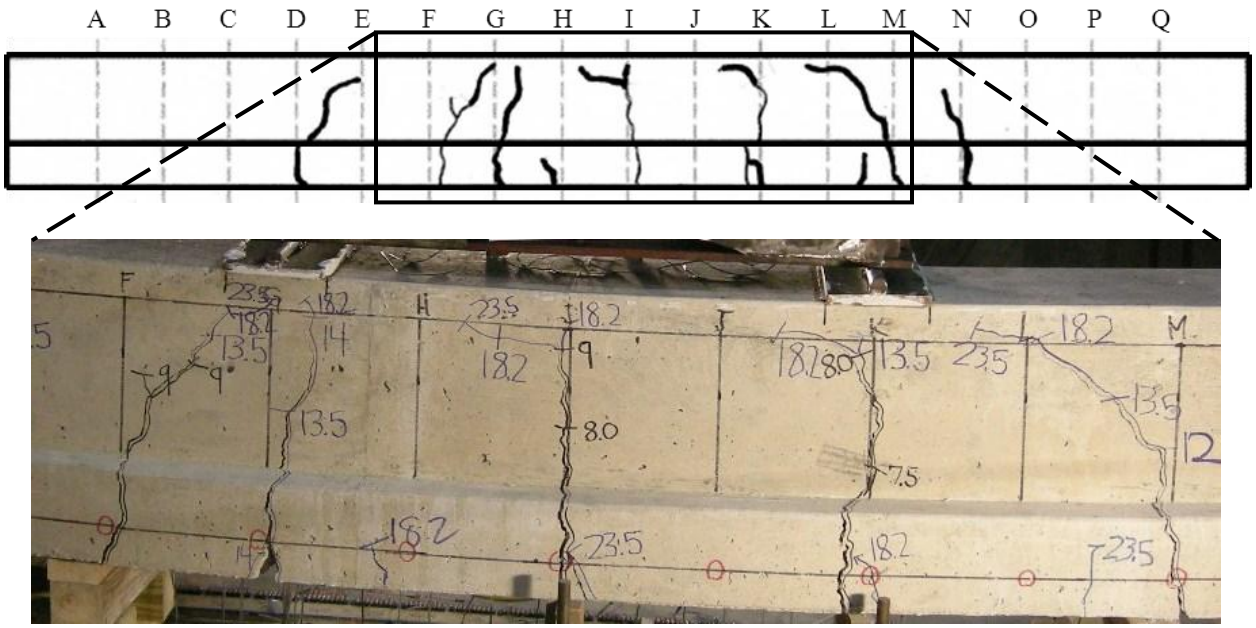

Figure 7.12 Crack Pattern and Detail at Failure—LS2F03

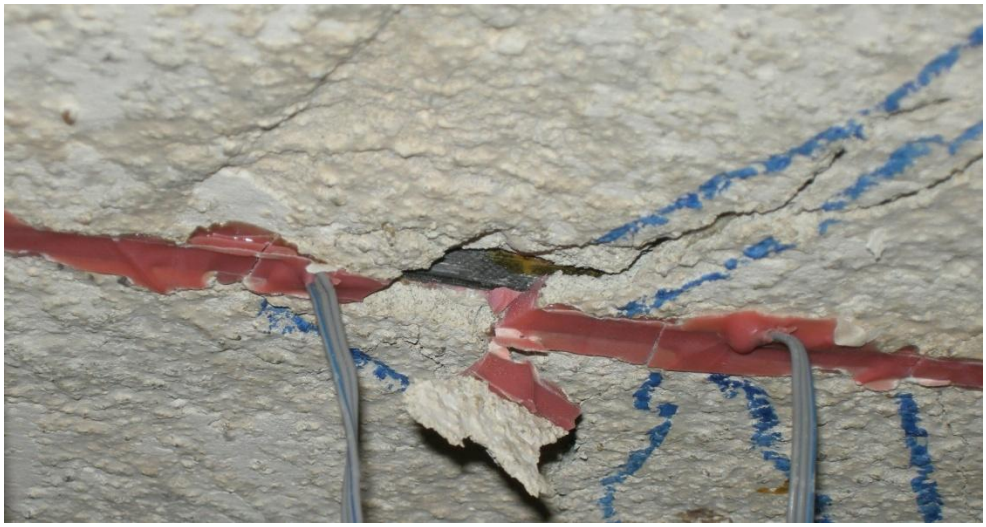

Figure 7.13 Loss of Cover at Failure—LS2F03

The condition of LS2F08 is shown in Figure 7.14, where the observed failure mode seemed to derive from a combination flexural and shear failure. The increase in the amount of FRP in the specimen resulted in an increased number of cracks, while the average crack width began to diminish.

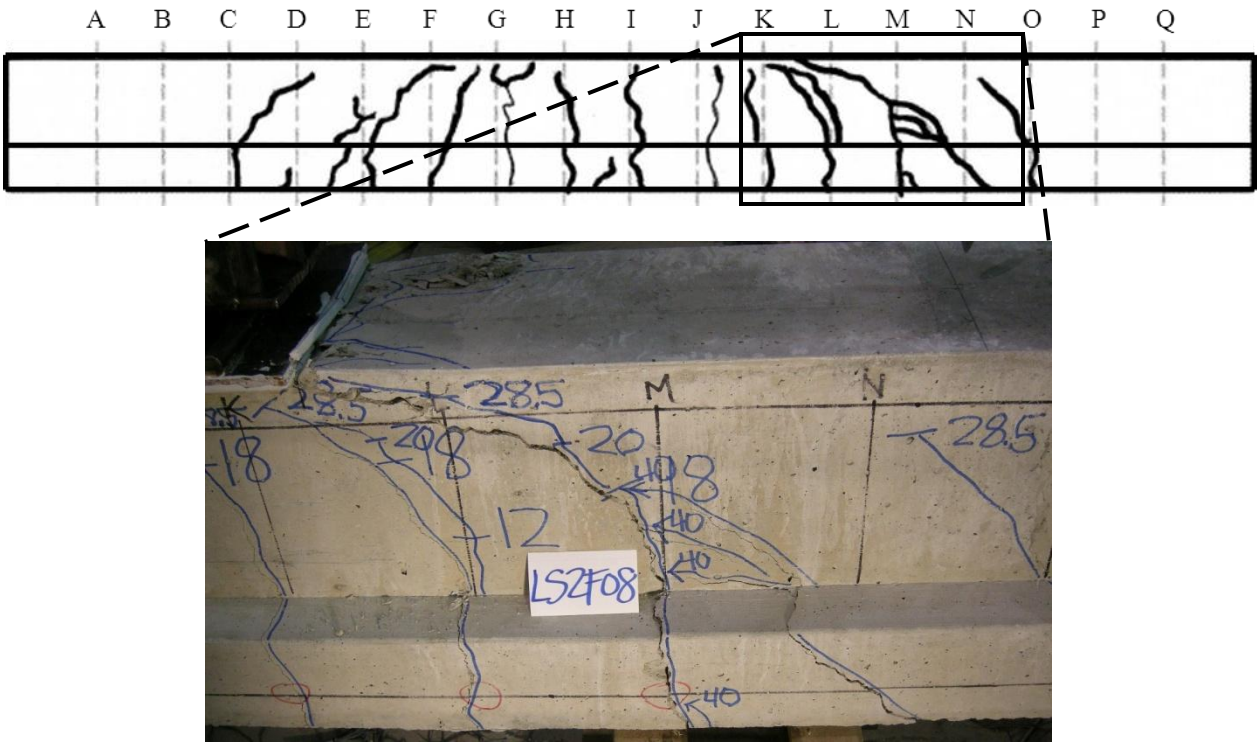

Figure 7.14 Crack Pattern and Detail at Failure—LS2F08

Figure 7.15 shows the failure plane occurring near the FRP. The three strips within the specimen seem to function as a single unit of longitudinal reinforcement due to the relatively tight spacing of the FRP, with the larger failure cracks running parallel to the reinforcement rather than crossing the strips.

Figure 7.15 Failure Planes on Tension Face—LS2F08

Failure of LS2F16 occurred as a result of concrete crushing near the load point of the specimen, as seen in Figure 7.16. Multiple new cracks formed throughout the length of the beam, while crack widths remained relatively small due to the increase in FRP quantity.

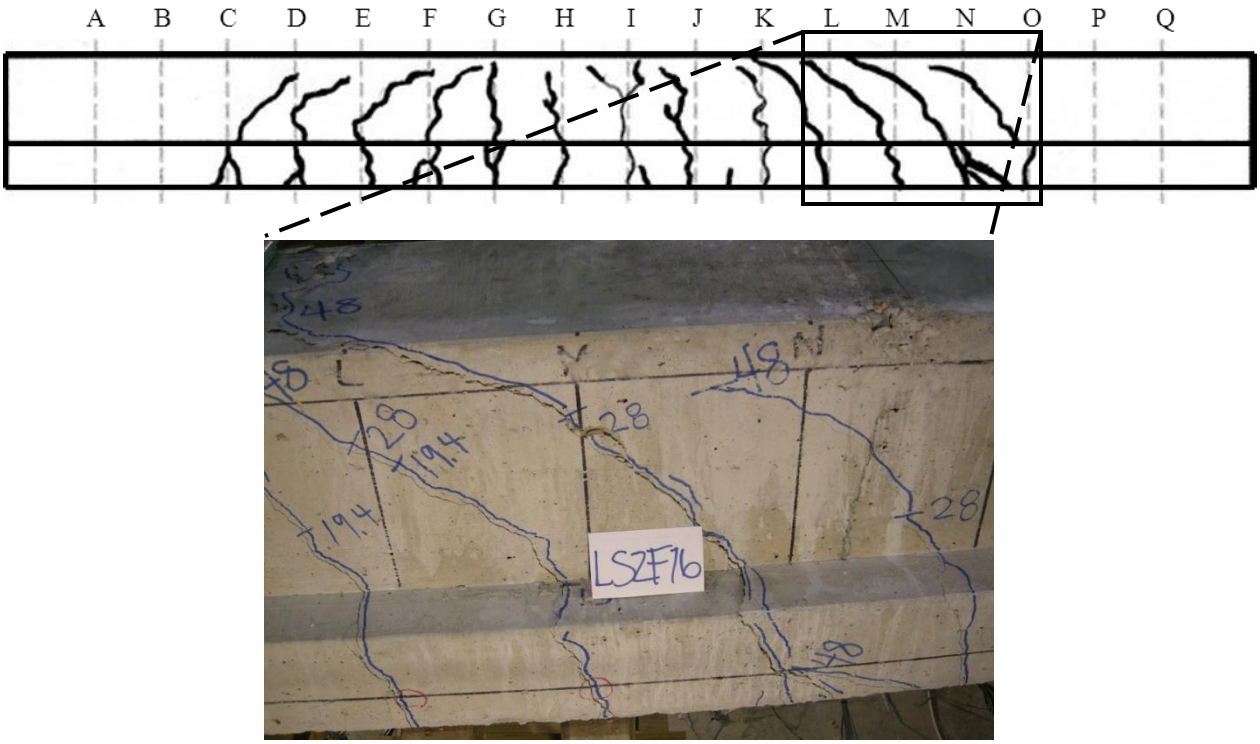

Figure 7.16 Crack Pattern and Detail at Failure—LS2F16

LS6F03, as shown in Figure 7.17, failed due to crushing of the concrete within the maximum moment region of the specimen. Prior to failure, new cracks were observed forming in the flange and propagating until joining with existing cracks.

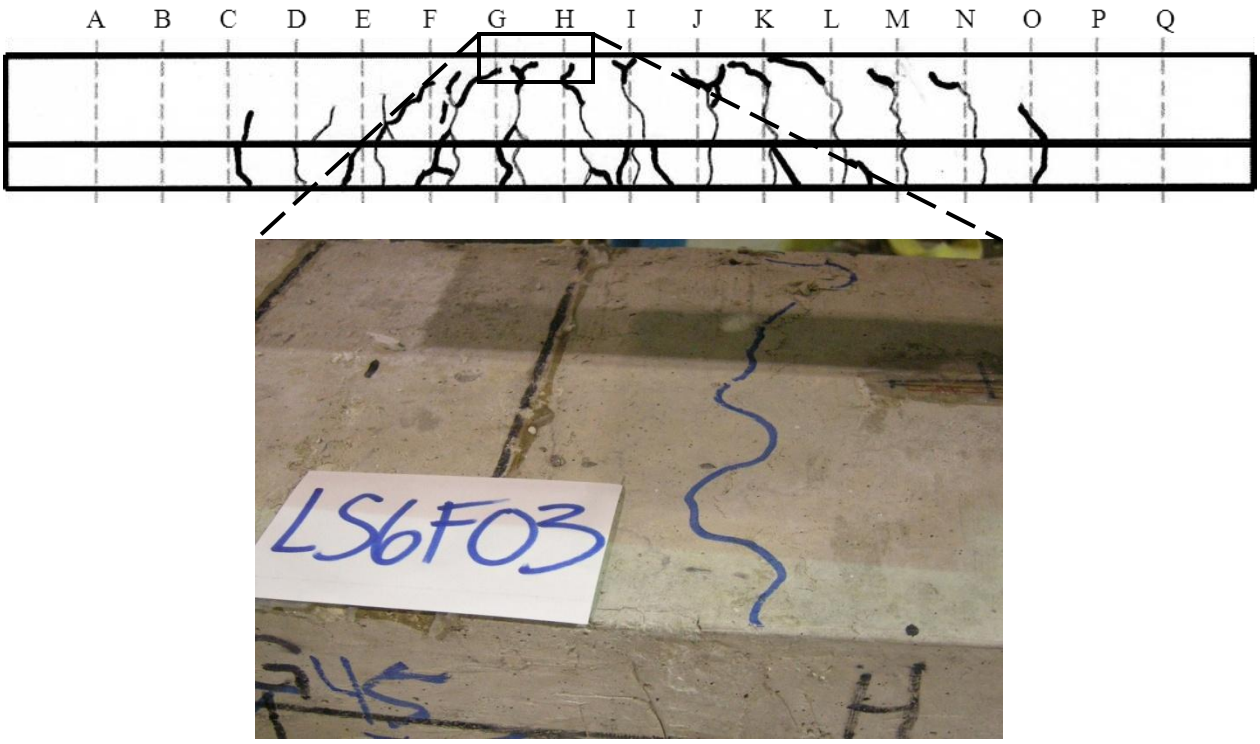

Figure 7.17 Crack Pattern and Detail at Failure—LS6F03

As shown in Figure 7.18, the observed failure mode for LS6F08 was the crushing of the concrete near one of the load points, with new cracks forming in the flange between existing cracks.

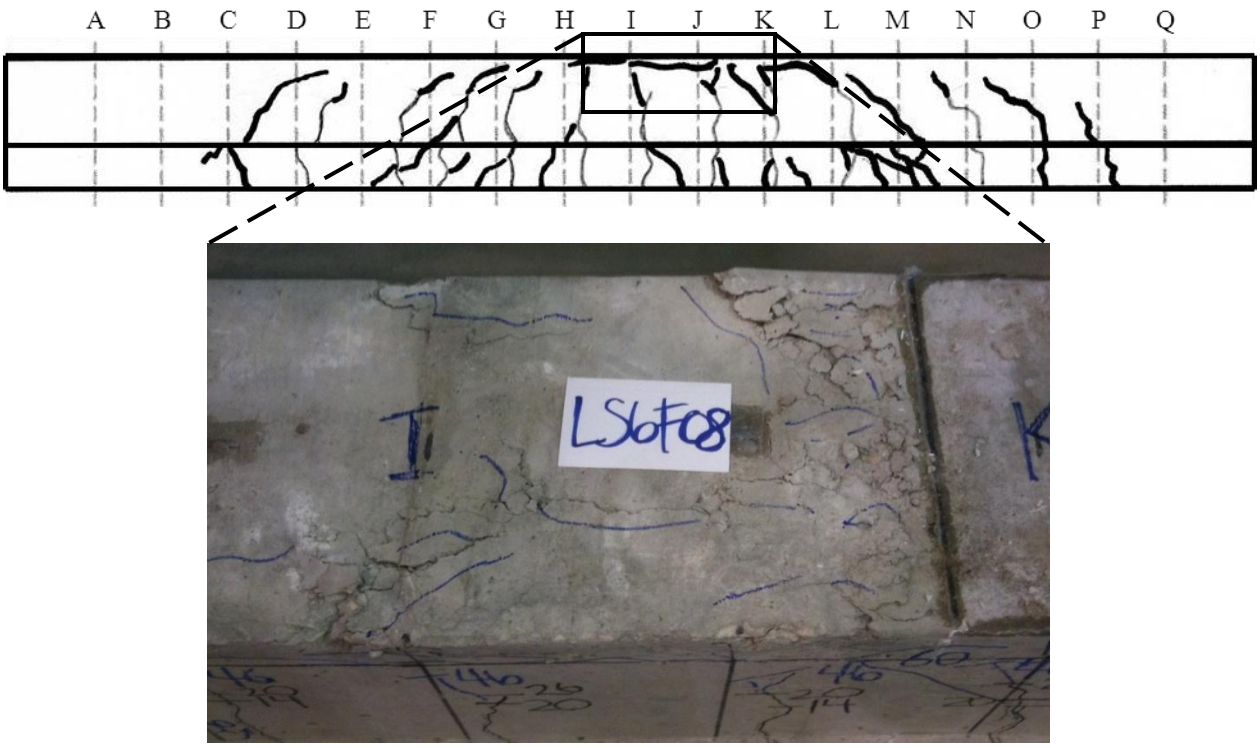

Figure 7.18 Crack Pattern and Detail at Failure—LS6F08

LS6F16 failed violently, as seen in Figure 7.19, with the concrete crushing outside the maximum moment region near a load point due to a combination of flexure and shear.

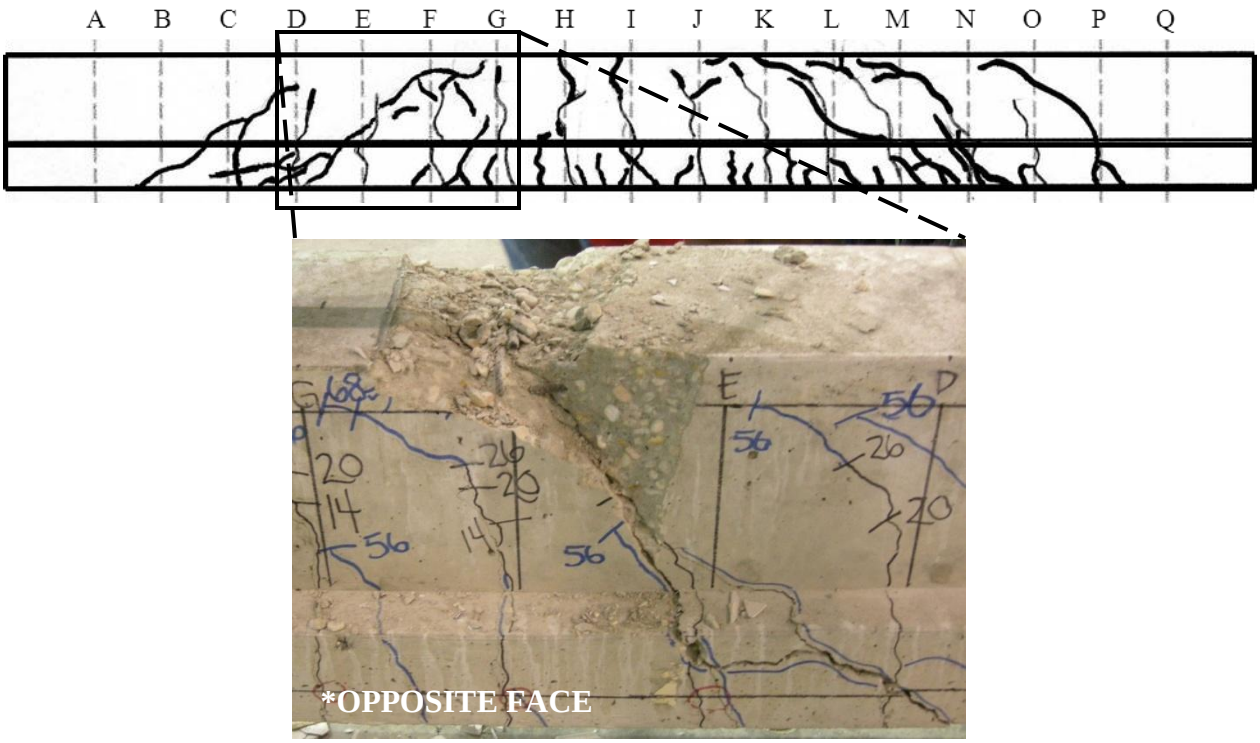

Figure 7.19 Crack Pattern and Detail at Failure—LS6F16

For specimens with ρ_f = 0.03%—LS2F03 and LS6F03—the crack patterns on the tension face, as seen in Figure 7.20 and Figure 7.21, featured smaller cracks forming between primary flexural cracks near the FRP strip and propagating in a diamond pattern away from the FRP toward the larger, pre-existing cracks. At the strip, crack widths remained small, with the widths increasing outward as the deformations in the tension flange were concentrated at the few crack locations toward the sides of the beam.

Figure 7.20 Tension-Face Cracking Pattern—LS2F03

Figure 7.21 Tension-Face Cracking Pattern—LS6F03

For specimens with ρ_f = 0.16%—LS2F16 and LS6F16—all crack widths on the tension face remained small, with numerous cracks forming tightly together among the FRP strips, as seen in Figure 7.22 and Figure 7.23.

Figure 7.22 Tension-Face Cracking Pattern—LS2F16

Figure 7.23 Tension-Face Cracking Pattern—LS6F16

Specimens with ρ_f = 0.08%—LS2F08 and LS6F08—presented cracking on the tension face, as seen in Figure 7.24 and Figure 7.25, that combines the two patterns previously discussed, with the cracks within the FRP zone remaining small and more numerous while the cracks toward the edges of the flange following the same diamond pattern observed in specimens with ρ_f = 0.03%.

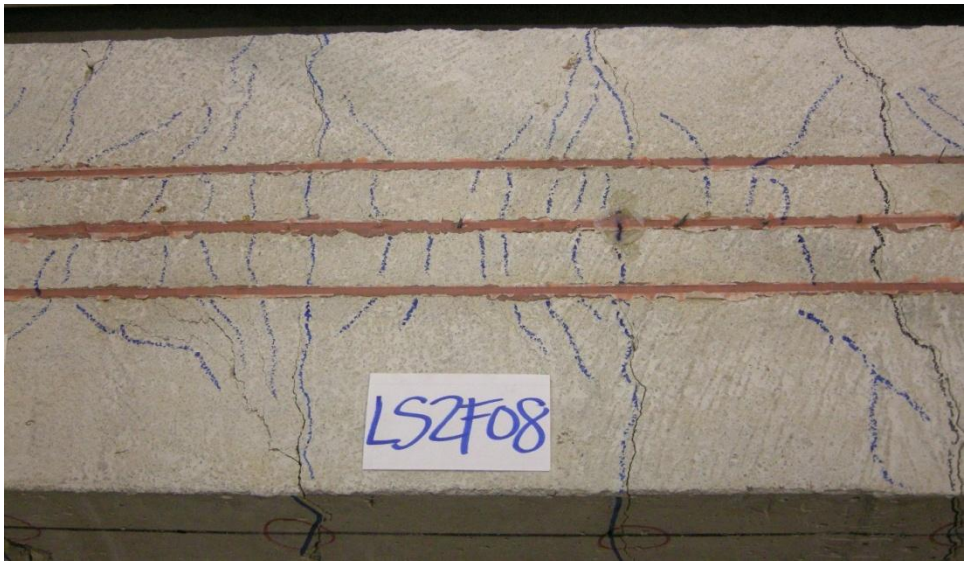

Figure 7.24 Tension-Face Cracking Pattern—LS2F08

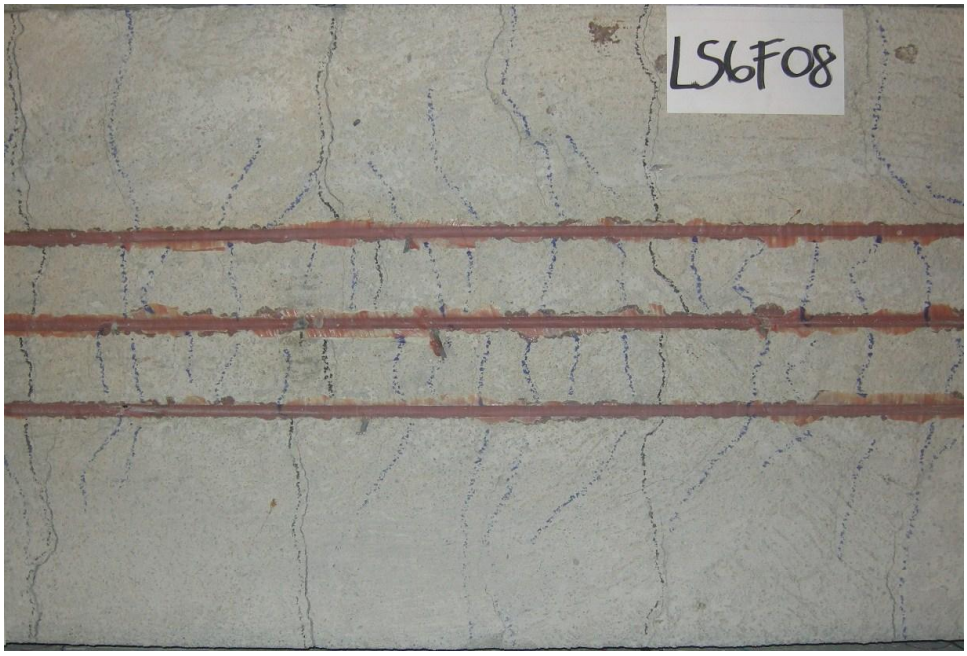

Figure 7.25 Tension-Face Cracking Pattern—LS6F08

Throughout all specimens, the cracks formed in patterns around the FRP strips that followed the behavior associated with normal crack development as a result of the distribution of tensile strength within the concrete (MacGregor and Wight 2005). The formation of numerous, smaller cracks near and among the NSM FRP strips indicates the continuing increase in tensile stress between cracks—the result of a strong bond between the FRP-epoxy composite and the concrete. Toward the edges of the flange, the cracks are fewer and wider. The diamond pattern that forms between the two regions is evidence of the transition from the stronger FRP-epoxy-concrete bond to the weaker tensile strength of the concrete alone. As the current proposed strip arrangements do not encroach on any of the minimum spacing requirements for NSM FRP, the limiting values that control flexural cracking should govern the spacing of the FRP reinforcement.

7.2.1.3 Concrete and Reinforcement Deformation Response to Applied Loads

Figure 7.26 shows the measured and predicted strains for LS2F00 during loading. Within the figure, the designations “Steel—Exp” and “Concrete—Exp” correspond to the strain data measured by the steel and concrete gages, respectively, at a cracked section during monotonic loading. The designations “Steel” and “Concrete” refer to the predicted strain values from the representative layers defined in the layer-by-layer analysis of the cross section *without* tension stiffening. In order to directly compare the data gathered from gages to the results of the theoretical model, tension stiffening cannot be applied at an individual cracked cross section. For the strengthened specimens, the additional designations “FRP—Exp” and “FRP” indicate the experimental and predicted values, respectively, obtained for the NSM FRP reinforcement using the previously stated data sources.

The experimental values for LS2F00 indicate yield occurring at a greater applied load than expected when compared with the theoretical curves—a result that, for this specimen alone, can be attributed to the gages not exactly matching the crack that formed near that cross section. However, the trend of the theoretical model both before and after yield seems to properly predict the trend displayed by the experimental curves for both concrete and steel behavior. Similarly, Figure 7.27—the material strains for LS6F00—displays good correlation between the predicted behavior and the experimentally obtained data. Both sets of strain data follow the expected behavior for an unstrengthened reinforced concrete beam.

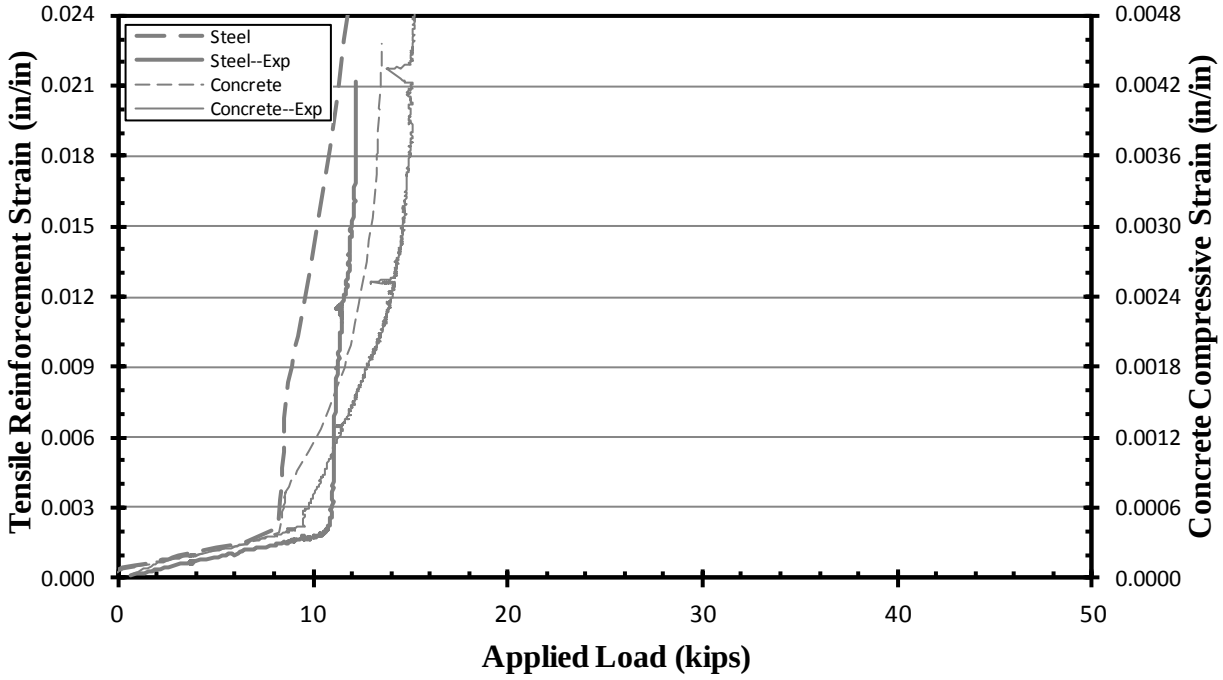

Figure 7.26 Material Strains versus Applied Load—LS2F00

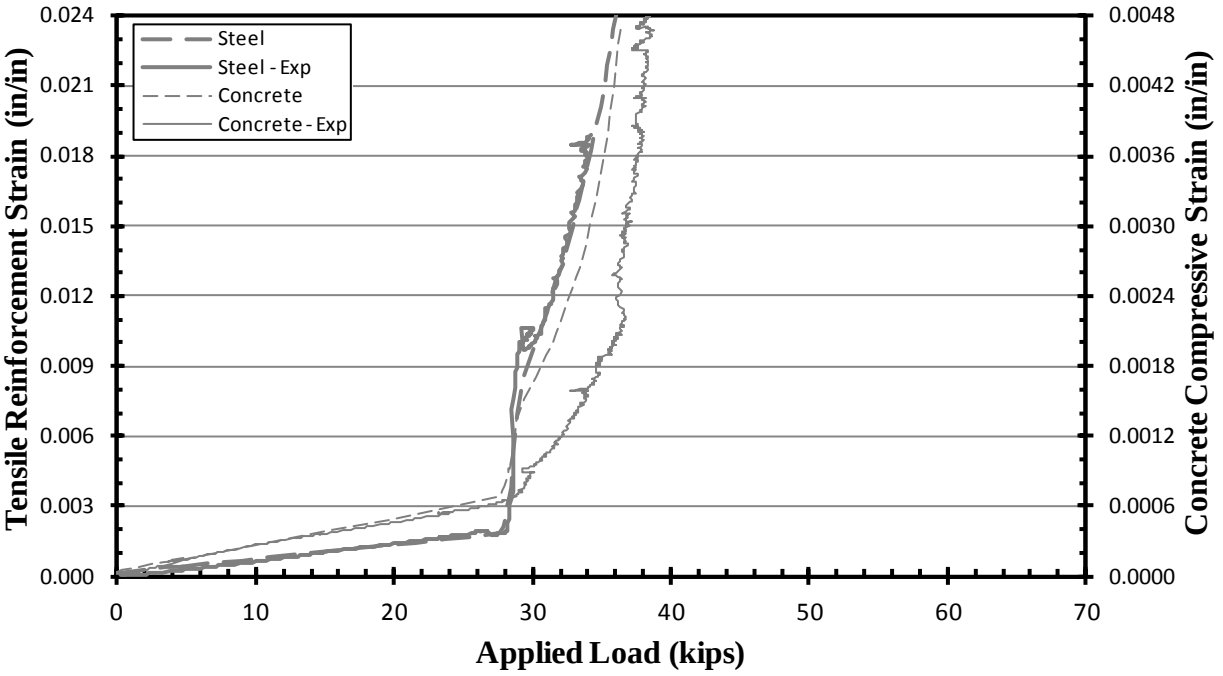

Figure 7.27 Material Strains versus Applied Load—LS6F00

The material strains for LS2F03, LS2F08, and LS2F16—shown in Figure 7.28, Figure 7.29, and Figure 7.30, respectively—again show the experimental yield point for the specimens occurring at a greater load level than predicted, a phenomenon likely resulting from the steel being pushed past yielding during the cracking process. The post-yield experimental strains performed in opposition to expected behavior, with the steel experiencing higher strains than the FRP, even though the steel reinforcement lies closer to the neutral axis than the FRP reinforcement, revealing that the strains for a given strengthened cross section are not proportional to the distance from the neutral axis. This behavior can also explain the significant difference between the strain responses indicated by the experimental and theoretical steel curves at yield, as the analytical model acts on the assumption that plane sections remain plane. The very small experimental strain results for the reinforcement in the linear-elastic region of LS2F03 and LS2F08 can be attributed in this case to the data coming from a cross section at which there was no pre-repair crack, while the theoretical values are based on an assumption of cracked-section behavior. As more FRP reinforcement is added to the specimens, the model more accurately predicts the strains at each gage location (after cracking occurs at that location).

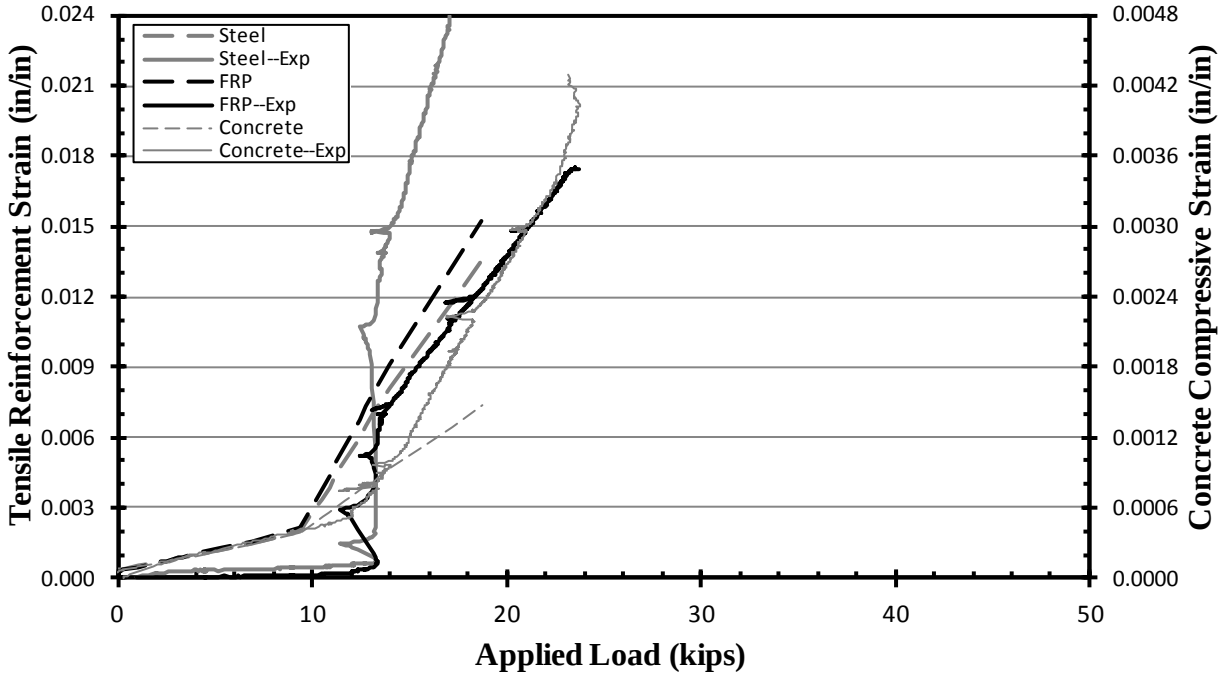

Figure 7.28 Material Strains versus Applied Load—LS2F03

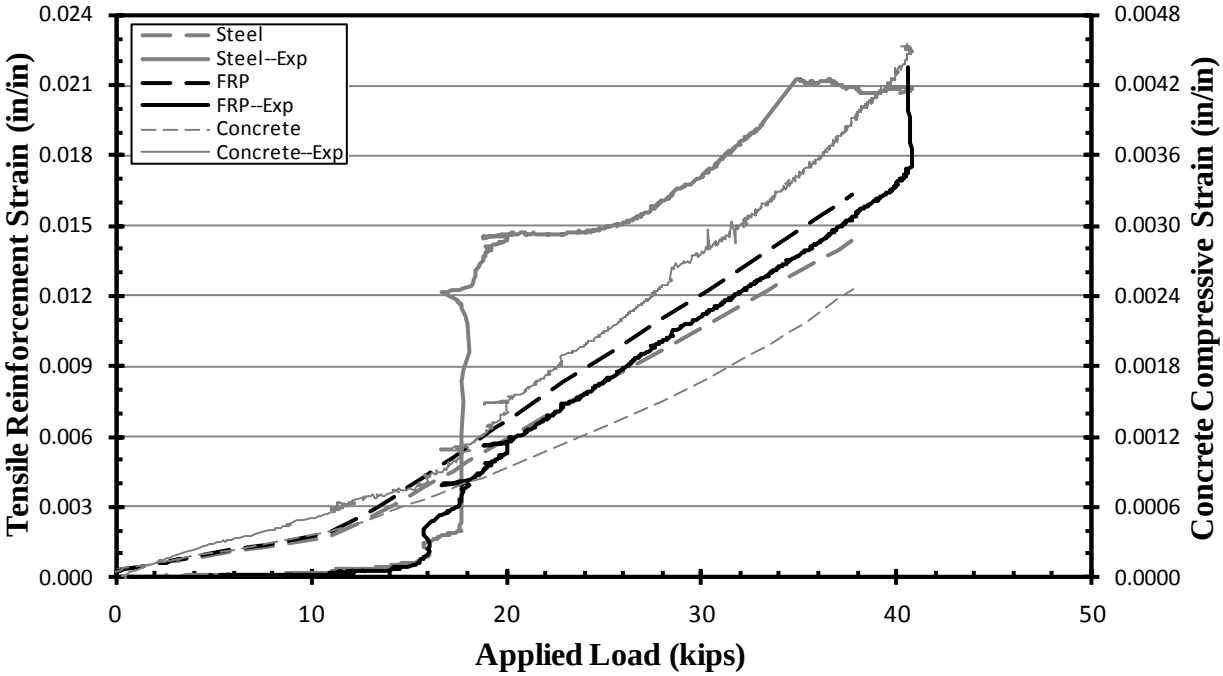

Figure 7.29 Material Strains versus Applied Load—LS2F08

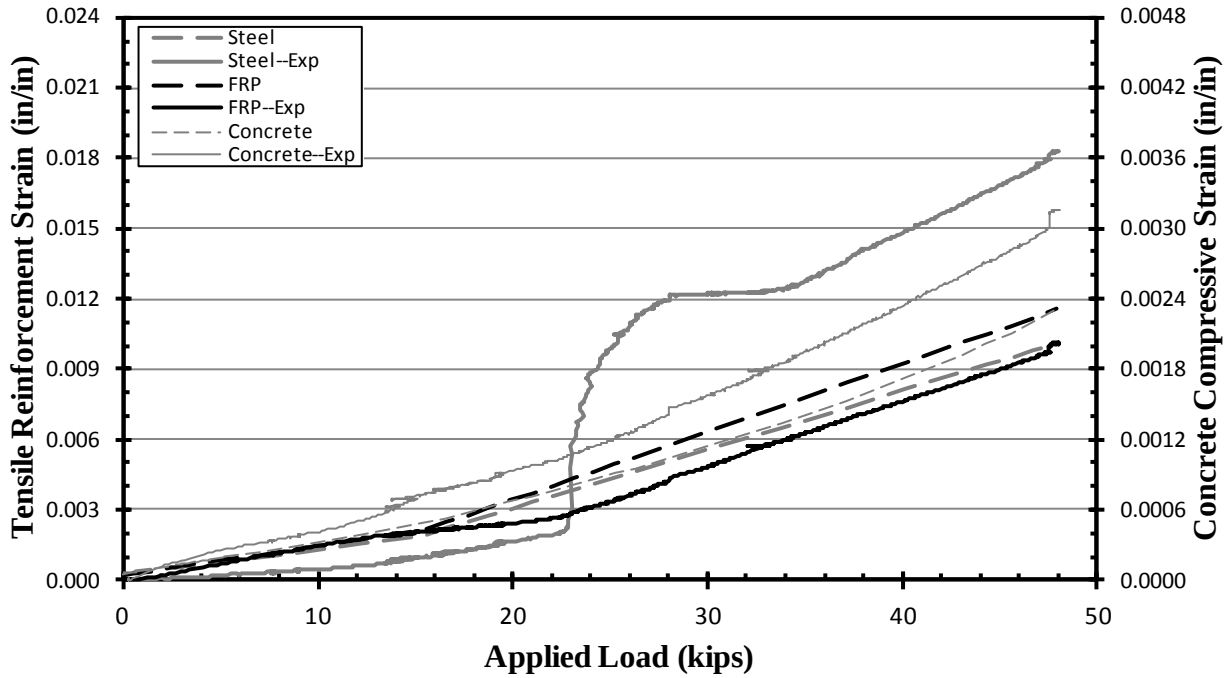

Figure 7.30 Material Strains versus Applied Load—LS2F16

Figure 7.31, Figure 7.32, and Figure 7.33 display the material strain data for LS6F03, LS6F08, and LS6F16, respectively. Both the theoretical and experimental curve sets possess a distinct increase in the change in strain relative to load at yield, with the predicted yield still falling at a lesser load than its observed occurrence and the expected behavioral relationship between the experimental steel and FRP strains again reversing following the yield point. The prediction of the compressive strains in the concrete continues to follow the behavioral trend of the experimental results.

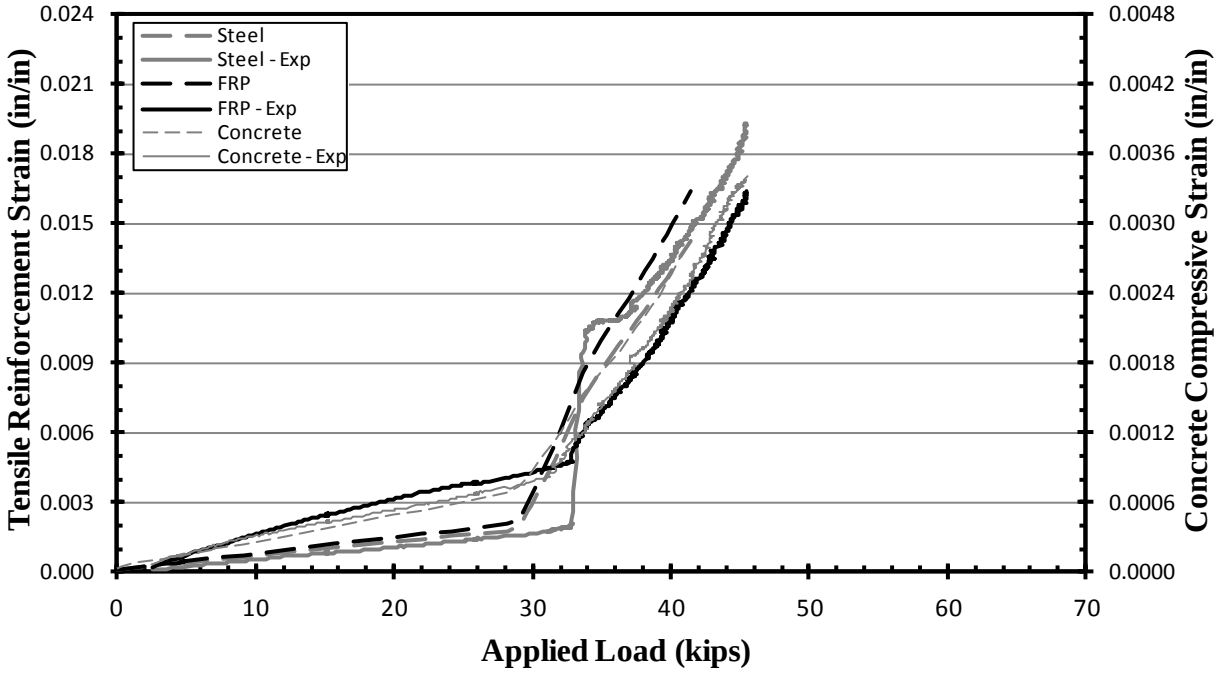

Figure 7.31 Material Strains versus Applied Load—LS6F03

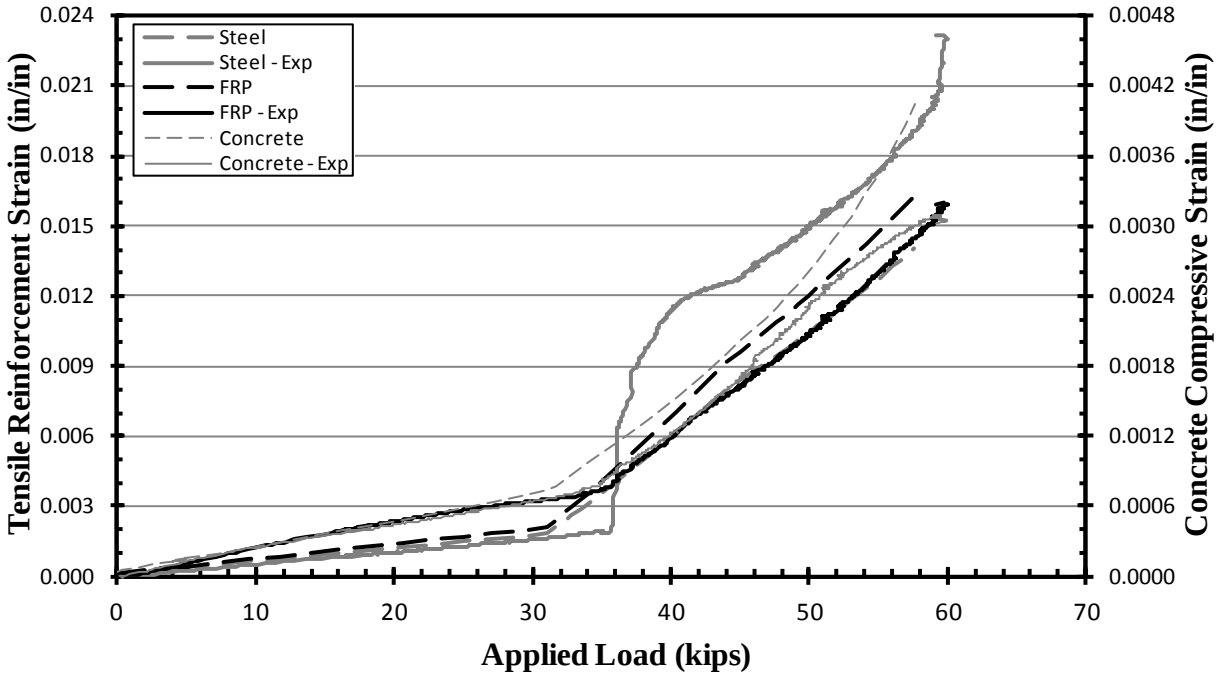

Figure 7.32 Material Strains versus Applied Load—LS6F08

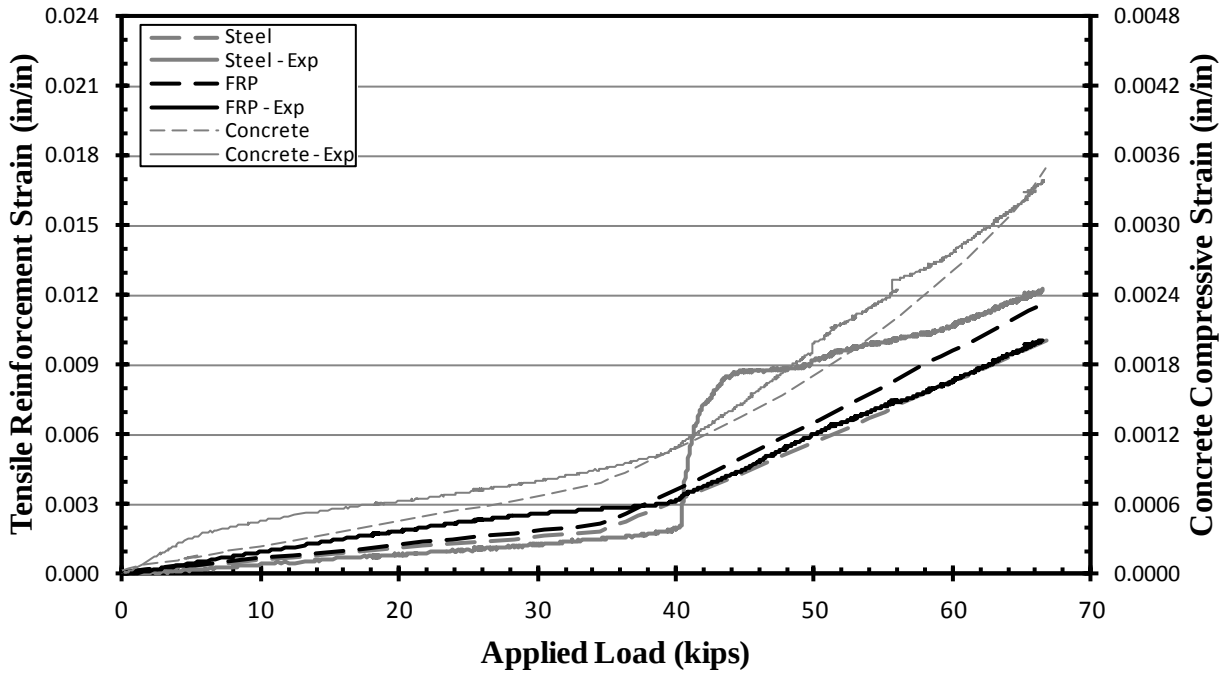

Figure 7.33 Material Strains versus Applied Load—LS6F16

7.2.1.4 Summary of Specimen Behavior

Analysis of the load-deflection curves for each specimen shows behavior consistent with strengthened concrete sections. The under-reinforced beams displayed linear-elastic behavior between the two modeled conditions—initially uncracked and precracked—with predictions of stiffer behavior after yield than were experimentally observed. The more moderately reinforced beams showed the same post-yield behavior, with the precracked predictions matching the experimental results in the linear-elastic range. For both levels of steel reinforcement, the precracked model provided a conservative estimate of specimen behavior prior to yield.

The observed failure mode for each specimen involved some form of concrete crushing, whether due to flexure, shear, or a combination of the two. This result coupled with the observed cracking patterns found on the flanges indicates an effective FRP-epoxy-concrete bond for these beams.

The concrete and reinforcement strains for the control specimens behaved as expected, while the strains for the strengthened beams presented two unexpected results: later steel yielding than predicted and an inversion of the relative steel-FRP strain relationship. The consistent appearance of the yield point at a load greater than expected can be attributed to the steel reinforcement being subjected to greater strains during the cracking process as a result of the overestimate of the load required to produce the targeted maximum moment. The overstressed condition of the steel delays the perceived onset of yield experienced in a repaired cross section. The inversion of the steel and FRP values after yield shows that the magnitude of the post-yield strains in a strengthened cross section is not proportional to the distance from the neutral axis—as assumed in traditional beam theory, i.e. plane sections remain plane. As seen in Figure 7.34, a similar inversion of the cross-sectional strains is apparent in the test results reported by Bergstrom, Taljsten, and Carolin (2009).

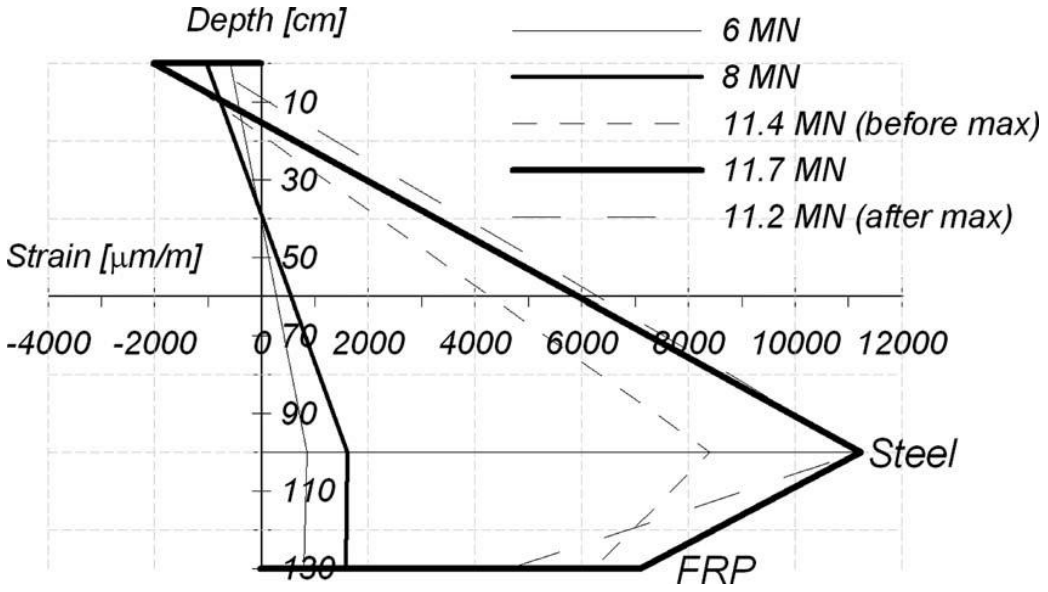

Figure 7.34 Strain Distribution in Section 4 of the East Beam before, during, and after Maximum Load (M) (Bergstrom, Taljsten, and Carolin 2009)

Prior to yielding, the strains in the FRP are bigger than the steel strains, as observed in the analysis of the data from the service-load range. However, as the moment of the cross section

increases, the stiffness of the (non-yielding) FRP-epoxy composite and the strong bond between the composite and the concrete result in lesser strains in the FRP reinforcement relative to the strains observed the steel reinforcement that lies closer to the neutral axis, as seen in Figure 7.35.

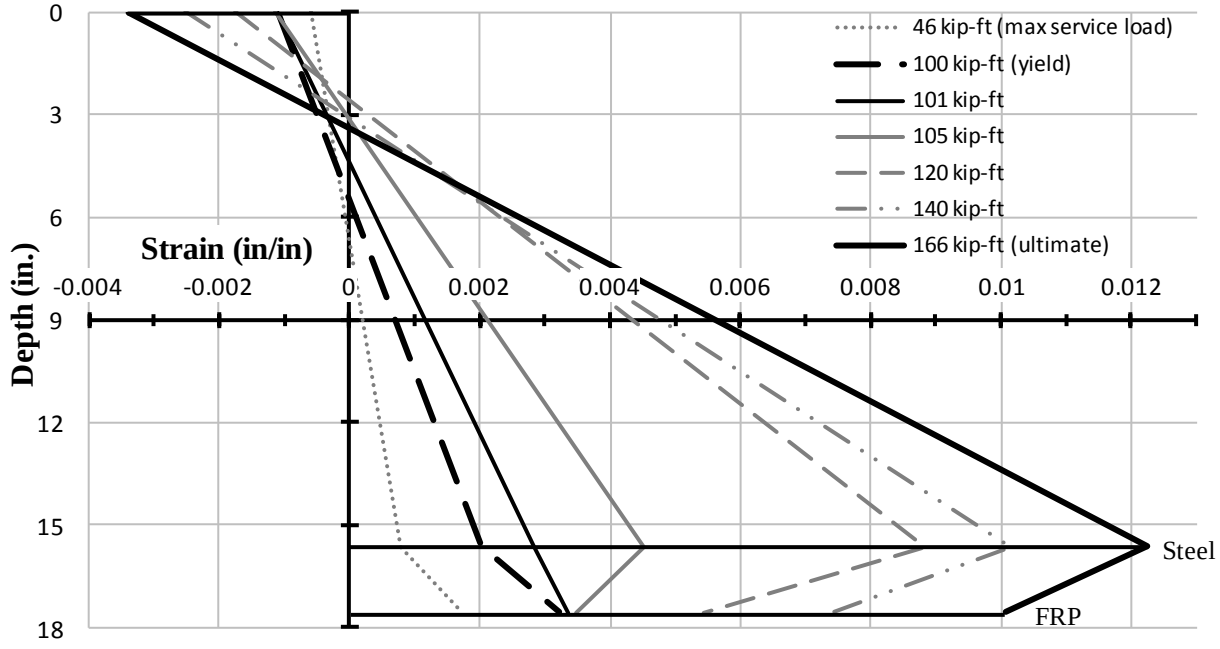

Figure 7.35 Cross-Sectional Strain Profiles under Monotonic Loading—LS6F16

7.2.2 Cross-Sectional Behavior

7.2.2.1 Strain in FRP Reinforcement

Table 7.4 displays the strains achieved during experimental testing set against the predicted ultimate strain values based on various models. The designations "ACI 440", "Said and Wu", "Seracino et al.", and "Standards Australia" refer to the values calculated using the equations recommended in the corresponding published research—ACI 440 (2008), Said and Wu (2008), Seracino et al. (2007), and Standards Australia (2008). Values under "ACI 440 $\bar{x}$" were calculated using the recommended equation from ACI 440 (2008) with actual mean-value-rupture strain determined from manufacturer material testing results, This limiting value was

created by the researcher solely to explore the impact on the capacity predictions of applying the full theoretical strain of the FRP instead of the design rupture strain based on the guaranteed ultimate tensile strength provided by the manufacturer. "Experimental Ultimate" corresponds to the values directly gleaned from the monotonic testing. The designation "Non-anch. Failure" refers to the first occurring of two possible non-anchorage failure limits predicted by the precracked, unstiffened model discussed in Section 6.1.1: either the predicted rupture of the FRP reinforcement or an extreme compression fiber strain of 0.003 in/in. For ACI 440 (2008), Seracino et al. (2007), and Standards Australia (2008), the predicted strain values do not vary based on reinforcement amount, as these approaches limit the strain in order to prevent IC debonding. Additionally, these three models predict nearly equivalent debonding strains (as well as highly similar moment capacities); this occurrence might be connected to the material parameters associated with these specimens. Table 7.5 shows the ratio between the values measured in the beam tests and the predicted values.

Table 7.4 Measured and Predicted Strain Achieved in FRP

Beam ID	Experimental Ultimate Strain (in/in x 10^{-6})	Predicted Limiting Strain (in/in x 10^{-6})					
		ACI 440	ACI* 440 $\bar{x}$	Said and Wu	Seracino et al.	Standards Australia	Non-anch. Failure
LS2F03	17500			5270			16500
LS2F08	21100	10000	11500	3590	9810	9770	16400
LS2F16	10100			2810			13300
LS6F03	16500			5270			16400
LS6F08	16000	10000	11500	3590	9810	9770	13000
LS6F16	10100			2810			10400

* ACI 440 using mean-value rupture strain, approximately equivalent to $0.8\varepsilon_{fu}$

Table 7.5 Test-to-Predicted Ratio of Strain Achieved in FRP

Beam ID	Experimental Ultimate Strain / Predicted Limiting Strain					
	ACI 440	ACI 440 $\bar{x}$	Said and Wu	Seracino et al.	Standards Australia	Non-anch. Failure
LS2F03	1.75	1.52	3.32	1.78	1.79	1.06
LS2F08	2.11	1.83	5.88	2.15	2.16	1.29
LS2F16	1.01	0.88	3.59	1.03	1.03	0.76
LS6F03	1.65	1.43	3.13	1.68	1.69	1.01
LS6F08	1.60	1.39	4.46	1.63	1.64	1.23
LS6F16	1.01	0.88	3.59	1.03	1.03	0.97

Overall, the ACI 440 (2008) model provides the closest prediction to the achieved strains while still remaining conservative, especially for higher amounts of NSM FRP reinforcement. However, the trend suggests that the ACI 440 (2008) relationship may not be conservative for FRP reinforcement amounts *greater* than the amounts utilized in this test program.

Analysis of the material strains for LS2F16 show that, of the three under-reinforced sections, this specimen has the lowest value for the ultimate strain in the concrete (0.003 in/in), possibly accounting for the extremely non-conservative result. For LS2F03—the specimen most representative of the proposed bridge strengthening scheme—the ratios of the experimental ultimate strains to the theoretical strain limits for ACI 440 (2008), Seracino et al. (2007), and Standards Australia (2008) are 1.75, 1.78, and 1.79, respectively. These results indicate that any strengthening scheme based on these three methods should provide the necessary change in strain to accommodate the required increase in capacity.

7.2.2.2 Nominal Moment Capacity

Table 7.6 lists the experimentally attained ultimate moment capacity for each specimen in conjunction with the capacities predicted by the denoted models. For all specimens, the ultimate capacity from testing exceeds the predicted design limits based on theoretical IC debonding;

similarly, all but one of the experimental capacities surpasses the non-anchorage failure predicted by the model introduced in Section 6.1. The moment capacities predicted by Seracino et al. (2007) and Standards Australia (2008) are nearly identical—an occurrence that can be attributed to the similarity of the research involved in the derivation of both models as well as the concrete compressive strength used for this testing program. The predictions from Said and Wu (2008) are overly conservative for an application involving NSM FRP reinforcement, which could be expected because the derivation of the employed limit came from a test database solely focused on externally bonded FRP.

Table 7.6 Measured and Predicted Moment Capacities

Beam ID	Experimental Moment Capacity (kip-ft)	Predicted Moment Capacity (kip-ft)					
		ACI 440	ACI 440 $\bar{x}$	Said and Wu	Seracino et al.	Standards Australia	Non-anch. Failure
LS2F00	43.8	-	-	-	-	-	37.4 [1]
LS2F03	64.9	42.2	45.1	34.2	41.8	41.7	54.5 [2]
LS2F08	107.6	70.6	77.8	41.6	69.8	69.6	100.3 [2]
LS2F16	125.6	112.2	125.0	50.0	110.5	110.2	139.8 [1]
LS6F00	102.4	-	-	-	-	-	90.1 [1]
LS6F03	119.3	93.1	97.1	84.2	92.6	92.5	109.0 [1,2]
LS6F08	155.5	120.0	127.8	90.8	119.0	118.8	135.0 [1]
LS6F16	177.9	158.7	170.9	98.2	157.1	156.7	162.2 [1]

[1]predicted concrete failure at 0.003 in/in [2]predicted rupture of FRP

Table 7.7 compares the predicted moment capacities to the ultimate capacities from the experimental testing, showing all design limits to be conservative. Likewise, all but one capacity predicted via the compatibility model yields a conservative result; the predicted result for LS2F16 represents a predicted failure due to concrete crushing and therefore gives no indication for or against bond failure.

At this magnitude of concrete compressive strength, ACI 440 (2008), Seracino et al. (2007), and Standards Australia (2008) show similar ratios relative to the experimentally achieved capacity.

Table 7.7 Test-to-Predicted Ratio of Moment Capacity

Beam ID	Experimental Moment Capacity / Predicted Moment Capacity					
	ACI 440	ACI 440 $\bar{x}$	Said and Wu	Seracino et al.	Standards Australia	Non-anch. Failure
LS2F00	-	-	-	-	-	1.17
LS2F03	1.54	1.44	1.90	1.55	1.56	1.19
LS2F08	1.52	1.38	2.59	1.54	1.55	1.07
LS2F16	1.12	1.00	2.51	1.14	1.14	0.90
LS6F00	-	-	-	-	-	1.14
LS6F03	1.28	1.23	1.42	1.29	1.29	1.09
LS6F08	1.30	1.22	1.71	1.31	1.31	1.15
LS6F16	1.12	1.04	1.81	1.13	1.13	1.10

The design limits assessed are used to predict the occurrence of IC debonding as the failure condition at ultimate. Examining the experimental results through this lens, debonding does not seem to have occurred in any of the specimens, despite having reached capacities above the limiting values proposed in prior research. Once again, the relationship from ACI 440 (2008) provides the most accurate yet conservative result.

7.2.2.3 Change in Moment Capacity

Table 7.8 lists the observed and predicted increases in capacity from the control specimens due to the addition of FRP to establish whether a consistent relationship exists between an increase in FRP reinforcement and an increase in capacity. The negative values within the table indicate that, for the specimens with the least amount of FRP, the relationship from Said and Wu (2008) predicted a capacity less than that provided by an unstrengthened specimen, showing Said and

Wu as an inaccurate indicator for capacity provided by NSM FRP. Cursory analysis reveals that no proportional relationship exists between an increase in the amount of FRP added to a specimen and the increase in the moment capacity of that specimen; rather, comparison of the experimental capacities shows the beginnings of diminishing return when adding more FRP reinforcement to garner greater capacity. For example, tripling the amount of FRP reinforcement triples the experimental increase in capacity, while using six times the FRP strips only increases the capacity by approximately 4.5 times.

Table 7.8 Increase in Moment Capacity due to FRP

Beam ID	Experimental Increase due to FRP (kip-ft)	Predicted Increase in Moment Capacity due to FRP (kip-ft)					
		ACI 440	ACI 440 $\bar{x}$	Said and Wu	Seracino et al.	Standards Australia	Non-anch. Failure
LS2F03	+21.1	+4.8	+7.7	-3.2	+4.4	+4.3	+17.1
LS2F08	+63.8	+33.2	+40.4	+4.2	+32.4	+32.2	+62.9
LS2F16	+81.8	+74.8	+87.6	+12.6	+73.1	+72.8	+102.4
LS6F03	+16.9	+3.0	+7.0	-5.9	+2.5	+2.4	+18.9
LS6F08	+53.1	+29.9	+37.7	+0.7	+28.9	+28.7	+44.9
LS6F16	+75.5	+68.6	+80.8	+8.1	+67.0	+66.6	+72.1

Table 7.9 compares the experimental increase in capacity to the predicted increases in capacity, showing that as the amount of FRP increases, the predicted increase in capacity becomes less conservative, with the capacity increase being overestimated relative to the experimentally observed increase in multiple cases.

Table 7.9 Test-to-Predicted Ratio of Change in Moment Capacity

Beam ID	Experimental Increase in Moment Capacity / Predicted Increase in Moment Capacity					
	ACI 440	ACI 440 $\bar{x}$	Said and Wu	Seracino et al.	Standards Australia	Non-anch. Failure
LS2F03	4.40	2.74	-6.59	4.80	4.91	1.23
LS2F08	1.92	1.58	15.19	1.97	1.98	1.01
LS2F16	1.09	0.93	6.49	1.12	1.12	0.80
LS6F03	5.63	2.41	-2.86	6.76	7.04	0.89
LS6F08	1.78	1.41	75.86	1.84	1.85	1.18
LS6F16	1.10	0.93	9.32	1.13	1.13	1.05

The predictions yielded by applying the full experimental strain limit of the FRP (ACI 440 $\bar{x}$) are usually more efficient than the values calculated from ACI 440 (2008) while still remaining conservative. As the amount of FRP increases, the modified relationship follows the same trend towards becoming non-conservative as the ACI 440 (2008) results. However, the benefit—if it exists—of applying a relationship similar to ACI 440 $\bar{x}$ rather than the prescribed limit value cannot be confirmed without a larger statistical sample.

As the predictions from ACI 440 (2008), Seracino et al. (2007), and Standards Australia (2008) continue to be nearly equivalent and consistently conservative, the conservative designs of six thin or five thick strips per girder as proposed by Alexy (2009) should be more than adequate to provide the necessary capacity increase for the Letohatchee bridge. Similarly, with the relationship from ACI 440 (2008) requiring the most efficient strip arrangements of the three—as seen in Figure 2.31and Figure 2.32—and thick strips costing approximately twice as much as thin strips, the three thick strips per girder allowed by ACI 440 (2008) in comparison to six thin strips should provide the most efficient strengthening option in terms of time and labor, as the material costs of the two designs are nearly equivalent.

Figure 7.36 and Figure 7.37 serve as visual representations of the relationship between increasing the amount of FRP reinforcement and the increase in the ultimate capacity of a specimen. Comparison of the experimental load-deflection curves shows a consistent increase in both the stiffness and ultimate strength of each specimen with addition of FRP. Because all eight specimens experience some form of concrete failure, the lack of an established trend for the ultimate deflections is most likely a result of the variability of the ultimate strain reached by the concrete on the compression face prior to failure. The yield strength of the repaired specimens follows the same consistent pattern of increase with each addition of FRP as the ultimate capacity. The capacity increase at yield is approximately 20–25% of the increase at ultimate over the unstrengthened specimens, possibly acting as a limiting value for design so as to prevent yielding of the steel reinforcement under service loads. However, analysis of the capacity increase—while helpful in predicting the relative contribution of the FRP to the capacity of a specimen—does not contribute to determining whether IC debonding occurs.

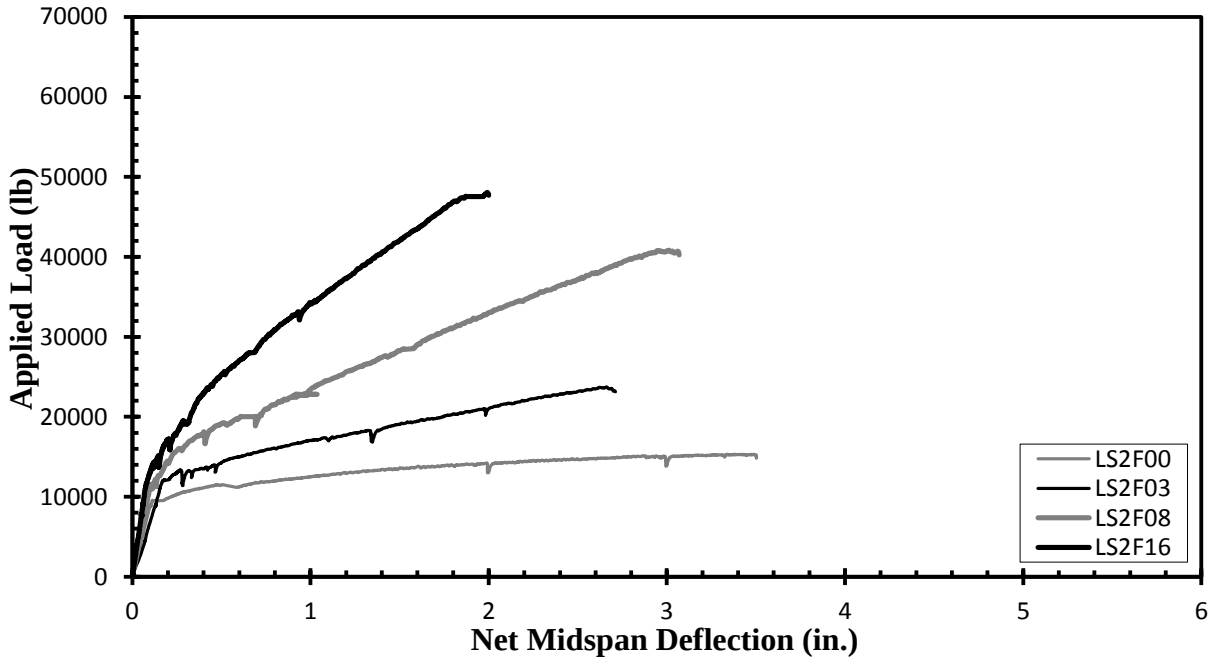

Figure 7.36 Monotonic Load versus Deflection—ρ_s = 0.2%

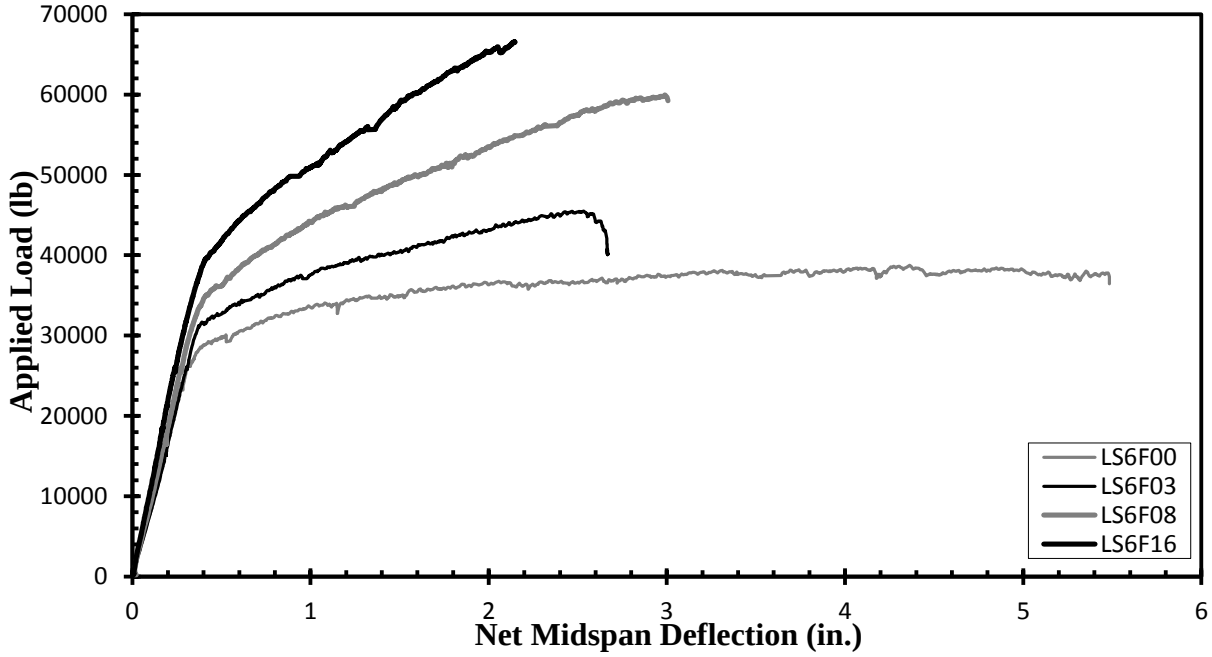

Figure 7.37 Monotonic Load versus Deflection—ρ_s = 0.6%

7.2.2.4 Longitudinal Strain Distribution in FRP Reinforcement

Figure 7.38 to Figure 7.43 depict the distribution of strain in the FRP along the length of the specimen as strain levels increase relative to the application of greater load to the specimen. A single gage within the maximum moment region of each beam was selected as the basis for the generation of the longitudinal distribution curves. For that gage, the strains equivalent to the interval values listed in each figure were then paired with the corresponding load at that level. The readings at that load for the remaining gages were used to generate the depicted series of curves.

Strain readings from the gages at cracks follow the gridlines that indicate the longitudinal position of the gage; the points between gridlines indicate gages neighboring the nearest crack for the purpose of analyzing strain distribution across the crack. The spikes in each plot indicate the formation of a new crack or the growth of an existing crack relative to the surrounding uncracked sections, while any gaps in the curves represent a dead gage at that cross section.

As the ultimate strains predicted by the IC-debonding models fall below the experimental ultimate strains, debonding should have occurred in every specimen prior to the ultimate capacities reached during testing. Debonding behavior would result in an inversion of the strain levels observed around cracks—with the strain at the crack holding steady or decreasing while the strains in the neighboring gages increased to a similar magnitude. However, the plots seem to indicate a state of strain consistent with the redistribution of stress along the length of the specimen as new cracks form rather than the propagation of debonding.

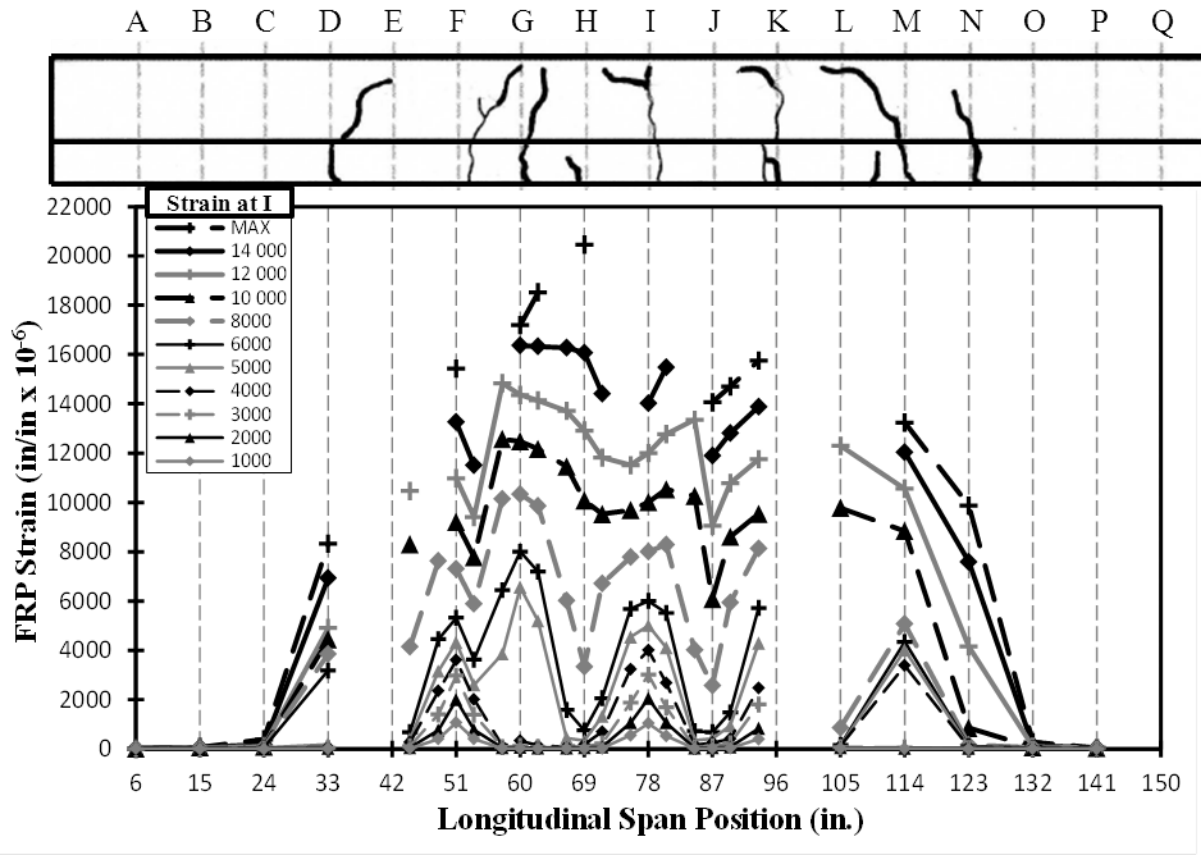

Figure 7.38 FRP Strain Distribution under Increasing Applied Load—LS2F03

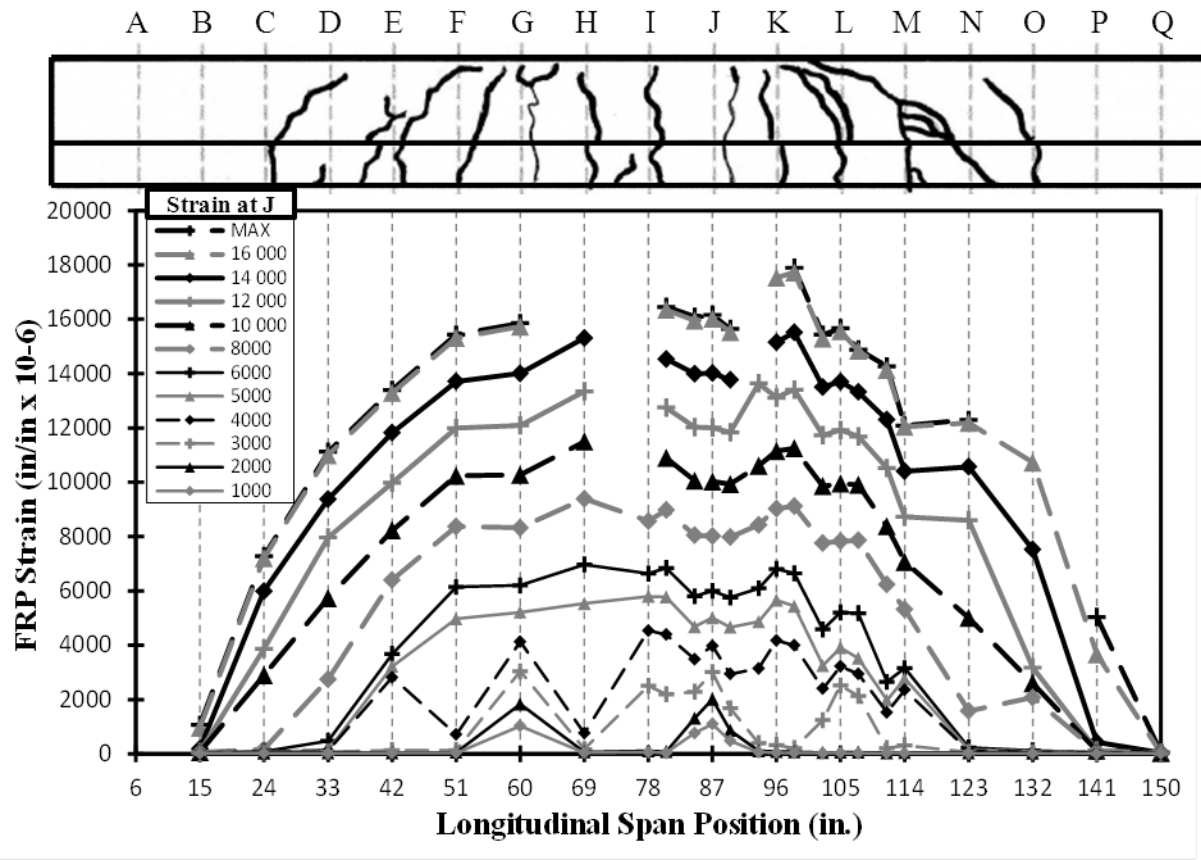

Figure 7.39 FRP Strain Distribution under Increasing Applied Load—LS2F08

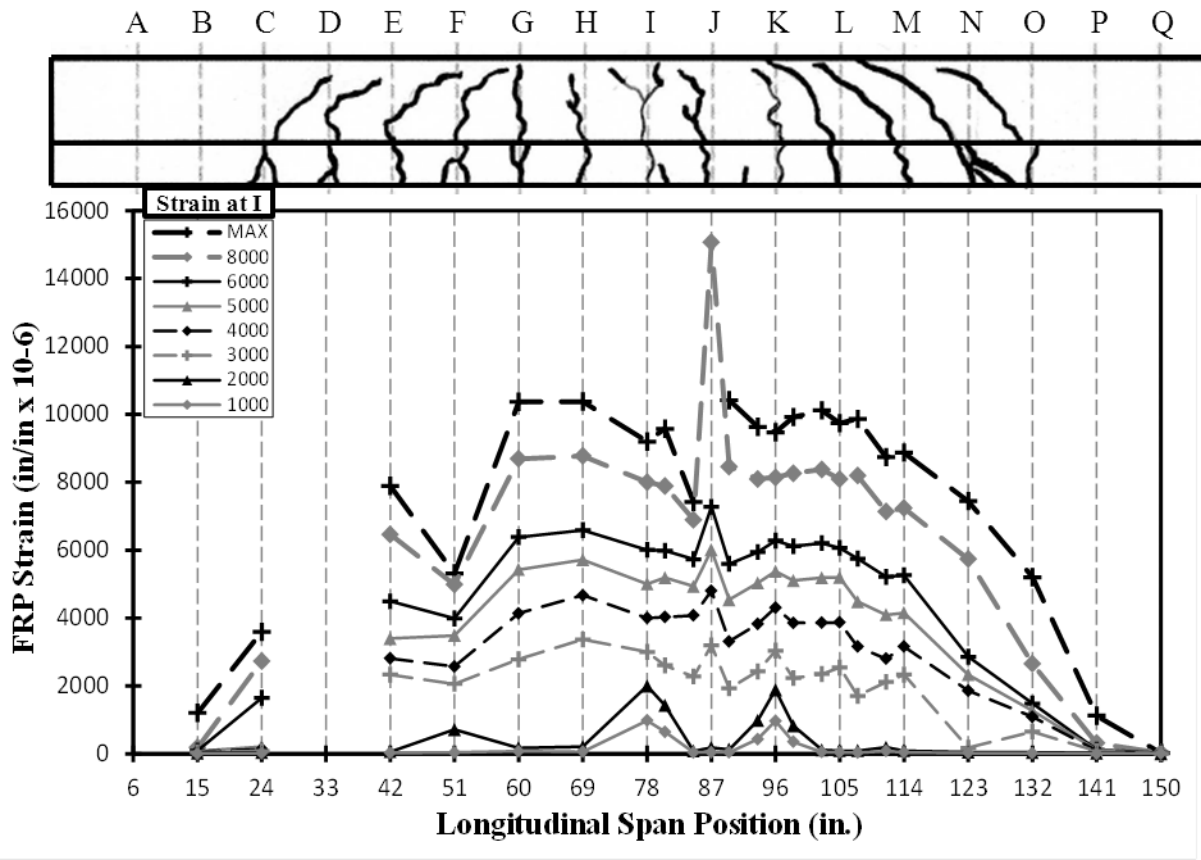

Figure 7.40 FRP Strain Distribution under Increasing Applied Load—LS2F16

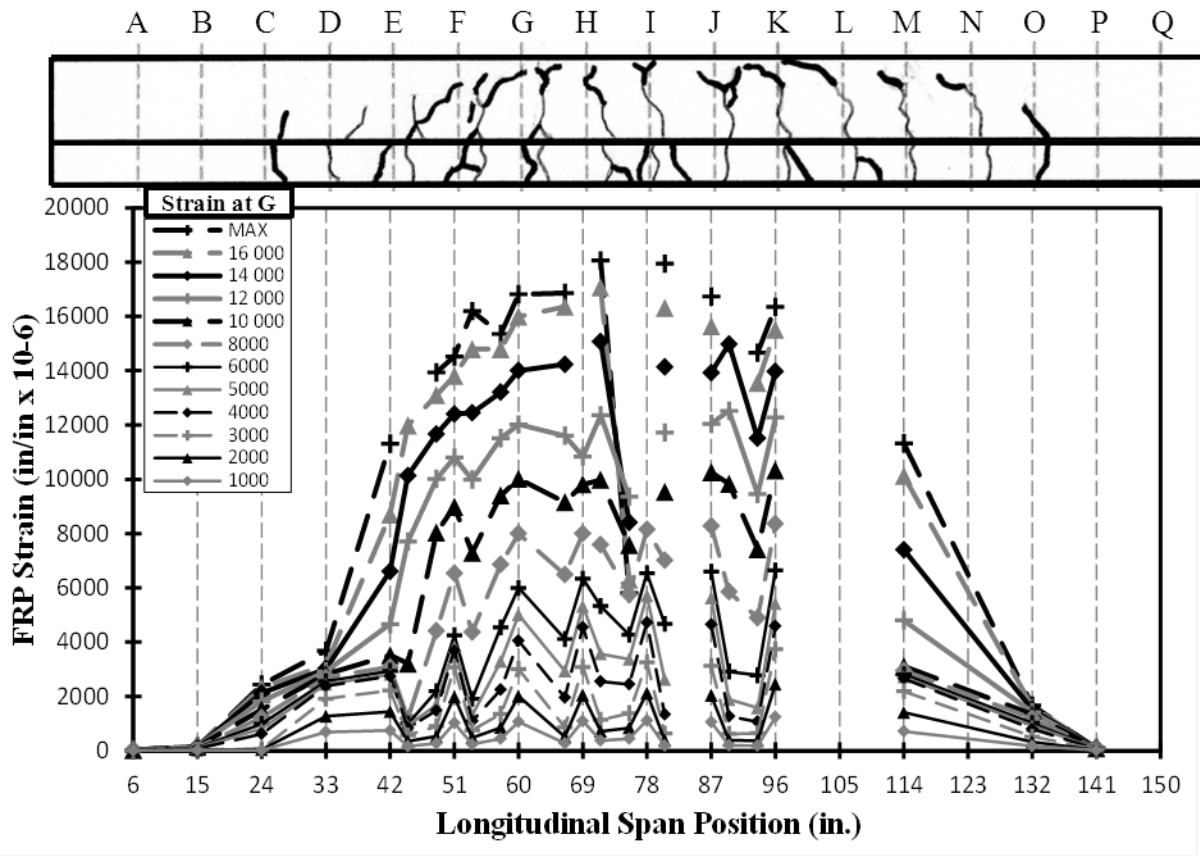

Figure 7.41 FRP Strain Distribution under Increasing Applied Load—LS6F03

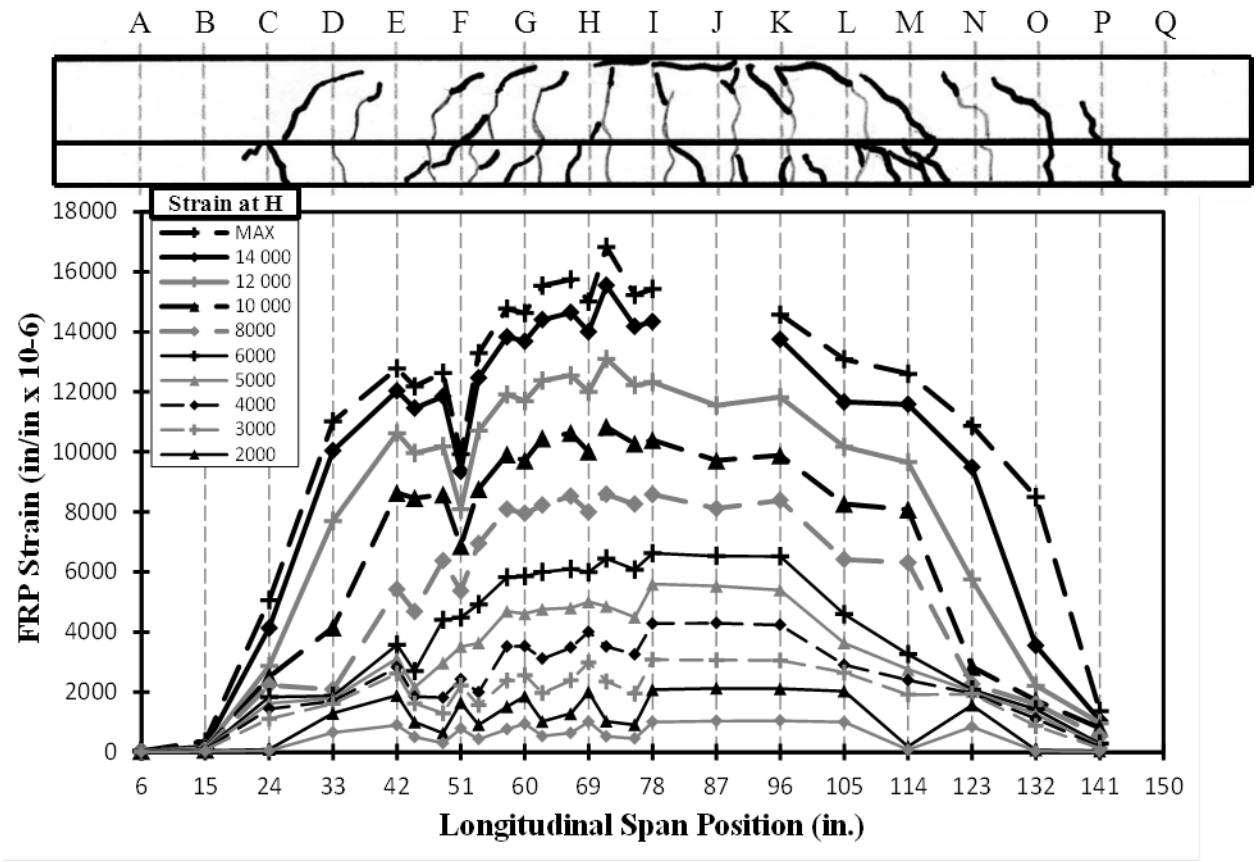

Figure 7.42 FRP Strain Distribution under Increasing Applied Load—LS6F08

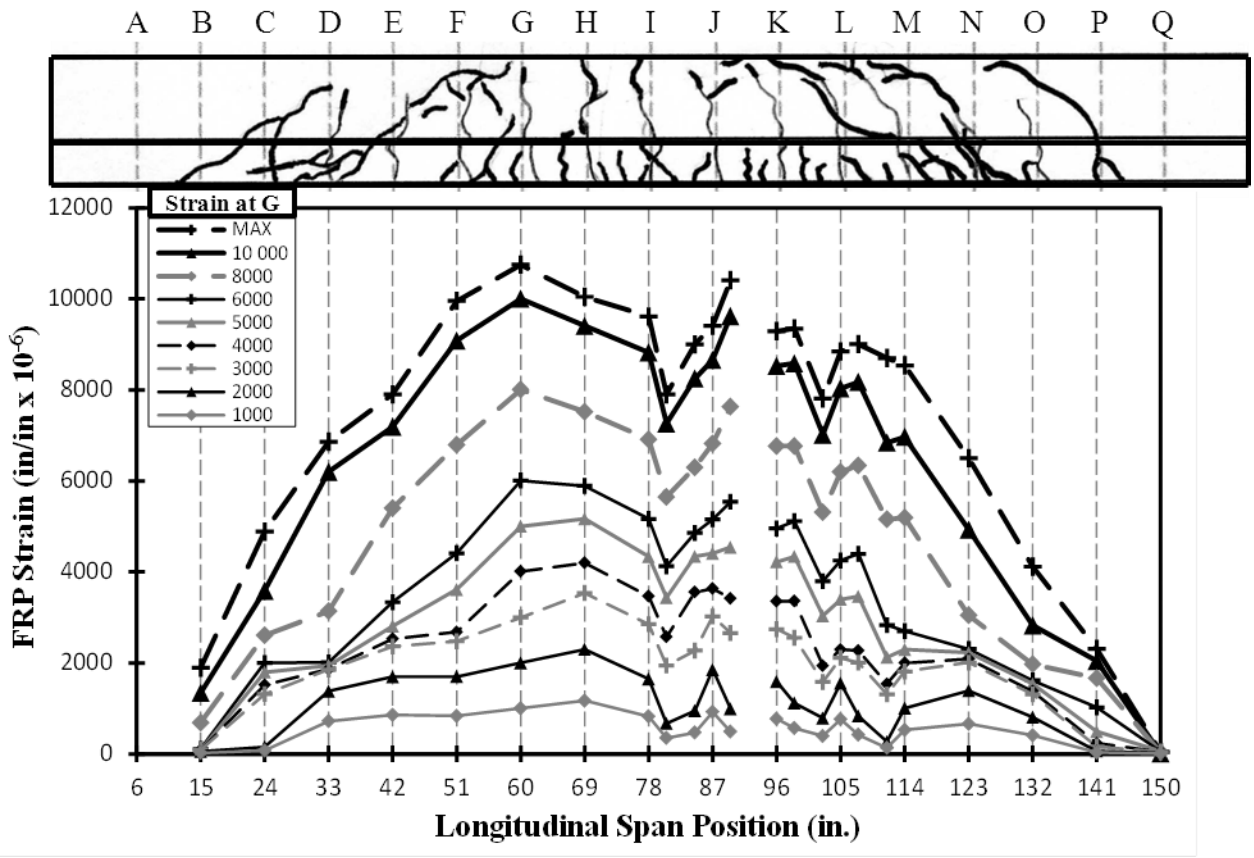

Figure 7.43 FRP Strain Distribution under Increasing Applied Load—LS6F16

7.2.2.5 Contribution of FRP to Internal Cross-Sectional Tensile Force

The internal forces in the reinforcement resulting from the application of load are shown in Figure 7.44 to Figure 7.49. The predicted internal forces correspond to the force values generated by the non-linear model for the tensile steel layer ("Steel") and the sum of the layers for the tensile steel and the FRP ("Combined"). The experimental internal forces ("Steel—Exp" and "Combined—Exp") were found by multiplying the experimental strain data for the reinforcement by the accompanying cross-sectional areas of the steel and FRP in the specimen. The difference between the combined internal forces and the force contribution from the steel indicates the contribution of the FRP to the overall tensile force at a given applied load. T_{FRP}

denotes the theoretical tensile contribution of the FRP; $T_{FRP,E}$, the experimental tensile contribution.

Each of the figures displays a nearly constant force contribution from the steel after yield, meaning that any increase in capacity is primarily related to the inclusion of greater amounts of FRP. Consequently, a proportional relationship exists between the increase in capacity and the increased contribution of the FRP to the tensile forces present in a given cross section. The predicted contribution of the FRP to the combined internal tensile force is approximately equivalent the contribution observed experimentally.

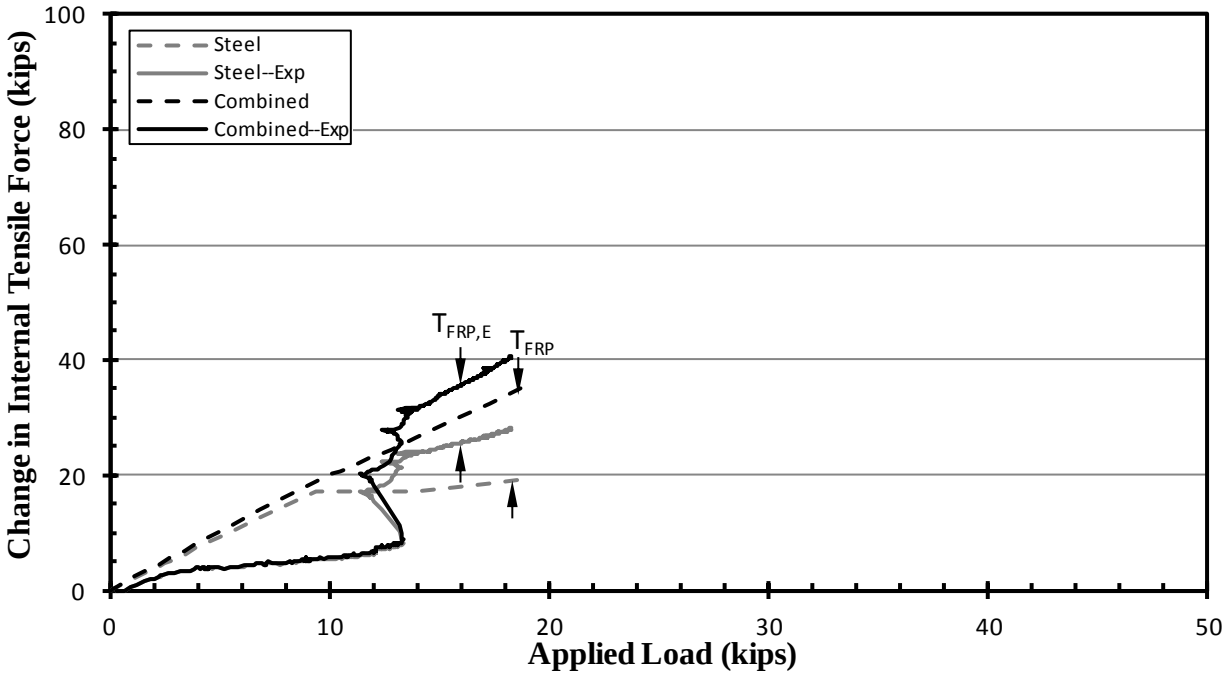

Figure 7.44 Internal Cross-Sectional Tensile Forces—LS2F03

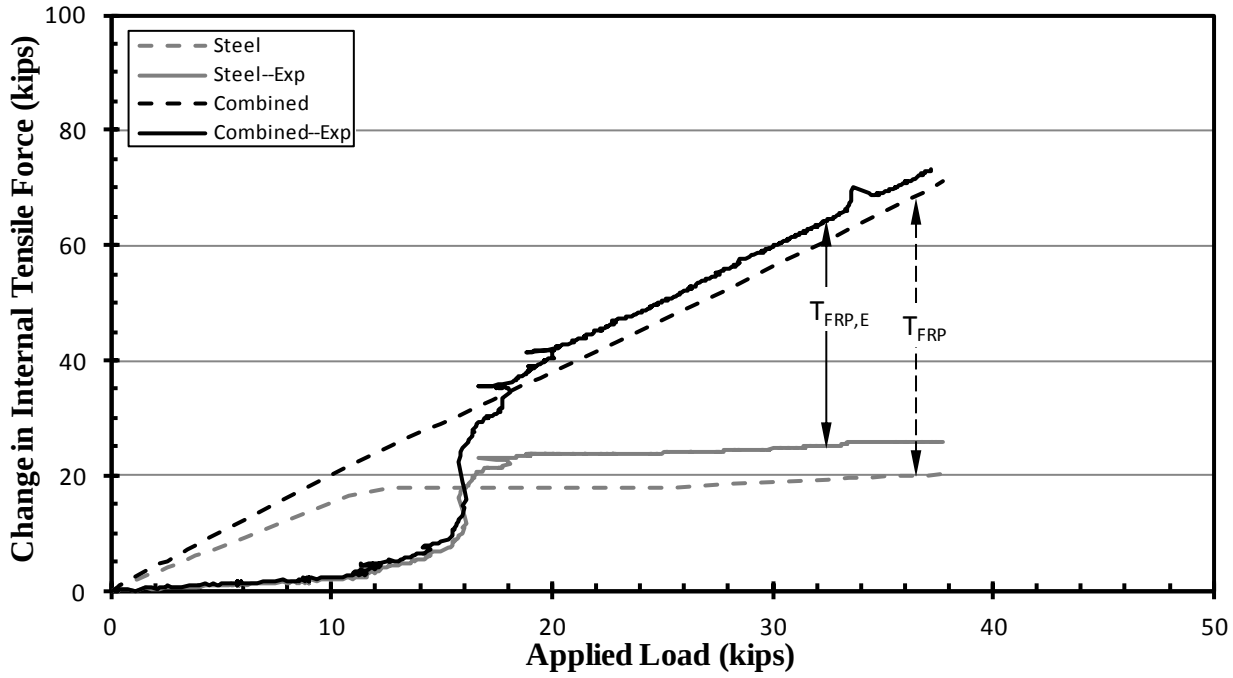

Figure 7.45 Internal Cross-Sectional Tensile Forces—LS2F08

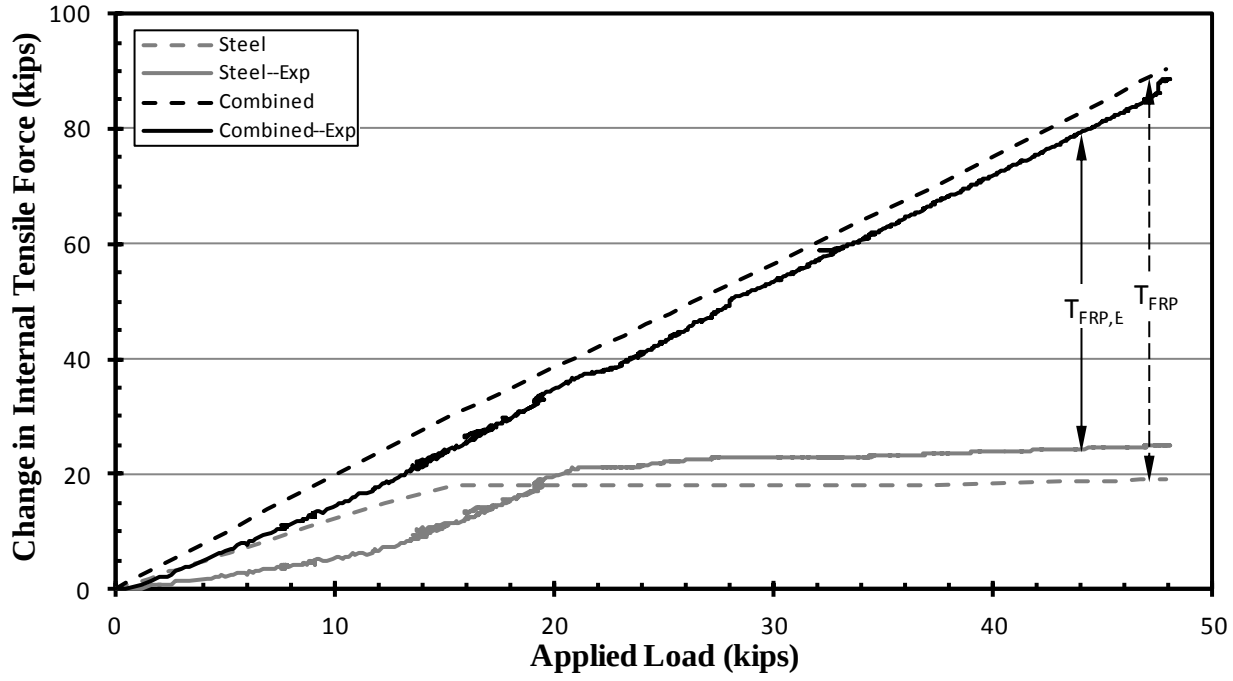

Figure 7.46 Internal Cross-Sectional Tensile Forces—LS2F16

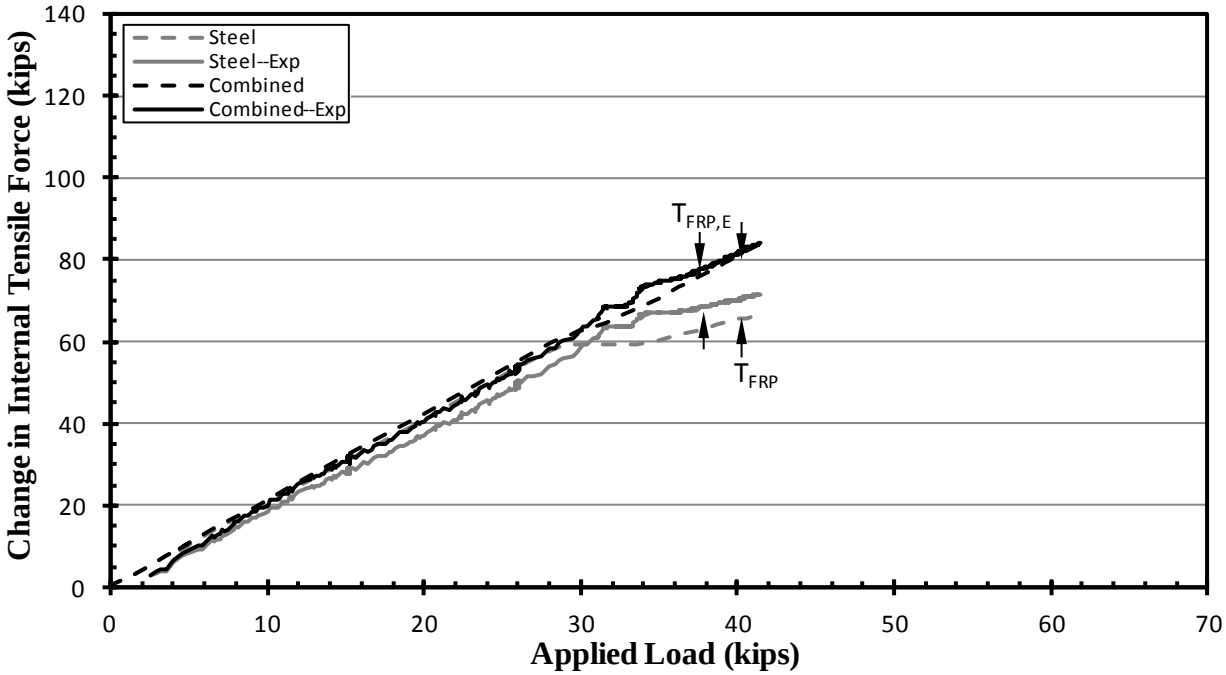

Figure 7.47 Internal Cross-Sectional Tensile Forces—LS6F03

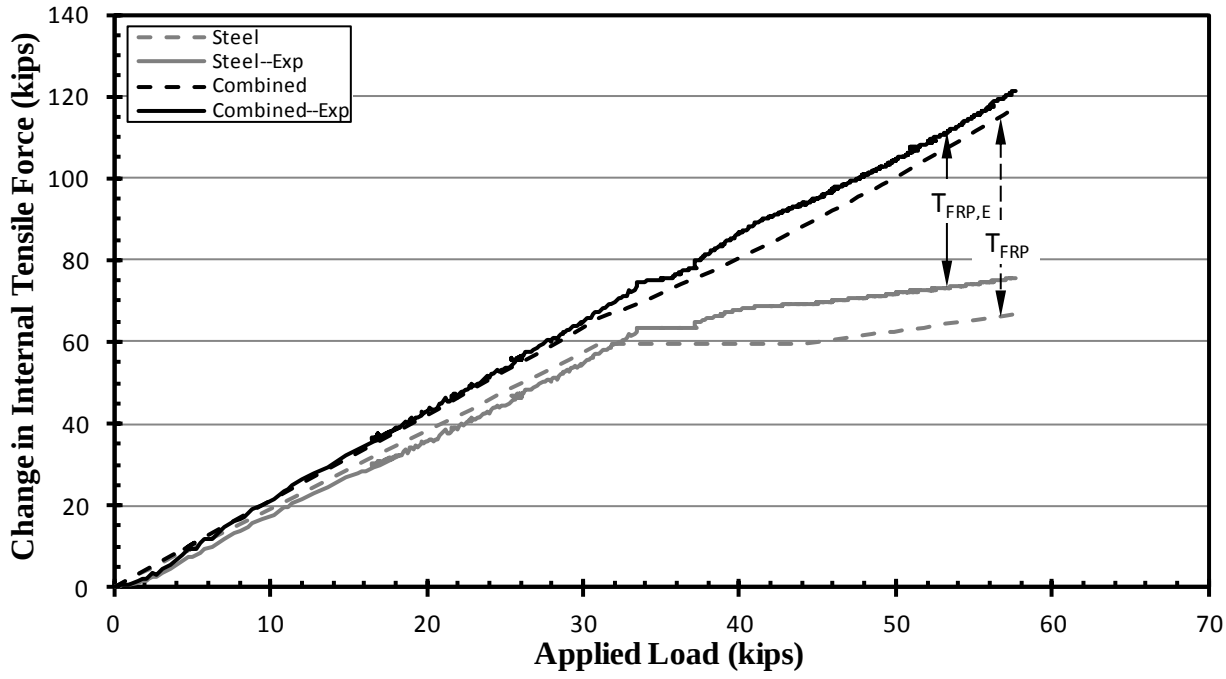

Figure 7.48 Internal Cross-Sectional Tensile Forces—LS6F08

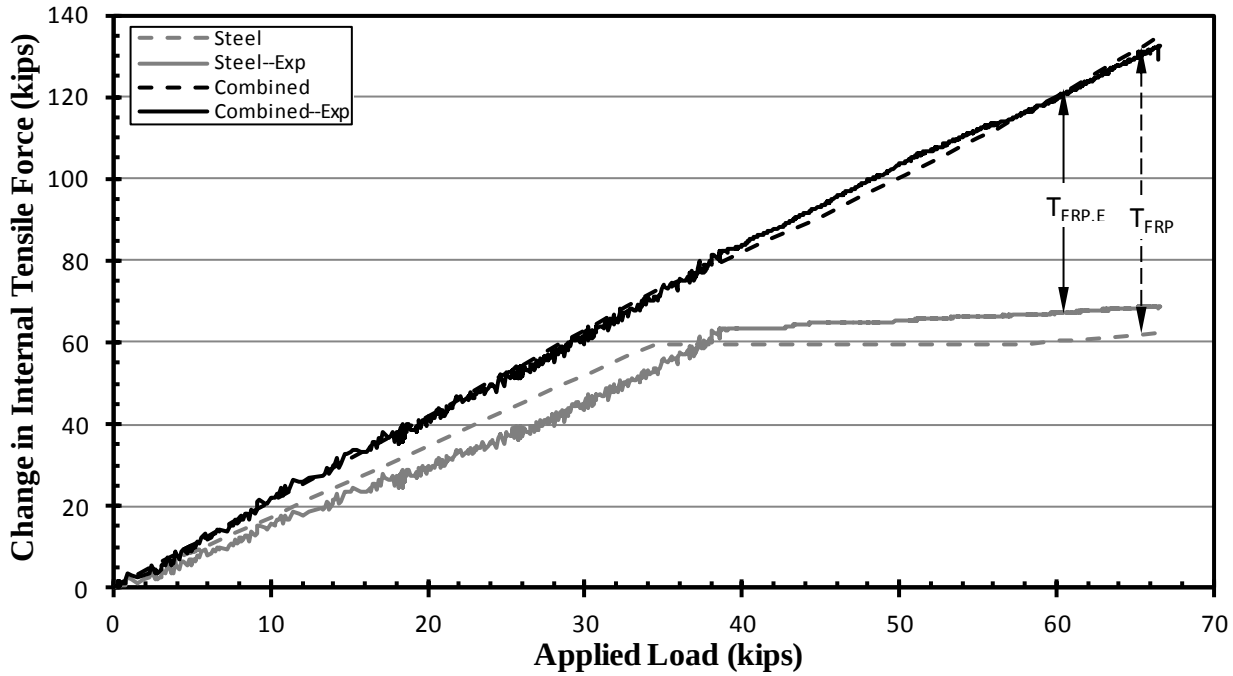

Figure 7.49 Internal Cross-Sectional Tensile Forces—LS6F16

Figure 7.50 and Figure 7.51 compare the internal force contribution of the FRP reinforcement based on the steel reinforcement ratio of the specimen. As observed, increasing the number of FRP strips provides approximately the same increased contribution to the internal tensile force capacity regardless of the amount of steel reinforcement. Both the theoretical and, more importantly, experimental curves display a linear relationship between the increase in the applied load and the increase in the internal force in the FRP after yield; this behavior indicates a consistent bond between the FRP and concrete with no evidence of IC debonding.

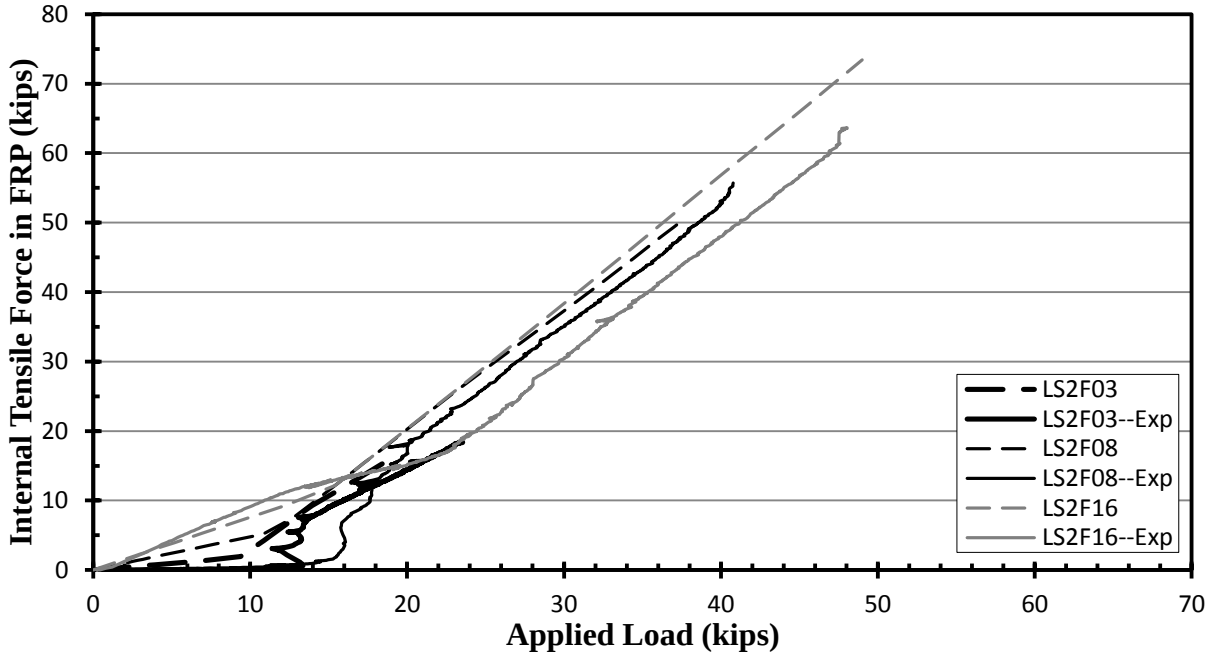

Figure 7.50 Internal Cross-Sectional Tensile Force in FRP—ρ_s = 0.2%

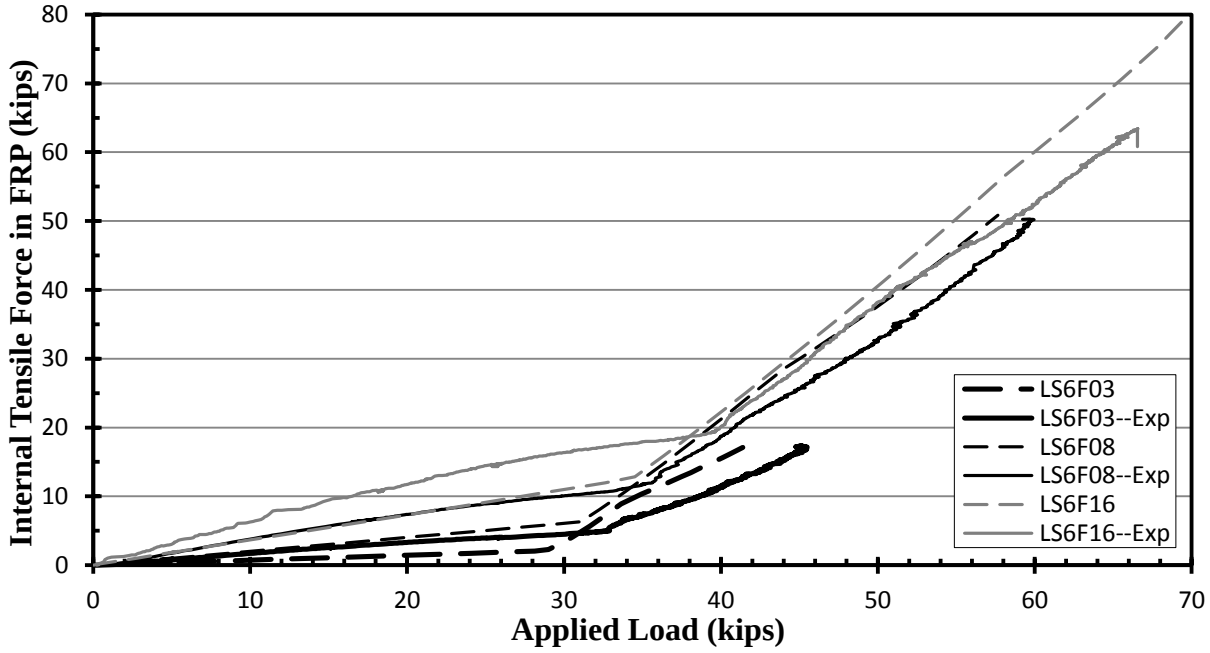

Figure 7.51 Internal Cross-Sectional Tensile Force in FRP—ρ_s = 0.6%

CHAPTER 8: SUMMARY AND CONCLUSIONS

8.1 Summary

The AL 97 bridge over I-65 near Letohatchee, Alabama, has been identified as having deficient capacity in the negative-moment regions of the girders, leading to load restrictions for the bridge. To remove these restrictions, near-surface-mounted (NSM) FRP strips are proposed as the strengthening system for the bridge.

Previous research at Auburn University (Alexy 2009) compared existing design limits against previous experimental results to determine the most accurate models for design. The three chosen models for IC-debonding resistance of NSM systems—ACI 440 (2008), Standards Australia (2008), and Seracino et al. (2007)—were applied with varying numbers of strips to find the most efficient arrangement of FRP that would produce the required moment capacity. However, the reinforcement ratios and historically representative concrete compressive strength for the Letohatchee bridge are lower than the ratios and strengths in the literature; additionally, very few of the NSM FRP test specimens were cracked prior to strengthening. Therefore, to provide experimental results that would directly correlate to the bridge, a laboratory test program for the NSM system was implemented.

Eight test specimens were fabricated, cracked, repaired, and tested in four-point loading scheme under service-load cycles followed by monotonic loading until failure. The beams were cast using concrete with a compressive strength of 3000 psi, reinforced with Grade 40 steel bars, and strengthened with NSM FRP strips placed in grooves after cracking. A nonlinear, layer-by-

layer flexural analytical model was performed using the material and geometric parameters for the test specimens in order to generate theoretical predictions for comparison with the experimental results.

Evaluation of the deflection and strain behaviors under service-load cycles shows no signs of degradation of the concrete-epoxy-FRP interface under sustained loading. The strains taken during monotonic load testing reveal that, after yield, plane sections no longer remain plane for the repaired cross sections, while examination of the cracking patterns and failures by concrete crushing displays evidence of excellent bond between the FRP and the concrete—further confirmed by the longitudinal strain distribution in the NSM reinforcement. Comparison between the ultimate strain, nominal moment capacity, and change in moment capacity found in each specimen and the predicted values based on the design limits and analytical model demonstrates that, for most of the specimens, the models offer conservative limits on the allowable strain in the reinforcement and conservative predictions of ultimate behavior. Assessment of the tensile force contribution of the FRP shows that the difference in capacity between specimens is based solely on the amount of NSM reinforcement applied and that the FRP exhibits no signs of debonding.

8.2 Conclusions

Several conclusions can be drawn from an assessment of the installation process for the NSM FRP strips, the performance of the strengthened test specimens, and the repair scheme for the Letohatchee bridge relative to observations from the testing process.

8.2.1 FRP Installation Process

Based on experienced gained in the laboratory application of the NSM FRP system, the following conclusions are justified:

1. The method and equipment used for cutting the required grooves for the NSM system should allow simple depth control and produce a continuous, straight cut.
2. Manual consolidation of the epoxy prevents the formation of voids and distributes the epoxy within the groove so as to facilitate proper bond to both the FRP and the concrete.
3. Proper placement of the FRP within the groove—allowing the epoxy to bond on all sides between the NSM strip and the concrete substrate—promotes full utilization of the FRP-epoxy-concrete bond for the desired repair.

8.2.2 Specimen Performance

By evaluating the experimental data for the eight test specimens and comparing the actual results with predicted values, the following conclusions were reached:

1. The modified tension stiffening relationship used to predict precracked behavior for the nonlinear analysis was too stiff for the lightly (steel) reinforced specimens, but appropriate for the moderately (steel) reinforced specimens in the pre-yield range of post-cracking behavior.
2. Analysis of the strain data and load-deflection behavior of the FRP reinforcement through 50,000 service-load cycles showed no signs of bond degradation.
3. Strain magnitudes within the cross section do not remain proportional to distance from the neutral axis after yield.
4. The consistent change in strain relative to increasing load and nearly linear internal force contribution recorded for the FRP after yield during monotonic testing show no evidence of IC debonding.
5. The presentation of numerous, small cracks near the FRP under load indicates a strong bond between the NSM reinforcement and the concrete.

6. Analysis of the strain distribution along the length of the strips showed no apparent stress concentrations as the load approached ultimate.
7. Strong bond of the FRP coupled with a concrete compressive strength of 3000 psi resulted in consistent failure from crushing of the concrete in the compression region.
8. The model developed by Said and Wu (2008) is overly conservative for the design of NSM FRP-strengthening schemes.
9. For reinforced concrete specimens with a concrete compressive strength of 3000 psi, the three main design approaches—ACI 440 (2008), Standards Australia (2008), and Seracino et al. (2007)—predict similar, conservative nominal moment capacities.
10. Within the parameters of this thesis, ACI 440 (2008) provides the most efficient prediction for the ultimate capacity of a NSM FRP-strengthened specimen.
11. The relationship recommended by ACI 440 (2008) may not remain conservative for FRP reinforcement amounts greater than the amounts utilized in this test program.
12. Altering the steel reinforcement ratio for a specimen within a range of 0.2–0.6% does not affect the strengthening provided by NSM FRP.

8.2.3 Field Application

Using the correlation between the test specimens and the girders in the Letohatchee bridge, the following conclusions can be drawn regarding the NSM FRP-strengthening of deficient bridges with similar designs:

1. The recommended strengthening scheme (Alexy 2009) of six thin FRP strips per girder per deficient region—or the reinforcement ratio corresponding to each arrangement—should be more than adequate to overcome the current moment capacity deficiency of the Letohatchee bridge based on test results.

2. For the Letohatchee bridge, the maximum spacing of the NSM FRP strips should be subject to limits designed to control both the propagation and size of present flexural cracks relative to the steel reinforcement.

8.3 Recommendations

For the installation of FRP in the field, the procedure as detailed in Chapter 4 can be used with little alteration. A modified concrete grooving trowel or similar tool should be used to seat the FRP strips to the proper depth to allow epoxy coverage for bond integrity and environmental protection. Care should also be taken to note the approximate ambient temperature at the time of installation for correlation with the curing time table for the epoxy—with the tape around the grooves being removed toward the end of the workable period to facilitate the removal of excess epoxy from the road surface. Taping the groove lines before cutting could also be explored in the interest of efficiency. The prescribed depth of the saw cuts should be carried through to the designated endpoints, ensuring the necessary bonded length for the FRP. Ground-penetrating radar should be used to ensure adequate concrete cover to fully embed the FRP strip without cutting into existing steel reinforcement. The exact effect of the exposure conditions on the life and performance of the NSM system could be explored in future research.

For the Letohatchee girders, cores should be taken to verify the current concrete compressive strength as 3000 psi to allow the implementation of more efficient strengthening schemes; likewise, cores from bridges of similar design with similar deficiencies should be tested prior to repair to ensure the proper correlation with the results and conclusions of this thesis. Further research should be conducted to examine the behavior of thick FRP strips when applied to girders with similar parameters to the Letohatchee bridge if less conservative, but still viable, design options are to be allowed for proposed strengthening schemes. The use of thicker strips

promises significant cost savings on construction and labor. Therefore, testing of thick-strip configurations is strongly recommended. Regardless of the amount of FRP installed, yielding of the steel reinforcement should be avoided under service loads. The yield load can be conservatively estimated using a linear-elastic, cracked-section analysis that includes the stiffness contribution of the reinforcing steel and the FRP. This constraint will often limit the amount of additional load that can be allowed on an FRP-strengthened structure.

Continued flexural testing should be performed in order to provide a larger statistical sample for establishing the behavioral trends observed in the strengthened, precracked specimens of this test series and to study the strengthening effect of NSM FRP on members with higher concrete compressive strengths and different cross-sectional shapes. The accuracy of the reduction factor for the ACI 440 (2008) relationship—as applied to specimens within the test parameters—could be examined by generating theoretical data based on multiple reduction values. Future test specimens should be redesigned with tighter stirrup spacing to prevent shear as the primary failure mode. If possible, full-scale testing is recommended to better establish the effectiveness of NSM FRP systems in direct correlation to existing structures.

REFERENCES

AASHTO. 1996. *AASHTO Standard Specifications for Highway Bridges*. 16th ed. Washington, D.C.: American Association of State Highway and Transportation Officials (AASHTO).

ACI Committee 318. 2008. Building Code Requirements for Structural Concrete (ACI 318-08) and Commentary. Farmington Hills, MI: American Concrete Institute (ACI).

ACI Committee 440. 2008. Guide for the Design and Construction of Externally Bonded FRP System for Strengthening Concrete Structures (ACI 440.2R-08). Farmington Hills, MI: American Concrete Institute (ACI).

Aidoo, J., K. A. Harries, and M. F. Petrou. 2006. Full-Scale Experimental Investigation of Repair of Reinforced Concrete Interstate Bridge Using CFRP Materials. *Journal of Bridge Engineering* 11, no. 3: 350-358.

Alexy, J. K. 2009. Near-Surface Mounted, Fiber-Reinforced Polymer Strips for Negative-Moment Strengthening of Concrete Bridges—Design Methodology. M.S. thesis, Auburn University.

ASTM Standard A615. 2009. Standard Specification for Deformed and Plain Carbon-Steel Bars for Concrete Reinforcement (ASTM A615-09b). West Conshohocken, PA: ASTM International.

ASTM Standard C78. 2010. Standard Test Method for Flexural Strength of Concrete (Using Simple Beam with Third-Point Loading (ASTM C78-10). West Conshohocken, PA: ASTM International.

ASTM Standard C192. 2007. Standard Practice for Making and Curing Concrete Test Specimens in the Laboratory (ASTM C192-07). West Conshohocken, PA: ASTM International.

Badawi, M., and K. Soudki. 2009. Fatigue Behavior of RC Beams Strengthened with NSM CFRP Rods. *Journal of Composites for Construction* 13, no. 5: 415-421.

Bazant, Z. P., and Z. Li. 1995. Modulus of Rupture: Size Effect due to Fracture Initiation in Boundary Layer. *Journal of Structural Engineering* 121, no. 4: 739-746.

Bergstrom, M., B. Taljsten, and A. Carolin. 2009. Failure Load Test of a CFRP Strengthened Railway Bridge in Ornskoldsvik, Sweden. *Journal of Bridge Engineering* 14, no. 5: 300-308.

Bonaldo, E., J. A. O. de Barros, and P. B. Lourenco. 2008. Efficient Strengthening Technique to Increase the Flexural Resistance of Existing RC Slabs. *Journal of Composites for Construction* 12, no. 2: 149-159.

Blaschko, M. 2003. Bond Behaviour of CFRP Strips Glued into Slits. In *6th International Symposium on FRP Reinforcement for Concrete Structures (FRPRCS-6)*, ed. K. H. Tan. Singapore: World Scientific, 205-214.

Carmichael, B. M., and R. W. Barnes. 2005. *Repair of the Uphapee Creek Bridge with FRP Laminates*. Final Report RP-930-466-2, Auburn, AL: Auburn University Highway Research Center.

Collins, M. P., and D. Mitchell. 1991. *Prestressed concrete structures*. Englewood Cliffs, New Jersey: Prentice-Hall.

El-Hacha, R., and S. H. Rizkalla. 2004. Near-Surface-Mounted Fiber-Reinforced Polymer Reinforcements for Flexural Strengthening of Concrete Structures. *ACI Structural Journal* 101, no. 5: 717-726.

Fanning, P. J., and O. Kelly. 2001. Ultimate Response of RC Beams Strengthened with CFRP Plates. *Journal of Composites for Construction* 5, no. 2: 122-127.

Google Maps. 2011. http://maps.google.com (accessed 7 December 2011).

Hamilton, H. R. III, A. Michael, and C. O'Neill. 2007. *Testing Bridge Decks with Near-Surface Mounted FRP Bars Embedded in Cement Based Grout*. Final Report to FDOT Structures Research Center, UF Project No. 00065162. Gainesville, FL: University of Florida.

Harrison, R. R., H. A. Rasheed, R. J. Peterman, and T. Alkhrdaji. 2006. Comparison of Four Techniques for Strengthening Concrete Beams Using Performance and Practicality Criteria. In *Structures Congress 2006: Structural Engineering and Public Safety*. *St Louis, MI. 18 May 2006*. Reston, VA: ASCE.

Hassan, T. K., and S. H. Rizkalla. 2004. Bond Mechanism of Near-Surface-Mounted Fiber-Reinforced Polymer Bars for Flexural Strengthening of Concrete Structures. *ACI Structural Journal* 101, no. 6: 830-839.

Hilti. 2008. Product Technical Guide 2008. http://www.hilti.com (accessed 31 March 2010).

Hughes Brothers. 2011. http://aslanfrp.com/Aslan500/aslan500-pg1.html (accessed 7 December 2011).

Jung, W.-T., Y.-H. Park, J.-S. Park, J.-Y. Kang, and Y.-J. You. 2005. Experimental Investigation on Flexural Behavior of RC Beams Strengthened by NSM CFRP Reinforcements. In *7th International Symposium: Fiber-Reinforced Polymer (FRP) Reinforcement for Concrete Structures*, eds. Carol K. Shield, John P. Busel, Stephanie L. Walkup, and Doug D. Gremel. Farmington Hills, MI: American Concrete Institute, 795-806.

Kang, J.-Y., Y.-H. Park, J.-S. Park, Y.-J. You, and W.-T. Jung. 2005. Analytical Evaluation of RC Beams Strengthened with Near Surface Mounted CFRP Laminates. In *7th*

International Symposium: Fiber-Reinforced Polymer (FRP) Reinforcement for Concrete Structures, eds. Carol K. Shield, John P. Busel, Stephanie L. Walkup, and Doug D. Gremel. Farmington Hills, MI: American Concrete Institute, 779-794.

Lee, D., and L. Cheng. 2011. Assessing the Strengthening Effect of Various Near-Surface-Mounted FRP Reinforcements on Concrete Bridge Slab Overhangs. *Journal of Composites for Construction* 15, no. 4: 615-624.

Liu, I. S. T., D. J. Oehlers, and R. Seracino. 2006. Tests on the Ductility of Reinforced Concrete Beams Retrofitted with FRP and Steel Near-Surface Mounted Plates. *Journal of Composites for Construction* 10, no. 2: 106-114.

MacGregor, James G., and James K. Wight. 2005. *Reinforced Concrete: Mechanics and Design*. 4th ed. Upper Saddle River, NJ: Pearson Prentice Hall

Oehlers, D. J., M. S. M. Ali, M. Haskett, W. Lucas, R. Muhamad, and P. Visintin. 2011. FRP-Reinforced Concrete Beams: Unified Approach Based on IC Theory. *Journal of Composites for Construction* 15, no. 3: 293-303.

Oehlers, D. J., M. Haskett, C. Wu, and R. Seracino. 2008. Embedding NSM FRP Plates for Improved IC Debonding Resistance. *Journal of Composites for Construction* 12, no. 6: 635-642.

Quattlebaum, J. B., K. A. Harries, and M. F. Petrou. 2005. Comparison of Three Flexural Retrofit Systems under Monotonic and Fatigue Loads. *Journal of Bridge Engineering* 10, no. 6: 731-740.

Rashid, R., D. J. Oehlers, and R. Seracino. 2008. IC Debonding of FRP NSM and EB Retrofitted Concrete: Plate and Cover Interaction Tests. *Journal of Composites for Construction* 12, no. 2: 160-167.

Reed, M. W. 2003. Effects of Traffic Loads during FRP Strengthening of the War Memorial Bridge. M.S. thesis, Auburn University.

Said, H., and Z. Wu. 2008. Evaluating and Proposing Models of Predicting IC Debonding Failure. *Journal of Composites for Construction* 12, no. 3: 284-299.

Seracino, R., N. M. Jones, M. S. M. Ali, M. W. Page, and D. J. Oehlers. 2007. Bond Strength of Near-Surface Mounted FRP Strip-to-Concrete Joints. *Journal of Composites for Construction* 11, no. 4: 401-409.

Seracino, R., M. R. Raizal Saifulnaz, and D. J. Oehlers. 2007. Generic Debonding Resistance of EB and NSM Plate-to-Concrete Joints. *Journal of Composites for Construction* 11, no. 1: 62-70.

Standards Australia. 2008. Design handbook for RC structures retrofitted with FRP and metal plates: beams and slabs (HB 305-2008). Sydney, Australia: Standards Australia.

Taljsten, B., and H. Nordin. 2007. Concrete Beams Strengthened with External Prestressing Using External Tendons and Near-Surface-Mounted Reinforcement (NSMR). In *SP-245CD Case Histories and Use of FRP for Prestressing Applications*, eds. Raafat El-Hacha and Sami H. Rizkalla. Farmington Hills, MI: American Concrete Institute, 143-164. CD-ROM.

Teng, J. G., L. De Lorenzis, B. Wang, R. Li, T. N. Wong, and L. Lam. 2006. Debonding Failures of RC Beams Strengthened with Near Surface Mounted CFRP Strips. *Journal of Composites for Construction* 10, no. 2: 92-105.

Tumialan, J. G., M. Vatovec, and P. L. Kelley. 2007. Case Study: Strengthening of Parking Garage Decks with Near-Surface-Mounted CFRP Bars. *Journal of Composites for Construction* 11, no. 5: 523-530.

Vasquez Rayo, D. L. 2008. Plate-End Debonding of Longitudinal Near-Surface Mounted Fiber Reinforced Polymer Strips on Reinforced Concrete Flexural Members. M.S. thesis, North Carolina State University.

Wahab, N., K. A. Soudki, and T. Topper. 2011. Mechanism of Bond Behavior of Concrete Beams Strengthened with Near-Surface-Mounted CFRP Rods. *Journal of Composites for Construction* 15, no. 1: 85-92.

Wyoming Department of Transportation. 2009. BRASS™ program. http://dot.state.wy.us/web/brass/index.html (accessed 21 April 2009).

Yost, J. R., S. P. Gross, D. W. Dinehart, and J. J. Mildenberg. 2007. Flexural Behavior of Concrete Beams Strengthened with Near-Surface-Mounted CFRP Strips. *ACI Structural Journal* 104, no. 4: 430-437.

APPENDIX A: NOTATION

a_b	=	smaller cross-sectional dimension for rectangular FRP bars
A_f	=	area of FRP reinforcement
A_p	=	cross-sectional area of FRP plate
A_s	=	area of tensile steel reinforcement
b	=	width of the member compression block
b_b	=	larger cross-sectional dimension for rectangular FRP bars
b_f	=	length of failure place parallel to concrete surface
b_p	=	FRP plate dimension parallel to concrete surface
c	=	neutral axis depth
$C1$	=	constant
$C2$	=	constant
$C3$	=	constant
c_{cr}	=	neutral axis of cracked cross section
C_E	=	environmental reduction factor
d	=	distance to centroid of tensile reinforcement from extreme compression fiber
d_b	=	FRP bar diameter (ACI 440 2008)
d_b	=	bar diameter of steel reinforcement
d_f	=	effective depth of FRP reinforcement
d_f	=	length of failure plane perpendicular to concrete surface (Seracino, Raizal Saifulnaz, and Oehlers 2007)
d_p	=	FRP plate dimension perpendicular to concrete surface
$(EA)_p$	=	axial rigidity of FRP
E_c	=	modulus of elasticity for concrete
E_f	=	modulus of elasticity for FRP reinforcement
E_s	=	modulus of elasticity for steel reinforcement
f_c	=	concrete compressive strength
f_c	=	concrete stress (Collins and Mitchell 2001)
f_c'	=	28-day compressive strength for concrete (Collins and Mitchell 2001)
f_{cr}	=	cracking stress of concrete
f_f	=	stress in FRP reinforcement

f_{fd} = design stress of FRP

f_{fe} = effective stress in FRP at failure

f_{fu} = design ultimate strength of FRP

f_{fu}^{*} = ultimate tensile strength of FRP as reported by manufacturer

f_r = apparent rupture stress of concrete

$f_{r,ASTM}$ = results of the rupture test specimens as specified by ASTM C-78

f_{rupt} = rupture stress of FRP

f_s = stress in tensile steel reinforcement

f_y = yield stress of steel reinforcement

h = overall height of member

$I_{cr,f}$ = cracked section moment of inertia

k = decay factor = $0.67 + \frac{f_c^{'}}{9000}$ if $\varepsilon_c \geq \varepsilon_c^{'}$, otherwise 1.0

L = bonded length of FRP

l_{df} = development length of FRP

L_{per} = length of debonding failure plane

M_{app} = maximum applied moment

M_{cr} = applied cracking moment

M_n = nominal moment capacity

M_w = maximum moment due to self-weight

M_y = moment for yielding of the tensile steel assuming linear-elastic, cracked-section behavior

n = curve-fitting factor = $0.8 + \frac{f_c^{'}}{2500}$

P_{app} = load applied by hydraulic actuator

P_{IC} = tensile resistance force to IC debonding

t_b = distance to failure plane from face of FRP

t_d = distance to failure plane from face of FRP

$t_{cure,full}$ = time until full cure and load capacity of epoxy

$t_{cure,ini}$ = time until initial cure of epoxy for limited loading capacity

t_f = thickness of the applied FRP plate

T_{FRP} = predicted internal force contribution of FRP reinforcement

$T_{FRP,E}$ = experimental internal force contribution of FRP reinforcement

t_{work} = workable time limit for epoxy

w/cm = water-to-cementitious materials ratio

α = confidence factor = 0.19 for mean values; 0.16 for characteristic values

α_1 = multiplier on $f_c^{'}$ to determine intensity of equivalent rectangular stress distribution (ACI 440 2008)

α_1 = reinforcement bond factor = 1.0 for deformed bars (Collins and Mitchell 2001)

α_2 = sustained/repeated loading factor = 1.0 for monotonic loading

α_p = confidence factor = 1.0 for mean; 0.85 for lower 95% confidence limit

β = bond-length factor

β_1 = ratio of depth of equivalent stress block to depth of neutral axis

ΔM = change in bending moment experience during service load cycle

$\Delta\varepsilon_f$ = expected change in strain in FRP during service load cycle

$\Delta\varepsilon_s$ = expected change in strain in tensile steel during service load cycle

ε_{bi} = strain in concrete substrate at time of FRP installation

ε_c = concrete strain in extreme compression fiber at failure

ε_c = concrete strain (Collins and Mitchell)

ε_c' = maximum strain of unconfined concrete corresponding to $f_c^{'} = 1.7\, f_c^i / E_c$ (ACI 440 2008)

$\varepsilon_c^{'}$ = concrete strain at $f_c^{'} = \frac{f_c^{'}}{E_c}\frac{n}{n-1}$ (Collins and Mitchell 2001)

ε_{cu} = maximum usable strain of unconfined concrete, generally taken as 0.003 in/in

ε_{db} = debonding strain

ε_f = strain in FRP reinforcement

ε_{fd} = debonding strain of FRP

ε_{fe} = effective strain level in FRP at failure

ε_{fu} = design rupture strain of FRP

ε_{fu}^* = ultimate rupture strain of FRP

ε_s = strain in nonprestressed steel reinforcement

ρ_f = FRP reinforcement ratio

ρ_f^* = normalized FRP reinforcement ratio

ρ_f^*/ρ_s = relative strengthening ratio

ρ_s = steel reinforcement ratio

τ_b = average bar stress for NSM FRP = 1000 psi (6.9 MPa)

φ_f = confinement ratio

ψ_f = additional strength reduction factor for FRP = 0.85 for flexure

ω_s = mechanical reinforcement ratio

APPENDIX B: CYCLIC LOAD VERSUS DEFLECTION CURVES

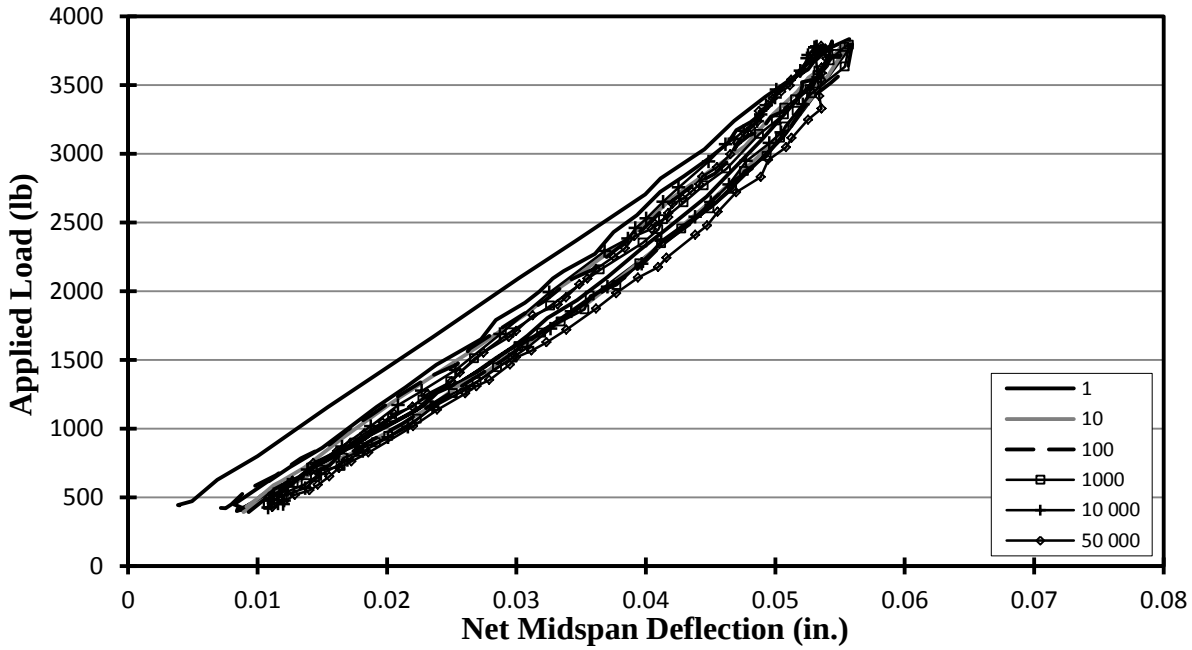

Figure B.1 Cyclic Load versus Deflection—LS2F00

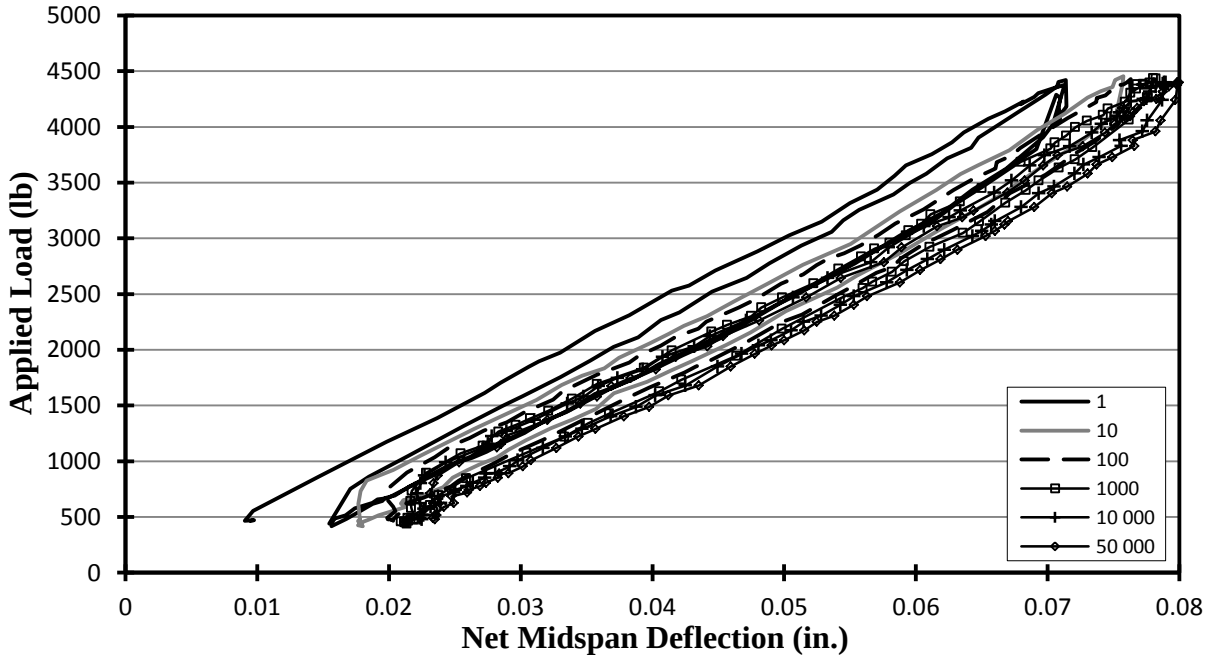

Figure B.2 Cyclic Load versus Deflection—LS2F03

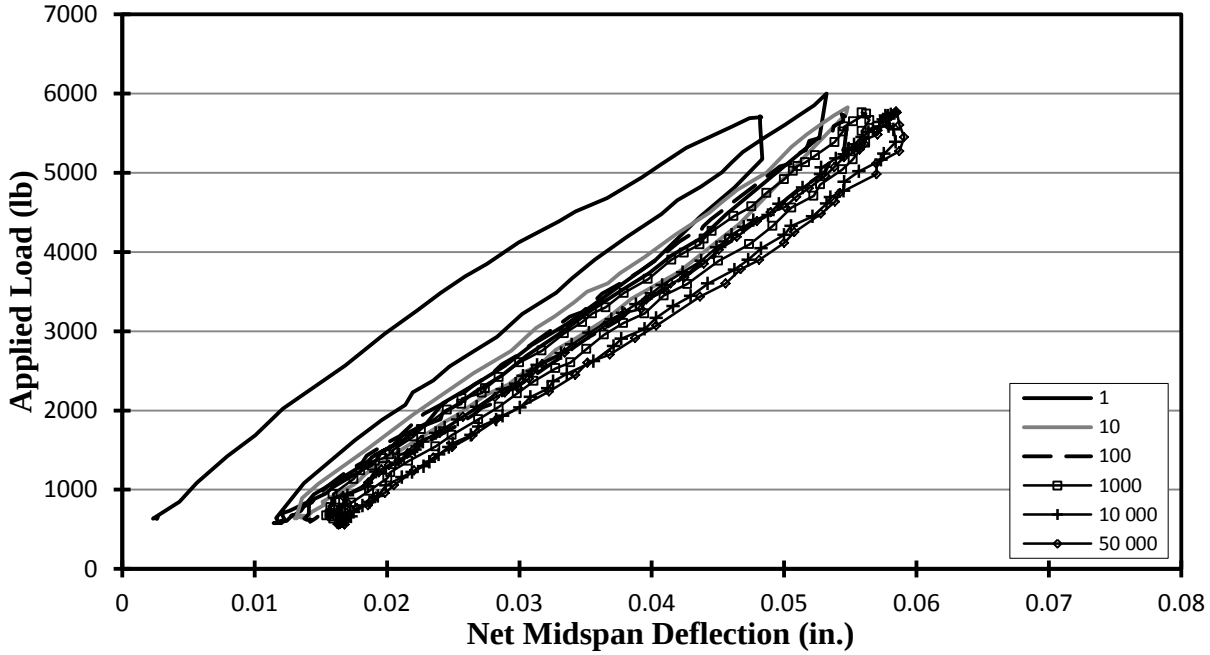

Figure B.3 Cyclic Load versus Deflection—LS2F08

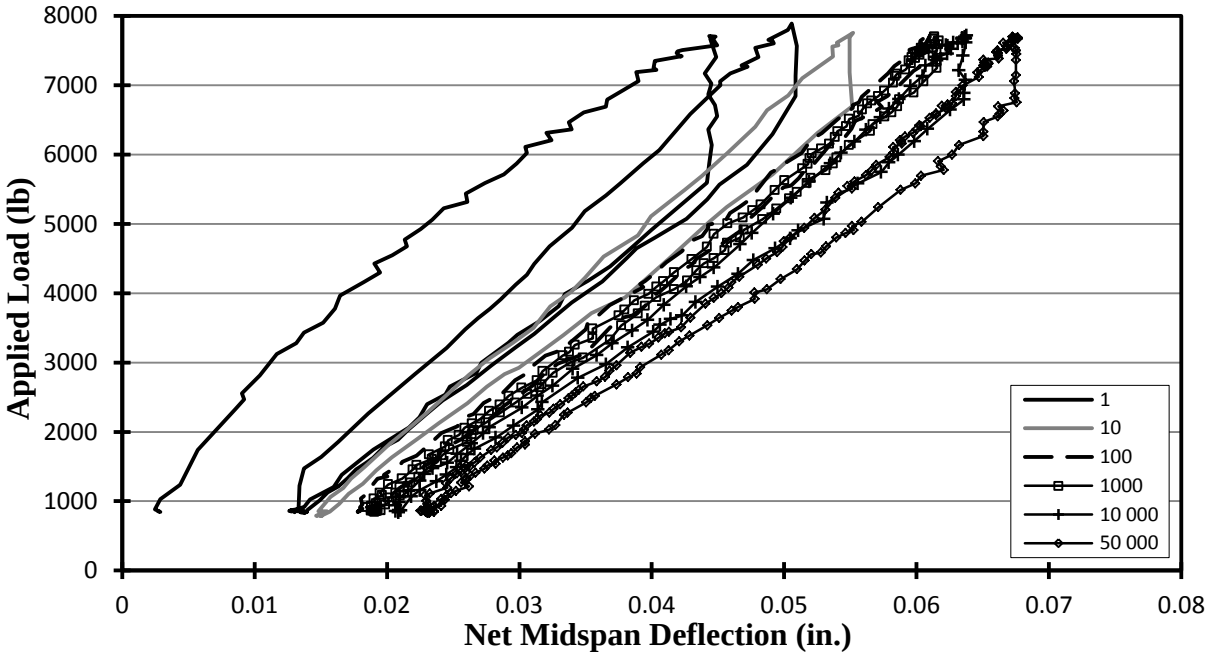

Figure B.4 Cyclic Load versus Deflection—LS2F16

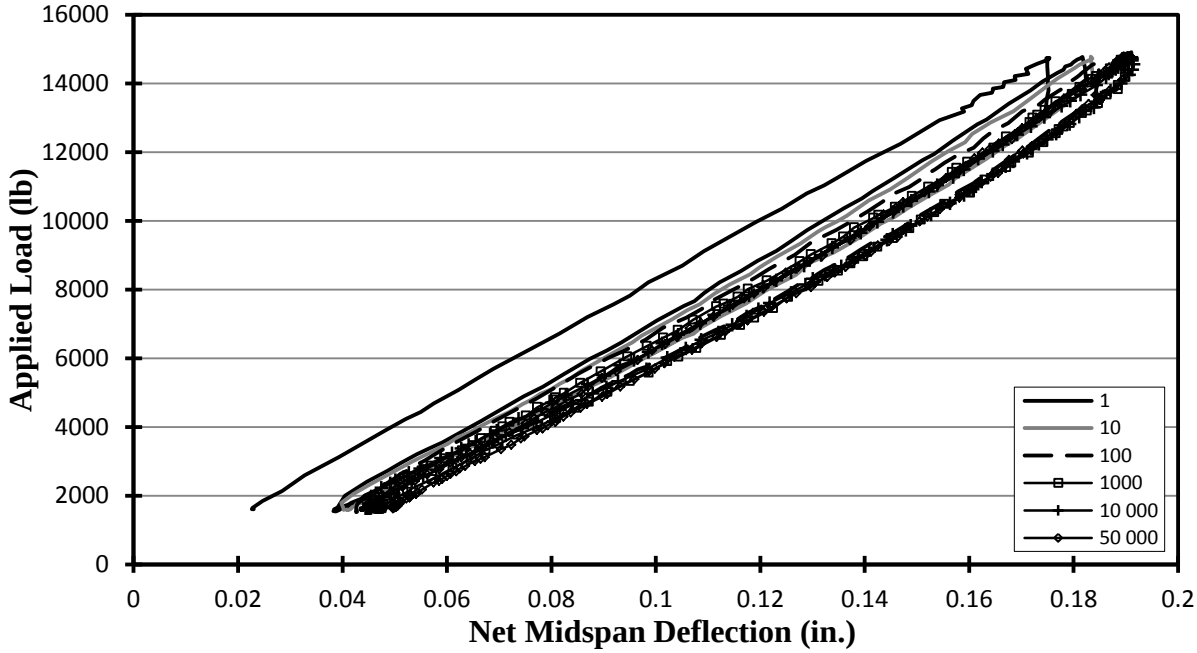

Figure B.5 Cyclic Load versus Deflection—LS6F00

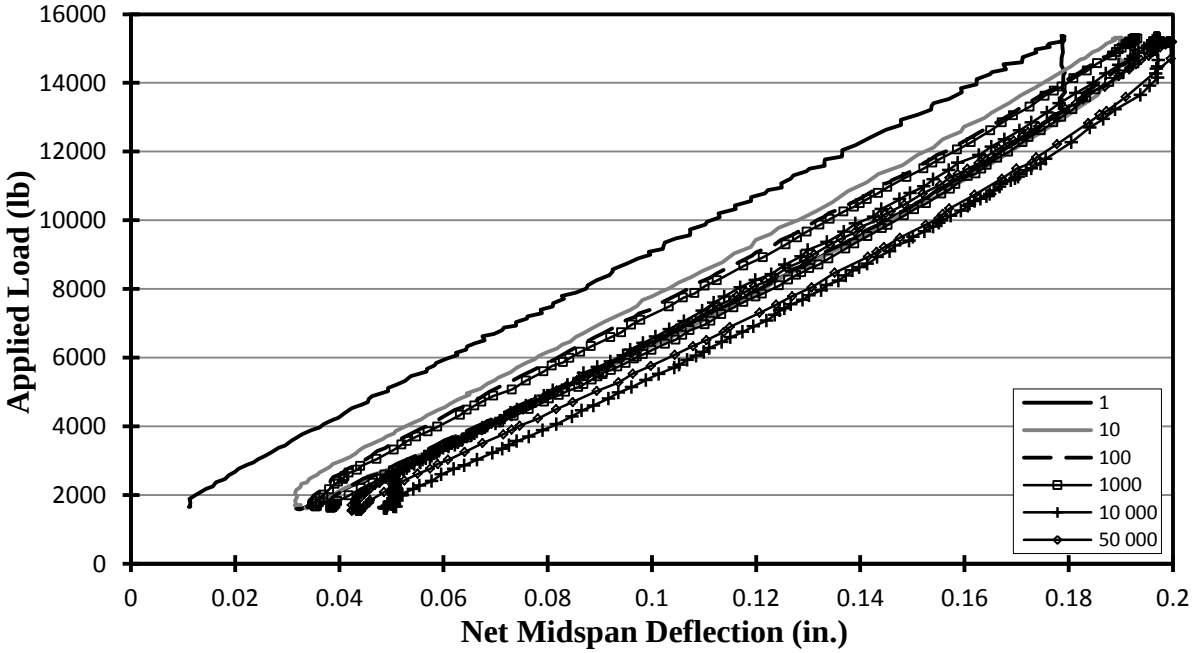

Figure B.6 Cyclic Load versus Deflection—LS6F03

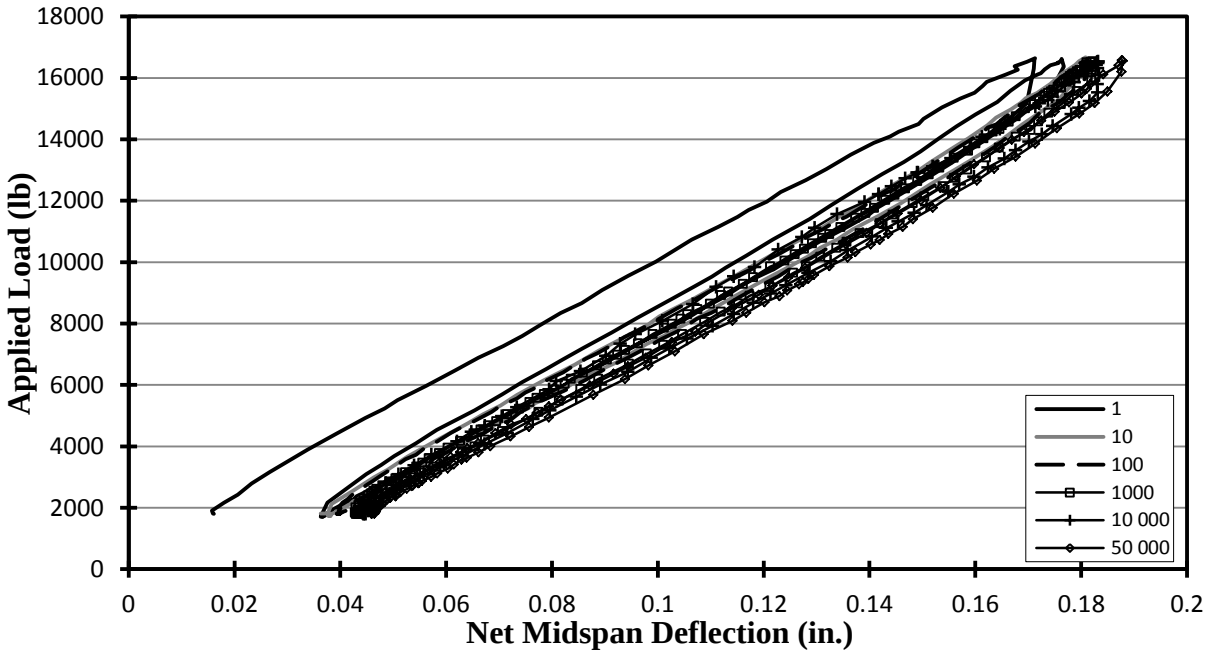

Figure B.7 Cyclic Load versus Deflection—LS6F08

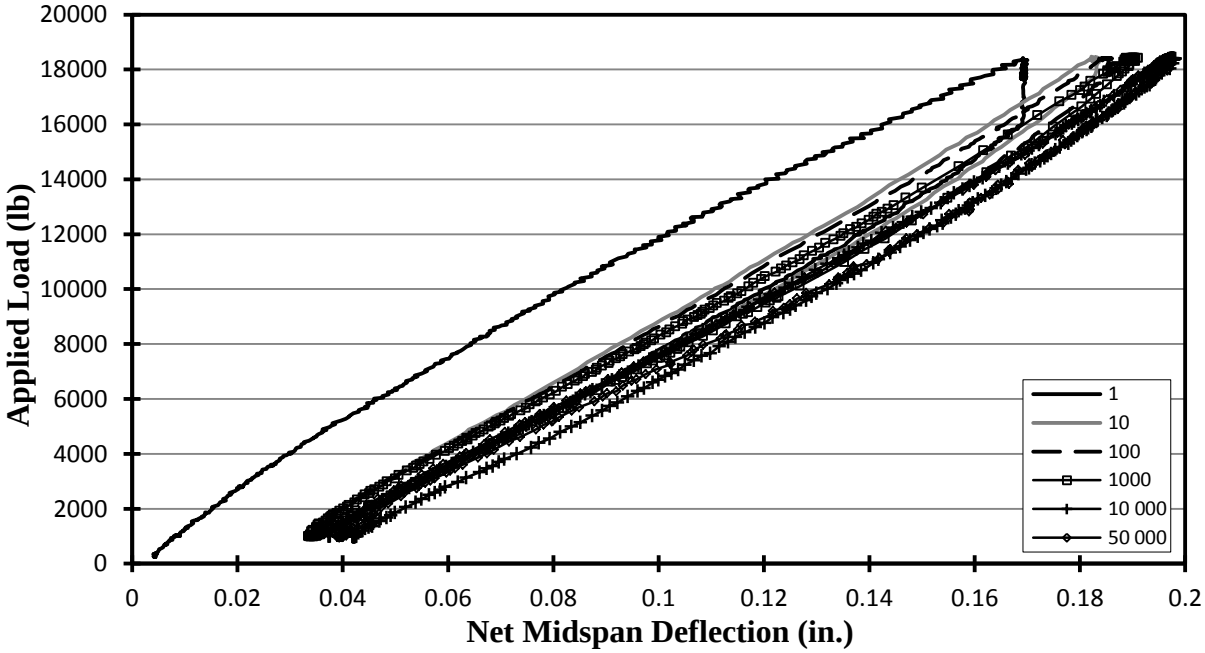

Figure B.8 Cyclic Load versus Deflection—LS6F16